



N7922140

**NTIS**<sup>®</sup>  
Information is our business.

---

---

# THE DEEP SPACE NETWORK PROGRESS REPORT 42-50 JANUARY AND FEBRUARY 1979

JET PROPULSION LABORATORY  
PASADENA, CA

APR 79



U.S. DEPARTMENT OF COMMERCE  
National Technical Information Service

---

---

# The Deep Space Network Progress Report 42-50

January and February 1979

(NASA-CR-158490) THE DEEP SPACE NETWORK  
Progress Report, Jan. 1979 - Feb. 1979 (Jet  
Propulsion Lab.) 249 p HC A11/MF A01

CSCI 14B

G3/12

N79-22140  
THRU  
N79-22171  
Unclas  
24827

April 15, 1979

National Aeronautics and  
Space Administration

Jet Propulsion Laboratory  
California Institute of Technology  
Pasadena, California



REPRODUCED BY  
U.S. DEPARTMENT OF COMMERCE  
NATIONAL TECHNICAL  
INFORMATION SERVICE  
SPRINGFIELD, VA 22161

# **The Deep Space Network Progress Report 42-50**

**January and February 1979**

**April 15, 1979**

**National Aeronautics and  
Space Administration**

**Jet Propulsion Laboratory  
California Institute of Technology  
Pasadena, California**

The research described in this publication was carried out by the Jet Propulsion Laboratory, California Institute of Technology, under NASA Contract No. NAS7-100.

## Preface

Beginning with Volume XX, the Deep Space Network Progress Report changed from the Technical Report 32- series to the Progress Report 42- series. The volume number continues the sequence of the preceding issues. Thus, Progress Report 42-20 is the twentieth volume of the Deep Space Network series, and is an uninterrupted follow-on to Technical Report 32-1526, Volume XIX.

This report presents DSN progress in flight project support, tracking and data acquisition (TDA) research and technology, network engineering, hardware and software implementation, and operations. Each issue presents material in some, but not all, of the following categories in the order indicated.

### Description of the DSN

#### Mission Support

- Ongoing Planetary/Interplanetary Flight Projects
- Advanced Flight Projects

#### Radio Astronomy

#### Special Projects

#### Supporting Research and Technology

- Tracking and Ground-Based Navigation
- Communications—Spacecraft/Ground
- Station Control and Operations Technology
- Network Control and Data Processing

#### Network and Facility Engineering and Implementation

- Network
- Network Operations Control Center
- Ground Communications
- Deep Space Stations
- Quality Assurance

#### Operations

- Network Operations
- Network Operations Control Center
- Ground Communications
- Deep Space Stations

#### Program Planning

- TDA Planning

In each issue, the part entitled "Description of the DSN" describes the functions and facilities of the DSN and may report the current configuration of one of the seven DSN systems (Tracking, Telemetry, Command, Monitor & Control, Test & Training, Radio Science, and Very Long Baseline Interferometry).

The work described in this report series is either performed or managed by the Tracking and Data Acquisition organization of JPL for NASA.

## Contents

### DESCRIPTION OF THE DSN

<b>Network Functions and Facilities</b> . . . . .	1
N. A. Renzetti	
<b>The DSN Programming System</b> . . . . .	4
A. P. Irvine	
NASA Code 311-03-41-15	
<b>DSN Test and Training System, Mark III-77</b> . . . . .	7
D. T. Herrman, Jr.	
NASA Code 311-03-43-10	

### MISSION SUPPORT

#### Ongoing Planetary/Interplanetary Flight Projects

<b>Voyager Support</b> . . . . .	19
J. Allen and H. Nance	
NASA Code 311-03-22-20	
<b>Pioneer Venus Multiprobe Entry Mission Support</b> . . . . .	24
B. Ryan, D. Hollingsworth, A. Bailey, and J. Wells	
NASA Code 311-03-22-60	
<b>Near-Earth Tracking and Data System Support for the Pioneer Venus 1978 Missions</b> . . . . .	27
M. R. Traxler and H. W. Calhoun	
NASA Code 311-03-22-60	

### SUPPORTING RESEARCH AND TECHNOLOGY

#### Tracking and Ground-Based Navigation

<b>Estimated Displacements for the VLBI Reference Point of the DSS 13 26-m Antenna</b> . . . . .	36
H. McGinness, G. Gale, and R. Levy	
NASA Code 310-10-61-05	
<b>Multipath Effects on the Time Delays of Microwave Cassegrainian Antennas</b> . . . . .	52
T. Y. Otoshi and W. V. T. Rusch	
NASA Code 310-10-01-05	

PRECEDING PAGE BLANK NOT FILMED

<b>Extrapolated UT1 Effect on VLBI Clock Sync</b> . . . . .	56
J. W. Layland and B.V.H. Saxberg	
NASA Code 310-10-60-10	

<b>Receiver Design Concepts for <math>\Delta</math>VLBI and Differential One-Way Range</b> . . . . .	60
J. W. Layland	
NASA Code 310-10-60-10	

<b>On Improved Ranging—II</b> . . . . .	68
J. W. Layland and A. I. Zygielbaum	
NASA Code 310-10-60-10	

### Communications—Spacecraft/Ground

<b>Spectral Shaping Without Subcarriers</b> . . . . .	74
L. R. Welch	
NASA Code 310-20-67-13	

### Station Control and Operations Technology

<b>Unattended Operations Software System Design Progress Report</b> . . . . .	78
L. Lim	
NASA Code 310-30-66-01	

<b>Dual A/D Converter With Automatic DMA Block-Transfer Capability</b> . . . . .	85
D. E. Wallis	
NASA Code 310-30-70-10	

<b>A Note on Digital Signatures</b> . . . . .	95
R. J. McEliece	
NASA Code 310-30-70-14	

<b>A General Logic Structure for Custom LSI</b> . . . . .	97
M. W. Sievers	
NASA Code 310-30-70-10	

<b>An Efficient Soft Decision Decoding Algorithm for Block Codes</b> . . . . .	106
H. J. Greenberger	
NASA Code 310-30-70-14	

# NETWORK AND FACILITY ENGINEERING AND IMPLEMENTATION

## Network

<b>Precise Extraction of Geometrical Dependence from Solar Wind Columnar Turbulence Measurements . . . . .</b>	<b>110</b>
A. L. Berman NASA Code 311-03-43-10	
<b>A Reexamination of the Radial Dependence of Weak Interplanetary Scintillation . . . . .</b>	<b>119</b>
A. L. Berman NASA Code 311-03-43-10	
<b>A Unified Observational Theory for Solar Wind Columnar Turbulence . . . . .</b>	<b>124</b>
A. L. Berman NASA Code 311-03-43-10	
<b>Further Results on Fast Transforms for Decoding Reed-Solomon Codes Over <math>GF(2^n)</math> for <math>n = 4, 5, 6, 8</math> . . . . .</b>	<b>132</b>
I. S. Reed, T. K. Truong, B. Benjauthrit, and R. L. Miller NASA Code 311-03-43-20	

## Ground Communications

<b>Wideband Data Error Rates . . . . .</b>	<b>156</b>
J. P. McClure NASA Code 311-06-40-00	

## Deep Space Stations

<b>Computerized Simulation and Parameterization of a New High-Performance Tubular Solar Collector . . . . .</b>	<b>161</b>
F. L. Lansing and C. S. Yung NASA Code 311-03-41-08	
<b>DOMSAT CW Transmission Bent Pipe Investigation: Initial Phase Noise Measurements via RCA SATCOM Link . . . . .</b>	<b>181</b>
M. H. Brockman and C. E. Jones NASA Code 311-03-43-20	
<b>DSN VHF Transmitting Array Backup Command Uplink for Voyager 2 . . . . .</b>	<b>189</b>
R. M. Dickinson NASA Code 311-03-41-05	

**X-3060 Klystron Design Improvement Program Status**

A. Goldfinger and M. A. Gregg . . . . . 196  
NASA Code 311-03-41-05

**Radio Frequency Carrier Arraying . . . . . 206**

R. Lay  
NASA Code 311-03-42-51

**Spectral Signal Indicator Progress Report . . . . . 216**

B. Chaney, H. Cooper, and B. Crow  
NASA Code 311-03-42-50

**S-X 34-Meter Conversion Receiver and  
Microwave Performance . . . . . 219**

H. R. Buchanan  
NASA Code 311-03-42-59

**Implementation of the DSN VLBI Correlator . . . . . 226**

J. C. Peterson and J. W. Dillon  
NASA Code 311-03-42-62

**The Symbol Synchronizer Assembly . . . . . 237**

M. J. Galitzen  
NASA Code 311-03-41-01

## Network Functions and Facilities

N. A. Renzetti

Office of Tracking and Data Acquisition

*The objectives, functions, and organization of the Deep Space Network are summarized; deep space station, ground communication, and network operations control capabilities are described.*

The Deep Space Network was established by the National Aeronautics and Space Administration (NASA) Office of Space Tracking and Data Systems and is under the system management and technical direction of the Jet Propulsion Laboratory (JPL). The network is designed for two-way communications with unmanned spacecraft traveling approximately 16,000 km (10,000 miles) from Earth to the farthest planets and to the edge of our solar system. It has provided tracking and data acquisition support for the following NASA deep space exploration projects: Ranger, Surveyor, Mariner Venus 1962, Mariner Mars 1964, Mariner Venus 1967, Mariner Mars 1969, Mariner Mars 1971, and Mariner Venus-Mercury 1973, for which JPL has been responsible for the project management, the development of the spacecraft, and the conduct of mission operations; Lunar Orbiter, for which the Langley Research Center carried out the project management, spacecraft development, and conduct of mission operations; Pioneer, for which Ames Research Center carried out the project management, spacecraft development, and conduct of mission operations; and Apollo, for which the Lyndon B. Johnson Space Center was the project center and the Deep Space Network supplemented the Manned Space Flight Network, which was managed by the Goddard Space Flight Center. The network is currently providing tracking and data acquisition support for Helios, a joint U.S./West German project; Viking, for which Langley Research Center provided the Lander spacecraft and project management until May,

1978, at which time project management and mission operations were transferred to JPL, and for which JPL provided the Orbiter spacecraft; Voyager, for which JPL provides project management, spacecraft development, and is conducting mission operations; and Pioneers, for which the Ames Research Center provides project management, spacecraft development, and conduct of mission operations. The network is adding new capability to meet the requirements of the Galileo mission to Jupiter, for which JPL is providing the Orbiter spacecraft, and the Ames Research Center the probe. In addition, JPL will carry out the project management and the conduct of mission operations.

The Deep Space Network (DSN) is one of two NASA networks. The other, the Spaceflight Tracking and Data Network (STDN), is under the system management and technical direction of the Goddard Space Flight Center (GSFC). Its function is to support manned and unmanned Earth-orbiting satellites. The Deep Space Network supports lunar, planetary, and interplanetary flight projects.

From its inception, NASA has had the objective of conducting scientific investigations throughout the solar system. It was recognized that in order to meet this objective, significant supporting research and advanced technology development must be conducted in order to provide deep space telecommunications for science data return in a cost effective

manner. Therefore, the Network is continually evolved to keep pace with the state of the art of telecommunications and data handling. It was also recognized early that close coordination would be needed between the requirements of the flight projects for data return and the capabilities needed in the Network. This close collaboration was effected by the appointment of a Tracking and Data Systems Manager as part of the flight project team from the initiation of the project to the end of the mission. By this process, requirements were identified early enough to provide funding and implementation in time for use by the flight project in its flight phase.

As of July 1972, NASA undertook a change in the interface between the Network and the flight projects. Prior to that time, since 1 January 1964, in addition to consisting of the Deep Space Stations and the Ground Communications Facility, the Network had also included the mission control and computing facilities and provided the equipment in the mission support areas for the conduct of mission operations. The latter facilities were housed in a building at JPL known as the Space Flight Operations Facility (SFOF). The interface change was to accommodate a hardware interface between the support of the network operations control functions and those of the mission control and computing functions. This resulted in the flight projects assuming the cognizance of the large general-purpose digital computers which were used for both network processing and mission data processing. They also assumed cognizance of all of the equipment in the flight operations facility for display and communications necessary for the conduct of mission operations. The Network then undertook the development of hardware and computer software necessary to do its network operations control and monitor functions in separate computers. A characteristic of the new interface is that the Network provides direct data flow to and from the stations; namely, metric data, science and engineering telemetry, and such network monitor data as are useful to the flight project. This is done via appropriate ground communication equipment to mission operations centers, wherever they may be.

The principal deliverables to the users of the Network are carried out by data system configurations as follows:

- (1) The DSN Tracking System generates radio metric data, i.e., angles, one- and two-way doppler and range, and transmits raw data to Mission Control.
- (2) The DSN Telemetry System receives, decodes, records, and retransmits engineering and scientific data generated in the spacecraft to Mission Control.
- (3) The DSN Command System accepts spacecraft commands from Mission Control and transmits the commands via the Ground Communication Facility to a

Deep Space Station. The commands are then radiated to the spacecraft in order to initiate spacecraft functions in flight.

- (4) The DSN Radio Science System generates radio science data, i.e., the frequency and amplitude of spacecraft transmitted signals affected by passage through media such as the solar corona, planetary atmospheres, and planetary rings, and transmits this data to Mission Control.
- (5) The DSN Very Long Baseline Interferometry System generates time and frequency data to synchronize the clocks among the three Deep Space Communications complexes. It will generate universal time and polar motion and relative Deep Space Station locations as by-products of the primary data delivery function.

The data system configurations supporting testing, training, and network operations control functions are as follows:

- (1) The DSN Monitor and Control System instruments, transmits, records, and displays those parameters of the DSN necessary to verify configuration and validate the Network. It provides the tools necessary for Network Operations personnel to control and monitor the Network and interface with flight project mission control personnel.
- (2) The DSN Test and Training System generates and controls simulated data to support development, test, training and fault isolation within the DSN. It participates in mission simulation with flight projects.

The capabilities needed to carry out the above functions have evolved in the following technical areas:

- (1) The Deep Space Stations, which are distributed around Earth and which, prior to 1964, formed part of the Deep Space Instrumentation Facility. The technology involved in equipping these stations is strongly related to the state of the art of telecommunications and flight-ground design considerations, and is almost completely multimission in character.
- (2) The Ground Communications Facility provides the capability required for the transmission, reception, and monitoring of Earth-based, point-to-point communications between the stations and the Network Operations Control Center at JPL, Pasadena, and to the JPL Mission Operations Centers. Four communications disciplines are provided: teletype, voice, high-speed, and wideband. The Ground Communications Facility uses the capabilities provided by common carriers throughout the world, engineered into an integrated system by Goddard Space Flight Center, and controlled from the

communications Center located in the Space Flight Operations Facility (Building 230) at JPL.

The Network Operations Control Center is the functional entity for centralized operational control of the Network and interfaces with the users. It has two separable functional elements; namely, Network Operations Control and Network Data Processing. The functions of the Network Operations Control are:

- (1) Control and coordination of Network support to meet commitments to Network users.
- (2) Utilization of the Network data processing computing capability to generate all standards and limits required for Network operations.
- (3) Utilization of Network data processing computing capability to analyze and validate the performance of all Network systems.

The personnel who carry out the above functions are located in the Space Flight Operations Facility, where mission opera-

tions functions are carried out by certain flight projects. Network personnel are directed by an Operations Control Chief. The functions of the Network Data Processing are:

- (1) Processing of data used by Network Operations Control for control and analysis of the Network.
- (2) Display in the Network Operations Control Area of data processed in the Network Data Processing Area.
- (3) Interface with communications circuits for input to and output from the Network Data Processing Area.
- (4) Data logging and production of the intermediate data records.

The personnel who carry out these functions are located approximately 200 meters from the Space Flight Operations Facility. The equipment consists of minicomputers for real-time data system monitoring, two XDS Sigma 5s, display, magnetic tape recorders, and appropriate interface equipment with the ground data communications.

## **The DSN Programming System**

A. P. Irvine  
TDA Engineering Office

*This article describes the DSN Programming System and its current status. A recapitulation of the System's description is included as well as major near-term milestones, plans, and some realized benefits.*

### **I. Introduction**

The goal of the DSN Programming System is the development of a body of knowledge and practices that would result in the controlled and predictable implementation of software and of those aggregates of data manipulated by software. The system incorporates a wide range of disciplines oriented toward lowering the life-cycle cost of software.

The DSN Programming System supports the on-going activities of the implementation of software in the Deep Space Network and consequently is a support system which levies requirements and provides services for all subsystems which contain software components. A discussion of all the components of the System is presented in Ref. 1.

### **II. Key Characteristics**

#### **A. Major Elements**

The DSN Programming System includes the following:

- (1) DSN Software Standard Practices.
- (2) DSN Standard Programming Languages.
- (3) Software Implementation Aids.
- (4) Management Aids.

#### **B. DSN Software Standard Practices**

The DSN software standard practices include the following:

- (1) Software Implementation Guidelines and Practices.
- (2) Preparation of Software Requirements Documents (SRD).
- (3) Preparation of Software Definition Documents (SDD).
- (4) Preparation of Software Specification Documents (SSD).
- (5) Preparation of Software Operators Manuals (SOM).
- (6) Preparation of Software Test and Transfer Documents (STT).
- (7) DSN Data Base Implementation and Operations Guidelines and Practices.

The Software Implementation Guidelines and Practices describe the overall Tracking and Data Acquisition (TDA) software methodology, policy, and software management plan. The other standard practices provide supporting detail as summarized below.

The Standard Practices on Software Requirements Documents and Software Definition Documents cover the early

activities of requirements identification and software architectural design. These are the conceptual phases where decisions made during these formative stages tend to have profound effects on the overall costs, commitments, and the general approach. The SDD describes the software architectural design, which permits a  $\pm 10\%$  accurate estimate to be made of the cost and schedule of the remaining implementation, which is the program construction. The architectural design can, in fact, be the basis for a bid by an outside contractor for a fixed-price implementation. Timing is critical and early reviews facilitate redirection, if needed. The documents covering the preparation of SSDs, SOMs, and STTs require that they be produced concurrently with the program construction and testing activities. They document the true "as-built" and "as-tested" computer program and are used to operate and maintain the transferred (delivered) program. The standard practice on data bases provides guidelines for standardizing and implementing the operational DSN Data Base. The DSN Data Base includes the data throughout the DSN in continual use for ongoing business, operations, and commitments.

### C. DSN Standard Languages

Two standard languages for the implementation of software funded by the Office of Tracking and Data Acquisition have been identified. For non-real-time DSN computer programs, the MBASIC<sup>tm</sup> language has been designated as the standard language. MBASIC<sup>tm</sup>, an advanced version of Dartmouth BASIC, is a high-level language that combines English and simple algebra in its syntax. The term MBASIC<sup>tm</sup> is derived from management-oriented BASIC.

The MBASIC<sup>tm</sup> interpreter has been implemented on the PDP-10, on the UNIVAC 1108, and a subset, DEMOMBASIC, has been implemented on the MODCOMP II. A language translator, the MBASIC<sup>tm</sup> Batch Processor, is currently being designed. This batch processor will provide a facility for MBASIC<sup>tm</sup> programs which have been debugged in the interpretive mode to be translated into a directly executable form and stored or executed from the MBASIC<sup>tm</sup> environment. The initial implementation will take place on the UNIVAC 1108. An adjunct to the MBASIC<sup>tm</sup> system, the DSN File Editor, will provide a machine-independent text and data editor for MBASIC<sup>tm</sup> users.

For real-time applications, HAL/S has been designated as the standard DSN language. HAL/S is a highly efficient, block-structured, high-order language which was originally developed for the NASA Space Shuttle flight software and has subsequently been designated as a NASA Standard Language.

The HAL/S compiler, to be hosted on a Modular Computer CLASSIC 7860, is being developed for JPL by Intermetrics,

Inc., the company which originally designed and developed HAL/S for NASA. The compiler, plus code generators for the MODCOMP II and the host machine, a MODCOMP CLASSIC, will be delivered in May 1980.

### D. Implementation and Management Aids

A variety of aids are being developed or investigated to augment software development efforts. Among them are:

- (1) The CRISP system (Ref. 2), a set of Control Restrictive Instructions for Structural Programming, which contains at its core a program design language CRISP. CRISP imposes a structural syntax on a design language.
  - (a) CRISPFLOW is a form of CRISP that turns CRISP documentation into structural flowcharts.
  - (b) CRISP-PDL is a program design and documentation tool that has as its output cosmetized indented listings, identifier cross-references, a tier chart, a glossary, a table of contents, stub status reports, and a statistical usage summary.
- (2) "How-To" Books. It is planned that the DSN Standard will be augmented by a series of handbooks that will explain in detail how to implement the standards. The first of these handbooks, "The Life-Cycle Cost Analysis Handbook," was published as a preliminary document in 1978. The second handbook, "Preparation Guidelines for Class B Software Specification Documents," is in its second draft. Other handbooks are planned on such subjects as:
  - (a) Work Breakdown Structures.
  - (b) The Anomaly Reporting System.
  - (c) Contracting for Software as an End Item.

### III. Milestones

Major milestones accomplished since the last report (Ref. 1) on the DSN Programming System are:

- (1) Completion of DSN Data Base Implementation and Operation Guidelines Practices . . . . . published December 1978
- (2) Completion of Software Methodology Textbook, Volume II, Standards . . . . . distributed January 1979

The near-term milestones associated with the DSN Programming System are:

- (1) MBASIC<sup>tm</sup> Batch Compiler,  
Operational . . . . . October 1979
- (2) HAL/S Compiler, hosted on a CLASSIC,  
Operational . . . . . May 1980

#### IV. Plans for the Future

It is possible that the replacement of the existing UNIVAC 1108 by the Large Computer Replacement (LCR) might impact the DSN Programming System. Efforts to minimize this impact have been instituted by implementing current efforts in a portable high-order language. However, past implementations such as the MBASIC<sup>tm</sup> interpreter are not in a high-order language and may have to be recoded, although not redesigned, once the LCR selection is made known. Implementation of the extensions to the MBASIC<sup>tm</sup> machine-independent design will have to be considered in light of the LCR selection.

One method of minimizing the impact of a new computer is to use a high-order language which will have some guarantee of portability. The TDA, in conjunction with the Flight Projects Support Office, is investigating the selection and acquisition of a standard PASCAL, which would be available

across the spectrum of computers available at the Jet Propulsion Laboratory to ensure portability. It has been proposed that the implementation of the DSN Standard File Editor be a test case to demonstrate portability between the UNIVAC 1108 and the MODCOMP II computers.

#### V. Benefits

An evaluation of the methodology developed under the DSN Programming System and applied to the DSN Mark III Data Subsystems Implementation Project (MDS) was made (Ref. 3). This evaluation showed that application of the methodology resulted in the following:

- (1) A small but significant savings in manpower.
- (2) A lower anomaly rate than industry-reported averages.
- (3) Sufficient management visibility to allow corrective action to be applied early enough to ensure timely delivery.

#### VI. Conclusion

Data has now been collected which provides evidence that the DSN Programming System does result in some expected benefits and that the goal of achieving lowered life-cycle costs for the implementation of software is realizable.

### References

1. Hodgson, W. D., "The DSN Programming System," in *The Deep Space Network Progress Report 42-41*, pp. 4-9, Jet Propulsion Laboratory, Pasadena, Calif., Oct. 15, 1977.
2. Tausworth, R. C., *Standardized Development of Computer Software, Vol. II - Standards*, Jet Propulsion Laboratory, Pasadena, Calif., Aug. 1978.
3. Irvine, A., and McKenzie, M., "Evaluation of the DSN Software Methodology," in *The Deep Space Network Progress Report 42-48*, pp. 72-81, Jet Propulsion Laboratory, Pasadena, Calif., Dec. 15, 1978.

## DSN Test and Training System, Mark III-77

D. T. Herrman, Jr.  
TDA Engineering Office

*Implementation of the DSN Test and Training System, Mark III-77, throughout the network has been completed. The Mark III-77 system, as configured, has supported testing and training for the Voyager and Pioneer Venus 1978 missions and all other ongoing, inflight missions. Multimission functions of the system will provide some capabilities for initial DSN Test and Training preparations for the Galileo Project. DSN Test and Training System capabilities include functions performed in the Deep Space Stations, Ground Communications Facility, and Network Operations Control Center.*

### I. System Definition

#### A. General

The DSN Test and Training System is a multiple-mission system which supports Network-wide testing and training by inserting test signals and data into subsystems of the Deep Space Stations (DSS), the Ground Communications Facility (GCF), and the Network Operations Control Center (NOCC). The system includes capabilities for:

- (1) On-site testing of the DSS portion of each DSN system.
- (2) Local testing of the NOCC portion of each DSN system.
- (3) End-to-end testing of each DSN system, including DSS, GCF, and NOCC functions.

Figure 1 describes the functions, elements, and interfaces of the system. This article updates the system description published in Ref. 1.

#### B. Key Characteristics

Design goal key characteristics of the DSN Test and Training System are:

- (1) Capability to function without alteration of DSN operational configurations.
- (2) Utilization of mission-independent equipment for DSN testing and training functions.
- (3) Capability to exercise NOCC, GCF, and DSS simultaneously for end-to-end testing of each DSN system.
- (4) Capability to supply test data to all DSN systems simultaneously.
- (5) Capability to support network loading tests with a combination of actual and simulated data streams.
- (6) Accommodation of flight-project-supplied simulation data via GCF.

- (7) Accommodation of other data sources, as follows:
  - (a) Spacecraft test data via JPL Compatibility Test Area (CTA 21).
  - (b) Spacecraft prelaunch data via Merritt Island, Florida, Spacecraft Compatibility-Monitor Station (STDN (MIL 71)).

### C. System Usage

Major testing and training activities supported by the DSN Test and Training System are summarized below:

- (1) Performance calibrations and prepass readiness verifications.
- (2) Real-time diagnostics and fault isolation.
- (3) DSN implementation activities and performance testing of DSN systems, DSS subsystems, and NOCC subsystems.
- (4) DSN operational verification tests to prepare for mission support.
- (5) Flight project ground data system tests, mission simulations, and operational readiness tests.

## II. Mark III-77 System Implementation

### A. Status

A functional block diagram showing the data-flow and signal-flow paths of the DSN Test and Training System, Mark III-77, is shown in Fig. 2. Implementation of the Mark III-77 system throughout the network was completed when DSS 11 returned to operation in early 1978.

Upgrading of the DSS portions of the system has been a part of the DSN Mark III Data Subsystems (MDS) implementation project, which began in 1976.

All system capabilities which were required during 1978 were initially implemented prior to 1978.

### B. Mission Set

The Mark III-77 configuration of the DSN Test and Training System includes all elements of the system required for support related to the following mission set:

- (1) Viking Orbiters 1 and 2 and Viking Landers 1 and 2 (extended mission).
- (2) Pioneers 6 through 9.
- (3) Pioneers 10 and 11.

- (4) Helios 1 and 2.
- (5) Voyagers 1 and 2 (including planetary encounters).
- (6) Pioneer Venus 1978 (PV78) Orbiter and Multiprobe.

### C. New Capabilities

- (1) Program software has been provided to perform System Performance Test (SPT) functions for the DSS Radio Science System.
- (2) The System Performance Test Executive and related procedures have been modified so that SPT software can be effectively utilized to support both System Performance Tests and Computer Aided Countdowns (prepass readiness tests).

## III. Deep Space Station Functions

### A. DSS Test and Training Subsystem

The functions of the DSS Test and Training Subsystem and the related interfaces are shown in Fig. 3.

- (1) Telemetry simulation and conversion. The telemetry simulation and conversion functions are performed by the Simulation Processor Assembly (SPA) and the Simulation Conversion Assembly (SCA), as diagrammed in Fig. 4. Digital and analog capabilities are itemized in Tables 1 and 2, respectively.
- (2) System performance test functions. The system performance test functions are performed by the SPT Software Assembly, as diagrammed in Fig. 5.

### B. Receiver-Exciter Subsystem

The Receiver-Exciter Subsystem provides the following test and training functions:

- (1) Generation of simulated S- and X-band downlink carriers.
- (2) Modulation of telemetry subcarriers from the SCA onto simulated carriers.
- (3) Variable attenuation of simulated downlink carrier signal level under control of the SPA.
- (4) Translation of S-band exciter uplink frequencies to S- and X-band downlink frequencies for tracking system calibrations and performance testing.
- (5) Generation of simulated Pioneer Venus entry probe carriers at DSS 14 and 43.

### **C. Antenna Microwave Subsystem**

The Antenna Microwave Subsystem provides the following test and training functions:

- (1) Routing of simulated downlink carriers to masers and/or receivers.
- (2) Mixing of simulated S-band downlink carriers.

### **D. Transmitter Subsystem**

The Transmitter Subsystem includes provision for feeding the transmitter output into a dummy load to support Command System and Tracking System test operations.

### **E. Frequency and Timing Subsystem**

The Frequency and Timing Subsystem provides the following support functions to the DSS Test and Training System:

- (1) Time code, to the SPT Assembly, and reference frequencies to the SCA and SPT Assembly.
- (2) Generation and distribution of a simulated time signal which can be substituted for the true GMT input to the various DSS subsystems. This capability is provided to support realistic mission simulations in flight project testing and training activities.

### **F. Pre- and Post-Detection Recording Subsystem**

One tape unit of the Pre- and Post-Detection Recording (PPR) Subsystem was used to play simulated data and subcarriers into the Pioneer Venus entry probe carrier simulators at DSS 14 and DSS 43. The CTA 21, SCA, and PPR were used to prepare the simulated data tapes that were used as inputs.

## **IV. Ground Communications Facility Functions**

The DSN Test and Training System utilizes the Ground Communications Facility Subsystems for communicating data and information between the Network Operations Control Center (NOCC) or any Mission Operations Center (MOC) and the Deep Space Stations.

### **A. High-Speed Data Subsystem**

The High-Speed Data Subsystem provides the following:

- (1) Transmission of text messages, control messages, low- to medium-rate simulated telemetry data, and simulated command data to any DSS from the NOCC or from any MOC.

- (2) On-site loop-back of test data for systems performance testing and readiness verifications in the DSS.

### **B. Wideband Data Subsystem**

The Wideband Data Subsystem provides the following:

- (1) Transmission of simulated high-rate telemetry data to the 34- and 64-m subnets (DSS's 12, 14, 43, and 63), the Compatibility Test Area (CTA 21), in Pasadena, California, and STDN (MIL 71) at Merritt Island, Florida, from the NOCC or from any MOC having wideband capability.
- (2) On-site loop-back of test data for telemetry system performance testing and readiness verification in the stations which have wideband capability.

### **C. Teletype and Voice Subsystems**

The Teletype and Voice Subsystems provide for communication of information for purposes of test coordination and monitoring the status of the DSN Test and Training System.

## **V. Network Operations Control Center Functions**

### **A. NOCC Test and Training Subsystem**

Functions and interfaces of the NOCC Test and Training Subsystem are shown in Fig. 6. Subsystem data flow is diagrammed in Fig. 7. Test and training capabilities presently implemented in the Network Operations Control Center are as follows:

- (1) Off-line generation of recordings of high-speed data blocks for testing of the real-time monitors in the NOCC Tracking, Telemetry, Command, Radio Science, and Monitor and Control Subsystems.
- (2) Output of text and control messages to the DSS for remote configuration and control of the SPA and SCA in support of DSN Operational Verification Tests.
- (3) Selection of stored data blocks and output of the data to the DSS for system readiness verification.

### **B. DSN Test and Training System Control Console**

A DSN Test and Training System Control Console in the Network Data Processing Area provides keyboard, card reader, magnetic tape unit, volatile display, and character printer for operation of the Test and Training System separate from the operations of the other DSN systems.

## VI. Compatibility Test Area (CTA 21)

The facilities of the Compatibility Test Area have been utilized to support non-real-time system performance tests for validation of the Radio Science Subsystem.

## VII. Future Planning

Effort has commenced toward development of the DSN Test and Training System, Mark III-81. This effort will require development of functional requirements and identification of system configurations that will be required to support both Simulation and System Performance Test functions in the 1981-1985 time frame.

Initial DSN Test and Training requirements in preparation for the Galileo mission are to support the upgrade of the DSS and NOCC Telemetry Subsystems and to support the implementation of CTA 21 for DSN-Spacecraft Compatibility Tests.

It is planned that these initial requirements can be supported by the existing DSN Test and Training System, Mark III-77, with minimal upgrades to support new data types. It is, however, expected that the new DSN Test and Training System, Mark III-81, will be required to support the full data system test and training requirements of Galileo and future projects.

## References

1. Thorman, H. C., "DSN Test and Training System, Mark III-77," in *The Deep Space Network Progress Report 42-44*, pp. 4-15, Jet Propulsion Laboratory, Pasadena, Calif., Apr. 15, 1978.
2. Yee, S. H., "Modification of Simulation Conversion Assembly for Support of Voyager Project and Pioneer Venus 1978 Project," in *The Deep Space Network Progress Report 42-39*, pp. 100-108, Jet Propulsion Laboratory, Pasadena, Calif., June 15, 1977.
3. Friedenber, S. E., "Pioneer Venus 1978 Multiprobe Spacecraft Simulator," in *The Deep Space Network Progress Report 42-38*, pp. 148-151, Jet Propulsion Laboratory, Pasadena, Calif., Apr. 15, 1977.

**Table 1. DSS Test and Training Subsystem digital telemetry simulation capabilities**

Capability	26-meter DSS, MIL 71	64-meter DSS, CTA 21
Maximum number of simultaneous real-time data streams	2 channels	Viking extended mission, 4 channels Other missions, 3 channels
Bi-orthogonal (32, 6) comma-free block coding	Viking, 2 channels Other missions, none	Viking, 3 channels Other missions, none
Short-constraint-length convolutional coding (k=7, r=1/2 or 1/3)	Voyager, rate = 1/2 2 channels Future missions, rate = 1/3, 1 channel	Voyager, rate = 1/2 3 channels Future missions, rate = 1/3, 2 channels
Long-constraint-length convolutional coding (k=32, r=1/2)	Helios, 1 channel Pioneer 10/11, 2 channels Pioneer Venus, 2 channels	Helios, 1 channel Pioneer 10/11, 2 channels Pioneer Venus, 3 channels
Variable rate control	1 bps to 600 kbps on 1 channel 1 bps to 190 kbps on 1 additional channel	1 bps to 600 kbps on 2 channels 1 bps to 190 kbps on 1 additional channel
Selection of discrete rates	8-1/3, 33-1/3 bps on each of 2 channels (for Viking)	8-1/3, 33-1/3 bps on each of 3 channels (for Viking)

**Table 2. DSS Test and Training Subsystem analog telemetry simulation capabilities**

Capability	26-meter DSS, MIL 71	64-meter DSS, CTA 21
Data and subcarrier signal conditioning, phase-shift keyed modulation	2 subcarriers	Viking extended mission, 4 subcarriers Other missions, 3 subcarriers
Subcarrier frequency output	512 Hz to 1.25 MHz, 1/4-Hz resolution	512 Hz to 1.25 MHz, 1/4-Hz resolution
Modulation-index angle control	Controllable from 0 to 89 deg on each subcarrier	Controllable from 0 to 89 deg on each subcarrier
Subcarrier mixing and downlink carrier biphasic modulation	Single or dual subcarriers onto each of 2 S-band test carriers or 1 S-band and 1 X-band	Single or dual subcarriers onto each of 3 test carriers or 2 S-band and 1 X-band
Downlink carrier signal level	Attenuation of 0 to 40 dB on each test carrier output	Attenuation of 0 to 40 dB on each test carrier output

**DSN SYSTEM INTERFACES**

**OPERATIONS INTERFACES**

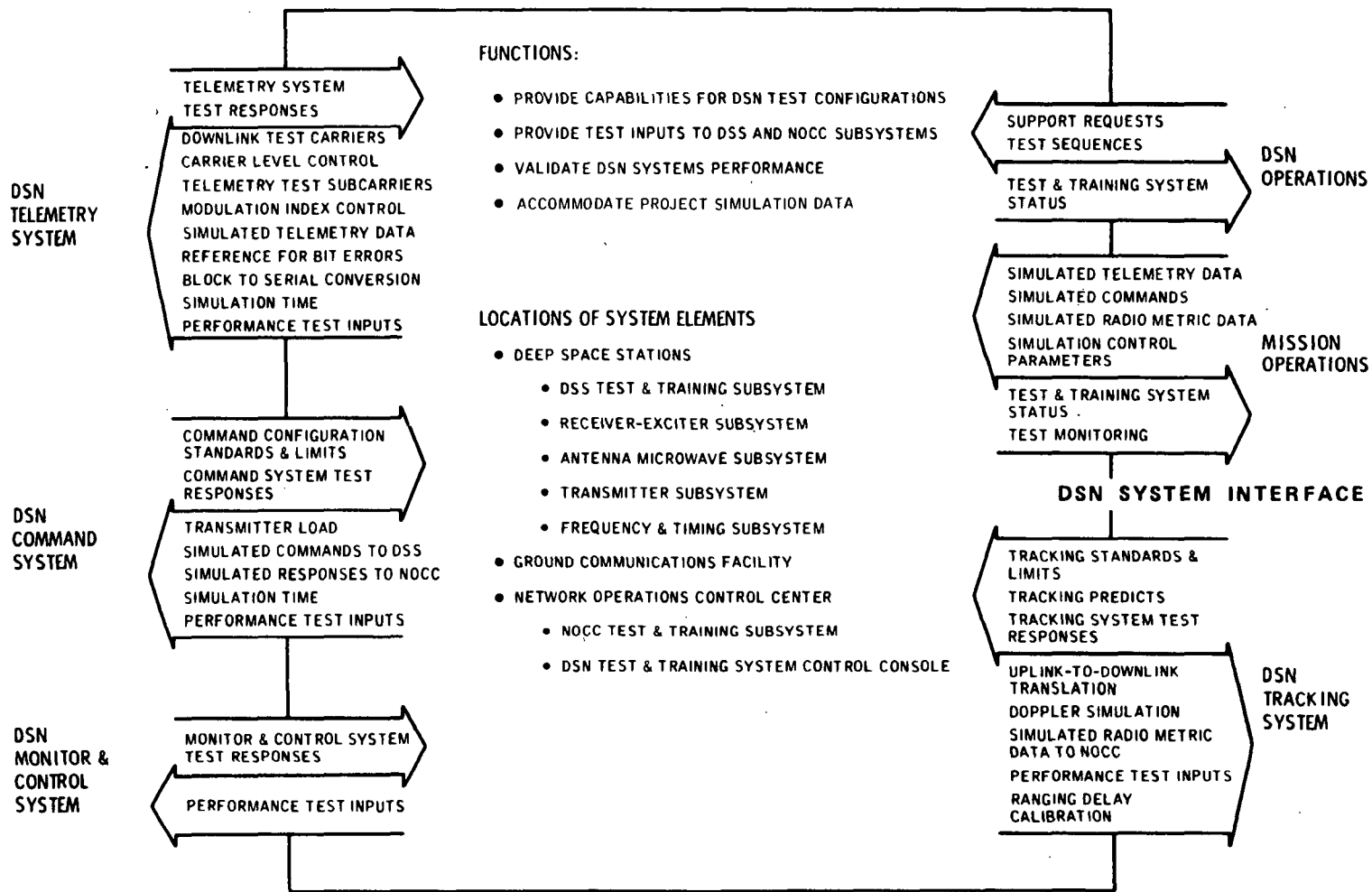


**Fig. 1. DSN Test and Training System functions and interfaces**

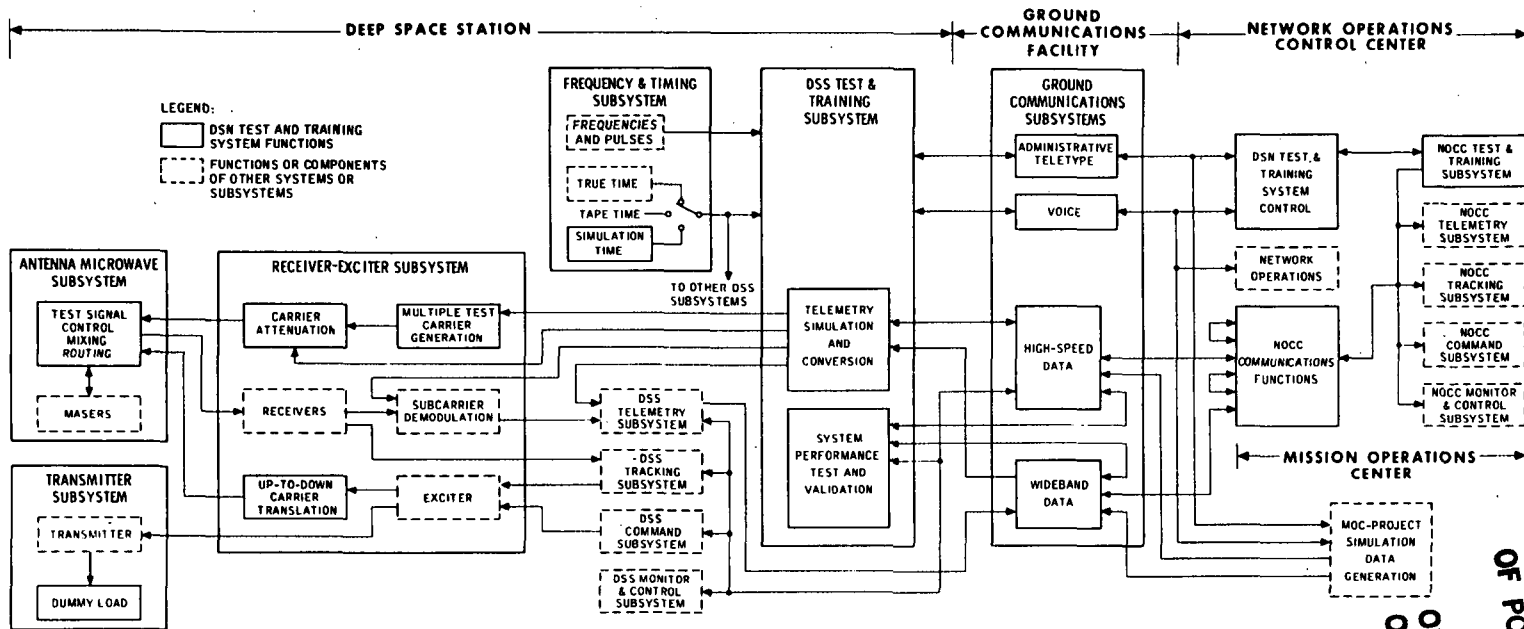


Fig. 2. DSN Test and Training System, Mark III-77, functional block diagram

ORIGINAL PAGE IS  
OF POOR QUALITY  
IS  
OF POOR QUALITY

DSS SUBSYSTEM INTERFACES

GCF SUBSYSTEM INTERFACES

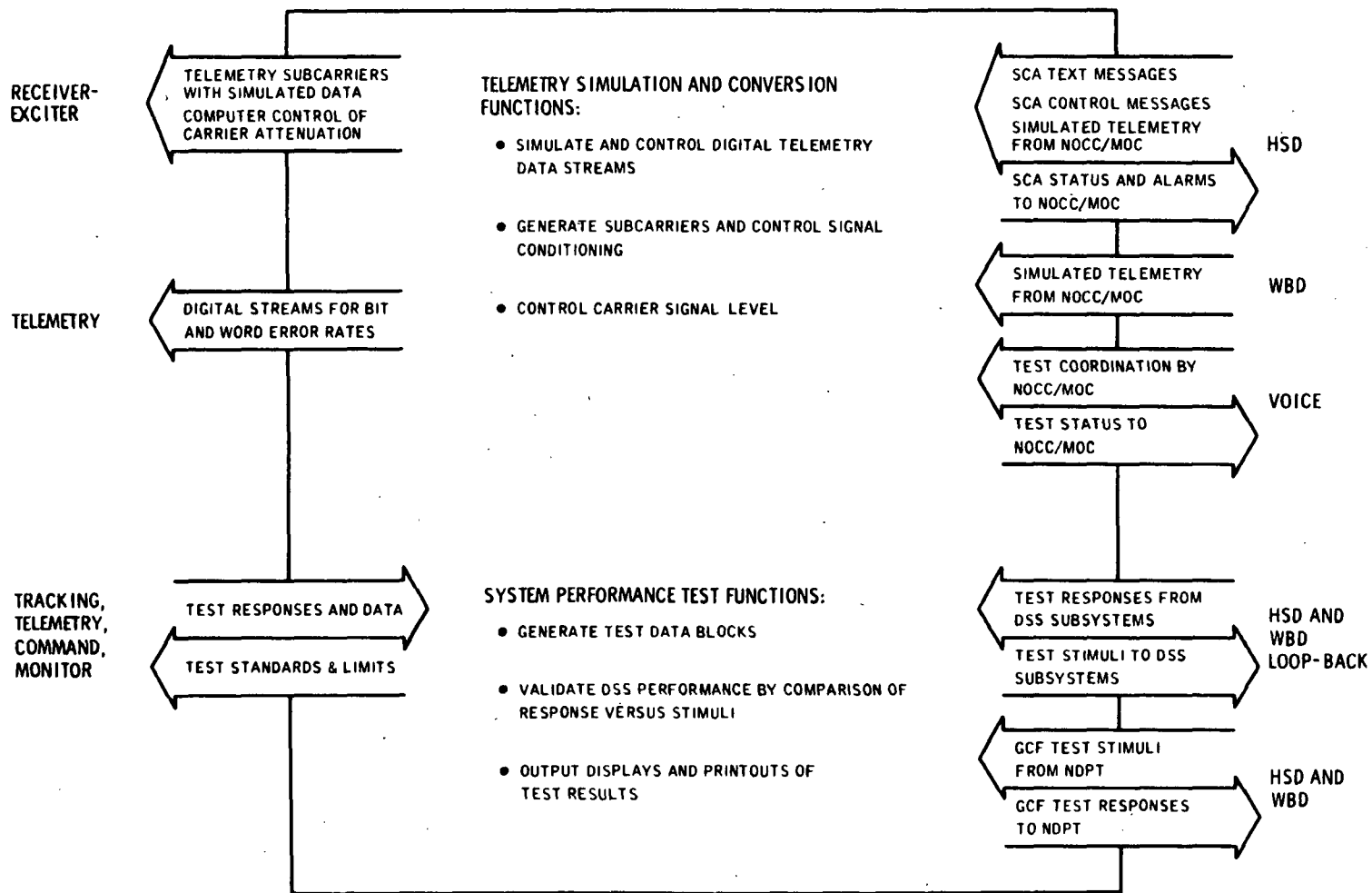


Fig. 3. DSS Test and Training Subsystem functions and interfaces

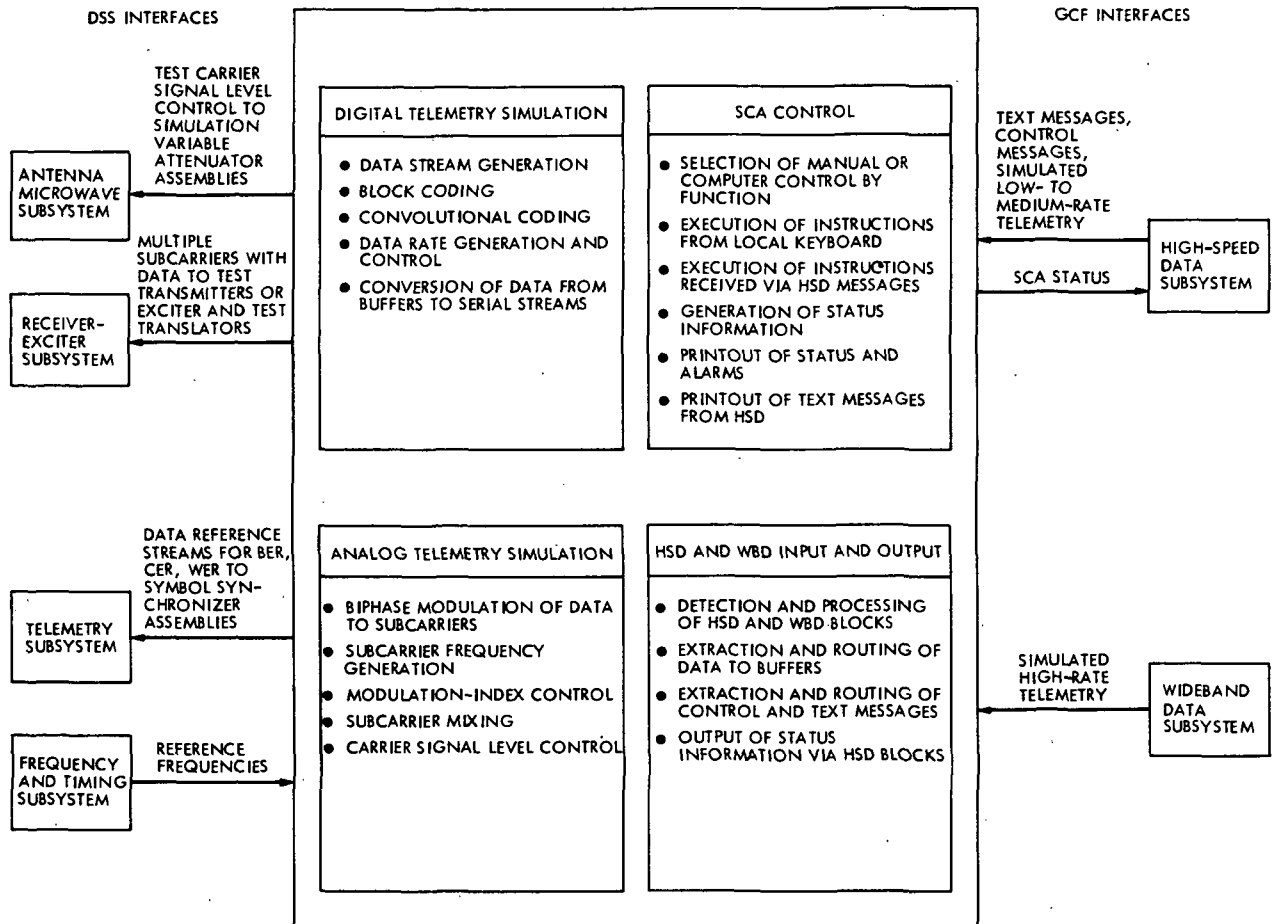


Fig. 4. Telemetry simulation and conversion functions and data flow

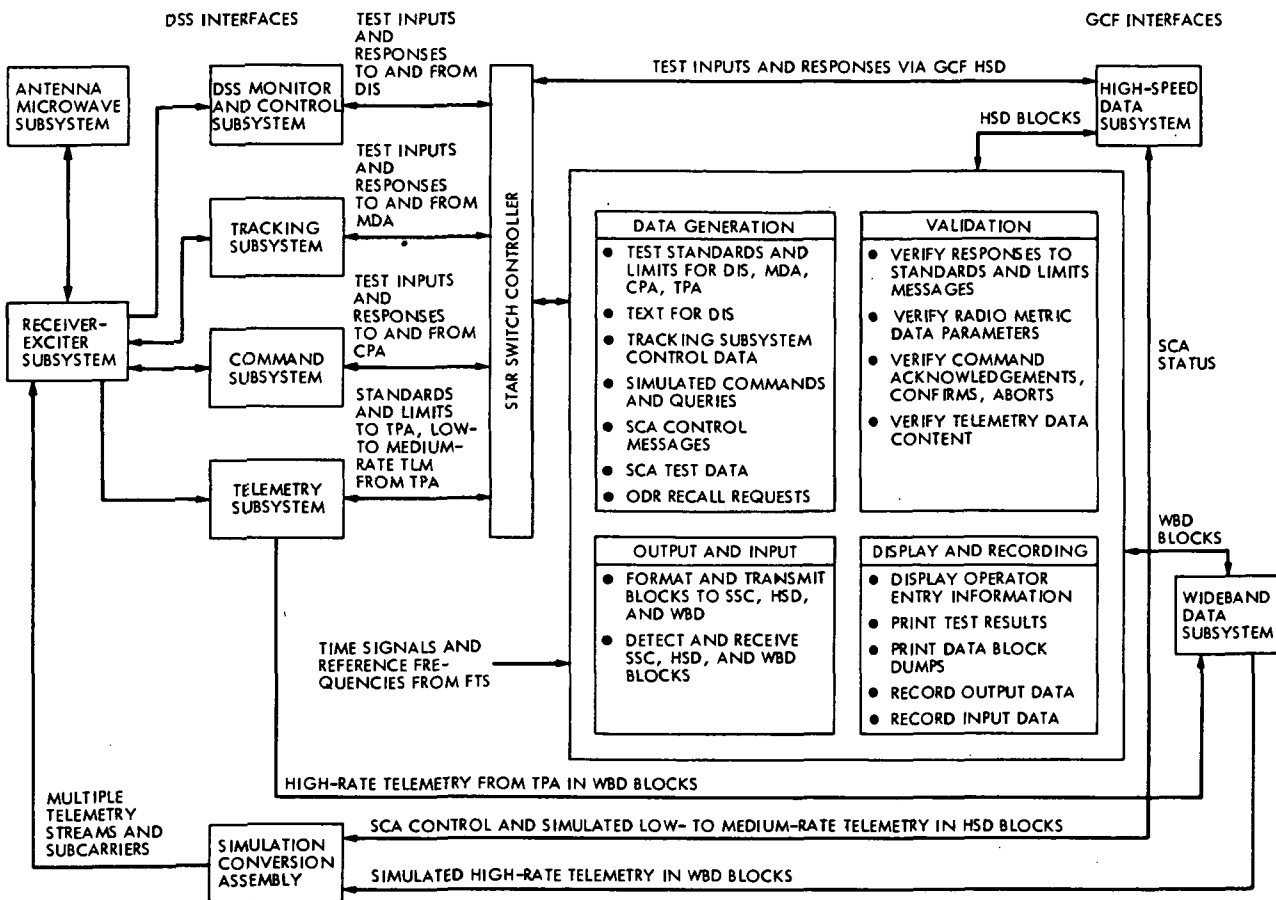
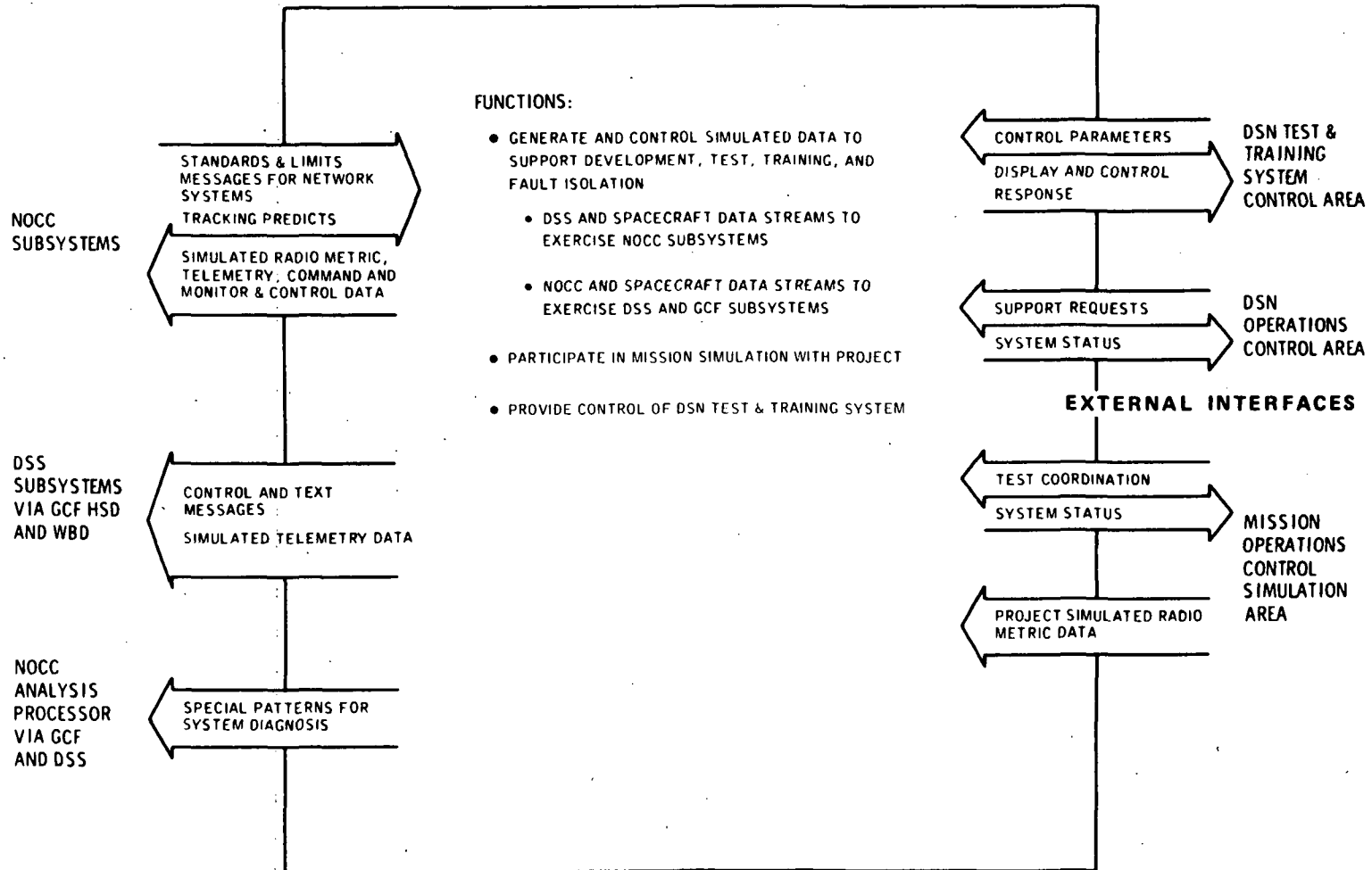


Fig. 5. System performance test functions and data flow

**SUBSYSTEM INTERFACES**

**OPERATIONS INTERFACES**



**Fig. 6. NOCC Test and Training Subsystem functions and interfaces**

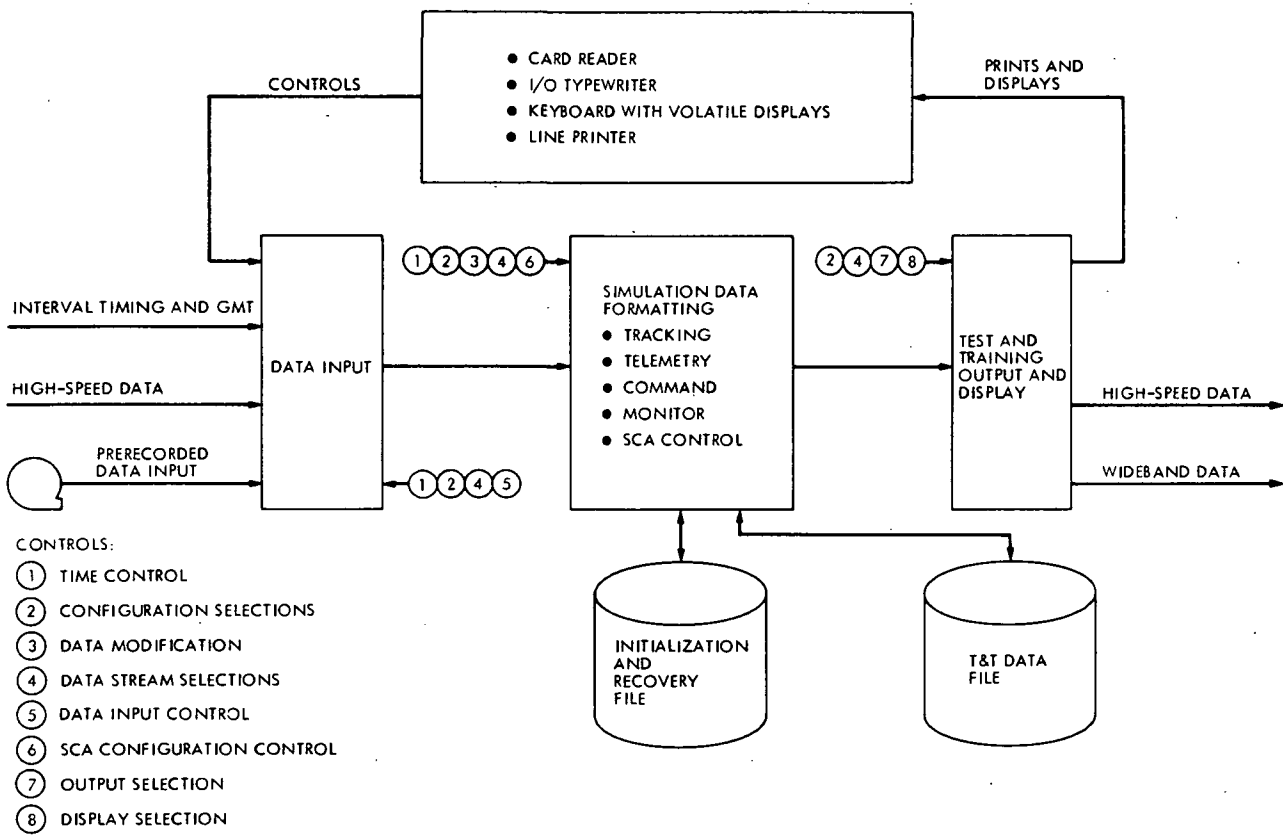


Fig. 7. NOCC Test and Training Subsystem data flow

## Voyager Support

J. Allen and H. Nance  
Deep Space Network Operations Section

*This is a continuation of the Deep Space Network Report on Tracking and Data Acquisition for Project Voyager. This report covers the period from May 1978 through December 1978.*

### I. Voyager Operation

#### A. Status

Both spacecraft are approaching their encounter with Jupiter. In mid-December Voyager 1 was approximately 80 days and 78 million kilometers (49 million miles) from Jupiter. It was traveling at a heliocentric velocity of 14 kilometers per second, with one-way communication time of 33 minutes, 51 seconds with Earth being 609 million kilometers (378 million miles) away.

Voyager 2 has 146 million kilometers (91 million miles) to go in the next seven months before its encounter. One-way light time was 31 minutes, 10 seconds, while its heliocentric velocity is 12.6 kilometers per second.

Workaround procedures have been developed and tested to compensate for some of the spacecraft problems. As of the end of December the probability of the project meeting its mission objectives at Jupiter Encounter is very high.

#### B. Spacecraft Problems

##### 1. Spacecraft 31

*a. Plasma main detector.* The loss of sensitivity has been diagnosed and simulated in the laboratory. The problem was

an open circuit in the feedback loop of an amplifier driving the buckout grid of the forward detector cluster. A procedure of temperature cycling was started and the instrument recovered completely on DOY 138.

*b. Scan platform pointing.* Continued slewing tests have not resulted in any difficulties as encountered in February 1978, and constraints on the scan platform slewing envelope were removed. The suspected cause was debris in the gears, which has now been apparently crushed and no further difficulty has been detected.

##### 2. Spacecraft 32

*a. Photopolarimeter filter wheel/analyzer wheel.* The specific reason for the problem has not been determined; however, an operation sequence has been developed so that the desired position can be attained.

*b. RCVR loss.* Remains same — Receiver 1 failed. Receiver 2 is being used, although the tracking loop capacitor has failed. Special procedures are being utilized for tracking operations.

#### C. Spacecraft Special Events

Superior conjunction on both spacecraft occurred during July. Spacecraft 31 entered Sun-Earth-Probe (SEP) angle of 5

degrees inbound on 6 July and SEP angle of 5 degrees outbound on 21 July – the minimum SEP angle was 0.75 degree. S-band AGC and SNR degradations were observed and correlated with the degradations recorded during the Mariner '69 conjunction.

Spacecraft 32 entered SEP angle of 5 degrees inbound on 9 July and SEP angle of 5 degrees outbound on 23 July. The minimum SEP angle was 2 degrees. The S-band AGC and SNR degradations correlated with degradation recorded during spacecraft 31 conjunction.

## II. DSN Operations

### A. Command System Update

The complexity of the Voyager Mission and the effort to reduce the actual real-time operation of the commanding effort placed a requirement on the DSN to revise its command system. The change at the DSSs to separate Command and Telemetry computers and the change of the MCCC from the IBM 360/75 computer to the Modcomp mini-computers (Mark III System) allowed a complete change in concept.

1. **Telemetry and Command Processor (Replaced).** Under the operation with the DSS Telemetry and Command Processor (TCP) and the MCCC 360/75 computers, only 24 commands could be stored at the station in four command modules, each with six commands in queue. During operation, after one module's commands were transmitted, another module was promoted in the stack; then the empty module could be refilled. This procedure required constant operator attention and intervention during long command loads.

2. **Command Processor Assembly (New).** The TCPs were replaced by a Command Processor Assembly (CPA) and a Telemetry Processor Assembly (TPA) as separate computers. The CPA was provided with the capabilities of the TCP with an alternate capability (store-and-forward mode) of storage space for eight files, each file capable of 256 elements (commands) for a total storage of 2048 commands. This total capacity can be used at any one time, or any part of it could be used, resulting in a greater flexibility in the command system operation. Likewise, the command files could be assigned a transmit time to be consistent with a command window or at any opportune time during a spacecraft tracking pass by the Voyager Project. Likewise, all checks for errors, computer handshaking, status reporting, etc., were expanded to provide a complete, more or less automatic, command system.

### B. Telemetry System Update

Concurrent with the Command System change, the Telemetry System was also changed. Again, the DSS was provided with a separate telemetry computer as was the MCCC. In preparation for the Voyager encounters, a capability was also provided at the 64-meter and 34-meter stations to interface with wideband data lines to support the data rates expected from the spacecraft. DSSs 14 and 63 were provided with the capability to return, in real-time, all of the high rate telemetry up to and including the 115.2-kb/s Imaging and General Science data. DSSs 12 and 43 were provided with the capability to return in real-time all of the high rate data up to and including the 44.8-kb/s Imaging and Playback data.

The limitation of the real-time capability at DSS 12 and especially at DSS 43 for high rate telemetry data return made it mandatory that a strategy be developed to return high rate telemetry data received at the higher data rates in near real-time. The procedure developed was to record the higher rate telemetry data and, after one tape was completed, start the replay of the data from one TPA over the 56-kb/s line at line rate while continuing to record on the other TPA. Since this method requires a longer transmission time as compared to receive time, the replay would continue post-pass into the next tracking period, regardless of Project. To implement this requirement required negotiation and understanding with the Pioneer Venus and Viking Projects.

### C. CMD and TLM Capability Testing

As the Command and Telemetry capabilities became available for testing in July, a series of Operational Verification Tests (OVTs) was conducted during July and August to provide training to the stations and Operation Control Team and to validate the capability. DSS 12 was not tested at this time; rather the station was tested in November after the update from a 26-meter to 34-meter station with S/X-band capability. These same capabilities were tested with Project and MCCC through the use of Ground Data System (GDS) tests during July through November, including all stations at different times. Included in the GDS tests were updates of software that corrected anomalies or provided additional capabilities in the DSN, MCCC or Project software as well as the conversion of the MCCC to the Mark III Data System. The tests had varying degrees of success, mainly due to problems with the Simulation Conversion Assembly (SCA) in generating the higher data rates and the interfacing of new systems. However, the test sequence was successful overall and the capabilities verified for encounter support. In total there were 26 Operational Verification Tests scheduled, each being approximately of 8 hours duration and supported by a minimum of 13 DSN personnel. This effort required 208 station hours and some 2700 manhours to complete the task.

#### D. DSS 12 Upgrade

DSS 12 was decommitted from Project support in June 1978. The station was converted from a 26-meter antenna/S-band station to a 34-meter antenna/S- and X-band station during the period June through September 1978. Subsystem and system tests were conducted at the station, by station and implementation personnel, during October 1978, with the station being available for DSN testing, training and demonstrating tracking capability during November. This required a program for all station personnel to become familiar with the new capability; therefore, support periods were scheduled so that each crew was exercised at least twice. The DSN activities included 11 OVTs, conducted by the Network Operations Project Engineers (NOPEs), each approximately 8 hours in duration and supported by a minimum 13 DSN operational personnel. This program required 88 station hours and 1144 manhours. Tracking demonstration passes included both spacecraft, on one pass each, and was of approximately 12 hours duration each. The subsystem/system testing took a week longer than scheduled, but the DSN activities schedule was condensed and the station was verified for operational support on schedule.

The verification of the new support systems and stations cited above required that GDS tests be conducted at various phases of system implementation. To validate, the updates required 35 GDS tests overall and 53 individual station tests. Each test required approximately 8 hours of station time and support by an average of 13 operations personnel. This resulted in expenditure of 424 station hours and approximately 5500 DSN manhours in addition to the MCCC/Project support manhours involved.

#### E. Special Tests

During November, the DSN participated with the project in exercising the Mission Operations Control Team (MOCT) anomaly detection and problem resolution capabilities. Anomalies, such as antenna offset, radio receiver anomaly, weather anomaly, were induced into the system and emergency or contingency plans were implemented.

#### F. Radio Science

A new digital Radio Science (RS) subsystem has been implemented at the 64-meter subnet to replace the analog method of recording radio science data. This new RS subsystem was implemented in different phases as new equipment became available. Basically, the system has a narrowband (prime) and wideband (back-up) capability.

The phase 1 subsystem implemented at DSSs 14 and 43 (until the narrowband multi-mission receiver becomes avail-

able) utilizes an S- and X-band open-loop receiver (OLR) (for narrowband) with the following filter bandwidth selection:

	<u>S-Band</u>	<u>X-Band</u>
(a)	1 kHz	3 kHz
(b)	2 kHz	7.5 kHz
(c)	5 kHz	15 kHz
(d)	10 kHz	30 kHz

The OLR output is fed to the Occultation Data Assembly (ODA) subsystem (A/D converters and mod comp computer) for digital tape recording at sample rates of 2K, 5K, 10K and 20K samples/s.

The wideband back-up system utilizes a wideband (1 MHz) multi-mission receiver which is recorded on a Digital Recording Assembly (DRA) in the megabit range.

To facilitate on-site observations of the digital recordings (since the data are usually mailed to JPL for data reduction) a new Spectrum Signal Indicator (SSI) subsystem is used to verify proper operation of the system during recording.

The ODA receives Radio Science predicts from JPL to drive the narrowband OLR programmable local oscillator to maintain the spacecraft downlink signal within the desired OLR filter bandwidth. These predicts are a series of linear ramps which profile the anticipated doppler signature from the spacecraft.

The DSS 63 RS subsystem (Phase 2) basically uses the same system described above except the wideband system uses the 300-kHz output of the OLR and the narrowband system uses the new narrowband MMR (7 filters, S- and X-band). The new narrowband Multi-Mission Receiver (MMR) will be available at DSS 14 for Voyager 2 encounter.

#### G. Meteorological Monitor Assembly Data

In the continuing effort to provide calibration data for the tracking system, in both the S- and X-band frequencies, the implementation of a meteorological atmospheric sampling capability was effected at the 64-meter stations. The primary data provided are temperature, barometric pressure, dew point, water vapor partial pressure, precipitation, precipitation rate, diurnal Faraday rotation, Faraday rotation angle, satellite azimuth, satellite elevation, solar insolation, microwave polarization angle, ellipticity and microwave mode. The initial capability was provided by an HP9821A calculator recording data on a seven-track recorder. The collected data were transmitted to JPL once a week, utilizing the station Digital Instrumentation System (DIS). An IDR was made from the received data and turned over to the Tracking System Analytical Calibration (TSAC) operation for further processing. The pro-

cessed data would then be available for Navigational Orbit Determination operations.

Upgrade of the initial system will be to provide for nine-track recorders instead of the seven-track recorders. This will bring the facility in line with other station recorders and the normal interface with the station CMF for data transmission. This upgrade is presently being implemented.

#### **H. Station Antenna Arraying**

During the Jupiter Near Encounter Phase of the Voyager 2 Mission, DSSs 12 and 14 will be arrayed to demonstrate the antenna array configuration. This configuration will be required for the Saturn Encounter Phase of the Voyager Mission at all three complexes. The main objective for antenna arraying is to provide an effective signal increase of approximately 1.2 dB on the X-band signal during Saturn Encounter.

At present, the antenna arraying is in the testing phase and is being readied for the configuration demonstration at DSSs 12 and 14. The arraying consists of both DSSs 12 and 14 tracking the spacecraft simultaneously, with the telemetry data microwaved from DSS 12 to DSS 14. At DSS 14 the signal from DSS 12 is input to the real-time signal combiner with the signal from DSS 14, and the combined output is transmitted to JPL.

#### **I. Range Accuracy**

The precision of the Planetary Ranging Assembly (PRA) range data was questionable since adequate capabilities to verify the accuracy were not readily available. The decision was made to install the MU2 ranging system at the DSS 42/43 conjoint station and conduct tests that would allow data comparison.

The MU2 equipment was shipped to DSS 42/43 and installed in October 1978. Data gathering passes were authorized and the data evaluated. Reports in December 1978 indicated that the MU2's higher code frequency (1 MHz) and filtering had dramatically reduced residual scatter. Preliminary results indicate a 3-fold increase in range precision (from approximately 6 meters to approximately 2 meters). The MU2 continued to be used for tests during December, and plans included utilizing the equipment for investigation of an inter-station range bias problem.

#### **J. Signal Enhancement**

During the Encounter Phase, it is necessary that maximum antenna gain be available. To optimize the antenna gain it is necessary to refocus the subreflector whenever the antenna elevation is below 40 degrees elevation. Three focus settings

(10, 30 and 50 degrees) are used and are elevation dependent. The X-band Subreflector Refocusing Assembly required calibration every four months. Settings established during the calibrations are used on a daily basis or as required to optimize antenna gain. When refocusing, the stations extract the elevation angle from the DSN predicts and performs the refocusing.

The subreflector refocusing tests conducted with DSS 14 on 1 December were very successful and showed that there is no effect on radio metric or radio science data during refocusing periods.

#### **K. Roll Turn Test**

On Day 363, a negative 360-degree roll turn with spacecraft 31 was successfully supported at DSS 63. The objective of the test was to determine the offset between the HGA electrical boresight with that of the turn axis. Preliminary analysis of the data provided by DSS 63 indicated an offset of 0.15 to 0.2 degree exists (which is within the design tolerance).

### **III. DSN Support Assessment**

As an indication of the high level support provided by the DSN Tracking Stations and the Network Operations Control Team, from 20 November through 31 December 1978 there were 170 scheduled Voyager tracks. The average track was between 8-1/2 and 9 hours long, resulting in approximately 1488 tracking hours for the time period. Of these tracks, 111 or 65 percent were trouble free. Of the 59 remaining passes that had problems, 12 passes concerned a CPA alarm that caused no loss of data. This essentially meant that 123 or 72 percent of the passes were trouble free as concerns data loss. Of the 47 remaining tracks, the problems on 8 passes were the result of communication problems, primarily High Speed or Wideband Data Line outages. The 39 remaining passes resulted in non-receipt of 23 hours, 27 minutes of data in real-time. Five hours, 8 minutes of this data was radio metric or ranging data and non-recoverable; the remaining 18 hours, 19 minutes of telemetry data and the non-receipt caused by the communication problems was recoverable, requiring only data recall from the stations to complete the required data records. Overall, 98.3 percent of the data was received in real-time, with only 0.3 percent of the radio metric/ranging data being non-recoverable and all of the telemetry data recoverable.

These 170 scheduled tracks required a minimum of 13 DSN personnel throughout the system per pass for support. Since each track averaged 8.75 hours in length and 13 support personnel, a total of 19,338 manhours were expended for the period. Considering the non-receipt in real-time of 23.45 hours

(23 hours, 27 minutes) of data, for the 19,338 manhours, a 0.12 percent error or non-receipt rate results. Likewise, the 23.45 hours of data non-receipt for 1488 tracking hours results in a 1.58 percent non-real-time data reception due to equipment problems. The 5.133 hours (5 hours, 8 minutes) of radio metric data loss in the 1488 tracking hours equals 0.34 percent of non-recoverable data due to mis-configuration or

human problem. Further, the 5.133 hours of data loss for 19,338 manhours expended is a 0.026 percent error rate. This error rate is considered negligible in relationship to the number of tasks performed, i.e., computer loading, knob turning, computer instruction inputs, interpretation of required configuration, scheduling codes, short turnarounds, etc., to complete a tracking pass.

## **Bibliography**

Voyager Mission Status Bulletins published by the Jet Propulsion Laboratory (JPL internal document).

Laeser, R. P., and Textor, G. P., Voyager Mission Operations Reports (JPL internal document).

Lopez, D., and Beyer, P., DSN Failure Statistics, IOM 376G-series (JPL internal document).

## Pioneer Venus Multiprobe Entry Mission Support

B. Ryan  
D. Hollingsworth  
A. Bailey  
J. Wells

Tidbinbilla Deep Space Complex

*The support of the Pioneer Venus Multiprobe entry event by DSS 42/43 is described. Support included aiding in procedure development, determining staffing requirements, equipment checkout, and determination of final detailed station configuration.*

### I. Introduction

The Pioneer Venus Multiprobe entry represented one of the most difficult challenges ever presented to a deep space station. For a critical five-hour period, the success of a major planetary mission literally rested in the hands of the DSN Goldstone and Australian 64-meter stations. The operational complexity of the event for the stations dictated more extensive participation by station personnel in the mission support planning and significantly more testing and training than is usually required by a planetary encounter. The test and training activity was, in the view of DSS 42/43, more extensive than for any other event supported by this complex, except perhaps for Apollo support.

The following describes the station support from the viewpoint of station personnel in preparing for the entry event on December 9, 1978. The report is divided into three sections, corresponding to the organizational structure at Tidbinbilla: Operations Section, and Engineering Group Data Acquisition Section and Data Handling Section.

### II. Operations Section

The involvement of this station's Operations Group in the Pioneer Venus Probe mission began in February-March 1978 with the participation of two shift supervisors (Ben Ryan and Dave Hollingsworth) at JPL in the generation of the preliminary station countdown and operational procedures and a detailed sequence of events. During their visit, the preliminary procedures were tried out at DSS 14, using the actual entry configuration (minus a few minor pieces). The five days of testing at DSS 14 convinced everyone involved that this mission really was going to be something different and would require extraordinary participation by a large number of people at the supporting stations.

Upon returning to Australia, the sequence of events and the project requirements were studied and discussed; out of this came the decision to amalgamate two of the four operations shifts into one large, 16-man "Probe Entry" shift. The delivered entry station configuration was also studied and several minor changes requested: time readouts to be added to the

Spectral Signal Indicator (SSI)/Subcarrier Demodulator Assembly (SDA) area and relocation of the Block III Receiver Program Oscillator Control Assembly (POCA's) to simplify the receiver operations. In September, an Engineering Change Request was generated to permit S-band maser switching while uplinking as part of the failure/recovery contingency plan.

The first "in-house" attempts at the entry sequence were very ragged; the Multiprobe simulator design and the telemetry simulation tape gave us a few headaches (spontaneous random frequency shifts, Large Probe not being keyed on by data appearance, etc.). These problems were gradually resolved, and we entered the combined operational verification tests with DSS 14 in August with a good knowledge of this equipment's idiosyncrasies. However, the simulator was less flexible than we would have desired, but indispensable in preparing for the Entry.

During the testing and training period, some 14 Pioneer Venus related Engineering Change Orders were implemented and, in addition, the DSN Mark III Data Subsystems software went through numerous revisions. Procedures were implemented on site to retain timely station response to mission test requirements during this difficult period. Programs were written for the HP 9810 in lieu of the SSI microcontroller to permit the closed-loop receivers to participate in these early tests in a realistic manner. These programs enabled the rapid conversion of frequencies determined with the SSI into the proper level for the closed-loop receiver operator input.

Operationally, this station was concerned, from early in the year, with the planning for contingency/failure support. Initially, it was thought that the activity level during the entry would be too high to permit recovery action without possible confusion affecting the receipt of other data. However, as repeated operational verification tests increased operator proficiencies, the problem did not appear so intractable. Possible reconfigurations were small in number as most normally redundant equipment would be in use. However, by early November, priorities of data streams had been determined and agreement reached on a failure recovery strategy.

In May, concurrent with the ongoing probe entry support activities, DSS 42 supported the operational readiness test, the configuration verification test, and the launch of the Orbiter. New communication and monitor format and telemetry processing assembly software introduced just prior to launch required JPL task team formulation to resolve deficiencies. Short notification and late documentation was experienced in the prelaunch period. During the week prior to launch, DSS 42 antenna oscillations in tape drive mode caused some concern and was the subject of intense investigation. The anomaly was never fully resolved.

During June, the Multimission Receiver (MMR)/Digital Recording Assembly (DRA) subsystem underwent considerable testing in support of the DLBI wind experiment. MMR phase stability caused concern, as did the DRA performance, for the next five months. Operationally, the stream of operational verification tests, performance demonstration tests, mission operations tests, and DLBI tracks was very extensive.

The launch of the Bus on August 8 was supported by DSS 42 in a nominal manner – the only significant problem was a failure in the autotrack reference channel at the time of uplink acquisition. Tape drive was selected and only a momentary telemetry outage occurred.

MMR phase stability continued to cause concern until September, when a revised Engineering Change Order, 77.183A, was implemented. The DRA problems were straightened out, and confidence in our DLBI support improved as the station exercised the radio science equipment with other missions.

Also by September, the third SSI was in operation, and we could get acquainted with the microcontroller mode of operation. The microcontroller was found to be disappointingly slow in action – much slower than using our own software in the HP 9810. Procedures were established between the operators that obtained proper closed-loop receiver lockup. The rapid integration of the SSI into the normal operational environment of this station seemed to be another illustration of the "law of inverse effect" – put an interesting, sophisticated piece of equipment into the operations room, don't provide much in the way of information about it, and we achieve maximum operational cognizance in the minimum of time.

Entry preparations stabilized in November with the final operational readiness test and operational verification test, although new communications and monitor format and DSN Mark III Data Subsystems software were used at this late stage due to the requirements of other missions. Support on these tests was mostly nominal; however, sequential decoder lock times and Block IV exciter POCA performance caused concern. The station's pretrack preparation plan, including the detailed -3 and -1 hour check lists, was published, and engineering section support requirements were determined.

### **III. Engineering Group**

#### **A. Data Acquisition Section**

Activity to support Pioneer Venus started early in 1978 with an effort to install sufficient hardline on the tricone of the 64-meter antenna to accommodate the additional front-end equipment required to support the Entry event. An early start was made so that use could be made of small portions of

antenna time as they became available and station stocks of spiroline were used; thus the installation on the tipping assembly was completed without any scheduled downtime. A similar approach was adopted for tricorne equipment in that unistrut supports were installed well ahead of time. Knowing the dimensions of the items to be installed, a minimum of downtime was then required for the installation of the tricorne equipment.

Proposed location of control room equipment went through a number of alternatives before a satisfactory arrangement for operations was achieved. Actual installation of the RF equipment progressed quite smoothly both in the control room and on the antenna.

The testing phase revealed some problems. The most noticeable one was poorer phase stability of the MMR than expected, and this was eventually improved by removing an amplifier which was running into saturation.

#### **B. Data Handling Section**

The major activity in support of Pioneer Venus operations was the installation and checkout of the digital recording assembly recorders.

Recorder A arrived in mid-January, followed by Recorder B in mid-April. On completion of equipment installation, acceptance testing was initiated. At this point it was discovered that Recorder B was set up to a Seasat specification and required a complete realignment. Acceptance tests were completed on both recorders by the end of June.

Although the tests carried out on site were successful, subsequent network recording tests revealed an incompati-

bility between the CTA-21 and DSS 43 recorders. Data recorded at DSS 43 could not be replayed with an acceptable bit error rate at CTA 21, while error rates from DSS 14 were very good.

This was a head alignment problem, and in October a calibration tape was sent from CTA 21 to be used as a reference against which the recorder heads at DSS 43 could be set up. After realigning the recorder heads, test data from both recorders was shipped to CTA 21 and successfully validated. Notification of this result was received by the station on November 10.

#### **IV. Summary**

In late November, we felt we were "green to go" and, given a nominal mission, were sure we could support in the expected manner, notwithstanding the new meaning of the word "final" when applied to the "last" entry sequence of events and uplink sweep message due to late shifting of the Small Probe assignments by the Project and problems experienced at JPL in the Navigation to Predict interface.

The events of December 9 are history now and need no elaboration — the mission was so close to nominal it was as though it were a simulation. The elation of success could be seen from one end of the station operations room to the other, and few events in the space program could compare to the feeling at the detection of the first Probe's RF signal. It appears that all data possible was successfully captured, and station personnel have the satisfaction of a difficult job well done.

# Near-Earth Tracking and Data System Support for the Pioneer Venus 1978 Missions

M. R. Traxler

TDA Mission Support Office

H. W. Calhoun

Flight Project Test and Operations Section

*This article reports on the support provided by the Near-Earth Tracking and Data System (NETDS) for the Pioneer Venus 1978 Missions.*

## I. Introduction

The Near-Earth Phase Network for the Pioneer Venus Missions was composed of selected resources of Kennedy Space Center (Central Instrumentation Facility, Hangar AE Telemetry Laboratory and Communications), the Eastern Test Range (Range Instrumentation Stations, Real-Time Computer System, and Communications), 4950th Aerospace Test Wing (Advance Range Instrumentation Aircraft - ARIA), Goddard Space Flight Center (Spaceflight Tracking and Data Network - STDN), Deep Space Network (until initial DSN two-way acquisition), and NASA Communications Network (NASCOM).

A small group of JPL Eastern Test Range (ETR) Station personnel, headed by the Pioneer Venus NETDS Coordinator, operated under the guidance and direction of the JPL Pioneer Venus TDS Manager. The group participated in gathering requirements for near-Earth phase tracking and data support and monitored the levying of those requirements upon responsible implementing agencies via the appropriate documentation systems. The group monitored the planning and implementing efforts by such agencies and provided appropriate reporting to the TDS Manager to assure that all essential requirements were satisfied. This group also provided operational coordina-

tion between the Near-Earth Phase Network and the Project during launch operations.

## II. Mission Planning

The Pioneer Venus Orbiter Mission was particularly difficult to plan for because of the wide variation in launch trajectories as indicated in Figs. 1 and 2. Geometric launch azimuths from 39 to 108 deg were considered with three basic configurations being selected. May 20 through June 3 had launch azimuths between 93 and 108 deg with Ascension Island and two or three Advanced Range Instrumentation Aircraft (ARIA) planned for the second Centaur Burn through spacecraft separation support interval. June 4 and June 5 were planned with 80-deg launch azimuths and four ARIA supporting from Africa. June 6 through June 10 launch data were planned using 60-deg launch azimuths and TDS downrange support from Wallops Island, Madrid, and four ARIA staging from Spain.

Two other factors had a major impact on the trajectories selected to enhance TDS support on the early launch days. The first was to have a long enough tracking interval from Ascension to send one command to the spacecraft after

separation. The other was to have at least a two-hour view from Canberra (initial DSN acquisition station) to accomplish planned near-Earth science sequences. The major Near-Earth Phase Network resource problem regarding support of these varied trajectories was the scheduling of enough ARIA aircraft and moving them between staging bases on consecutive days.

The Multiprobe launch opportunity extended from August 7 through September 3. All launches were in the 93-to-108-deg flight azimuth sector. Geometrical requirements placed most of the Centaur second burn and Centaur/spacecraft separation events well beyond the Ascension Island tracking capabilities. Figure 3 illustrates the Earth tracks for selected Multiprobe launch days.

Again the major Near-Earth Phase Network resource problem with supporting the Multiprobe launch was scheduling enough ARIA. Four ARIA were scheduled and the trajectories designed such that the two downrange aircraft could fly far enough down-range from Ascension to acquire the last portion of the near-Earth TDS data interval.

The planning for both missions had one additional complication in that the spacecraft antenna pattern was such that the ARIA could not track a 60-deg cone at the rear of the spacecraft. This, in most cases, is what caused ARIAs 3 and 4 to be scheduled.

### III. Implementation and Configuration

The ETR radars at Merritt Island, Patrick Air Force Base, Cape Canaveral, Grand Turk, Antigua, and Ascension were configured to transmit high-speed metric data to the Real Time Computer System (RTCS) at the Cape for both missions. The STDN Bermuda radar site was also configured to provide high-speed metric data to the RTCS on both missions.

The ETR RTCS was configured to process the metric data and compute (in real-time) JPL orbital elements, standard orbital parameter messages, acquisition data for selected NETDS stations and I-matrices. The Kennedy Space Center Central Instrumentation Facility was configured to process the real-time Centaur telemetry data and to provide Centaur state vector parameters to the RTCS for use by the RTCS in computing the Centaur transfer and postdeflection orbits.

Stations that were configured to support the launch vehicles and spacecraft telemetry links were Merritt Island, TEL-IV at ETR, Grand Bahama Island, Bermuda, Grand Turk, Antigua, Ascension (both ETR and STDN sites), and two to four ARIA. Also, the Wallops Flight Center and the STDN Madrid

telemetry sites were configured to support a 60 degree launch azimuth.

For spacecraft real-time retransmission, all sites with the exception of Wallops Flight Center, Grand Turk, and the ETR Ascension site were configured.

MIL 71 received real-time spacecraft telemetry data from STDN stations, ETR stations, and ARIAs via 203 and 202D modems, as applicable. The MIL 71 Automatic Selection Unit source-selected one data stream for processing and reformatting into high-speed data blocks. These high-speed data blocks were transmitted to the DSN Network Operations Control Center at JPL and to the Pioneer Mission Operations Control Center at Ames Research Center. Spacecraft data were also provided by hard line and high-speed data line from MIL 71/MIL to the Spacecraft System Test Complex at the Cape.

Real-time retransmission of the launch vehicle telemetry data to Kennedy Space Center was from the same sites as indicated for spacecraft telemetry data. One additional telemetry site was configured for launch vehicle telemetry data only. This was the Orroral Valley site in Australia.

### IV. Prelaunch Testing

The TDS Near-Earth Phase Test Plan identified and defined the planned prelaunch testing required to verify the readiness of the NETDS to participate in and support the Pioneer Venus 1978 Project test, training, and readiness program. It outlined support configurations and developed criteria and schedules for those prelaunch tests. The tests described therein preceded NETDS participation in the major readiness demonstration tests, i.e., the Mission Operations System and Operational Readiness Tests.

The test plan included a series of six spacecraft telemetry tests which were designed to (1) demonstrate the performance of MIL 71, and (2) demonstrate the performance of the STDN and ETR networks and of the ARIA's. All were successfully performed prior to the Orbiter launch. Applicable tests were repeated prior to the Multiprobe launch.

The Atlas-Centaur telemetry system was standard and had been flown prior to the Orbiter mission. The principal test efforts related to the real-time retransmission systems. The STDN 56 kb/s system was implemented and tested for the Orbiter mission. The ARIA 2.4-kb/s system containing Centaur DCU guidance parameters was implemented and tested for the Multiprobe mission. These systems were successfully demonstrated during the respective operations readiness tests.

A series of three tests were designed to demonstrate the performance of the ETR RTCS. An acquisition predicts test was conducted to verify the format and content of the RTCS-committed DSN predicts. A Venus B-Plane Mapping Test was conducted to determine the accuracy of the RTCS mapping program output parameters as compared to JPL mapping program output parameters. Both these tests were readily performed and the computations were validated. The third test was to validate the ETR RTCS-developed software change to process the new DSN high-speed metric data format. The test demonstrated that the RTCS was not able to consistently process this data. Evaluation indicated that the cost would be high to develop this capability, and the requirement for processing this data was subsequently dropped by the Project.

Various elements of the NETDS supported the Orbiter and Multiprobe prelaunch Mission Operations System and operational readiness tests as requested by the Project. Full participation in one operational readiness test prior to each launch was provided by all NETDS agencies. All Mission Operations System and operational readiness tests were successfully supported by the NETDS.

## V. Orbiter Launch Support

The countdown for the Orbiter launch was reasonably smooth. One significant problem was a 24-min outage of the high-speed data flow from MIL 71 to the Project Mission Operations Control Center. This outage occurred just at the time scheduled for the spacecraft to read out the launch command sequence that had been stored by the Hughes equipment at the Cape for validation by Project personnel at the Control Center. The duration of the outage was extended, in part, by the use of a 33-bit error detector instead of a 22-bit error detector at the West Coast Switching Center. Fortunately, the Project was able to carry out the validation using the Hughes Cape equipment. The spacecraft activities proceeded such that it was possible later in the countdown to read out the command sequence at the Project Mission Operations Control Center after the circuit was restored.

Thunderstorms threatened the planned test support positions for the ARIAs. Alternate test site positions and look angles were selected and provided to the aircraft by teletype and by voice. However, it was not necessary to change to the alternate test site positions.

Data flow checks with NETDS stations and ARIAs were performed satisfactorily. Due to the lack of MARISAT availability, no spacecraft data flow was conducted by the ARIA's.

The Orbiter was launched at the opening of the launch window on May 20, 1978, at 1313 GMT. The launch vehicle performance and spacecraft injection were very nominal. The required spacecraft first midcourse correction, delayed from the planned date of launch plus seven days, was 3.193 m/s on the twelfth day.

All NETDS stations supported their respective data intervals essentially as planned. Major inflight (Mark) events through Mark 13, "Start Centaur Blowdown," were reported in real-time. The final event, Mark 14, "End Centaur Blowdown," occurred while out of view of NETDS stations. All Mark events received were within the nominal limits, with spacecraft separation occurring 4.4 seconds earlier than predicted.

Real-time spacecraft telemetry data from the Ascension STDN site were processed and displayed at the Project Mission Operations Control Center at Ames Research Center and at the Spacecraft System Test Complex at Building AO at Cape Canaveral Air Force Station. The data at Building AO indicated that the spacecraft was normal, but the data at the Control Center indicated that a tremendous number of spacecraft problems existed. This ambiguity in the spacecraft status caused the Project to elect not to send the spacecraft command via Ascension to start the science sequence. The problem was subsequently identified as a hardware problem at the Control Center, in which a bit error detector improperly reflagged bad data blocks as good.

The real-time computations (orbital elements, Inter-Net Predicts, Inter-Center Vectors, I-matrix, and planetary mapping) performed by the ETR RTCS were valid and delivered on time. Local and NASCOM long line voice and data communications were excellent. NETDS performance was essentially flawless, with almost all of the supporting stations providing more coverage than expected.

The expected vs actual radar coverage for the uprange stations is provided in Fig. 4. The two Ascension radars also provided more coverage than predicted. One radar provided actual coverage from 20 minutes 33 seconds to 28 minutes 18 seconds. The other provided 23s less coverage. The spacecraft and launch vehicle expected vs actual coverage for the stations is provided in Figs. 5 and 6.

The MIL 71 site transmitted 116% of the planned real-time spacecraft data to JPL and the Ames Project Mission Operations Control Center. Only 16s of nonplanned data dropouts occurred.

## VI. Multiprobe Launch Support

The countdown for the Multiprobe mission went well except for a few communications problems. At about launch minus 190 min, the spacecraft telemetry data circuit between TEL-IV and MIL 71 failed. This circuit was the one which provided spacecraft data as received by TEL-IV backing up MIL during the early phase of flight and the circuit over which ARIA spacecraft data were to be transmitted through TEL-IV to MIL 71. After about 45 min of troubleshooting, a switch was made to an alternate circuit which was used through launch. At about 15 min after the switch, a frame module at KSC was replaced and the original circuit was made good.

At about launch minus 45 min, one data circuit between the Cape and Bermuda went down. The STDN Network Operations Manager requested that one of two Bermuda 7.2-kb/s circuits be released from real-time launch vehicle telemetry support for Launch Trajectory Acquisition System data to Bermuda. The circuit for launch vehicle Format B was released. The circuit that went down was made good prior to launch.

The extreme operating range of ARIAs 2 and 4, the take-off order of all four ARIAs, and the prelaunch functions of the ground stations resulted in a minimal time period during which data flow checks with the ARIAs could be conducted. The available time was depleted by a variety of unexpected problems. One aircraft (ARIA 4) radiated for a while at too high a power level, which saturated the satellite and resulted in unfounded suspicions of interference by unauthorized users. Another aircraft (ARIA 1) had a defective summing amplifier which invalidated the launch vehicle telemetry portion of the combined launch vehicle and spacecraft data through the satellite. Good launch vehicle data leaving ARIA 2 arrived at Bldg AE via the HF path, but for an undetermined reason, did not do so via the satellite path. Delays incidental to the above precluded any opportunity to attempt a data flow check with the fourth aircraft (ARIA 3).

Based on the extent and success of the prelaunch data flow checks, it was decided that ARIAs 1 and 4 would be prime for real-time retransmission for launch.

The Multiprobe was launched at the opening of the launch window on the second day of the launch opportunity, August 8, at 7:33 GMT. The first day was missed due to insufficient liquid helium needed for prelaunch cooling of the Centaur engines being available at KSC. The launch vehicle perfor-

mance and spacecraft injection were very nominal. The actual midcourse correction was 1.93 m/s at launch plus seven days.

All NETDS stations supported their respective data intervals essentially as planned. Major inflight (Mark) events through Mark 11, "Centaur/Spacecraft Separation," were reported in real-time. Mark 12, "Start Centaur Deflection," occurred within ARIA's view, but the aircraft were not equipped to make the real-time readout. Mark 13, "Start Centaur Blowdown," and Mark 14, "End Centaur Blowdown," occurred while out of view of NETDS stations.

All mandatory data intervals were supported. ARIAs tracked the spacecraft well past predicted coverage. ARIA 4's early loss of launch vehicle data was covered by the backup ARIA 2 (recorded only), justifying the commitment of ARIA backup resources.

MARISAT A support was excellent. Real-time spacecraft telemetry data relayed through the MARISAT link enabled the PMOCC to verify spacecraft spinup, a significant bonus that had not been entirely expected. The real-time computations (orbital elements, Inter-Net Predicts, and planetary mapping) performed by the ETR RTCS were valid and delivered on time. Local and NASCOM long-line voice and data communications were excellent, as was the overall support by the near-Earth trajectory and data system.

The radar expected vs actual coverage for the uprange stations is provided in Fig. 7. The two Ascension radars provided slightly more data than predicted. The TPQ-18 radar provided data from 20 min 41 s to 24 min 50 s, and the 12.15 radar provided data from 21 min 4 s to 26 min 25 s.

The spacecraft and launch vehicle expected vs actual coverage for the Near-Earth Phase Network stations is provided in Figs. 8 and 9.

The MIL 71 site transmitted 102.8% of the planned real-time spacecraft data to JPL and the Ames PMOCC during the interval, launch through Antigua loss of signal. There were an unusually high number of switches (15) by the Automatic Switching Unit between incoming data sources. All but 32 s of the planned data was provided, however. The MIL 71 site transmitted 12.5 min from Ascension and the ARIA. Most of the additional data were provided by longer than planned coverage from the ARIA, which fortunately allowed Ames Research Center to observe spacecraft spinup.

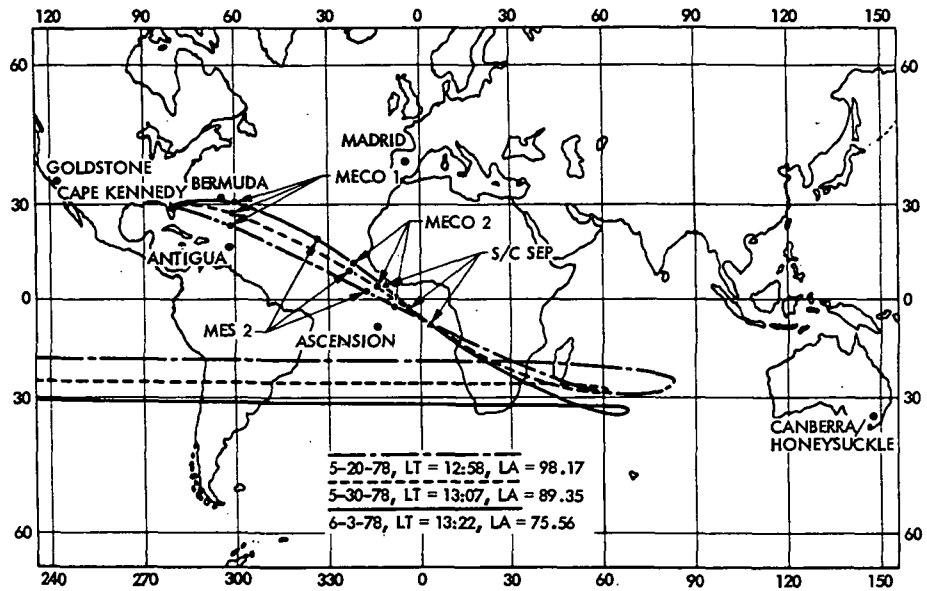


Fig. 1. Earth tracks for a Pioneer Venus Orbiter launch on May 20, May 30, and June 3, 1978

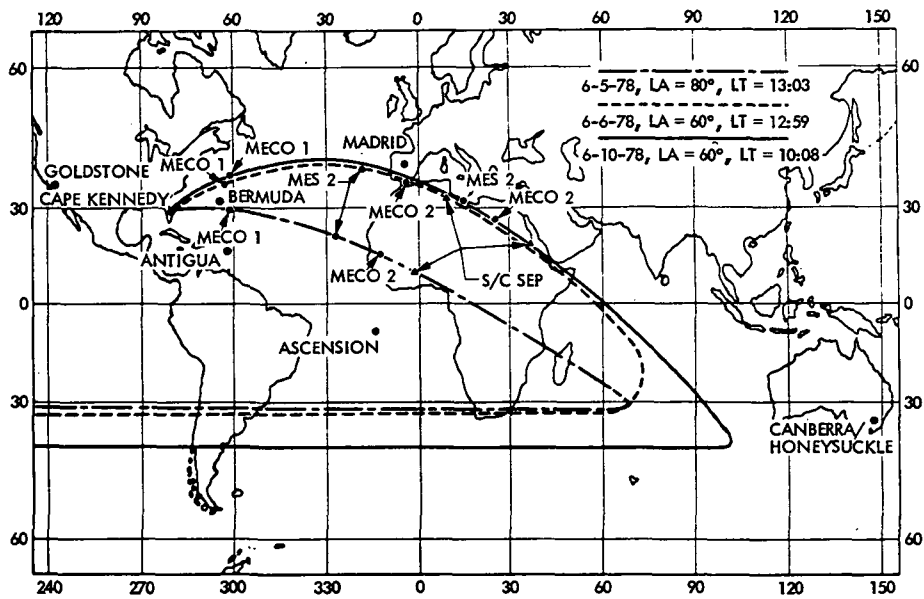


Fig. 2. Earth tracks for a Pioneer Venus Orbiter launch on June 5, June 6, and June 10, 1978

ORIGINAL PAGE IS  
OF POOR QUALITY

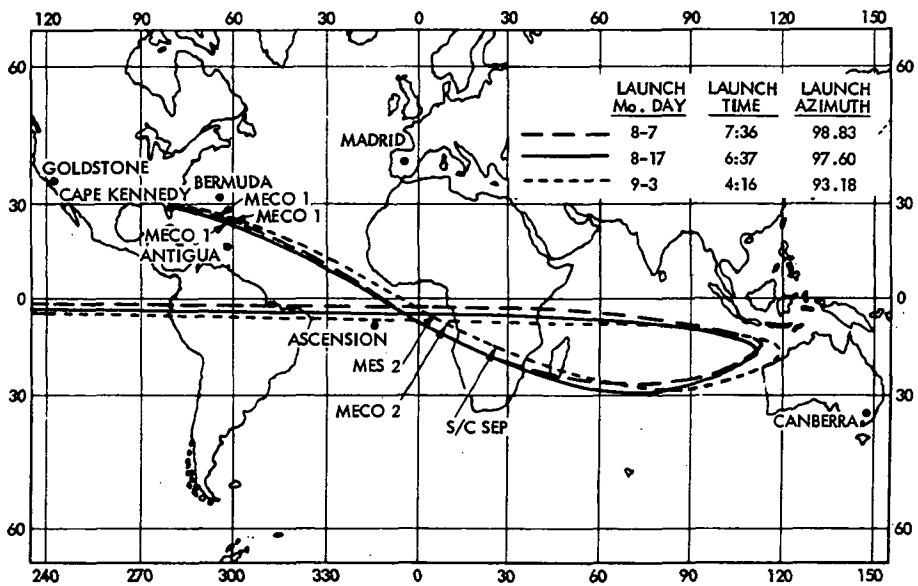


Fig. 3. Earth tracks for a Pioneer Venus Multiprobe launch

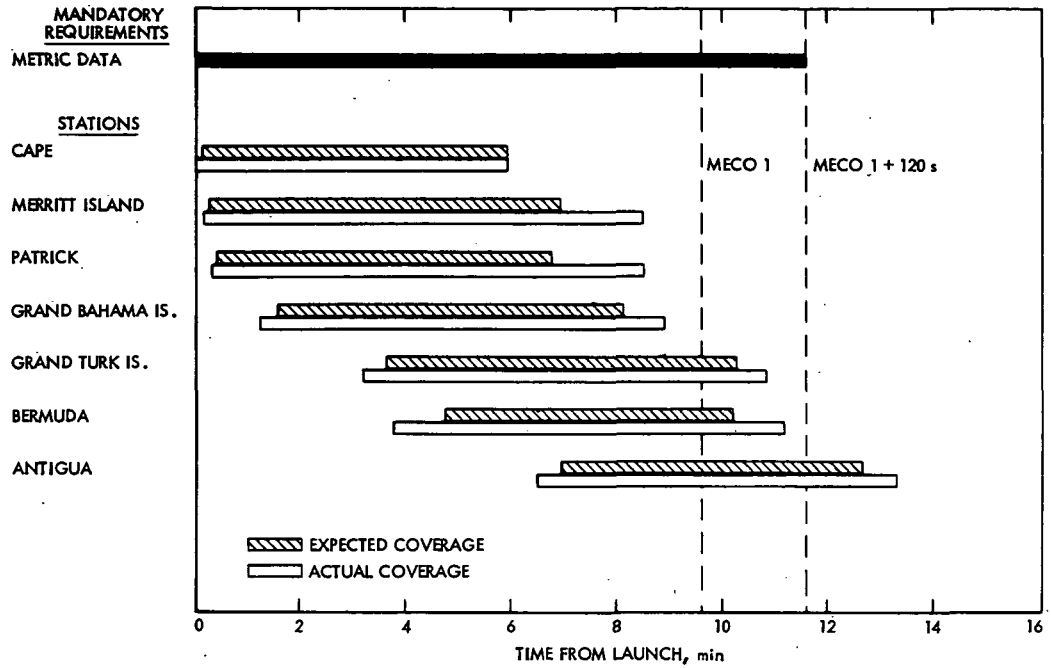


Fig. 4. Radar coverage for Pioneer Venus 78 Orbiter launch

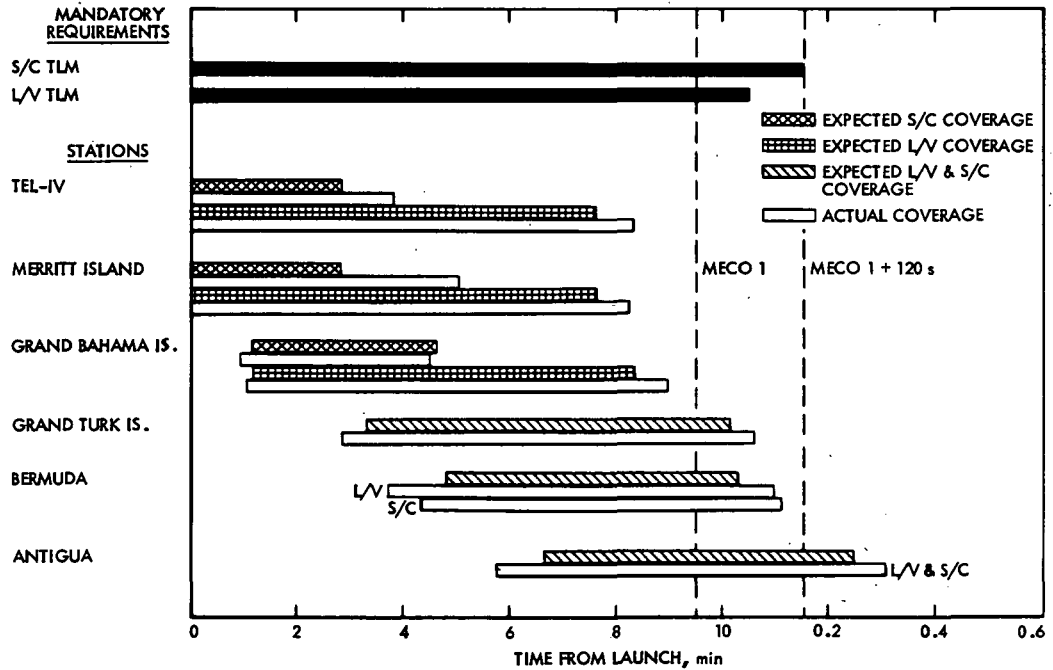


Fig. 5. Launch vehicle and spacecraft coverage for Pioneer Venus 78 Orbiter launch

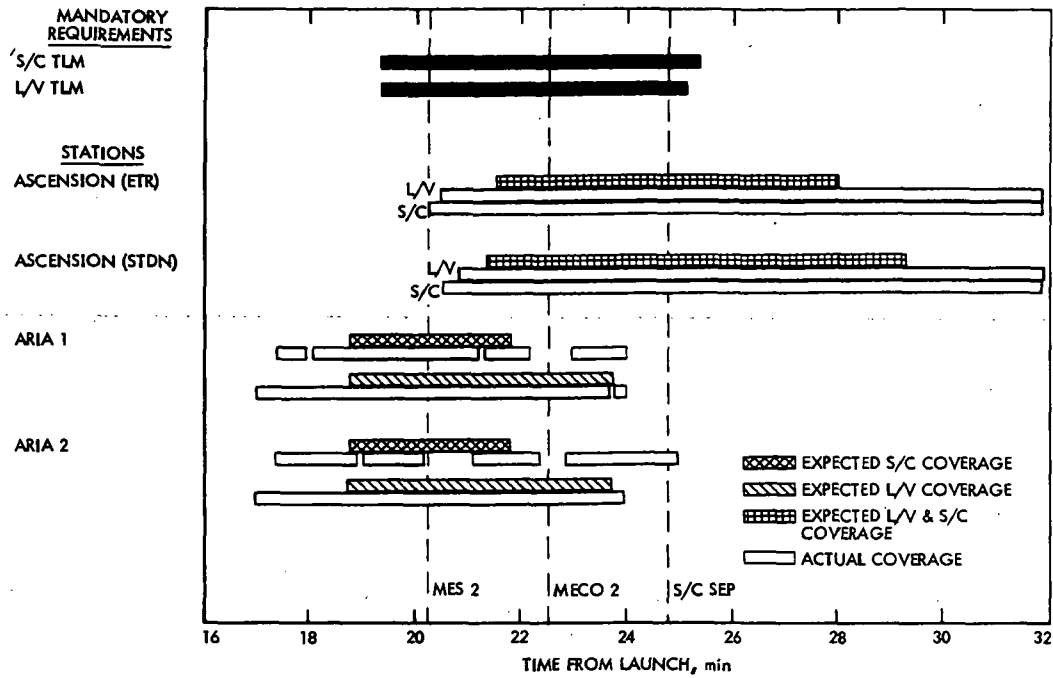


Fig. 6. Launch vehicle and spacecraft coverage for Pioneer Venus 78 Orbiter launch

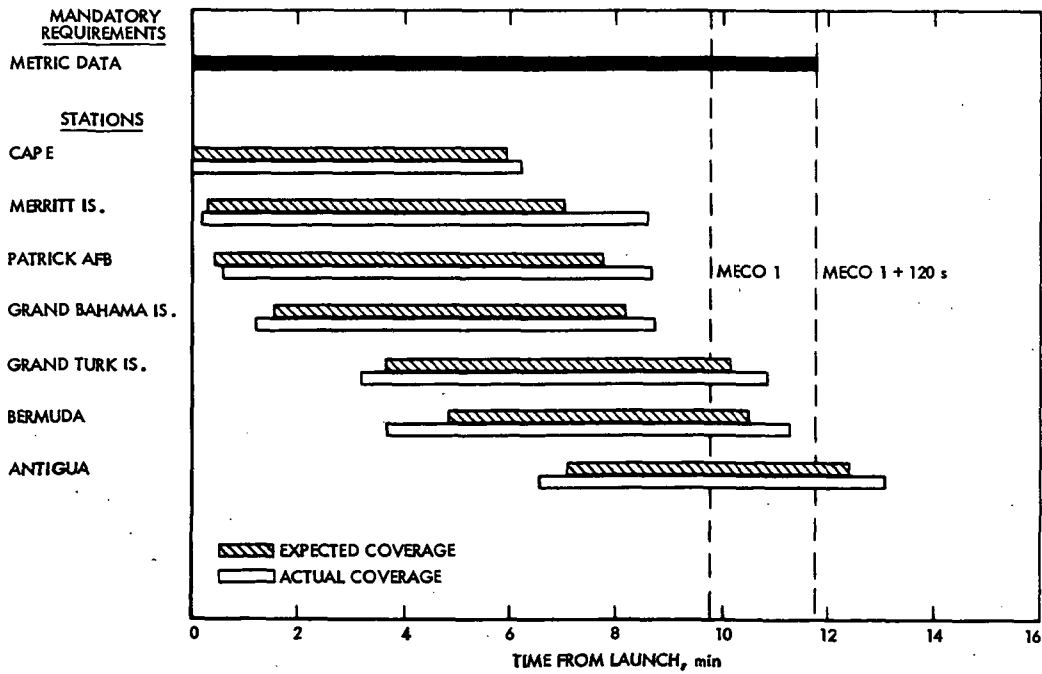


Fig. 7. Radar coverage for Pioneer Venus 78 Multiprobe launch

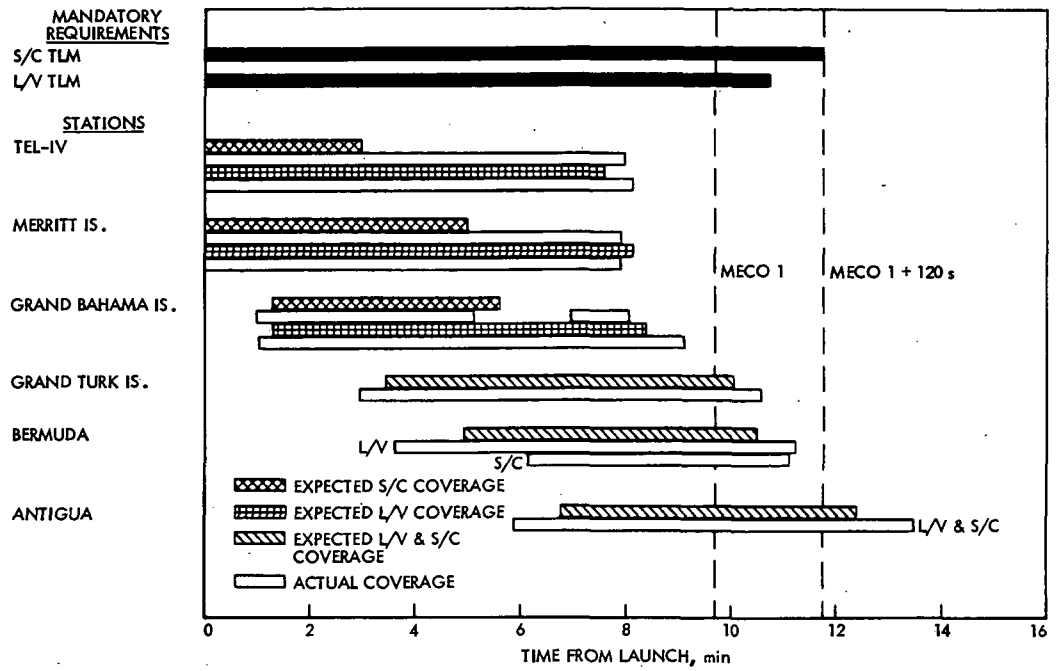


Fig. 8. Launch vehicle and spacecraft coverage for Pioneer Venus 78 Multiprobe launch

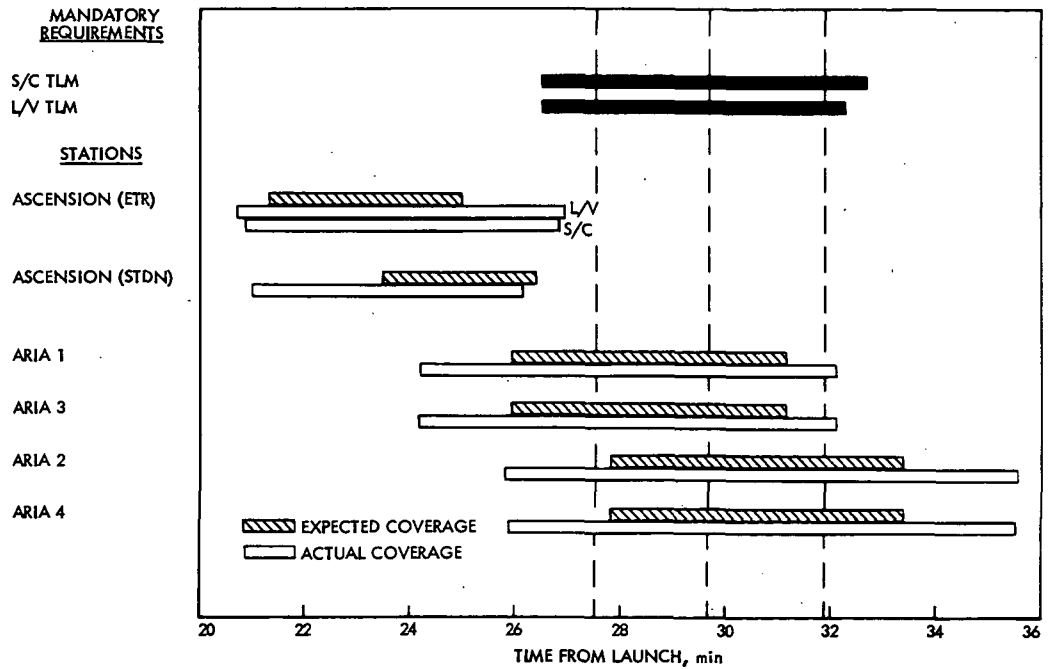


Fig. 9. Launch vehicle and spacecraft coverage for Pioneer Venus 78 Multiprobe launch

97  
N79-22147

## Estimated Displacements for the VLBI Reference Point of the DSS 13 26-m Antenna

H. McGinness, G. Gale, and R. Levy  
DSN Engineering Section

*It is shown that the displacement of the defined reference point caused by bearing runout, temperature change, and wind loading, under expected environmental conditions, will not exceed a few millimeters.*

### I. Introduction

One of the tasks associated with the very long base interferometry (VLBI) project is the estimation of the displacements of the reference point of the 26-m antenna at DSS 13. This antenna is of the azimuth-elevation type, and its reference point is defined as a point on the azimuth axis at the level of the elevation axis. The desired displacements are the horizontal and vertical displacements of the reference point, with respect to the ground, caused by azimuth bearing runout, wind, and temperature variations.

At first it was believed that these displacements could be obtained by placing a target near the reference point and observing it with two theodolites spaced 90 degrees about the antenna azimuth axis as shown in Fig. 1. Experiments made with a 1/48 scale model of the antenna indicated that the reference point target could be seen from theodolites located as shown in Fig. 1 and that displacements caused by bearing runout, wind, and temperature changes could be observed. Concrete monuments were placed as indicated in the figure and theodolites mounted on them. It was then realized that the antenna was different enough from the model to prevent

the target from being seen at many azimuth positions, thus making the proposed bearing runout test impossible.

Three attempts were made to measure the vertical and horizontal displacements caused by temperature gradients. The antenna was parked and theodolite readings made at various times of the day. On one windless day, when the ambient temperature ranged from 43°C at hour 1530 to 21°C at hour 0700, both theodolites showed an azimuth change of 2 arc seconds. The corresponding horizontal resultant displacement is 0.56 mm. The changes in the theodolite elevation angles during this time were 26 and 33 arc seconds. These elevation changes are not only much more than was anticipated for such a temperature change, but the signs of both angular changes are wrong in that the reference point seems to be highest at the lowest ambient temperature! This paradox may be explained by vertical temperature gradients in the air affecting its refractive properties. Another possible explanation is that the distances between the reference point and the theodolite monuments increase slightly as the ambient increases, thus producing smaller elevation angles. Neither of these hypotheses would affect the azimuth angle changes. Therefore, it seems proper to accept the measured azimuth angle changes, but to consider

the elevation changes as spurious. It was necessary to develop other methods for obtaining the reference point displacements.

The methods employed for these measurements are discussed as follows:

- (1) Horizontal displacement from bearing runout.
- (2) Displacement caused by wind loading.
- (3) Vertical displacement from temperature change.

## II. Horizontal Displacement from Bearing Runout

The horizontal displacement of the reference point caused by runout of the antenna azimuth bearings was calculated from a set of runout measurements taken at a point near ground level and a set of clinometer measurements taken at the top of the alidade. The runout measurements were made by utilizing a device curiously called the "magic tee." Figure 2 shows the position of this device, the purpose of which is to transmit the azimuth displacement of the antenna dish (the dish elevation bearings) to the azimuth encoder mounted on a pedestal near the ground. As designed, the device transmits the azimuth displacement without distortion.

Preparation for the test consisted of the removal of the azimuth encoder, drilling and reaming for and insertion of two taper pins through the lower guide bearing flange and the encoder pedestal, dropping the vertical leg of the magic tee 3 mm by turning the nut at its center support by 1-1/2 turns, thus allowing the lower guide bearing to drop away from the encoder pedestal structure, and installing three equally spaced struts between the magic tee and alidade kingpost. The lower end of the magic tee was now free from any external constraint and rigidly connected to the alidade, yet could be restored exactly to its original configuration. Since the azimuth encoder was gone, a cardboard chart with 10-degree angular marks was placed in the encoder pedestal just below the end of the magic tee. A stylus clamped to the magic tee completed the temporary azimuth angle contrivance. The installation of two dial indicators, one on the east side and one on the south side, and the placement of two levels (clinometers) shown in Fig. 2 completed the preparation. The cylindrical surface of the magic tee touching the dial indicators had been measured and found to be truly circular.

If the azimuth bearings were perfect, the dial indicator readings plotted versus the azimuth angle would be perfect sinusoids, the amplitudes corresponding to the distance that the center of the circular surface was offset from the centerline of the perfect azimuth bearings. The phase angle between

the two sinusoids would be 90 degrees since the two dial indicators were 90 degrees apart. Similarly, if the azimuth bearings were perfect, the level readings plotted against the azimuth angle would produce perfect sinusoids, the amplitude corresponding to the amount that the bearing centerline was off vertical. The phase angle would also be 90 degrees because the levels were 90 degrees apart. The true runout of the lower end of the magic tee is the difference between the curve plotted from the dial indicator readings and the fictitious perfect sinusoid. The fictitious sinusoid can be approximated closely by best fitting a sinusoid to the experimentally derived curve. The difference between the best fitted sinusoid and the experimental curve is a good approximation to the true bearing runout at the lower end of the magic tee. Similarly, the angular change in the position of the vertical axis is the difference between the best fitted sinusoid of the clinometer readings and the actual clinometer readings.

The horizontal runout at the reference point was calculated as follows:

The curves of Fig. 3 were plotted by considering compression of the dial indicators to be positive. The variations of the measured points from the best fitted sinusoids,  $\delta_E$  and  $\delta_S$ , are defined as positive as shown in Fig. 3. These are the runouts at the lower end of the magic tee.

The curves of Fig. 4 were plotted by considering clinometer "a" reading positive when its "W" end went downward and clinometer "b" reading positive when its "n" end went downward. The variations of the measured points from the best fitted sinusoids,  $\theta_a$  and  $\theta_b$ , are defined as positive as shown in Fig. 4. These are the angular changes in the position of the vertical axis, and each is a function of the antenna azimuth angle  $\psi$ .

Consider a view of the bearing axis when looking northward. The angular change of the bearing axis as seen in this view,  $\theta_{EW}$ , is:

$$\theta_{EW} = \theta_a \cos \psi - \theta_b \sin \psi \quad (1)$$

The positive direction of  $\theta_{EW}$  is when the upper end of the bearing axis is tilted to the west. Consider a view of the bearing axis when looking eastward. The angular change of the bearing axis as seen in this view,  $\theta_{NS}$ , is:

$$\theta_{NS} = \theta_b \cos \psi + \theta_a \sin \psi \quad (2)$$

The positive direction of  $\theta_{NS}$  is when the upper end of the bearing axis is tilted to the north.

At the reference point the horizontal displacements to the east and to the south are  $\delta_{RE}$  and  $\delta_{RS}$ , respectively:

$$\delta_{RE} = \delta_E - \ell\theta_{EW} \quad (3)$$

$$\delta_{RS} = \delta_S - \ell\theta_{NS} \quad (4)$$

where  $\ell$  is the vertical distance from the dial indicators to the reference point. Its numerical value is 8.5 m as shown in Fig. 2.

The substitution of (1) and (2) into (3) and (4), respectively, yields the following:

$$\delta_{RE} = \delta_E - \ell[\theta_a \cos \psi - \theta_b \sin \psi] \quad (5)$$

$$\delta_{RS} = \delta_S - \ell[\theta_b \cos \psi + \theta_a \sin \psi] \quad (6)$$

which are, respectively, the east and south components of the horizontal displacement at the reference point caused by azimuth bearing runout. The resultant horizontal runout,  $\delta_T$ , is:

$$\delta_T = \sqrt{\delta_{RE}^2 + \delta_{RS}^2} \quad (7)$$

Dial indicator and clinometer readings were taken for six complete turns of the antenna. In all instances the wind was near zero and the weather was sunny. The elevation angle was 30 degrees for four runs and 4.7 degrees and 60.2 degrees for the other two runs. It was observed that the instrument readings were not affected by a change in elevation angle. The readings from two typical runs are plotted in Figs. 3 and 4. The values of  $\delta_E$ ,  $\delta_S$ ,  $\theta_a$ , and  $\theta_b$  were read from these plots and are tabulated in Table 1 as a function of the antenna azimuth angle  $\psi$ . Then the total horizontal displacement at the reference point,  $\delta_T$ , was calculated using Eqs. (5), (6), and (7), and the results entered in the last column of Table 1. The largest entry in the  $\delta_T$  column is 0.782 mm, which represents the maximum horizontal displacement at the reference point caused by runout of the antenna azimuth bearings.

A corroborative check was made by attaching a pencil to the lower end of the magic tee so that its point was bearing against a paper fixed to the encoder pedestal. The antenna was rotated 360 degrees and the pencil trace compared to a perfect circle. The maximum discrepancy appeared to be approximately 0.50 mm, which agrees with the maximum values of  $\delta_E$  and  $\delta_S$  of Table 1. It was observed that the center of the angle chart serving as a temporary azimuth indicator was displaced 6.35 mm from the center of the antenna rotation. True antenna azimuth angles were calculated to correspond to the

indicated angles on the chart, and these true angles were used in plotting Figs. 3 and 4.

### III. Displacements Caused by Wind

A finite element model is available to estimate displacements at a set of nodal points of the DSS 13 26-m antenna mount. In addition to nodes of the mount, the model contains one node simulating the reflector vertex. The model, a source program to perform analysis, and input wind loading data for a spectrum of antenna attitudes relative to the wind direction are preserved on tape. The defined reference point is approximately halfway between two nodes, and its displacement may be taken as the mean displacement of these two nodes.

In order to check the accuracy of the analysis regarding the horizontal displacement of the elevation bearings, an experiment was made. As shown in Fig. 5, steel cables of 16-mm diameter were attached to the antenna near each elevation bearing and connected to a large truck by means of a snatch block. The truck was parked with its rear wheels in a ditch about 50 m south of the antenna. A cable jack and force scale were connected into the cable as shown in Fig. 5. Figure 6 shows the position of the eye bolts through which the free ends of the cables were looped and clamped. Each eye bolt was approximately 25 cm from the center of the elevation bearing and was attached to a 1.27-cm thick plate near a corner welded to heavy sections, thus insuring that local deflections would be negligible. A controlled force was applied by the jack.

The deflection of one of the eye bolts was measured by the device shown in Fig. 5. A 1.6-mm diameter steel cable was attached to the west eye bolt, extended 38 m southward, passed over a 15-cm diameter pulley mounted in a plywood bracket, and attached to a 23-kg steel mass. From the bottom of the steel mass was suspended the piston of the displacement gage as is shown in Fig. 7. Kerosene was poured into the glass cylinder to an appropriate level. The relationship between the downward displacement of the piston,  $Y_P$ , and the upward displacement of the liquid level,  $Y_L$ , is:

$$Y_L = \frac{d^2}{D^2 - d^2} Y_P \quad (8)$$

For the dimensions shown in Fig. 7,  $d^2/(D^2 - d^2)$  is 15.226; thus the device magnifies the piston displacement by this amount and makes small piston displacements easy to measure.

A jack force of 40,000 newtons was applied to the cable. It was observed that the angle between the cable and the hori-

zontal was approximately 7.5 degrees. The small cable to the 23-kg mass made an angle of 9.5 degrees with the horizontal. The lowest point of the liquid level was marked on the glass cylinder, and then the jack was operated to remove the cable force. It is estimated that the load was removed within a minute. The lowest point of the liquid level was marked immediately and measured. It had lowered by 7.62 mm (0.30 in.). It is believed that the measurement is accurate to within 0.75 mm.

The horizontal force applied near each elevation bearing was  $40,000 \times \cos 7.5$  degrees or 39,658 newtons. The horizontal deflection at the west elevation bearing was  $(7.72/15.226) \cos 9.5$  degrees or 0.514 mm. According to the structural analysis, a horizontal force of 39,658 newtons applied horizontally at each elevation bearing would produce a horizontal displacement of 0.546 mm, which is approximately the measured amount. Therefore, it seems that the pedestal and alidade structures were successfully modeled in the structural analysis and that the analysis may reliably be employed to predict any displacements caused by wind loading.

This test was conducted on August 28, 1978. The wind speed was less than 2.23 meters per second (5 mph) and the weather was sunny.

Figure 8 shows calculated displacements at the antenna reference point. Both the  $X$  component (the horizontal displacement perpendicular to the elevation axis) and the resultant magnitude are shown as functions of the wind azimuth angle and antenna elevation angle. Since the above described experiment verified the analysis on which these curves are based, it is believed these curves are reliable. Displacement at other wind speeds can be determined by considering the displacements proportional to the square of the wind speed.

Figure 9 shows the calculated displacements at the antenna vertex, due to the flexibility of the antenna pedestal and alidade structure, under a 14.14-meter per second wind loading.

The curves of Figs. 8 and 9 were plotted from the data listed in Table 2, which are the displacement components for various elevation and azimuth angles.

#### IV. Vertical Displacement from Temperature Changes

Experiments made with the displacement gages, as shown in Fig. 7, indicated that they would serve well for measuring the vertical displacement of each end of the alidade. The experiments consisted of moving the piston a known amount and

measuring the vertical excursion of the lowest point of the fluid level. Because of capillary effects, the fluid height was not constant. By moving the piston horizontally until it touched the glass cylinder, the liquid on the opposite side would be at the lowest level. Many trials showed that the displacement magnification obtained experimentally was essentially the same as that calculated by Eq. (8).

The vertical displacement at the reference point would be the mean of the displacements at the alidade ends, provided there was no bowing or warpage of the alidade. Figure 10 shows the test setup. Three pairs of active and dummy displacement gages were disposed as shown in the figure. Figure 11 is a photograph of a pair of the displacement gages. The purpose of the dummy gage was to allow for evaporation and thermal expansion of the liquid (kerosene), since the test would last for many hours. In order to account for any bowing of the alidade, a displacement gage was placed between the center of the alidade and a taut cable stretched between the elevation bearings. The cable was kept taut by being passed over a pulley clamped to one elevation bearing and loaded by a dead weight. Since the elevation bearings are near the alidade ends, it may be assumed that the displacement of the bearings is essentially the same as the end displacements.

The other two pairs of displacement gages were put on steel blocks leveled against the pavement directly beneath the alidade ends. Steel angles were temporarily bolted to the upper surface of the alidade and the 1.00-mm diameter Invar A36 wire clamped to the angles. The lower ends of the wires were attached to the gage pistons as shown in Fig. 7. A downward force of approximately 125 newtons was applied to each piston to insure that the wire was yielded to a straight condition. Kerosene was put into all gage units. Each dummy unit was adjusted so that the amount of kerosene below its piston approximately matched that in the corresponding active gage. Also, the liquid levels of the dummy and active gages were approximately matched. Thus, both the evaporation and thermal expansion effects would be matched at each pair of gages.

The first test was begun on September 11, 1968 at hour 1630. Five sets of readings were taken during the 15-hour period that the antenna was stationary at zero azimuth and 5-degree elevation. The results are listed in Table 3 from which it may be seen that there was no relative displacement between the active and reference gages at the top center of the alidade. Thus, there was no bowing of the alidade over the ambient temperature range from 33.3 to 21.8°C. This indicates that the mean of the vertical displacements at the east and west ends of the alidade would represent the vertical displacement of the defined reference point. During this test the wind was less than 2 meters per second and the sky was clear.

A subsequent test was begun on October 13, 1978 when there was an opportunity to record data for two consecutive days with the antenna parked at zero azimuth and 45-degree elevation. Only the east and west displacement gages were installed at this time, since the previous test had established that there was no bowing of the alidade structure. The results are listed in Table 4. With one exception the readings were taken at approximately 3-hour intervals. The displacement at a gage is proportional to the relative displacement between the active and dummy gage. These relative displacements were divided by the magnification factor of the gages, namely, 15.23, averaged, and plotted versus time as shown in Fig. 12. Also shown in the figure are the ambient air temperature and the mean temperature of the two thermometers mounted on the pedestal structural members. Under the assumption that the Invar wire supporting the active gage has a zero coefficient of expansion, the displacement curve of Fig. 12 gives directly the vertical displacement of the antenna reference point during the 48-hour test. The total excursion over this period was 0.525 mm. The ambient air temperature range was 17°C, and the mean thermometer reading was 8.6°C. The inside of the pedestal is air conditioned, and this partially accounts for the large difference between the two temperature ranges.

Actually, the Invar wire has a finite expansion coefficient, which is about 1/11 that of steel. Also, the temperature of the small diameter Invar wire is likely to be very close to the ambient air temperature. Since the ambient range was approximately twice that of the measured steel temperature range, the vertical displacement of the reference point is likely to be 2/11 more than the curve of Fig. 12 shows. Therefore, over the test period of 48 hours, a better estimate of the total vertical excursion of the reference point is 0.62 mm.

The vertical displacement of the reference point,  $\delta_v$ , may be expressed as follows:

$$\delta_v = \ell \alpha \Delta T \quad (9)$$

where  $\ell$  is the effective height of the steel structure,  $\alpha$  is the expansion coefficient of steel, and  $\Delta T$  is the average temperature change.

Taking  $\ell = 9000$  mm,  $\delta_v = 0.62$  mm, and  $\alpha = 11 \times 10^{-6}$  per degree C, and solving for  $\Delta T$ , there is obtained:  $\Delta T = 6.26^\circ\text{C}$ , which is appreciably less than the mean thermometer reading range of 8.6°C. This suggests that the average temperature of the steel structure did not change as much as the two thermometers indicated.

It would appear that with the air conditioning system currently in use, the effective diurnal temperature change of the steel pedestal and alidade is less than half the diurnal ambient temperature change.

## V. Conclusions

The displacements of the defined antenna reference point will not exceed the following values:

- (1) 0.782-mm horizontal component caused by runout of the azimuth bearings.
- (2) 1.00-mm horizontal component caused by a wind of 14.14 meters per second.
- (3) 0.62-mm vertical component caused by an ambient air temperature change of 17°C.

Table 1. Experimental data for bearing runout

Azimuth angle $\psi$ , deg	$\delta_E$ , mm	$\delta_S$ , mm	$\theta_a$ , mrad	$\theta_b$ , mrad	$\delta_{RE}$ , mm	$\delta_{RS}$ , mm	$\delta_T$ , mm
0	0.076	-0.076	0.003	-0.015	0.051	0.051	0.071
10	0.076	0	-0.020	-0.015	0.221	0.155	0.270
20	0.127	0.076	-0.020	-0.010	0.254	0.213	0.332
30	0.127	0.203	-0.045	-0.010	0.416	0.467	0.626
40	0	0.330	-0.039	0.015	0.330	0.444	0.554
50	-0.127	0.381	-0.040	0.012	0.170	0.574	0.599
60	-0.254	0.279	-0.040	0.035	0.152	0.424	0.451
70	-0.381	0.279	-0.040	0.030	-0.024	0.508	0.509
80	-0.305	0.254	-0.039	0.030	0.004	0.535	0.536
90	-0.432	0.508	-0.030	0.030	-0.175	0.762	0.782
100	-0.279	0.127	-0.028	0.025	-0.101	0.399	0.411
110	-0.127	-0.127	-0.025	0.010	-0.119	0.102	0.157
120	-0.228	-0.279	-0.025	0.010	-0.254	-0.053	0.260
130	-0.127	-0.381	-0.020	-0.015	-0.333	-0.333	0.471
140	0	-0.508	-0.029	-0.020	0.305	-0.480	0.569
150	0.254	-0.305	-0.026	-0.030	-0.066	0.025	0.071
160	0.279	-0.381	-0.030	-0.030	-0.076	-0.533	0.539
170	0.381	-0.254	-0.045	-0.030	-0.041	-0.432	0.434
180	0.279	-0.508	-0.050	-0.030	-0.148	-0.762	0.776
190	0.254	-0.203	-0.040	-0.025	-0.043	-0.353	0.356
200	0.305	0	-0.018	-0.020	0.218	-0.211	0.304
210	0.229	-0.076	-0.020	-0.010	0.122	-0.234	0.263
220	0.127	0	0.008	-0.010	0.234	-0.021	0.235
230	0	0.127	0.005	0	0.028	0.160	0.162
240	0	0.254	0.010	-0.005	0.079	0.307	0.317
250	-0.152	0.279	0.020	0	-0.094	0.439	0.449
260	-0.279	0.229	0.022	0.005	-0.287	0.419	0.508
270	-0.305	0.076	0.032	0.005	-0.348	0.348	0.492
280	-0.330	0.127	0.035	0	-0.381	0.419	0.566
290	-0.203	0.127	0.035	-0.005	-0.264	0.419	0.495
300	-0.102	0	0.033	-0.015	-0.130	0.307	0.333
310	-0.127	-0.127	0.030	-0.020	-0.160	-0.041	0.165
320	0	-0.127	0.030	-0.025	-0.058	0.201	0.209
330	0	-0.076	0.025	-0.030	-0.056	0.251	0.258
340	0.152	-0.127	0.030	-0.030	-0.0002	0.201	0.201
350	0.127	-0.051	0.030	-0.025	-0.086	0.203	0.221
360	0.228	-0.076	0	-0.025	0.229	0.135	0.265

ORIGINAL PAGE IS  
OF POOR QUALITY

**Table 2. Computed wind loading displacements in millimeters  
for 14.14-m/s wind speed**

Elevation angle, deg	Vertex				Reference point			
	<i>N</i>	<i>A</i>	<i>S</i>	$\sqrt{N^2 + A^2 + S^2}$	<i>x</i>	<i>y</i>	<i>z</i>	$\sqrt{x^2 + y^2 + z^2}$
<b>(a) Antenna azimuth with respect to wind = 0</b>								
0	1.219	2.540	-0.003	2.817	0.937	-0.002	0.356	1.002
10	1.219	2.286	-0.007	2.590	0.864	-0.003	0.295	0.912
20	1.219	2.032	-0.003	2.370	0.838	0	0.244	0.873
30	1.219	1.803	0.007	2.177	0.762	0	0.203	0.789
40	1.193	1.575	0.012	1.976	0.711	-0.005	0.165	0.730
50	1.168	1.372	0.013	1.801	0.635	-0.008	0.142	0.651
60	1.118	1.194	0.009	1.635	0.584	-0.010	0.132	0.599
70	0.889	0.864	0.005	1.239	0.432	-0.008	0.117	0.447
80	0.685	0.864	-0.002	1.103	0.330	-0.005	0.109	0.348
90	0.483	0.330	-0.006	0.585	0.236	-0.001	0.117	0.264
<b>(b) Antenna azimuth with respect to wind = 30 degrees</b>								
0	1.092	2.311	0.122	2.559	0.864	0.043	0.320	0.922
10	1.27	2.311	0.137	2.641	0.889	0.058	0.305	0.942
20	1.346	2.184	0.135	2.569	0.864	0.069	0.279	0.910
30	1.321	1.905	0.099	2.320	0.787	0.076	0.234	0.825
40	1.346	1.753	0.109	2.213	0.762	0.076	0.206	0.793
50	1.346	1.575	0.107	2.074	0.711	0.053	0.193	0.739
60	1.245	1.321	0.081	1.817	0.610	-0.007	0.175	0.634
70	0.965	0.914	0.064	1.331	0.457	-0.028	0.145	0.480
80	0.711	0.584	0.046	0.921	0.330	-0.033	0.130	0.356
90	0.533	0.381	0	0.655	0.254	-0.038	0.122	0.284
<b>(c) Antenna azimuth with respect to wind = 60 degrees</b>								
0	0.914	1.880	0.124	2.094	0.686	0.071	0.254	0.735
10	1.067	1.956	0.196	2.236	0.737	0.081	0.254	0.783
20	1.118	1.803	0.170	2.128	0.711	0.043	0.241	0.752
30	1.118	1.600	0.069	1.953	0.660	0.0064	0.211	0.693
40	1.041	1.346	0.112	1.706	0.559	-0.051	0.173	0.587
50	0.863	0.991	0.102	1.318	0.457	-0.142	0.130	0.496
60	0.668	0.711	0.122	0.978	0.330	-0.160	0.091	0.378
70	0.483	0.457	0.107	0.673	0.241	-0.160	0.063	0.296
80	0.356	0.305	0.046	0.470	0.170	-0.145	0.053	0.230
90	0.216	0.147	-0.006	0.261	0.109	-0.130	0.053	0.178
<b>(d) Antenna azimuth with respect to wind = 90 degrees</b>								
0	-0.056	-0.140	-0.117	0.191	-0.066	0.006	-0.017	0.068
10	0.036	0.025	-0.137	0.144	-0.020	-0.047	0.012	0.052
20	0.076	0.089	-0.102	0.155	0.002	-0.076	0.025	0.080
30	0.076	0.081	-0.051	0.122	0.005	-0.086	0.028	0.091
40	-0.023	-0.043	-0.014	0.051	-0.028	-0.091	0.005	0.096
50	-0.001	-0.013	0.008	0.015	-0.013	-0.097	0.011	0.098
60	0.084	0.074	0.025	0.114	0.022	-0.107	0.033	0.114
70	-0.010	-0.021	0.030	0.038	-0.011	-0.091	0.011	0.093
80	-0.104	-0.104	0.023	0.149	-0.046	-0.074	-0.012	0.088
90	-0.094	-0.091	0.005	0.131	-0.041	-0.063	-0.011	0.076

Table 2 (contd)

Elevation angle, deg	Vertex				Reference point			
	N	A	S	$\sqrt{N^2 + A^2 + S^2}$	x	y	z	$\sqrt{x^2 + y^2 + z^2}$
(e) Antenna azimuth with respect to wind = 120 degrees								
0	-0.251	-0.533	0.356	0.689	-0.206	-0.058	-0.074	0.226
10	-0.246	-0.457	-0.279	0.590	-0.193	-0.097	-0.061	0.224
20	-0.254	-0.432	-0.193	0.537	-0.193	-0.132	-0.056	0.240
30	-0.305	-0.457	-0.099	0.558	-0.203	-0.152	-0.056	0.260
40	-0.381	-0.483	-0.043	0.616	-0.221	-0.185	-0.061	0.295
50	-0.431	-0.508	0.015	0.667	-0.231	-0.191	-0.066	0.307
60	-0.457	-0.483	0.036	0.666	-0.231	-0.188	-0.069	0.306
70	-0.432	-0.432	0.046	0.612	-0.211	-0.168	-0.066	0.277
80	-0.381	-0.330	0.030	0.505	-0.180	-0.150	-0.058	0.242
90	-0.254	-0.196	-0.006	0.321	-0.130	-0.130	-0.053	0.191
(f) Antenna azimuth with respect to wind = 150 degrees								
0	-0.685	-1.448	-0.206	1.615	-0.533	-0.021	-0.201	0.570
10	-0.787	-1.422	-0.170	1.635	-0.533	-0.056	-0.196	0.571
20	-0.813	-1.295	-0.107	1.533	-0.533	-0.084	-0.180	0.569
30	-0.889	-1.270	-0.076	1.552	-0.508	-0.102	-0.178	0.548
40	-1.041	-1.295	-0.036	1.662	-0.533	-0.119	-0.206	0.584
50	-0.965	-1.067	-0.010	1.439	-0.457	-0.134	-0.185	0.511
60	-0.864	-0.889	-0.004	1.239	-0.406	-0.127	-0.163	0.456
70	-0.813	-0.762	-0.008	1.114	-0.381	-0.099	-0.147	0.420
80	-0.711	-0.584	0.006	0.920	-0.330	-0.061	-0.134	0.362
90	-0.558	-0.406	0	0.691	-0.279	-0.038	-0.122	0.307
(g) Antenna azimuth with respect to wind = 180 degrees								
0	-0.668	-1.473	0	1.614	-0.584	0.001	-0.198	0.617
10	-0.762	-1.448	-0.006	1.636	-0.610	-0.004	-0.188	0.638
20	-0.889	-1.448	-0.023	1.699	-0.610	-0.012	-0.191	0.639
30	-1.117	-1.549	0.005	1.910	-0.635	-0.003	-0.218	0.672
40	-1.372	-1.702	-0.005	2.186	-0.711	-0.002	-0.254	0.755
50	-1.295	-1.422	-0.004	1.924	-0.635	-0.008	-0.241	0.679
60	-1.092	-1.092	-0.011	1.545	-0.508	-0.015	-0.208	0.549
70	-0.940	-0.838	-0.009	1.259	-0.432	0.012	-0.180	0.468
80	-0.737	-0.610	-0.006	0.956	-0.356	0.010	-0.145	0.385
90	-0.533	-0.406	-0.006	0.671	-0.254	-0.001	-0.114	0.279

Reference: RIL AZEL UPDATE, 08:26:33 Nov. 28, 1978

Table 3. Preliminary experimental data for thermal displacement

Date (1978)	Time	East gages, cm		West gages, cm		Top gages, cm		Pedestal temperature, °C		Average of north and south	Ambient temperature, °C
		Active	Reference	Active	Reference	Active	Reference	North	South		
Sept. 11	1630	4.60	4.50	4.35	5.05	5.50	5.80	26.53	27.78	27.15	33.3
	1900	4.35	4.40	3.35	4.75	5.10	5.40	25.56	24.72	25.14	27.5
	2100	3.90	4.40	3.20	4.60	5.00	5.30	23.89	23.33	23.61	26.4
	2300	3.80	4.30	3.20	4.50	5.00	5.30	23.61	23.61	23.61	24.2
Sept. 12	0600	3.90	4.30	3.30	4.40	4.95	5.30	22.78	23.33	23.05	21.8

Table 4. Experimental data for thermal displacement

Date (1978)	Time	East gages, cm		West gages, cm		Pedestal temperature, °C		Average of north and south	Ambient temperature, °C	Weather
		Active	Reference	Active	Reference	North	South			
Oct. 13	2100	4.50	4.75	6.15	5.00	26.94	26.67	26.81	19.83	Calm & clear
Oct. 14	0008	4.50	4.75	6.20	4.80	25.28	25.14	25.21	20.38	Calm & clear
	0330	4.40	4.70	6.40	4.80	22.22	22.78	22.50	16.05	Calm & clear
	0605	4.40	4.70	6.40	4.70	22.22	21.94	22.08	13.68	Calm & clear
	0900	5.00	5.40	6.90	4.85	23.89	24.17	24.03	26.58	Calm & clear
	1155	4.80	5.50	6.70	5.40	25.83	29.44	27.64	29.03	Calm & clear
	1500	4.40	5.00	6.90	5.90	29.17	32.08	30.63	30.45	Calm & clear
	1730	4.55	4.90	6.40	5.70	29.17	29.17	29.17	-	Calm, sundown
	2100	4.40	4.65	6.00	4.85	23.33	23.06	23.19	16.61	Clear, wind 5 m/s
Oct. 15	0002	4.45	4.65	6.25	4.85	23.06	23.33	23.19	18.51	Clear, wind 5 m/s
	0630	4.70	4.65	6.40	4.65	22.50	23.06	22.78	21.58	Before sunup, wind 5 m/s
	0900	4.75	4.75	6.65	4.70	23.06	23.61	23.33	24.07	Wind 7 m/s
	1200	4.90	4.90	6.40	4.90	24.72	26.39	25.56	26.85	Calm & bright
	1500	4.50	4.85	6.60	5.15	26.39	28.61	27.50	28.54	Calm & bright
	1730	4.45	4.70	6.25	5.10	27.50	28.06	27.78	26.29	Calm, sundown
	2100	4.40	4.60	5.95	4.55	24.17	23.61	23.89	22.58	Clear, wind 9 m/s

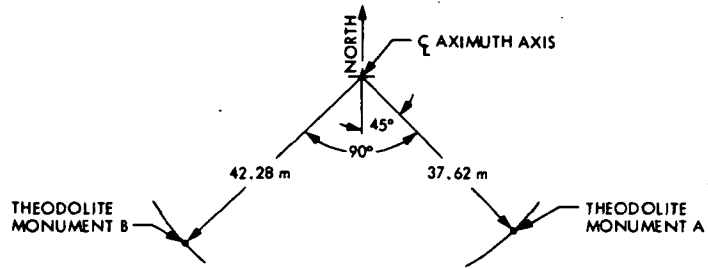


Fig. 1. Location of theodolite monuments

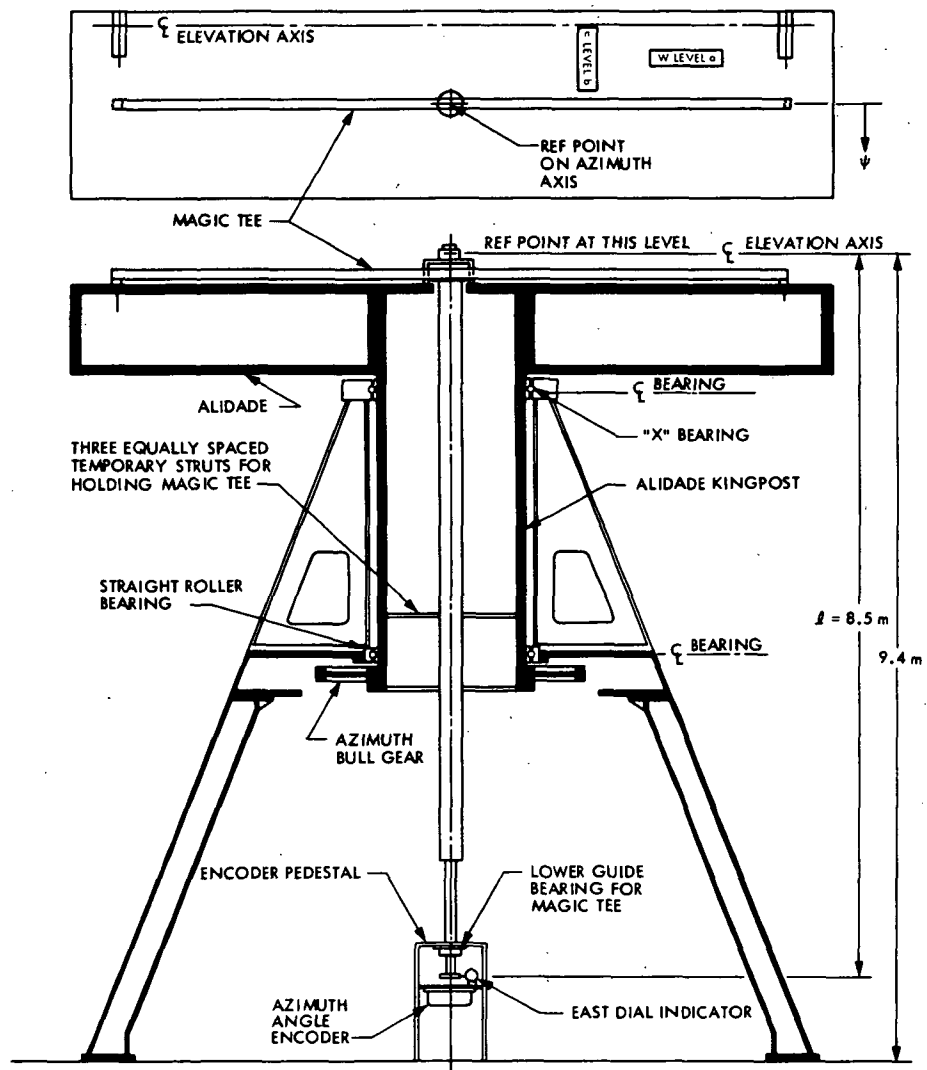


Fig. 2. Bearing runout instrumentation

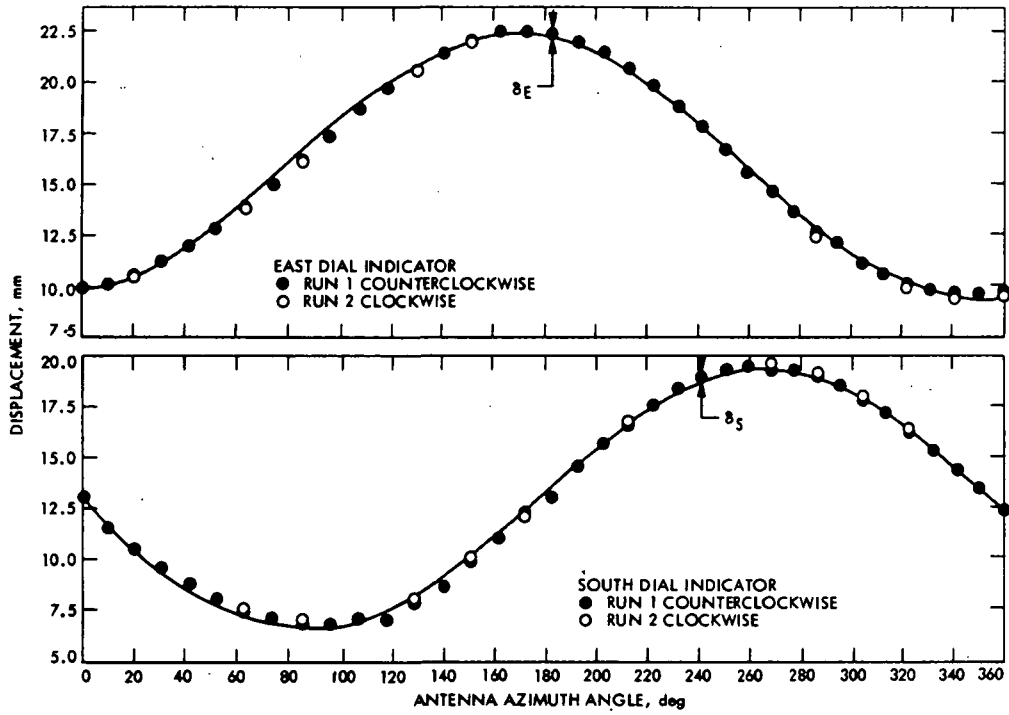


Fig. 3. Dial indicator displacements versus azimuth angle

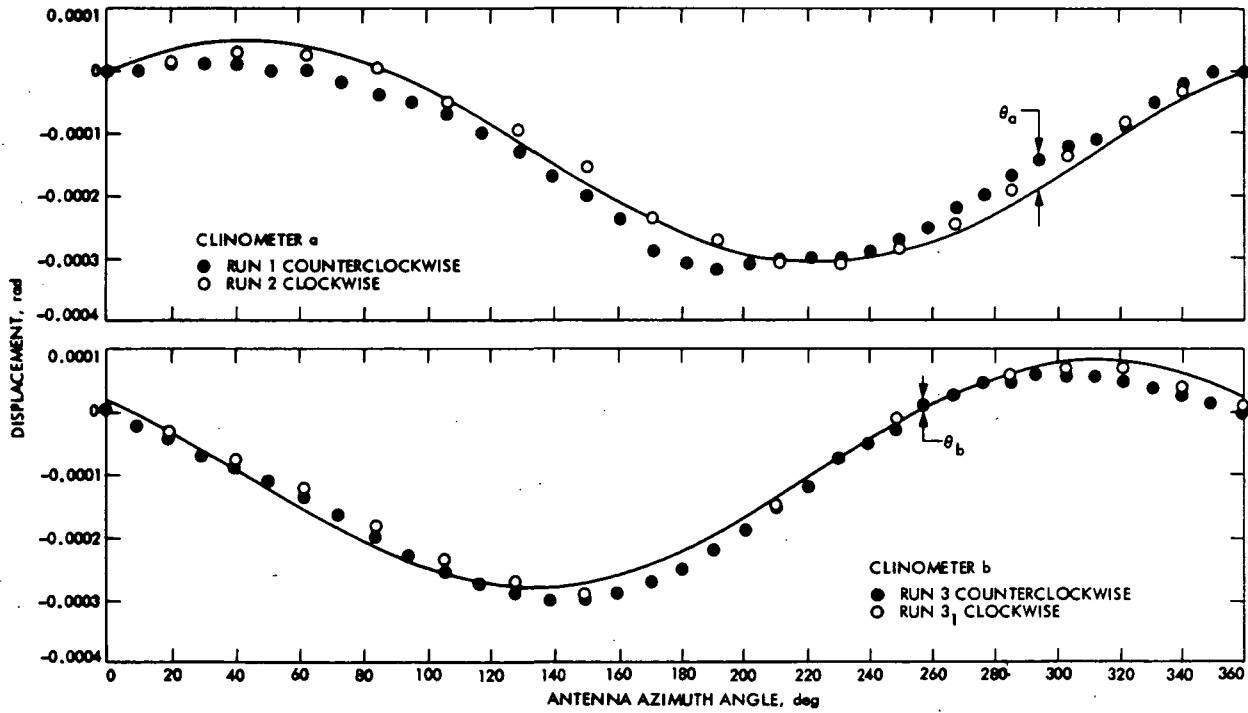


Fig. 4. Angles  $\theta_a$  and  $\theta_b$  versus azimuth angle

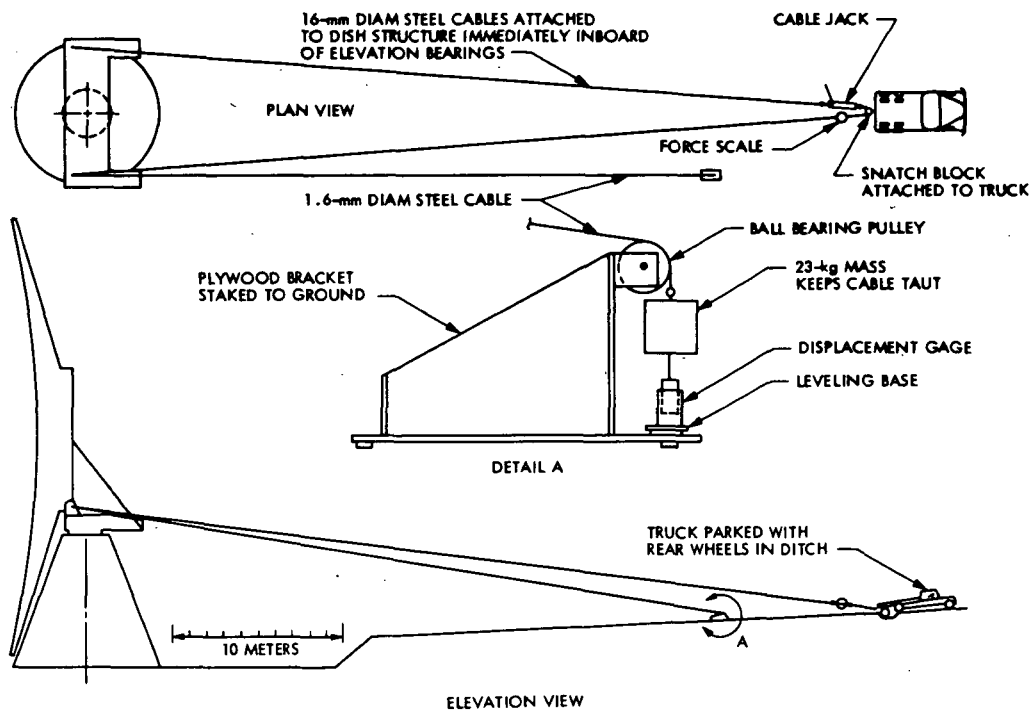


Fig. 5. Configuration of pull-displacement test

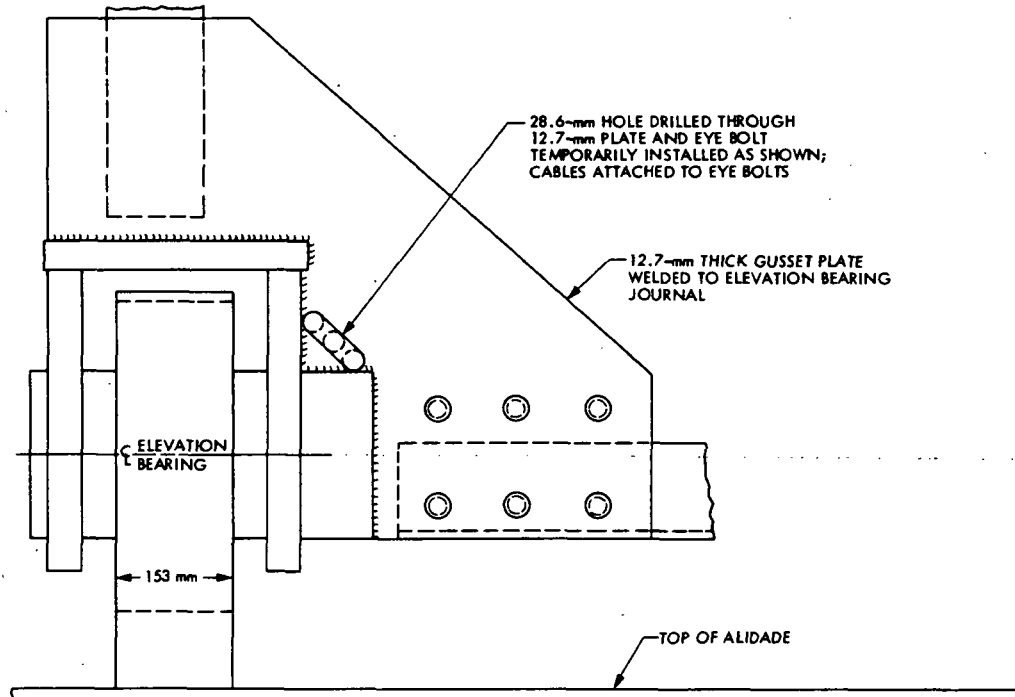


Fig. 6. Method of attaching cables near elevation bearings

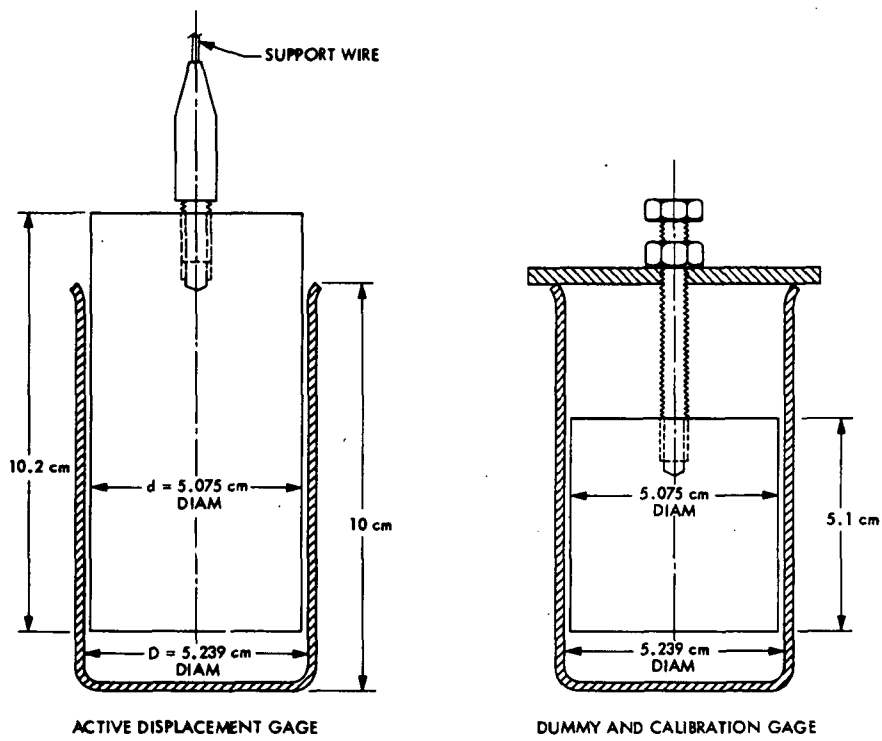


Fig. 7. Details of displacement gages

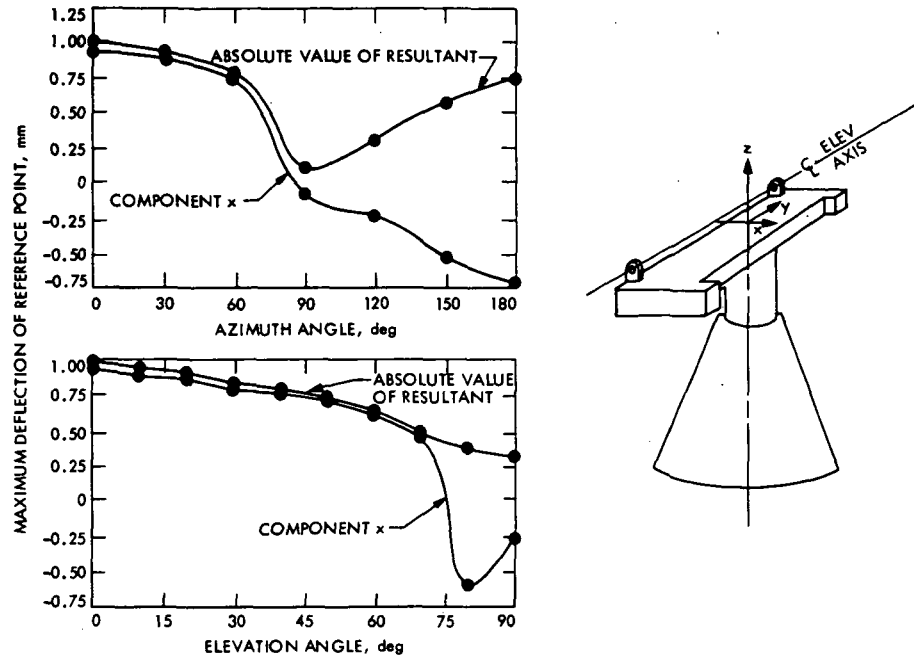


Fig. 8. Deflection of DSS 13 26-m antenna reference point in 14.14-m/s wind

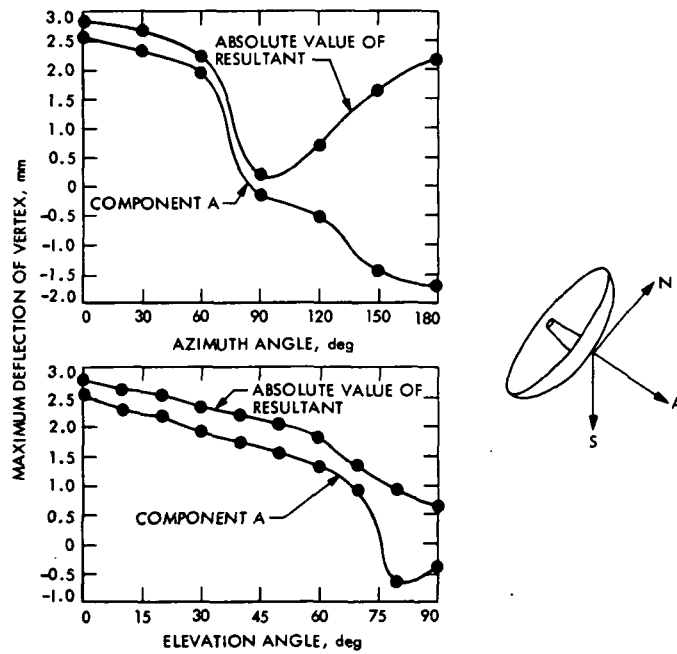


Fig. 9. Deflection of DSS 13 26-m antenna vertex in 14.14-m/s wind

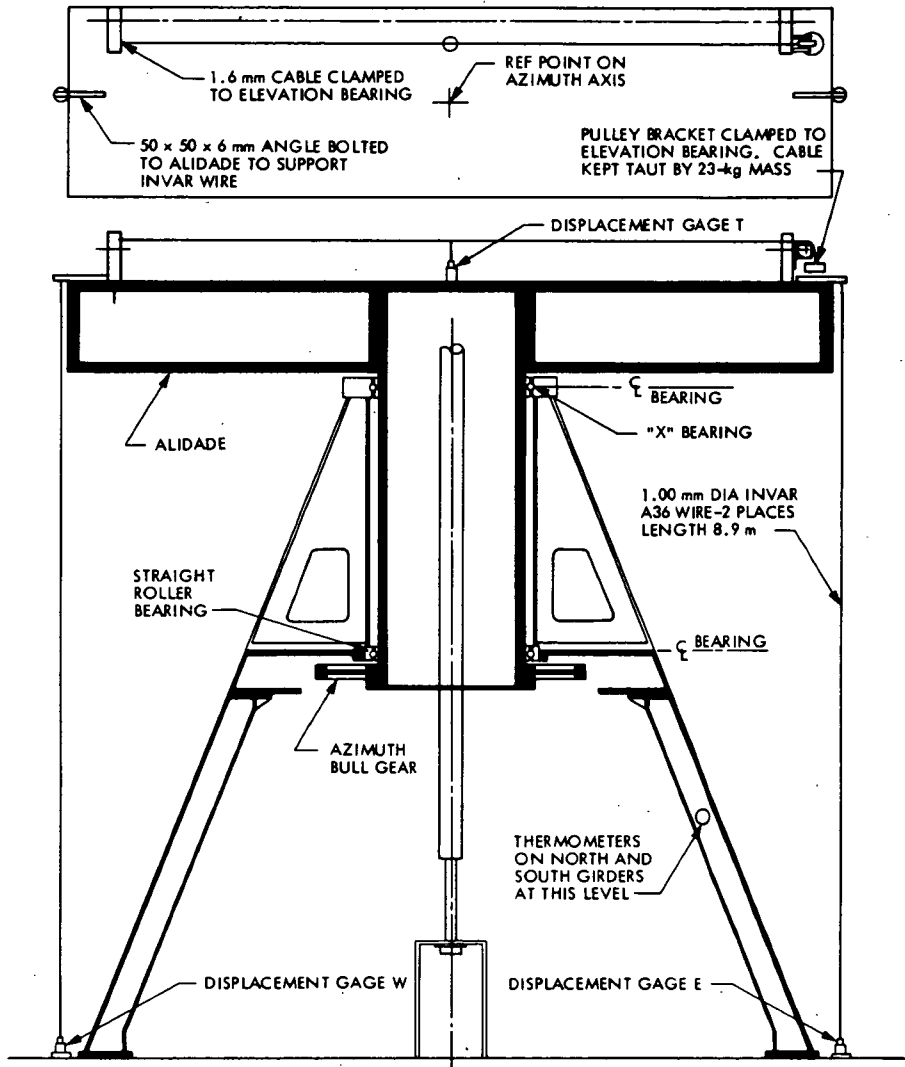
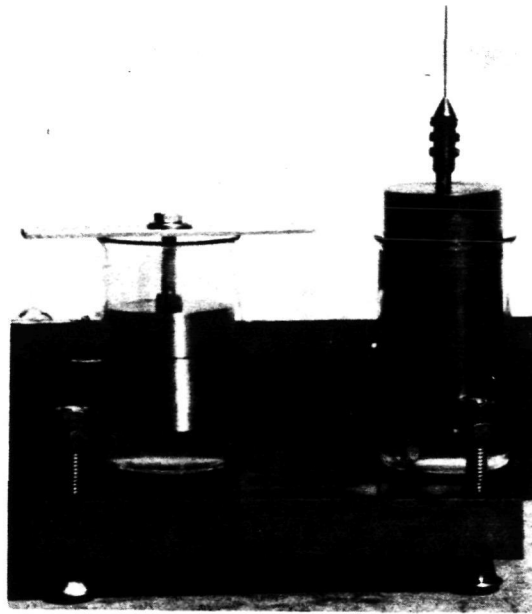


Fig. 10. Vertical motion instrumentation



ORIGINAL PAGE IS  
OF POOR QUALITY

Fig. 11. Photograph of dummy and active displacement gages

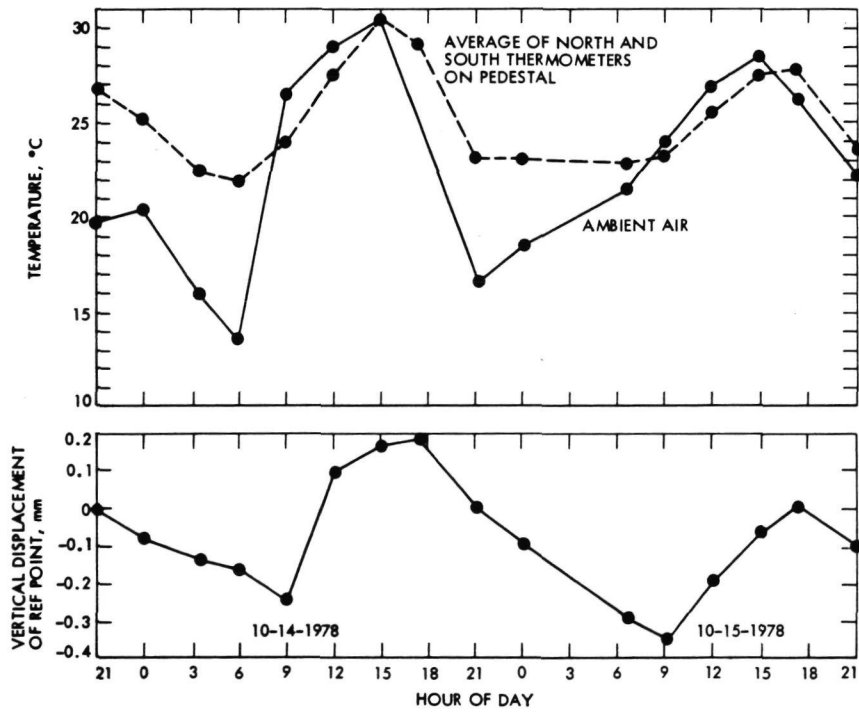


Fig. 12. Vertical displacement of reference point caused by temperature changes

# Multipath Effects on the Time Delays of Microwave Cassegrainian Antennas

T. Y. Otoshi

Radio Frequency and Microwave Subsystems Section

W. V. T. Rusch

Department of Electrical Engineering  
University of Southern California

*Preliminary results of a theoretical study of multipath errors on antenna time delays are discussed. A computer program has been developed to simulate multipath scattering between cone surfaces and the subreflector.*

## I. Introduction

During the early years of development of Cassegrainian antennas for space applications, the emphasis was on high-gain and low-noise performance. More recently, it has become equally important for deep space tracking antennas to have a high degree of phase and group delay stability as a function of antenna pointing angles and environmental changes.

Requirements for measurements of group delay through the antenna originated from navigation requirements for updated information on the absolute range (distance) of a spacecraft from earth-based tracking stations. More accurate measurement requirements later evolved from radio science projects which needed antenna time delay information for such experiments as electron content measurement in the interplanetary media and for verification of Einstein's general theory of relativity which involved using time delayed spacecraft signals passing through the solar corona. More recently,

knowledge of antenna group delay and delay stability has become very important to such projects as ARIES for Earth crust movement studies, Very Long Baseline Interferometry (VLBI) for determining station locations, and VLBI clock synchronization work.

When a large antenna is used to track a signal coming from a spacecraft or VLBI radio source, gravity loading causes deformations of the antenna structure as a function of antenna pointing angle. The antenna time delay change due to gravity loading could cause significant errors in station location determination if the effect of this error-source is not analyzed and accounted for. A primary cause of time delay changes of Cassegrainian antennas (due to gravity loading) is defocusing of the subreflector. This paper discusses two forms of subreflector defocus-related time delay changes. These are time delay changes in the absence and in the presence of multipath signals.

## II. Effects of Subreflector Defocusing

### A. Primary Signal Delay

Figure 1 shows the geometry of a Cassegrainian antenna with an S- and X-band reflex feed system. The cones are aluminum housings which contain feed assemblies as well as transmitter and receiver equipment. A single ray is shown to depict a typical primary ray path, but it is understood that the farfield signal is a plane wave and similar rays impinge upon the entire dish surface and subsequently arrive at the receive horn via the Cassegrainian antenna optical paths.

In the past when more accurate values of time delays were not required, it was reasonable to assume that the RF path length change resulting from subreflector defocusing was just twice the distance that the subreflector was defocused. A more careful study (Ref. 1) of the typical 64 m Cassegrainian antenna showed that the path length change is closer to 1.76 times the defocused distance, as shown in Fig. 2. For this result, the feed horn pattern was accounted for and amplitude and phase relationships precisely calculated after finding the specular reflection points on the subreflector in the defocused positions. This more rigorous treatment is necessary because these data will be useful for modeling and correcting one of the VLBI measurement errors caused by antenna time delay changes.

### B. Multipath Error

An error that is difficult to model and analyze accurately is the multipath error. It is currently one of the largest uncertainties in VLBI measurements. This error is caused by a small portion of the primary rays undergoing multiple reflections between the cone surfaces and the subreflector. Near-field experiments using time domain instruments have pinpointed the cone roof and cone support platform as the dominant multipath generating surfaces. The composite multipath signal combines in and out of phase with the primary signal when the subreflector defocuses. This results in a cyclical error pattern not only in amplitude and phase but also in the group delay characteristics of the antenna (e.g., see Fig. 2). The existence of these multipath signals was also verified by a farfield experiment (Ref. 2) that involved measurements of the round trip group delay changes while ranging to the Viking spacecraft in its interplanetary flight to Mars.

## III. Computer Program

In order to correlate experimental results to theory, a theoretical analysis was performed and a computer program developed for the multipath geometry, shown in Fig. 3. Although the multipath sources cannot be modeled exactly,

the computer-aided analysis is very useful for verifying sensitivity of the multipath errors to antenna geometry and frequency and also for establishing bounds of the error magnitudes. In this computer program, cone reflecting surfaces are simulated by a circular plate whose diameter and location along the axis of dish symmetry are selectable.

In determining the initial paraboloid illumination, the three "first-order" rays considered are: (Fig. 3a)

- (1) feed  $\rightarrow$  hyperboloid  $\rightarrow P: R_1$
- (2) feed  $\rightarrow$  hyperboloid edge #1  $\rightarrow P: E_{11}$
- (3) feed  $\rightarrow$  hyperboloid edge #2  $\rightarrow P: E_{21}$

In determining the dominant components of higher-order scattering, the following multiply-reflected rays have been included: (Fig. 3b).

- (4) feed  $\rightarrow$  hyperboloid  $\rightarrow$  plate  $\rightarrow$  hyperboloid  $\rightarrow P: R_3$
- (5) feed  $\rightarrow$  hyperboloid  $\rightarrow$  plate  $\rightarrow$  hyperboloid edge #1  $\rightarrow P: E_{13}$
- (6) feed  $\rightarrow$  hyperboloid  $\rightarrow$  plate  $\rightarrow$  hyperboloid edge #2  $\rightarrow P: E_{23}$
- (7) feed  $\rightarrow$  hyperboloid  $\rightarrow$  plate upper edge  $\rightarrow P: E_{P3}$

Where necessary, the blocking effects by the plate have been accounted for. All transition region effects have been accounted for using the method of Kouyoumjian and Pathak (Ref. 3) although, under far-field assumptions, the Uniform Asymptotic Theory treatment (Ref. 4) produces nearly the same numerical values. An iterative solution of the geometrical-optics problem permits arbitrary positioning of the feed, hyperboloid, and plate (Ref. 1).

## IV. Results

A typical result from the computer program is shown in Fig. 4. The result is for a geometry consisting of a circular plate 569 cm in diameter placed 519 cm behind the S-band feed horn of a 64-m Cassegrainian antenna. The far field phase was first computed in the presence of multipath and then in the absence of multipath and then differenced. These calculations were done at two VLBI microwave frequencies  $f_2$  and  $f_1$ . From these data the time delay change due to multipath can be calculated at any subreflector defocus position from the VLBI bandwidth synthesis equation  $\Delta\tau = - [\Delta\phi_2 - \Delta\phi_1] / [360(f_2 - f_1)]$  where  $\Delta\phi_2$  and  $\Delta\phi_1$  are the data in Fig. 4. Comparisons between experimental data from S- and X-band multipath tests and results of the computer program described in this paper will be presented in a future report.

## References

1. A. G. Cha, W. V. T. Rusch, T. Y. Otoshi, "Microwave Delay Characteristics of Cassegrainian Antennas," *IEEE Transactions on Antennas and Propagation*, Vol. AP-26, No. 6, pp. 860-865, November 1978.
2. T. Y. Otoshi and D. L. Brunn, "Multipath Tests on 64-m Antennas Using the Viking Orbiter-1 and -2 Spacecraft as Far-Field Illuminators," in *The Deep Space Network Progress Report 42-31*, Jet Propulsion Laboratory, Pasadena, California, pp. 41-49, February 15, 1976.
3. R. G. Kouyoumjian and P. H. Pathak, "A Uniform Geometrical Theory of Diffraction for an Edge in a Perfectly Conducting Surface," *IEEE Proceedings*, Vol. 62, No. 11, pp. 1448-1462, November 1974.
4. S. W. Lee and G. A. Deschamps, "A Uniform Asymptotic Theory of Electromagnetic Diffraction by a Curved Wedge," *IEEE Transactions on Antennas and Propagation*, Vol. AP-24, No. 1, pp. 25-34, January 1976.

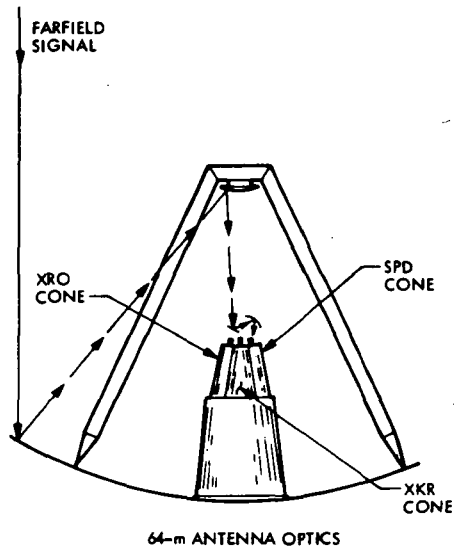


Fig. 1. 64-m-diameter Cassegrainian antenna optics of a reflex-feed system

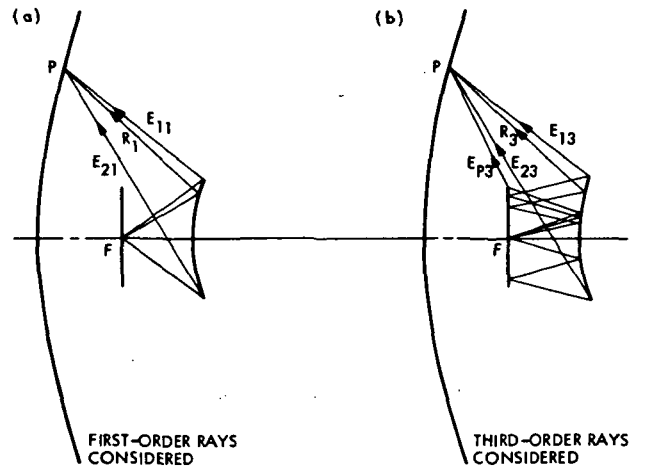


Fig. 3. Geometry for multiply-reflected rays from a circular plate on Cassegrainian antenna

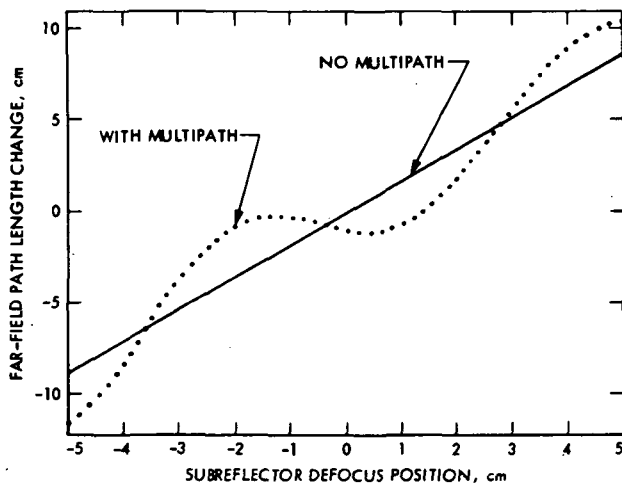


Fig. 2. Theoretical far-field delay due to subreflector defocusing on 64-m antenna at 2285 MHz center frequency and 40 MHz spanned bandwidth

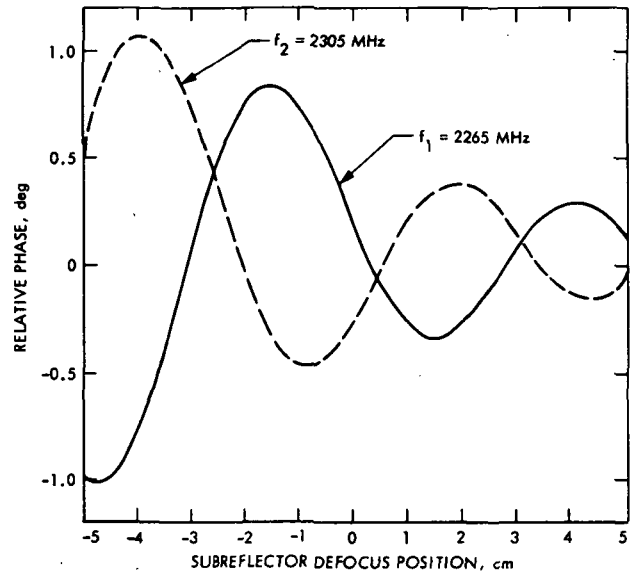


Fig. 4. Example of far-field phase ripple due to multipath and defocusing

## Extrapolated UT1 Effect on VLBI Clock Sync

J. W. Layland and B. V. H. Saxberg  
Communications Systems Research Section

*In this article we calculate the two-sample Allen Variance of the extrapolated UT1 numbers, and use this calculation to infer its effect on DSN clock stability measures obtained via VLBI clock synchronization. For measurement time  $T < 300$  s, or  $T > 3$  days, the error in UT1 and its variations do not seriously degrade the stability measurement relative to anticipated variations in the clocks themselves.*

### I. Introduction

The DSN is currently beginning the attempt to monitor the stability of its clocks and frequency standards in the 64-meter net by means of VLBI. The utility of this monitoring effect depends upon both its accuracy and the timeliness of the measurement results.

Many recent VLBI clock sync experiment data sets have been received and processed within less than a week of the acquisition of this data. Software which processes this data must know the Earth's precise (angular) position (i.e., UT1) within the Quasar coordinate frame. In Ref. 1, it was assumed that this positional information would be available in the form of the BIH "Rapid Service" measurements of UT1, the Earth's rotational phase, and polar motion (Ref. 2). For real-time or near-real-time processing, this form of the data is not available, and we must either rely upon extrapolated values for UT1, or obtain data in a form which can be used to solve for UT1. The fundamental purpose of the VLBI clock sync experiments is to measure the relative stability of the frequency standards in the three 64-m tracking stations of the DSN. This stability (instability) is usually specified in terms of the square-root of

the two-sample Allan Variance (Ref. 3) of the time differences of two clocks. We calculated this instability measure for UT1 itself, in its several available forms, and used this result to infer its effect on VLBI Clock Sync.

### II. Inter-Day Instability of UT1 Values

The data set analyzed consisted of the USNO Extrapolated, BIH "Rapid Service," and BIH "Final" Values for UT1-UTC for the period 76 July 1 to 78 May 1, taken from the USNO Time and Frequency Bulletins, Series 7. Figure 1 shows log-log plots of the square-root Allan Variance for these three data types. Both the extrapolated and rapid service UT1 have regions of high variance in the smaller measurement times, due presumably to white-noise effects upon the raw observations from which UT1 is derived. The final UT1, being derived with the help of observations in a several-week time span surrounding each day for which it is computed, shows the effect of this smoothing with a much decreased variance in this region. All three, extrapolated, rapid-service, and final value UT1, reach a peak at a roughly 60- to 90-day measurement

interval. This peak presumably results from seasonal variations in the Earth's rotation, which are known to exist but hard to predict. The amplitude of this peak is itself seasonally variable when the Allan Variance is computed for six-month time intervals (not shown). The dramatic dropoff for measurement intervals of over 200 days is an artifact of the short time span of data analyzed since it disappears over a five-year interval (Ref. 1, Fig. 3).

Figure 2 shows log-log plots of the square-root Allan Variance of the pair-wise differences between these three data types. All three curves show the effect of white-noise for measurement intervals less than five days. This noise adds as if independent between the extrapolated and rapid-service UT1 values, which further reinforces the identification of this segment as white (independent) noise of measurement. The curves using extrapolated data reach a peak at 30- to 60-day measurement times, indicating that the seasonal variations are not well predicted in the extrapolation process. The rapid service-final curve has a small bump in this region, but for the most part, the variational patterns in these two estimates of UT1 agree increasingly well as the measurement intervals increase. The interesting kink which appears in all these curves at the 150- to 200-day measurement interval is probably an artifact of the small data set used.

Errors in UT1 can masquerade as clock errors in VLBI time delay measurements to the tune of at worst  $2 \mu\text{s}$  clock error per second of UT1 error. When an inter-day Allan Variance of these clocks is derived from the VLBI clock offsets, the error in UT1 contributes a term to the square-root Allan Variance which is a factor  $2 \times 10^{-6}$  smaller than the square-root Allan Variance of the error in the estimate of UT1 itself. If we assume that the BIH Final Values follow correctly all of the (slow) variations in UT1, then the square-root Allan Variance of the differences plotted in Fig. 2 closely represents the instability measure of the error in following UT1 by the extrapolated (or rapid service) estimate of it. For  $t > 3$  days, these numbers are all less than  $5 \times 10^{-9}$ , and hence their contribution to the clock instability measure is less than  $10^{-14}$ . Thus it seems that extrapolated UT1 will contribute to the clock instability measure roughly at the level of the H-masers themselves, while rapid service UT1 would contribute negligibly for  $t > 10$  days.

### III. Short-Term Effects

The VLBI-observed frequency shift can also be used to estimate the short-term stability of the interferometer, including, of course, the two frequency standards. In particular, the absolute difference of the interferometer frequency shift measured over two consecutive  $T$ -second time intervals is one sample of the square-root Allan Variance. This measure, too, is affected by errors in Quasar position and UT1. We have no information on the very short-term variations of UT1 from the BIH data because they are masked by observing errors in the BIH raw data. We expect these short-term variations to be small, presumably less than the  $2 \times 10^{-9}$  observed at 30 to 300 days, and that their effect on the measured  $\sigma(\Delta F/F)$  would be dominated by the relatively constant error in the daily estimate of UT1.

The VLBI fringe frequency equations (Ref. 4) can be easily manipulated to show the effect of a constant error in UT1 on the measured stability. For the frequency measurement interval  $T$ , and a fixed error  $E_{UT}$

$$\sigma_T(\Delta f/f) = \frac{\omega_e}{\sqrt{2}} \frac{r_b}{c} \cdot (\omega_e \cdot E_{UT}) \cdot (\omega_e \cdot T) \\ + \text{other effects}$$

where  $\omega_e$  is the Earth rotation rate in radians/s,  $r_b$  is the length of the interstation baseline projection onto the equatorial plane, and  $c$  is the speed-of-light.

### IV. Conclusion

Figure 3 shows the anticipated effect of fixed errors in UT1 upon the VLBI frequency stability measurements, for UT1 errors of 3 ms (Rapid Service) and 10 ms (extrapolated, conservative) on the DSN intercontinental baselines. The effect of UT1 errors on inter-day time stability measurement is also shown. For measurement time  $T < 300$  s or  $T > 3$  days, the error in UT1 and its variations do not seriously degrade the stability measurements. For the region between, the UT1 effect via either time or frequency measurements is large enough to mask the variations in the frequency standards unless UT1 is concurrently solved for.

## References

1. Layland, J. W., and Mathews, A. N., "VLBI Clock Sync and the Earth's Rotational Instability," in *The Deep Space Network Progress Report 42-42*, pp. 81-84, Jet Propulsion Laboratory, Pasadena, Calif., Dec. 1977.
2. Feissel, Martine, "The Determination of UT1 by the Bureau Internationale de l'Heure," Proceedings of the Eighth Annual Precise Time and Time Interval Meeting, pp. 47-54, USNO, Dec. 1976, Washington, D.C.
3. Barnes, J. A. et al., Characterization of Frequency Stability, NBS Technical Note 394, Oct. 1970.
4. Williams, J. G., "Very Long Baseline Interferometry and Its Sensitivity to Geophysical and Astronomical Effects." *Space Programs Summary 37-62*, Vol. II, pp. 49-55, Jet Propulsion Laboratory, Pasadena, Calif., Mar. 1970.

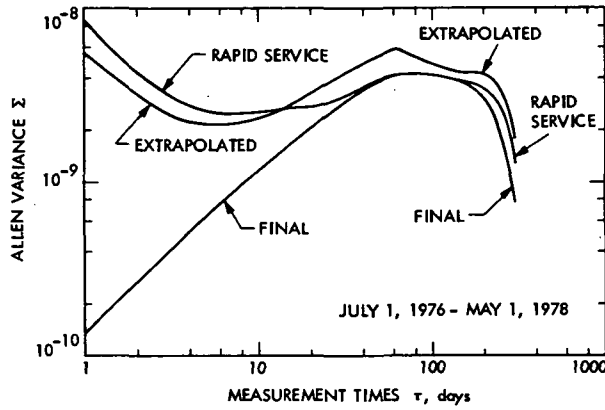


Fig. 1. Square-root Allan Variance of Earth rotation data (UT1)

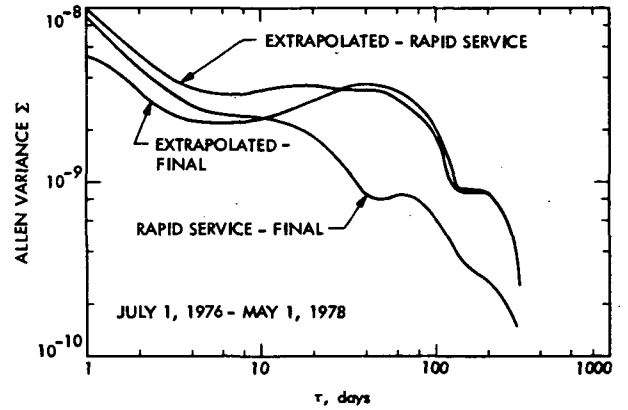


Fig. 2. Square-root Allan Variance of pair-wise differences between various UT1 estimates

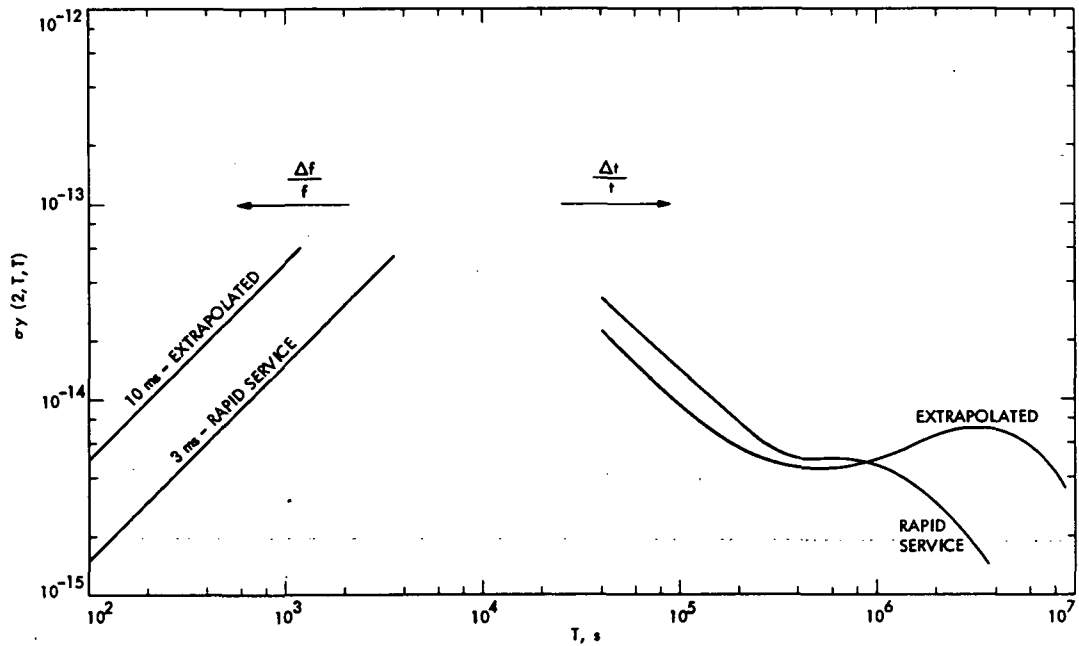


Fig. 3. Anticipated UT1 effect on VLBI clock-stability measurements

# Receiver Design Concepts for $\Delta$ VLBI and Differential One-Way Range

J. W. Layland

Communications Systems Research Section

*This report describes three alternative structures for the receiving instrument for wideband spacecraft  $\Delta$ VLBI or differential one-way range navigation. It does not contain a fully definitive analysis of this subject. Rather, it is intended to introduce to the reader ways of thinking about the  $\Delta$ VLBI instrument that are more closely related to a conventional spacecraft instrument than to a radio-science VLBI instrument.*

## I. Introduction

This report describes three alternative structures for the receiving instrument for wideband spacecraft  $\Delta$ VLBI or differential one-way range navigation. It does not contain a fully definitive analysis of this subject. Rather, it is intended to introduce to the reader ways of thinking about the  $\Delta$ VLBI instrument that are more closely related to a conventional spacecraft instrument than to a radio-science VLBI instrument. While it is true that this radio-science VLBI instrument can be augmented to detect the spacecraft tones, this approach designs-in some errors which can be avoided by a more direct approach toward the spacecraft signal detection part of  $\Delta$ VLBI navigation. A much more complete error analysis should, of course, be invoked in the process of designing the actual  $\Delta$ VLBI navigation instrument.

In wideband  $\Delta$ VLBI navigation, differential delay measurements to two tracking stations are alternately made between a natural radio source (quasar) and a spacecraft (Ref. 1). The quasar is assumed to be far enough away that it is absolutely

immobile within the celestial coordinate system. Its position may be precisely known as well. The quasar observations calibrate (or partially calibrate) the relative station clocks, station delays, propagation medium delays, and Earth platform orientation. The spacecraft observation, corrected by this calibration-by-quasar, effects a measure of the angular separation between the spacecraft and quasar. An appropriate series of such observations will measure the vector separation between spacecraft and quasar in the plane of the sky.

Differential one-way ranging is a weakened form of  $\Delta$ VLBI, wherein the calibrating quasar observations and the spacecraft observations are widely separated in time or spatial orientation, such that much of the commonality of propagation medium delays and platform orientation is lost. Only the commonality of clocks and receiver delays is retained, perhaps degraded by significant drifts with time or other environmental factors.

One of the principal concerns in the design of an instrument for wideband  $\Delta$ VLBI is that the electrical path lengths

through that instrument not be different for the spacecraft signals and the quasar noise. We could have greatly diminished this concern by making the spacecraft emit a narrowband noise signal, and processing it on the ground in a manner identical to the quasar signal processing. Such a tactic, however, in quite reasonable circumstance, requires either an astonishingly strong signal from the spacecraft or an impossibly long integration time. Consequently, it is expected that the wideband signals emanating from a spacecraft for  $\Delta$ VLBI use will be of a nature such that they can be coherently detected at each station. In particular, the precision-defining signal is expected to be a sine wave modulated at low level onto the spacecraft carrier. Having chosen to let the signals from the spacecraft and the detection process for it differ in character from the quasar signals, and their detection, it is incumbent upon the instrument designer to avoid letting the difference result in a differential delay error.

## II. The Conventional VLBI Instrument

The conventional radio-science VLBI instrument could be used to sample and record the spacecraft signals for subsequent detection. Figure 1 shows a functional overview of this instrument, and the first stage of processing the spacecraft signal from it. A "phase calibrator" provides the fundamental timing reference for this system (Ref. 2). The IF mixer and SSB down-converters are used to bring the pertinent components of the spacecraft signal to baseband where they are filtered, hardlimited, sampled, and recorded. The hardlimiting of the sampled data causes a 2-dB loss in SNR, but its use in the spacecraft signal path acts to keep the electrical path length the same as for the quasar signals. Extraction of the spacecraft and phase-calibrator tones from the sampled data could as well take place in real-time without recording, and would effect a considerable reduction in the number of bits needed to characterize these signals. This factor will be important when the  $\Delta$ VLBI data are to be shipped to JPL via data lines instead of by mailing tapes. Only short-duration correlation sums would be generated in real-time, with the more complex phase tracking process being deferred to where it can be performed at leisure.

Tracking of the phase-calibrator tones is relatively straightforward because they are very slowly varying and vary over a limited range corresponding to the delay variations of the receiving instrument itself. Use of the phase-calibration tones in VLBI on natural radio sources has previously been described in detail (Refs. 3 and 4). Their use with spacecraft signals is similar. The measured phase-shift of the calibration tones which results from passing through the receiver is combined with such detailed information as exists on phase-shift ripples in the receiver, to produce an estimate of the receiver phase-

shift at the frequency of the embedded spacecraft tone. The correlation sums for the spacecraft tone are then corrected for this estimated receiver phase-shift to produce a sequence of correlation sums as they would exist at the calibrator-injection point using a "perfect" phase reference.

Tracking of the spacecraft tones from their correlation sums is complicated by doppler effects, and by spectral spreading. The carrier tone can be phase-tracked relative to predicts to produce a delay-rate estimate akin to conventional doppler. The bandwidth of this tracking need only be narrow enough to produce a strong SNR, and should be comparable to the bandwidth of the conventional carrier tracking loop. The signal strength of the precision-defining tones is sufficiently lower than that of the carrier that they very likely cannot be tracked directly. We are interested, however, only in the group delay of this signal, which appears as the phase differences between the upper and lower precision-defining tones. This phase difference is much narrower and more slowly varying than the individual tones, and can thus be tracked at a bandwidth appropriate to detecting this lower-strength signal. Quadrature-component correlation sums for the phase difference between either precision-defining tone and the carrier can be directly computed from the quadrature correlation sums of the carrier and the appropriate tone. This computation incurs virtually no loss in SNR as long as the SNR for the correlation sums of the carrier tone is at least moderate (e.g., 3-10). These carrier side-tone phase differences are also narrowband and can be tracked to a bandwidth at which the SNR will permit a lossless computation of the phase difference between the upper- and lower-precision-defining tones. Tracking of the other side tones provided to resolve the ambiguities of the precision-defining tones would proceed similarly.

Many of the instrumental error sources which one would anticipate here are common mode between the quasar signals and spacecraft signals processed as described above. Closely spaced phase ripples in the receiver passband, such as those designed into the single-sideband demodulator, are one apparent source of non-common-mode errors. For a concrete example, assume an SSB demodulator with logarithmically spaced ripples of  $\pm 5$ -degree magnitude (Ref. 5). If the spacing between precision-defining tones is 40 MHz, one such 5-degree phase error would cause a group-delay error of 1/3 ns or 10 cm. In computing the differential one-way range between two stations, there is not one but four opportunities to suffer this 5-degree phase shift — one at each station on each of the upper- and lower-precision-defining tones. Thus, a probable (RSS) error of 20 cm or a worst-case error of 40 cm results, relative to the average channel phase.

If the same local reference frequencies are used to down-convert the quasar signals and the spacecraft signals, the quasar

signals intrinsically average the channel phase, and the calibration tones serve only to carry this information along through the processing. This is true only as long as the calibrations are applied identically to the quasar and spacecraft signal processing. An interesting thing happens if we attempt to improve accuracy by using a wider spanned bandwidth for the quasar signals than for spacecraft signals, in that now the phase calibrator is an essential part of the connection between quasar delay and spacecraft delay. We now have four *more* opportunities for a 5-degree phase shift to occur – on the calibration tones in each channel. The (unlikely) worst-case error is thus raised to 80 cm!

The above discussion assumes that we admit to no knowledge of these designed-in phase ripples, whereas we do know at least their intended characteristics. Some numerical calculations have been performed using the demodulator simulation models used previously on quasar VLBI (Ref. 3), and the assumption of a 5 percent manufacturing tolerance for the physical filters. The calculated worst-case error reduced to 15-20 cm for this condition. We could alleviate the need for a model by reducing the limits on the allowed phase ripple to well below the  $\pm 5$  degrees, but manufacturing tolerances could still induce errors that were a sizeable fraction of one ns (30 cm).

### III. A Range Demodulator

A coherent detection receiver like the DSN receiver with a range demodulator could be used to detect the spacecraft tones, provided only that a suitably accountable reference signal can be generated. The phase of the received range signal is measured relative to this reference signal, so that the absolute specification of the received signal phase includes that of the reference signal. A digitally controlled oscillator/synthesizer (e.g., the DANA DIGIPHASE SYNTHESIZER with modification) appears to be capable of generating within its range an arbitrary sine wave with “absolutely” known phase. This knowledge of phase is described by the digital phase numbers in the synthesizer control logic, and the timing signals with which that logic operates. These timing signals should be generated as directly as possible from the tracking station’s primary frequency standard in order to minimize the errors in the knowledge of phase. Figure 2 shows a rough block diagram of the envisioned range demodulator. The phase-locked loop of the DSN receiver will track the phase of the received spacecraft carrier, thus enabling coherent detection of the precision-defining sideband signals. Doppler information from this carrier tracking, or doppler predict information, is used to adjust the phase of the reference signal generator so that the signal integration can continue long enough to obtain a strong (30-60 dB) SNR. The primary group

delay path for this signal is through the low noise amplifier, the IF down-converter, the reference signal mixers, and the reference signal generator/synthesizer to the station timing standard. Ancillary errors can come into the system through DC offsets or gain imbalances in the demodulator channels, but can be reduced to an almost negligible level by time-multiplexing the roles of the demodulator channels as was done in the MU-I ranging system (Ref. 6).

The range demodulator can be easily augmented as shown in Fig. 2 to be a DSB down-converter and recorder for VLBI signals. In doing VLBI recording, the code reference generator is programmed to correct for Earth-rate doppler predicts. This way, the primary group-delay path is through the code reference generator to the station time standard, with little contribution from the low-pass signal channels. The sampling times for the quadrature channel samples should be displaced by one-half a sample interval from the in-phase channel samples to limit the time delay offset between corresponding samples at the two stations, and thus limit the corresponding SNR degradation.

The DSB demodulator channels do not have the designed in-phase ripples that are characteristic of the SSB channels, but their low-pass filters can have curvature to their phase characteristics so that the average channel phase shift as perceived via the quasar noise signals is not the same as the phase shift perceived by the spacecraft signals. The effect should be small, but needs to be analyzed.

As a  $\Delta$ VLBI instrument, the principal errors seem likely to occur within the reference signal generator (synthesizer). These may be drifts resulting from environmental changes, or they may be systematic phase delay errors that depend upon the frequency at which the synthesizer is operating, or upon start-up transients. The number of distinct circuit elements which are critical to the reference timing in a continuous-time sense is not large, and the complexity of the logic necessary to avoid gross systematic errors is also not large. Therefore, there seems to be no intrinsic reason why the reference sine wave could not be generated with a reference phase which was accurate to a small part of a nanosecond in its time origin. We do *not* presently know if any existing commercially available synthesizers will perform as needed.

As a differenced one-way ranging instrument, additional errors result from drifts in the receiver and cable delays which are relatively slow compared to the time intervals between quasar and spacecraft observations in  $\Delta$ VLBI, but which are significant over several hours. Such drifts are suspected to be on the order of a nanosecond. They could be largely eliminated if the delay of the receiving system were measured during or prior to both quasar and spacecraft observations. A

device like the VLBI "phase" calibrator could provide the necessary signals at the receiver inputs. Calibration during the spacecraft signal observation risks cross-talk errors between signals. Calibration prior to each observation creates operational complexity unless event sequencing is performed automatically. Drifts in the time standard itself may make calibration of the receiver delays irrelevant. For instance, if 24 hours elapse between calibration of the clocks by quasar and a one-way range observation, the clock uncertainty alone is around 1 ns if the station reference has a  $10^{-14}$  stability.

This same basic instrument could be used as the receiving portion of a two-way ranging instrument. The transmitting code reference signals could be generated by a synthesizer identical to that used in the receiving side. Whatever systematic errors existing in the setting of the reference signal phase are now committed twice in one station, instead of once in each of two stations in the differenced one-way/ $\Delta$ VLBI mode. Doppler corrections can be programmed into the receiver reference signal phase in a "fully" accountable fashion. A sequence of sine waves of related frequencies can be generated by the synthesizers in very much the same manner as sequential components are generated by the present ranging systems (Refs. 6 and 7). A suitable computer and control program is needed to drive the reference synthesizer through their desired sequence of events, and to untangle the phase measurement into a range measure.

The resulting machine provides more flexibility than is needed for two-way ranging, but offers commonality with the one-way range instrument, and may offer an increased precision in the accountability for phase of doppler correction. The principal error contribution is probably in the instrument drifts between calibration (pre-pass) and measurement time, and timing standard drifts during the range signal round-trip propagation time. These again are of the order of 1 ns, unless real-time calibration or other control techniques are applied.

#### IV. Digital Demodulation

One way to minimize the growth of errors in a precise system is to concentrate as much as possible the precision-defining element of the system into one "basket" – and then very carefully control that "basket." If, for example, the received signal is sampled and digitized at some fairly wide-band point in the IF stream of the receiver, only this sampler, and the parts of the receiver ahead of it, can effect delay errors (cf Fig. 3). The reference signal generator, mixers, and demodulator channels have been deleted as continuous-time error sources, because they operate only on sampled data. When elements such as these do not work, they should fail in a clear and visible way, rather than with a degraded delay precision.

Such elements should, in fact, be able to be designed for intrinsic failure detection, if desired. The MU-II ranging system was a successful proof-of-concept for digital demodulation techniques, using the 10-MHz IF stream (Ref. 7).

The sampler/digitizer converts the received signals from the continuous-time domain to a sample stream whose timing is completely defined by the station's frequency standard and clock system. Several types of error are possible. The connection between sampler and timing system can admit time-base errors – amplifier/buffer delays, etc. Digital signals can feed back through the digitizer and affect the apparent analog level input unless the digitizer is carefully isolated. Hysteresis in the threshold elements of the digitizer can effect modulation phase biases that vary by as much as 0.01 rn., which implies differenced delay errors on the order of 0.1 ns for a 20-MHz signal. To achieve this modulation bandwidth, the IF that is sampled has to be at least at 50-55 MHz with a sampling frequency of four times that being desirable for convenient signal processing. With some care in design, the variability of the effective sampling instant should be able to be held to a fraction of a nanosecond for the circuitry that can sample at this speed.

The reference signal generator is a fairly complex module if done completely digitally. We could as an alternate develop the reference signal with a synthesizer, as in Fig. 2, and immediately sample and hardlimit it. We admit in this way some additional continuous-time errors, which depend upon the circuitry used.

System and time-base calibration of the digital instrument can be done by quasar observing like the Burst-Sampler VLBI clock-sync system (Ref. 8). This technique is affected by the average group delay of the receiver passband, which may differ by several nanoseconds from the effective delay imposed upon the 20-MHz sine wave modulation anticipated from the spacecraft. This effect of the receiver passband can be eliminated if we know what it is precisely. One obvious way to measure the receiver characteristic is to use a device like the VLBI "phase calibrator," acting at high signal level, as a pulse train with which to probe the impulse response of the receiver. The actual measurement is obtained from the digitized IF samples by accumulating samples over the pulse repetition interval (Ref. 9). This passband measurement could be performed as part of the pre-pass checkout, and admit errors on the order of a nanosecond from receiver delay drift over several hours. It could be performed immediately adjacent to each observation of quasar or spacecraft and eliminate such drift as an error source, but at the cost of a more complex operational sequence.

System calibration can also be done by quasar observing with the digital counterpart of the DSB system of Fig. 2. In this case, the part of the quasar signal that passes through the digital channel filters has suffered almost the same phase shift from the receiver IF passband as the spacecraft signals, and hence their delays will be largely common mode. The digital filters themselves have a fully accountable phase shift, so the only significant potential error source is receiver IF and sampler/digitizer drifts and aberrations.

## V. Ambiguity Resolution

The 20-MHz signal from the spacecraft has a period of about 25 ns. Unless the differential range to this spacecraft is known more precisely than this, other signals from the spacecraft must be used to resolve the 25 ns ambiguity. If performed digitally within the sampled-data time base, Costas loop tracking of the telemetry subcarrier and/or its harmonics can provide this ambiguity resolution, with or without telemetry on that subcarrier. This tracking is not particularly difficult, being similar to that which must be performed to extract telemetry data bits from the spacecraft signals. Performing it digitally ensures the accountability of phase/delay relative to the sampler time base, thus making it a feasible estimator for the differenced range.

Analog Costas loop tracking of the telemetry subcarrier or its harmonics can also be an ambiguity resolving detector for any of the configurations, with some care. The differential delay through the receiver to the subcarrier reference point versus through the receiver to the reference point for the precision-defining tones must be known much more accurately

than the 25-ns ambiguity that needs resolving. The phase of the tracking VCO must be absolutely accounted for with respect to the same time base as the other spacecraft tones are detected. This arises naturally if the tracking VCO is in fact a digital synthesizer as used in the Fig. 2 configuration for the precision-defining tones.

The most obvious way to resolve the ambiguity does not use the telemetry signal, but adds to the spacecraft additional modulation tones which are a subharmonic of the precision-defining tones. With any of the configurations, detection of these tones is identical to detection of the precision-defining tones. It is performed either via additional hardware channels or by time-multiplexing the use of a minimal set of channels. The current expectation is that such tones as needed will be available on the spacecraft carrying the wideband  $\Delta$ VLBI beacon.

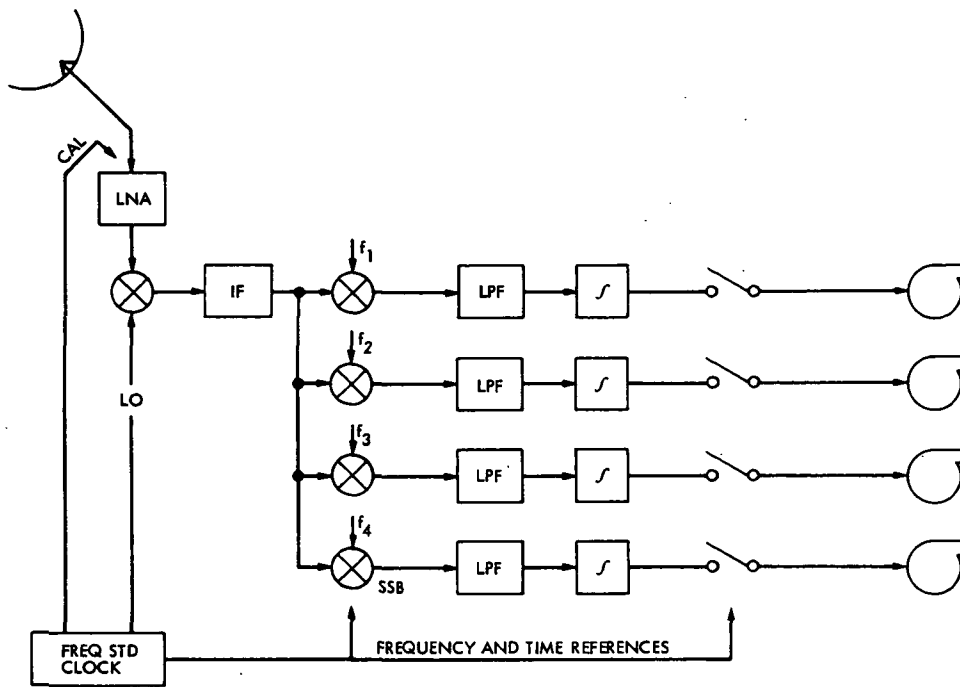
## VI. Summary

This report contains a very subjective discussion of three possible receiver structures for wideband spacecraft  $\Delta$ VLBI. It is not a definitive analysis of any one of them, but should be treated as background material for the design of the "right"  $\Delta$ VLBI instrument. Each of the instruments described here has some advantages relative to the others.

Instrumental errors on any of the  $\Delta$ VLBI receivers appear to easily approach or exceed 1 ns (30 cm). Design of an instrument with a goal of better than 10-cm accuracy should be quite a challenge.

## References

1. Melbourne, W. G., and Curkendall, D. W., "Radio Metric Direction Finding: A New Approach to Deep Space Navigation," paper presented at the AAS/AIAA Astrodynamics Specialist Conference, Jackson Hole, Wyoming, Sept. 7-9, 1977.
2. Rogers, A. E. E., et al., "Very Long Baseline Interferometry Hardware," Final Report for Contract No. NAS 5-20777, Feb. 1976, Part 13, "A Receiver Phase and Group Delay Calibration System," Haystack Technical Note 1975-6.
3. Layland, J. W., and Hurd, W. J., "VLBI Instrumental Effects, Part I," in *The DSN Progress Report 42-42*, pp. 54-80, JPL, Pasadena, CA, Dec. 15, 1977.
4. Thomas, J. B., "The Tone Generator and Phase Calibration in VLBI Measurements," in *The DSN Progress Report 42-44*, pp. 63-74, JPL, Pasadena, CA, Apr. 15, 1978.
5. Rogers, A. E. E., "Broadband Passive 90° RC Hybrid With Low Component Sensitivity for Use in the Video Range Of Frequencies," *IEEE Proceedings Letters*, pp. 1617-1618, Nov. 1971.
6. Martin, W. L., "Information System: A Binary-Coded Sequential Acquisition Ranging System," in *The DSN, Space Programs Summary 37-57*, Vol. II, pp. 72-81, JPL, Pasadena, CA, May 31, 1969.
7. Martin, W. L., and Zygielbaum, A. I., *MU-II Ranging*, TM 33-768, JPL, Pasadena, CA, May 15, 1977.
8. Hurd, W. J., "Preliminary Demonstration of Precision DSN Clock Synchronization By Radio Interferometry," in *The DSN Progress Report 42-37*, pp. 57-68, JPL, Pasadena, CA, Feb. 15, 1977.
9. Milenkovic, P. H., et al., "Report on Calibration of Wideband VLBI," in preparation.



SEPARATE CHANNELS RECORD CARRIER, UPPER- AND LOWER-EDGE TONES AND AMBIGUITY-RESOLVING TONE

CALIBRATOR EFFECTS THE PRECISE TIME BASE

Fig. 1a. Functional diagram of radio-science VLBI instrument

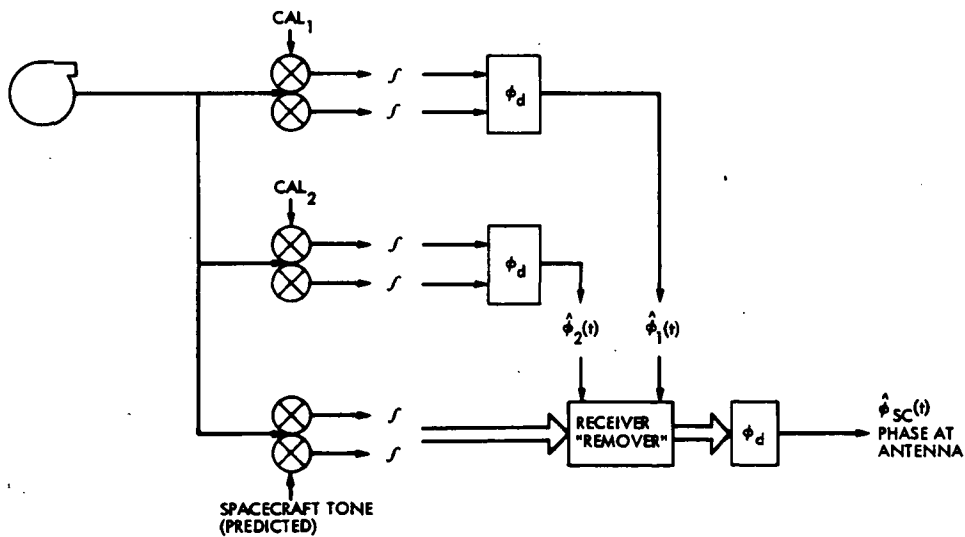


Fig. 1b. Functional diagram of spacecraft signal extraction from each VLBI channel

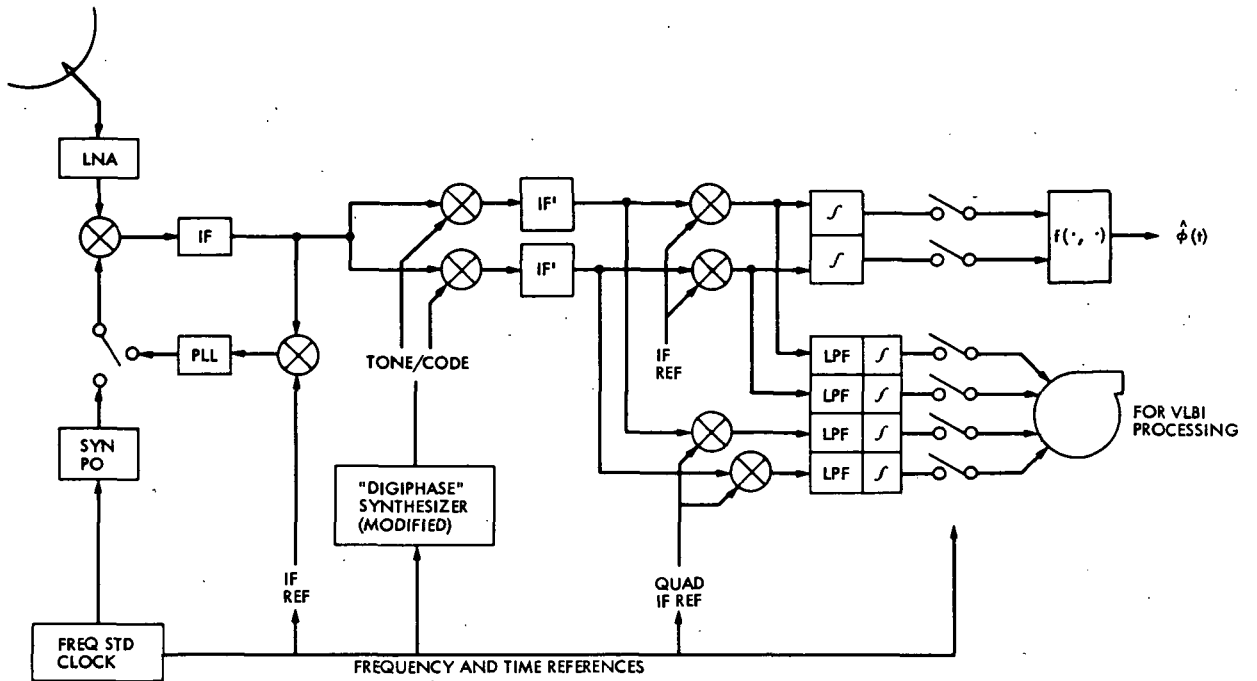


Fig. 2. Functional diagram of range demodulator and DSB VLBI receiver

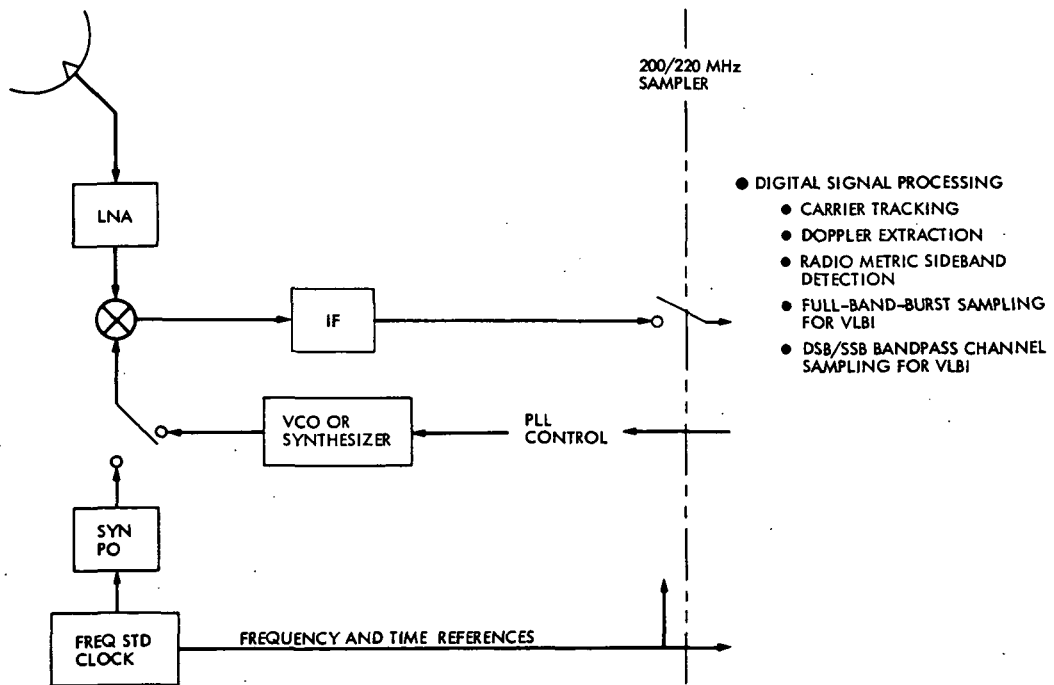


Fig. 3. Concept for digital radio metric receiver

## On Improved Ranging – II

J. W. Layland and A. I. Zygielbaum  
Communications Systems Research Section

*This is the second in a series of articles intended to develop a road map for future developments in two-way range instrumentation. In the first article, we presented a rationale and experimental evidence for improvements to ranging which seem to be achievable through reasonably minor changes to the tracking station. In this article, we develop a heuristic overview of the principal systematic error sources for ranging, and some of the remedies for them. Our principal recommendations are for wider system and range-code bandwidths, and for simplification of the precision-defining form of the range code.*

### I. Introduction

This is the second in a series of articles intended to develop a road map for future developments in two-way range instrumentation. In the first article (Ref. 1), we presented a rationale and experimental evidence for improvements to ranging which seem to be achievable through reasonably minor changes to the tracking station. In this article, we develop a heuristic overview of the principal systematic error sources for ranging, and some of the remedies for them. As far as we can see now, it appears that both wider system bandwidth and real-time calibration are needed to achieve ranging accuracy at a few decimeters.

### II. A Heuristic Review of Ranging Errors

Interpreting the influence of range code bandwidth on thermal noise errors can be done by analysis of simple problems with exact solutions. In the final analysis, systematic effects seem to almost always provide the limits for range

system accuracy, and it seems painfully difficult to achieve more than a subjective understanding of these limiting errors. We are in the somewhat awkward position of developing approximate solutions for approximate problems, in order to compare the impact of various configuration options for future ranging machines. Only when a specific option is selected for detailed design, sensitivity analysis, and eventual testing, will some of this inexactness disappear.

Table 1 is a matrix description of the principal errors contributed to the ranging system by the ground instrumentation. The various ranging machines considered include the present configuration with the 0.5 MHz code with or without minor improvements, and alternative configurations with range codes of 1 MHz and 8 MHz, both with and without real-time calibration. All of these codes can be generated by the MU-II R&D ranging machine. The block diagram for real-time calibration of the range machine will be presented later.

Systematic errors which limit the current ranging system's accuracy appear to be dominated by harmonic distortion

errors which may be 7-10 ns (or perhaps more) with the conventional 500 KHz code. Most other known error sources should be smaller, but should not be considered negligible. A part of the term we have labeled harmonic distortion is in fact due to mismatch between the algorithm used to compute range delay from the code correlations, and the waveform which we know is received. When taken through the transponder, the received waveform consists of a fundamental plus (somewhat attenuated) third harmonic. An algorithm which matches the true shape of this received waveform greatly reduces this error source, but is highly sensitive to minor changes in the relative amplitudes of the fundamental and its harmonic. This persistent error should be at the level of 3-7 ns when the algorithm is a good match to the median waveform.

We can further reduce the harmonic distortion error by filtering the waveform received at the tracking station to its fundamental component only. This eliminates the algorithm mismatch for the waveform, but leaves the harmonic interactions within the transponder's range code detector and mixer operative. The remnant error is estimated to be at the 2-3 ns level.

Leaving the transponder alone and increasing the range code to 1 MHz significantly reduces the harmonic distortion error because now only the fundamental term of the range code is present at the transponder modulator, the third harmonic being sheared away in the ranging channel filter. The distortion error is believed to be on the order of 0.5 ns or less. Further increases in the range code frequency must be accompanied by transponder bandwidth increases, as well as bandwidth increases in the tracking station transmitting equipment. With a code frequency of 8 MHz, the harmonic distortion term should be much less than 0.1 ns.

Multipath effects in the antenna have been found to contribute a 2-3 ns error for the 500 KHz code (Ref. 2). Due to the exact numerology of the bounce-lengths involved, this error will not be noticeably reduced by using the 1 MHz code, but is reduced to on the order of 0.3 ns by the 8 MHz code. Because of its position in the receiving system, attempting to calibrate the multipath effects could create more error through near-field effects in the antenna.

Multipath effects in cables combine with environmentally induced drifts in the cable electrical length to offer potential for significant errors. If the cable VSWR becomes as large as its specifications allow (VSWR = 1.5:1), the group delay error induced could be on the order of 30 ns, which would explain some of the larger errors encountered in the TDL tests (Ref. 1). On the other hand, the typical VSWR is believed to be far below the specified limit, making the typical error on the order of 1-2 ns for either the 500 KHz, or 1 MHz codes. The

8 MHz code is a large enough fraction of the center frequency of the modulated IF signal, so that the error is now dominated by direct electrical length changes of the cables. With both the direct cable length variation and the VSWR, induced errors are subject to measurement and calibration, and could reasonably be reduced to 0.1 ns by this means.

Sideband folding effects errors at the spacecraft transponder only when there is imbalance in both amplitude and phase shift in the ranging signal as transmitted. This imbalance results from filtering by the transmitter bandpass. It is an error only because the transponder coherently detects the signal, folding its sidebands together, while the zero-delay device and test translator do not. The estimates of its magnitude are based on a numerical example calculated for an assumed transmitter (Klystron) 4-pole 5-7 MHz passband (Ref. 3) and an assumed receiver 6-pole 30 MHz passband (Ref. 4). For the 500 KHz range code, the sideband folding induces a probable error of 0.2 ns. For the 1 MHz code this increases to 0.5 ns, because the sidebands are closer to the hand-edges of the klystron. This error would increase to 5 ns with the 8 MHz code if enough of it would pass through the klystron filter to be measurable. As new uplink equipment is needed to use this wider code bandwidth, we assume that it will induce errors of 0.2 ns or less. Real-time calibration could determine the amplitude and phase of the uplink range modulation, and hence remove at least half of the error induced by the imbalance.

Realistic devices in a digital demodulator effect phase ripples of around 0.01 rn peak-peak in the ranging modulation (Ref. 5). For the 500 KHz code, such ripples correspond to induced errors of roughly 2 ns. This delay-estimate error is inversely proportional to the ranging frequency, so it is reduced to roughly 1 ns for the 1 MHz code and 0.1 ns for the 8 MHz code.

The code generator is one element of the group delay circuit for which drift in characteristics causes a strictly delay-like error independent of the code frequency used. We tentatively guesstimate this error at 0.2 ns, or 10% of a typical ECL gate delay. It could, in fact, be much larger, depending upon details of the implementation. Delays of this magnitude are of little or no concern with the 500 KHz or 1 MHz code frequencies. They become significant when higher code frequencies are considered, and must be carefully considered when the code generator is designed for a new higher accuracy range machine.

Taken together, these error sources aggregate to limit the precision of the present system to roughly 8-12 ns, but there is some potential of significantly larger errors due to cable drifts and VSWR. Nominal precision can be improved by 5-8 ns by changing the ranging software to model the waveform passed

by the transponder. Inserting a narrowband filter into the IF ranging signal path, so that only the fundamental component of the range code is detected, will further improve nominal precision to around 5 ns. There is no degradation relative to SNR from this filtering (Ref. 6).

Further improvements require more extensive changes to the range machine. A 1 MHz code is filtered by the transponder itself to the fundamental term only. With further filtering on the ground to scrub off harmonic distortions, the resultant precision should be on the order of 3 ns or better. The 1 MHz code has also been shown to have substantial immunity to anomalous equipment-induced errors which may be substantially larger than those we have been able to rationalize with nominal instrument behavior (Ref. 1). Addition of the real-time calibration mechanism improves the apparent precision to 2.3 ns, which seems an inadequate return for a great deal of complexity.

Higher code frequencies require an extensive rebuild of the ranging instrumentation. To use an 8 MHz code, for example, the transponder (one-sided) bandwidth should increase to 12 MHz, and the ground transmitter klystron bandwidth must also be increased. We probably also require use of an X-Band uplink because of frequency-allocation limits at the DSN S-Band uplink frequency. For the wider bandwidth, we achieve a nominal 0.65 ns precision. For the X-Band uplink, in place of the S-Band, we obtain a factor-of-two reduction in the errors inherent in charged particle calibration of range. The dominant error source now is in position to be calibrated out, and a real-time calibration scheme, to be discussed in the next section, should hopefully be able to further improve the nominal instrument precision to 0.4 ns overall.

It should be realized that the precision estimated here for an instrument with higher code frequencies is still only an estimate, and the actual achievable precision will only be known through extensive laboratory measurement and testing. In addition, no allowance has been made for drifts in the transponder itself. Code-detection cleanup on the transponder may be necessary to achieve sub-ns delay stability of range, and a great deal of care in design will be required to restrict errors in the code generator, the demodulator(s), or even the calibrator itself, to a small part of a ns. Any range code in the 5-20 MHz region may be, in fact, wide enough that dominant errors are related to circuit delays, and are not subject to reduction by increased bandwidths. Effective use of such higher code frequencies and achievement of decimeter precision ranging may well require either real-time calibration or careful stabilization of the instrument delays.

### III. Real-Time Calibration of Ranging

Figure 1 shows one concept for real-time calibration of the tracking station for ranging. It may not be the best scheme, and is certainly not the only scheme for such calibration.

A VLBI-type phase calibrator (Ref. 7) injects its pulse train into the front end of the DSN receivers to measure their transfer-function and delay. The pulse train is stable and known in time relative to the tracking station primary frequency-and-time standard, e.g. an H-Maser. The one receiver carries signals as received from the spacecraft. The second receiver carries a sample of the signal being transmitted to the spacecraft. The output of the calibration detectors attached to these receivers are labeled  $\tau_3$  and  $\tau_2$ , but should in fact be measures of the complex transfer functions for these two receivers. These transfer functions are then inputted to the range code detectors to map their calculations back to the calibrator injection point.

The design of the range code detectors and calibration detectors must permit such mapping to be done without introducing errors which exceed those calibrated out.

The principal worry in doing the real-time calibration as shown is that interaction between the phase-calibrator signals and the ranging signal could prevent adequate measurement of either.

### IV. Experimental Corroboration

Our claims with respect to the 1 MHz range code were in large part experimentally confirmed by TDL tests which demonstrated up to an order of magnitude reduction in range instrument biases (Ref. 1). In order to extend this demonstration into the actual spacecraft tracking environment, the R&D MU-II ranging machine has recently been installed at the Australian conjoint stations DSS 42/43 (Ref. 8). This machine is normally being used with its 1 MHz range code, and band-limiting filters in its receive channels.

Preliminary recent results of ranging Voyager 1 spacecraft from DSS 43 with the MU-II show an RMS range residual scatter of 1.7 ns, or about one-quarter of that which typifies the standard DSN range machine at the same signal conditions (Ref. 9). The full results of testing at the Australian conjoint station will be published when available.

### V. Recommendations

The recommendations which we can make now are primarily those made earlier (Ref. 1).

Firstly, increase the range code frequency to 1 MHz, processing the received signal for the fundamental component only. No changes to spacecraft transponder, or to uplink transmitter should be needed to achieve a factor of two-to-four improvement in range instrument precision.

For the overall ranging system, it is not the instrument, but charged particles in the signal path that induce the dominant errors. Replace the S-Band uplink with X-Band to reduce the after-calibration (S/X downlink) delay error by a factor-of-

two, and to reduce the dynamic charged particle errors by an order-of-magnitude.

Finally, increase the bandwidth of the uplink, the transponder, and the range machine to accommodate the fundamental component of a 10-20 MHz range code. The X-Band uplink is needed to accommodate this bandwidth, and to avoid or lessen charged particle effects. Either real-time calibration or careful stabilization of the instrument delays seem to be needed to achieve the accuracy potential of this higher code frequency.

## References

1. Layland, J. W., et al., "On Improved Ranging," in *The Deep Space Network Progress Report 42-46*, Pasadena, Calif., Aug. 15, 1978, pp. 40-45.
2. Otoshi, T. Y., and Brunn, D. L., "Multipath Tests on 64-m Antennas Using the Viking Orbiter-1 and -2 Spacecraft as Far Field Illuminators," in *The Deep Space Network Progress Report 42-31*, Pasadena, Calif., Feb. 15, 1976, pp. 41-49.
3. Otoshi, T. Y., Private Communication.
4. Hurd, W. J., "Preliminary Demonstration of Precision DSN Clock Synchronization by Radio Interferometry," in *The Deep Space Network Progress Report DSN-PR 42-37*, Pasadena, Calif., Feb. 15, 1977, pp. 57-68.
5. Layland, J. W., "Digital Demodulation With a Non-Ideal Quantizer," in *The Deep Space Network Progress Report 42-32*, Pasadena, Calif., April 15, 1976, pp. 100-105.
6. Martin, W. L., and Layland, J. W., "Binary Sequential Ranging with Sinewaves," in *The Deep Space Network Progress Report 42-31*, Pasadena, Calif., Feb. 15, 1976, pp. 30-40.
7. Rogers, A. E. E., et al., "Very Long Baseline Interferometry Hardware," *Final Report for Contract No. NAS5-20777*, Feb. 1976, Part 13, "A Receiver Phase and Group Delay Calibration System," Haystack Technical Note 1975-6.
8. Zygielbaum, A. I., "The MU-II Installation at DSS-42/43" (report in preparation).
9. Koch, R. E., of Voyager Navigation Team, Private Communication, Dec. 15, 1978 and Jan. 11, 1979.

**Table 1. Ranging system errors contributed by ground instrumentation**

	Harmonic Distortion	Antenna Multipath	Cable Drift & VSWR	Sideband Folding	Demod. Quantizer	Code Generator Delays	RSS	New Equipment Req'd.
Present System	7-10	~2	1-2	0.2	2	0.2	8-12	---
Model Distortion	3-7	~2	1-2	0.2	2	0.2	5-8	RS
Fundamental 1/2 MHz	2-3	~2	1-2	0.2	2	0.2	4-5	RS, RH
Fundamental 1 MHz	<0.5	~2	1-2	0.5	1	0.2	3	RS, RH
R/T Calibration at 1 MHz	<0.5	~2	~0.1	0.2?	1	0.2	~2.3	RS, RH, $\phi_c$ , CR
8 MHz Code New Klystron New Transponder	~0	~0.3	~0.5	~0.2	~0.1	0.2	0.65	RS, RH, XP, XM
R/T Calibration at 8 MHz	~0	~0.3	~0.1	0.1?	~0.1	0.2	0.4	RS, RH, XP, XM, $\phi_c$ , CR

Equipment Legend: RS = Range Software  
 RH = Range Hardware  
 $\phi_c$  = Phase Calibrator  
 CR = Calibration Receiver  
 XP = Transponder  
 XM = DSS Transmitter

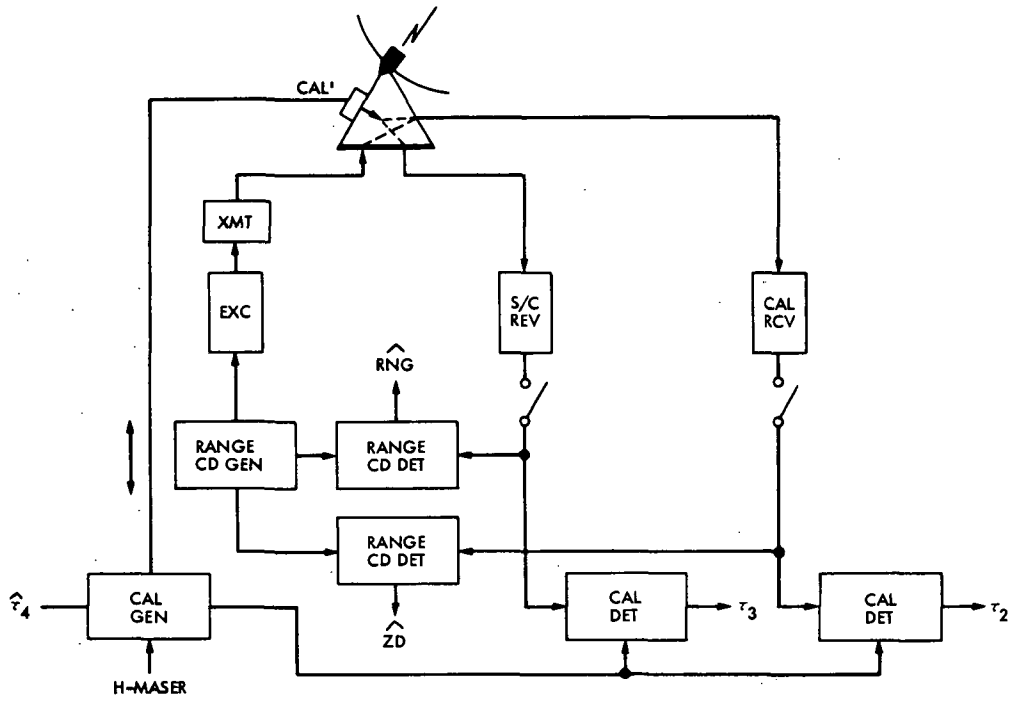


Fig. 1. Real-time calibration of ranging

## Spectral Shaping Without Subcarriers

L. R. Welch\*

Communications Systems Research Section

*For proper operation of the phase lock loop which tracks a carrier, it is important to minimize the spectral energy at frequencies near the carrier. A traditional method is to modulate the data onto a subcarrier in such a way that there is little energy near DC. The resulting signal is then used to modulate the carrier. The problem with such a scheme is that the total bandwidth is much larger than necessary to transmit the data. This paper proposes and analyzes a simpler scheme that increases the data bandwidth by a very small fraction, yet reduces the energy near DC to nearly zero.*

### I. Introduction

We will do our analysis at baseband and begin with a statistic which will allow us to estimate the energy of a process between the frequencies  $-B$  and  $+B$ .

For a stationary process  $X(t)$  with spectral density  $S_X(f)$ , define a new process by

$$Y_B(t) = \frac{1}{T} \int_0^T X(t - \tau) d\tau$$

where  $T = 1/2B$ . Then the spectral density of  $Y$  is

$$S_Y(f) = S_X(f) \left( \frac{\sin \pi f T}{\pi f T} \right)^2 \quad (1)$$

and the power in  $Y$  is

$$E\{Y^2(t)\} = \int_{-B}^B S_Y(f) df = \int_{-B}^B S_X(f) \left[ \frac{\sin(\pi f T)}{\pi f T} \right]^2 df \quad (2)$$

Now

$$\left[ \frac{\sin(\pi f T)}{\pi f T} \right]^2 \geq \begin{cases} \left( \frac{2}{\pi} \right)^2, & \text{for } |f| \leq \frac{1}{2T} = B \\ 0, & \text{otherwise} \end{cases} \quad (3)$$

So Eq. (2) implies that

$$E\{Y^2(t)\} \geq \left( \frac{2}{\pi} \right)^2 \int_{-B}^B S_X(f) df$$

\*Consultant from University of Southern California.

or

$$\int_{-B}^B S_X(f) df \leq \left(\frac{\pi}{2}\right)^2 E\{Y^2(t)\} \quad (4)$$

Thus, the second moment of  $Y(t)$  gives an estimate of the amount of energy in  $X$  between frequencies  $-B$  and  $B$ .

For an application of this statistic, consider the process  $X(t)$  which is  $+1$  or  $-1$  on each interval  $[nT_0, (n+1)T_0]$ . Assume the values on different intervals are independent and have probability  $1/2$ .

Then

$$\begin{aligned} E\{Y^2(t)\} &= E\left\{\frac{1}{T} \int_0^t X(t) dt\right\}^2 \\ &= E\left\{\frac{T_0}{T} \sum_{n=1}^{T/T_0} X((n-1)T_0)\right\}^2 \\ &= \left(\frac{T_0}{T}\right)^2 \frac{T}{T_0} = \frac{T_0}{T} = 2BT_0 \end{aligned} \quad (5)$$

and the bound is

$$\int_{-B}^B S_X(f) df \leq \left(\frac{\pi}{2}\right)^2 2BT_0 \quad (6)$$

Of course, for the process

$$S_X(f) = \left(\frac{\sin(\pi T_0 f)}{\pi f}\right)^2$$

and for small  $B$  the energy between  $-B$  and  $B$  is  $2BT_0$ . The factor  $(\pi/2)^2$  indicates the looseness of the bound.

The signal design problem is to encode the data into a signal  $X(t)$  such that  $E\{Y^2(t)\}$  is small.

## II. Proposed Solution

The proposed solution is to expand the data stream by inserting a redundant bit every  $L^{\text{th}}$  bit, the value of the bit being chosen to bring the total number of  $+1$ 's and  $-1$ 's into balance.

More precisely (see Figs. 1 and 2):

Let  $X_n$  be a sequence of  $\pm 1$ 's, defined below

Define  $X(t) = X_n$  for  $t \in [(n-1)T_0, nT_0]$

$$\text{Define } C_n = \sum_{m=1}^n X_m \quad (7)$$

Let  $L$  be an even integer

Then  $X_n$  is defined as follows: When  $n$  is not a multiple of  $L$ ,  $X_n$  is a data bit ( $\pm 1$ ). When  $n$  is a multiple of  $L$ , then

$$X_n = -\text{sgn}[C_{n-1}]$$

(Since  $L$  is even,  $n-1$  is odd. Then, from its definition,  $C_{n-1}$  must be odd and cannot be zero.)

The derivation of a bound on the power between  $-B$  and  $B$  is given below, resulting in Eq. (15). For non-redundant data (flat random data) the amount of power is  $2T_0B$ , so the factor  $[T_0B(3\pi^2/8)L^2]$  indicates what the gain has been when a redundancy of  $1/L$  has been inserted. In particular, when  $T_0 = 1/30$  MHz and  $B = 1$  kHz, if the value of  $L$  is 30, then the factor is  $1/8$  or a gain of 9 dB. If  $L = 10$ , then the gain is 18.5 dB.

## III. Analysis

It is clear from the definitions that, when  $T/T_0$  is an integer,

$$Y(nT_0) = (C_n - C_{n-T/T_0}) \frac{T_0}{T}$$

Therefore, the second moments of  $\{C_n\}$  must be studied. We will assume  $n$  so large that the stationary distributions have been obtained so that

$$E\{C_n^2\} = E\{C_{n-T/T_0}^2\}$$

In the case that the data bits are independent it can be shown that

$$E\{C_n C_{n-T/T_0}\} \geq 0$$

From this we have

$$E\{Y^2(nT_0)\} \leq \frac{2T_0^2}{T^2} E\{C_n^2\} \quad (8)$$

To analyze  $C_n$ , let

$$Z_k = \sum_{n=kL+1}^{kL+L-1} X_n$$

That is,  $Z_k$  is the sum of  $L-1$  consecutive data bits. For most of the analysis we will assume only that the odd moments of  $Z_k$  are 0, but for the best result we must also assume that the  $X_n$  contributing to  $Z_k$  are mutually independent.

From the definition of  $X_n$  we have

$$X_{(k+1)L} = -\text{sgn} [C_{kL} + Z_k] \quad (9)$$

and

$$C_{(k+1)L} = C_{kL} + Z_k - \text{sgn} [C_{kL} + Z_k]$$

Multiplying through by  $\text{sgn} [C_{kL} + Z_k]$  gives

$$C_{(k+1)L} \text{sgn} [C_{kL} + Z_k] = |C_{kL} + Z_k| - 1 \quad (10)$$

Since subtracting 1 from a positive odd integer cannot change the sign, the left side of Eq. (10) must be non-negative, and we have

$$|C_{(k+1)L}| + 1 = |C_{kL} + Z_k| \quad (11)$$

Next define

$$\mu_j = E\{Z_k^j\}$$

and

$$M_j = E\{|C_{kL}|^j\}$$

Then from Eq. (11) and the assumption that  $\mu_k = 0$  for odd  $k$ , we get

$$M_2 + 2M_1 + 1 = M_2 + \mu_2$$

$$M_4 + 4M_3 + 6M_2 + 4M_1 + 1 = M_4 + 6M_2\mu_2 + \mu_4 \quad (12)$$

From these equations and the Swartz inequality for positive random variables  $M_1 M_3 \geq M_2^2$ , the following inequality can be derived:

$$\left[ M_2 - \frac{3}{8}(\mu_2 - 1)^2 \right]^2 \leq (\mu_2 - 1) \left[ \frac{\mu_4 - 4}{8} - \frac{\mu_2 - 1}{4} + \frac{9}{64}(\mu_2 - 1)^3 \right]$$

or

$$M_2 \leq \frac{3}{8}(\mu_2 - 1)^2 + \frac{1}{8} \sqrt{(\mu_2 - 1) [8\mu_4 - 16 - 16\mu_2 + 9(\mu_2 - 1)^3]} \quad (13)$$

When the data bits are independent,  $\mu_2 = L - 2$ , and Eq. (13) implies

$$M_2 \leq \frac{3}{4} L^2 \quad (14)$$

This combined with Eqs. (4) and (8) give

$$\begin{aligned} \int_{-B}^B S_X(f) df &\leq \left(\frac{\pi}{2}\right)^2 (2T_0 B)^2 \frac{3}{4} L^2 \\ &= (2T_0 B)^2 \left[ \frac{3\pi^2}{8} L^2 \right] \end{aligned}$$

or

$$\int_{-B}^B S_X(f) df \leq 2T_0 B \left[ T_0 B \frac{3\pi^2}{8} L^2 \right] \quad (15)$$

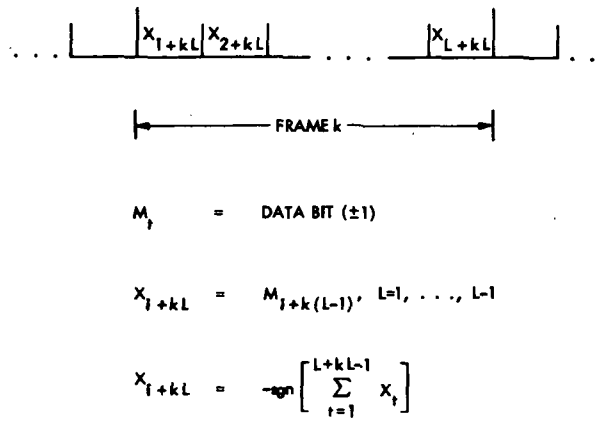


Fig. 1. Frame layout for data and redundant bit

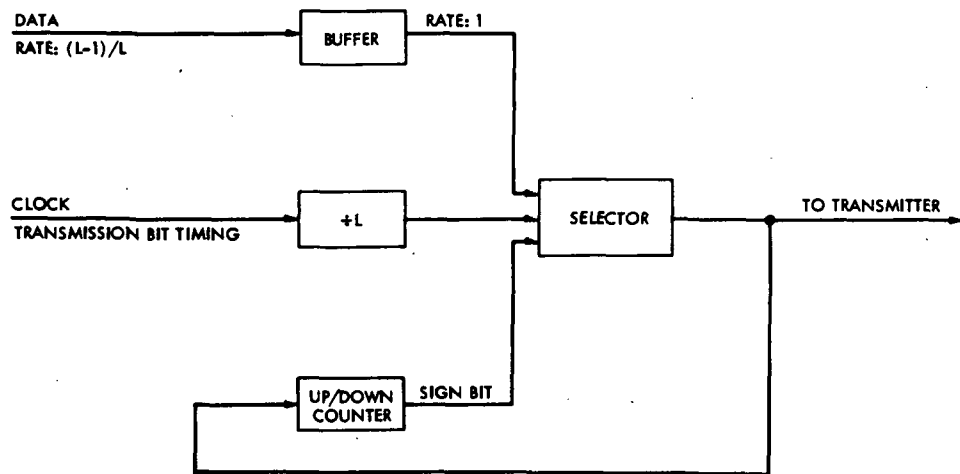


Fig. 2. Circuit for redundant bit computation and insertion

DB  
N79-22153

## Unattended Operations Software System Design Progress Report

L. Lim

Radio Frequency and Microwave Subsystems Section

*A small MBASIC<sup>tm</sup> program called ORGNIZE has been developed to assist the software designer in the organization of MDS PL/M programming modules. It provides a logical way to distribute the various programming procedures in the proper module. The program also provides a consolidated listing of any procedure call and a summary of all procedures used by any procedure call.*

The DSS 13 Unattended Station Controller has been in operation since December 1, 1977. The station controller design is based on an Intel 8080 microprocessor. The main program which controls the subsystem is a large computer program written in PL/M, a high level programming language. The program contains 87 procedures and was developed on the UNIVAC 1108, a maxicomputer. The station controller program was then cross-compiled from the U1108 to the station controller. Because of the inaccessibility of the U1108 and the excessive cost of cross-compilation of large PL/M programs, a Microcomputer Development Systems (MDS) has been acquired. The MDS has a resident PL/M compiler and other software development tools. However, the sizes of the memory storage and the auxiliary storage are obviously less than the U1108. Therefore, if the conversion of the U1108 PL/M program to the MDS PL/M system is to be possible, one must reorganize the large program into a number of smaller programming modules, compile these modules separately, then link and collect these modules on the MDS to form the final executable program.

A small MBASIC<sup>tm\*</sup> program, called ORGNIZE, has been developed to assist the software designer in the organization of MDS PL/M programming modules. It provides a logical way to distribute the various programming procedures in the proper module. The program also provides a consolidated listing of any procedure call and a summary of all procedures used by any procedure call.

The MBASIC<sup>tm</sup> program ORGNIZE requires a file which contains all the procedure names, sorted in lexicographic order, used by the various modules. Procedure names which are used by the module are surrounded by parentheses (i.e., external procedure); otherwise parentheses are omitted for public procedure within the modules and source files of each module. These files are available from the MDS. The program will prompt the user to input which procedure call is to be analyzed.

\*A trademark of the California Institute of Technology.

The program ORGNIZE was designed to analyze three PL/M syntaxes: (1) definition of procedure, (2) end of procedure, and (3) the calling of procedures. Procedure definition takes the following form:

Procedure name: PROCEDURE;

End of procedure takes the following form:

END procedure name;

Procedure call takes the following form:

CALL procedure name;

The basic function of the program ORGNIZE is to trace through all procedure calls generated by the user's input, i.e., the procedure call which the user wanted to be analyzed. The program first determines the file location of the User's request from the sorted file, PROCEDURE TABLE. The located PL/M source file is then opened for input. The requested procedure is then analyzed for procedure calls. These calls are then

stacked onto a queue to be used as the next procedure to be analyzed. The program will terminate when the queue is empty. The file PROCTBL is shown in Fig. 1, and the listing of the program ORGNIZE is shown in Fig. 2.

The DSS 13 Unattended Station Controller PL/M program contains four basic procedures: INITIATE, CONFIGURE, CALIBRATE, and OPERATE. Figure 3 shows the listing of all procedure calls by each of the above four procedures. Figure 4 shows a summary of these called procedures in tabular form.

From this summary, the MDS version of the PL/M program will be reorganized to have a program module which contains the following procedures: INITIATE, CONFIGURE, CALIBRATE, OPERATE, ALLCAL, ANALYZECAL, CHANNELCFG, DOWNLINK1CAL, DOWNLINK2CAL, IOCHECK, MISSIONOP, OPERATORIN, PORT, RCVALD1, RCVCALD2, RNGDELAYBERTEST, SDAACQD1, SDAACQD2, SDACALD1, SDACALD2, STARTCAL, STARTOPERATE, and ULCAL. All other procedures should then be grouped accordingly (e.g., all input and output functions: SEND, STARIN, STARO, etc).

ALLCAL	5A6DH	PROCEDURE	STACK=0006H,VARCCM
ANALYZECAL	5B6AH	PROCEDURE	STACK=0008H,VARCCM
AP	3361H	PROCEDURE	ADDRESS PUBLIC STACK=0002H,VARMAIN,(VARIO)
APPEND	2127H	PROCEDURE	EXTERNAL(15) STACK=0000H,(VARIO),(VARW1),VARW2
BUILDCFG	543FH	PROCEDURE	EXTERNAL(64) STACK=0000H,(VARCCM),VARW2
BUILDERRMSG	3AF6H	PROCEDURE	STACK=0004H,VARIO
CALIBRATE	5BC0H	PROCEDURE	EXTERNAL(8) STACK=0000I,(VARMAIN),VARCCM
CALLCI	22CDH	PROCEDURE	BYTE EXTERNAL(16) STACK=0000H,(VARIO),VARW2
CALLCO	22D5H	PROCEDURE	PUBLIC(71) STACK=0000H,VARMON,(VARIO),(VARW
CALLRI	22D1H	PROCEDURE	BYTE EXTERNAL(68) STACK=0000H,VARW2
CHANNELCFG	5611H	PROCEDURE	STACK=0002H,VARCCM
CKSUM	2642H	PROCEDURE	EXTERNAL(42) STACK=0000H,(VARW1),VARW2
COMPCHK	325CH	PROCEDURE	EXTERNAL(79) STACK=0000H,(VARMON),VARW1,(VARW2)
CONCAT	21A5H	PROCEDURE	EXTERNAL(60) STACK=0000H,(VARCCM),(VARMON),VARW2
COND1	4AD8H	PROCEDURE	EXTERNAL(66) STACK=0000H,(VARMON),VARW1
COND2	4A2AH	PROCEDURE	STACK=0004H,VARW1
CONFIGURE	56C6H	PROCEDURE	EXTERNAL(7) STACK=0000H,(VARMAIN),VARCCM
CONIN	22FEH	PROCEDURE	EXTERNAL(65) STACK=0000H,(VARMON),VARIO
CONOUT	2618H	PROCEDURE	EXTERNAL(59) STACK=0000H,(VARCCM),(VARMON),VARIO,(VARW1),(VARW2)
CONX	2672H	PROCEDURE	EXTERNAL(74) STACK=0000H,(VARMON),VARW2
DEVICE	395AH	PROCEDURE	STACK=0002H,VARIO
DOWNLINK1CAL	5A59H	PROCEDURE	STACK=0004H,VARCCM
DOWNLINK2CAL	5A63H	PROCEDURE	STACK=0004H,VARCCM
EQUAL	26ACH	PROCEDURE	BYTE EXTERNAL(73) STACK=0000H,(VARMON),(VARIO),VARW2
EQUATE		PROCEDURE	BYTE PUBLIC VARW2,(VARMAIN),(VARCCM),(VARIO),(VARMON),(VARW1)
GETCHR	22ECH	PROCEDURE	BYTE STACK=0002H,VARIO
GETSTS	22DDH	PROCEDURE	BYTE EXTERNAL(80) STACK=0000H,(VARMON),VARIO,(VARW2)
HEXTOASCII	41A5H	PROCEDURE	EXTERNAL(63) STACK=0000H,(VARMON),(VARIO),(VARW1),VARW2
INITIATE	52D9H	PROCEDURE	EXTERNAL(6) STACK=0000H,(VARMAIN),VARW2
IOCHECK	31FEH	PROCEDURE	EXTERNAL(68) STACK=0002H,VARW1,(VARW2)
KEY	40F7H	PROCEDURE	STACK=0004H,VARMON
LIST	4801H	PROCEDURE	STACK=0004H,VARMON
LISTOUT	2569H	PROCEDURE	EXTERNAL(72) STACK=0000H,(VARMON),VARIO
MESSAGE	33C9H	PROCEDURE	STACK=0002H,VARIO
MISSIONOP	5D91H	PROCEDURE	PUBLIC STACK=0004H,VARW2
MONITOR	4FE9H	PROCEDURE	STACK=0008H,VARMON
NOCCINP	4EA0H	PROCEDURE	STACK=0004H,VARMON
NULL	2059H	PROCEDURE	PUBLIC STACK=0000H,VARW2
OPADD	2A44H	PROCEDURE	PUBLIC STACK=0000H,VARMAIN,(VARW1)
OPERATE	5DFCH	PROCEDURE	EXTERNAL(3) STACK=0000H,(VARMAIN),VARW2
OPERATORIN	5D19H	PROCEDURE	PUBLIC STACK=0002H,VARW2
PORT	264CH	PROCEDURE	EXTERNAL(40) STACK=0000H,(VARW1),VARW2
PROMPTCALDISPLAY	3ED5H	PROCEDURE	STACK=0002H,VARCCM,(VARMON)
PROMPTCFGDISPLAY	3C7EH	PROCEDURE	PUBLIC STACK=0002H,VARCCM,(VARMON)
PROMPTERR1MSG	3B29H	PROCEDURE	EXTERNAL(68) STACK=0000H,(VARMON),VARW1
PROMPTERR2MSG	3B5EH	PROCEDURE	EXTERNAL(69) STACK=0000H,(VARMON),VARIO
PROMPTERR3MSG	3B8BH	PROCEDURE	STACK=000AH,VARIO
PROMPTERR4MSG	3BDCH	PROCEDURE	STACK=0002H,VARW1
PROMPTERR5MSG	3BF8H	PROCEDURE	EXTERNAL(67) STACK=0000H,(VARMON),VARW1
PROMPTHALTMSG	3C1FH	PROCEDURE	STACK=0002H,VARW1
PROMPTOPRDISPLAY	3F28H	PROCEDURE	EXTERNAL(62) STACK=0000H,(VARMON),VARW1
RCVCALD1	593EH	PROCEDURE	STACK=0002H,VARCCM
RCVCALD2	59B7H	PROCEDURE	STACK=0002H,VARCCM
RNGDELAYBERTEST	5AA2H	PROCEDURE	STACK=0002H,VARCCM
SDAACQD1	5992H	PROCEDURE	STACK=0002H,VARCCM
SDAACQD2	5A0BH	PROCEDURE	STACK=0002H,VARCCM
SDACALD1	5968H	PROCEDURE	STACK=0002H,VARCCM
SDACALD2	59E1H	PROCEDURE	STACK=0002H,VARCCM
SEGMENT	2151H	PROCEDURE	PUBLIC STACK=0006H,VARW2
SEGMSG	42CFH	PROCEDURE	STACK=0002H,VARMON
SEGOPMSG	438BH	PROCEDURE	STACK=0004H,VARMON
SEND	4700H	PROCEDURE	EXTERNAL(63) STACK=0000H,(VARCCM),(VARMON),VARIO,(VARW1),(VARW2)
SENDAVAIL	47C5H	PROCEDURE	EXTERNAL(4) STACK=0000H,(VARMAIN),VARMON
SENDSTATUS	4E3CH	PROCEDURE	STACK=0006H,VARMON
SIMULATE	4BCFH	PROCEDURE	STACK=0006H,VARMON
STACK	51BFH	PROCEDURE	EXTERNAL(62) STACK=0000H,(VARCCM),VARMON,(VARW2)
STAR1	21EEH	PROCEDURE	STACK=0002H,VARMON
STARIN	2202H	PROCEDURE	STACK=0004H,VARMON
STARINIT	22C3H	PROCEDURE	EXTERNAL(1) STACK=0000H,(VARMAIN),VARW2
STARO	21F8H	PROCEDURE	EXTERNAL(59) STACK=0000H,(VARMON),VARW2
STAROUT	226AH	PROCEDURE	STACK=0002H,VARMON,(VARIO)
STARTCAL	5794H	PROCEDURE	STACK=0006H,VARCCM
STARTOPERATE	5BEBH	PROCEDURE	PUBLIC STACK=000AH,VARW2
STATUSSENDLIST	48ACH	PROCEDURE	STACK=0002H,VARW1
TABLEINIT	2656H	PROCEDURE	EXTERNAL(2) STACK=0000H,(VARMAIN),VARW1
TABLESEARCH	265AH	PROCEDURE	ADDRESS EXTERNAL(81) STACK=000,(VARMON),VARW1
TERMINATE	5E57H	PROCEDURE	EXTERNAL(10) STACK=0000H,VARMAIN
TIMEX	26A8H	PROCEDURE	EXTERNAL(47) STACK=0000H,(VARW1),VARW2
TOD	239DH	PROCEDURE	EXTERNAL(78) STACK=0000H,(VARMON),VARIO
TTY1	2565H	PROCEDURE	BYTE STACK=0002H,VARIO
TTYO	255DH	PROCEDURE	STACK=0002H,VARIO
ULCAL	5A30H	PROCEDURE	STACK=0002H,VARCCM
WAIT	2009H	PROCEDURE	EXTERNAL(5) STACK=0000H,(VARMAIN),(VARMON),VARW2
XCONOUT	2500H	PROCEDURE	STACK=0006H,VARIO
XENABLE	4583H	PROCEDURE	EXTERNAL(22) STACK=0000H,(VARIO),VARW1
XKEY	40F3H	PROCEDURE	EXTERNAL(0) STACK=0000H,(VARMAIN),VARMON
XXCON	2486H	PROCEDURE	EXTERNAL(77) STACK=0000H,(VARMON),VARIO

Fig. 1. Sorted procedure table

ORIGINAL PAGE IS  
OF POOR QUALITY

```

PROGRAM: *ORGNIZE

100 INPUT USING 'ENTER PROCEDURE NAME:#':P$
110 OPEN 'MBAOPS*MBAOPS.PROCTBL',INPUT,1\ '*QQ',OUTPUT,2
120 AT ENDFILE(1) GO TO 150
130 STRING PROCTB(100):132,NUMB:16,DUMMY:132
140 INPUT FROM 1 USING '(R)':PROCTB
150 STRING PROCTB(NTB):132,PROC:132,RECD:132,STACK(NS):30 WHERE NTB=ITEMS,&
    NS=1,NE=0
160 CLOSE 1
165 STRING EXIST(1):30 WHERE NE=1&

170 FOR I=1 UNTIL DONE WHERE DONE=0,PROC=P$,THERE=0
171 THERE=0\THERE=(PROC=EXIST(PP)) FOR PP=1 UNTIL THERE OR PP>NE IF I#1
172 GO TO 230 IF THERE
175 GO TO 230 IF LEFT(PROC,3)='ROM' !SKIP ALL ROMS ROUTINES
180 GOSUB 1000 !SEARCH PROCTB TO FIND P$
190 IF FIND=0 THEN GO TO 250 WHERE DONE=1
195 RECD=PROCTB((F+L)/2)
200 GOSUB 2000 !BRING IN THE P$ LISTING
210 GOSUB 3000 ! WRITE OUT THE LISTING ONTO *QQ
220 GOSUB 4000 ! FIND ALL CALLS IN THIS LISTING AND APPEND IT TO STACK
230 IF I<=NS THEN PROC=STACK(I) ELSE&
    DONE=1 ! WHERE STACK IS EMPTY
235 PRINT 'I=':I;'NS=':NS;'NE=':NE IF I MOD 10=0
240 NEXT I
245 CLOSE 1, 2
250 END 'DONE'&
&

1000 !BINARY SEARCH PROCEDURE
1010 NUMB=PROC,NUMB=RJUST(NUMB),PP=LENGTH(NUMB),NUMB=NUMB+RPT('.',16-PP),&
    F=1,L=NTB
1020 IF F>L THEN FIND=0 ELSE&
    IF NUMB=LEFT(PROCTB((F+L)/2),16) THEN FIND=1 ELSE&
    IF NUMB<LEFT(PROCTB((F+L)/2),16) THEN&
    GOSUB 1020 WHERE L=IP((F+L)/2)-1 ELSE&
    GOSUB 1020 WHERE F=IP((F+L)/2)+1
1030 RETURN&

2000 ! FIND MODULE AND BRING IT IN
2010 REAL POS(COMAS)=0 WHERE COMAS=COUNT(RECD,',')
2020 POSCMA=0\POS(K)=INDEX(RECD,',',POSCMA),POSCMA=POS(K)+1 FOR K=1 TO COMAS
2030 FLAG=0\FLAG=(SUBSTR(RECD,POS(K),2)#',(') AND (SUBSTR(RECD,POS(K),1)='(',')&
    FOR K=1 UNTIL FLAG OR K>COMAS\K=K-1
2040 IF K>=COMAS THEN FL$=SUBSTR(RECD,POS(K)+1) ELSE&
    FL$=SUBSTR(RECD,POS(K)+1,POS(K+1)-POS(K)-1)
2045 FL$=SUBSTR(FL$,4)
2046 THERE=0\THERE=(PROC=EXIST(PP)) FOR PP=1 UNTIL THERE OR PP>NE
2047 GO TO 2180 IF THERE
2050 OPEN FL$,INPUT,1
2060 AT ENDFILE(1) GO TO 2097
2070 FOR K=1 UNTIL FIND WHERE FIND=0
2080 INPUT FROM 1 USING '(R)':DUMMY

```

ORIGINAL PAGE IS  
OF POOR QUALITY

Fig. 2. Program listing

```

*ORGNIZE

2085 IF INDEX(DUMMY,'PROCEDURE') AND INDEX(DUMMY,'$') THEN&
      GO TO 2085 WHERE POS1=INDEX(DUMMY,'$'),DUMMY=LEFT(DUMMY,POS1-1)+&
        SUBSTR(DUMMY,POS1+1)
2090 FIND=(INDEX(''+DUMMY,''+PROC) AND INDEX(DUMMY,'PROCEDURE') AND&
        INDEX(DUMMY,'EXTERNAL')=0)
2095 GO TO 2100
2097 FIND=1
2100 NEXT K
2110 STRING LISTN(N):132:/DUMMY/ WHERE N=1
2115 AT ENDFILE(1) GO TO 2160
2120 FOR K=1 UNTIL FEND WHERE FEND=0
2130 INPUT FROM 1 USING '(R)':DUMMY
2135 IF INDEX(DUMMY,'END ') AND INDEX(DUMMY,'$') THEN&
      GO TO 2135 WHERE POS1=INDEX(DUMMY,'$'),DUMMY=LEFT(DUMMY,POS1-1)+&
        SUBSTR(DUMMY,POS1+1)
2140 IF INDEX(''+DUMMY,' END ') AND INDEX(DUMMY,''+PROC) THEN&
      STRING LISTN(N):132:/LISTN,DUMMY /WHERE FEND=1 ,N=N+1ELSE&
      STRING LISTN(N):132:/LISTN,DUMMY/ WHERE N=N+1
      GO TO 2170
2150 GO TO 2170
2160 FEND=1
2170 NEXT K
2175 CLOSE 1
2180 RETURN&
&

3000 ! WRITE IT OUT IF NOT ALREADY THERE
3010 NOK=0\NOK=(EXIST(K)=PROC) FOR K=1 UNTIL NOK=1 OR K>NE
3020 IF NOK#0 THEN GO TO 3050
3030 WRITE ON 2 USING '(R)':CHAR(13)\LISTN\CHAR(13)
3040 IF EXIST(1)=NULL THEN&
      STRING EXIST(NE):30:/P$/ ELSE&
      STRING EXIST(NE):30:/EXIST,PROC/ WHERE NE=NE+1
3050 RETURN&

4000 ! FIND ALL CALLS IN LISTN AND APPEND IT ON STACK
4010 FOR K=1 TO N
4020 POS1=INDEX(LISTN(K),' CALL ')
4030 IF POS1=0 THEN GO TO 4100
4040 DUM$=SUBSTR(LISTN(K),POS1+5),DUM$=LJUST(DUM$)
4050 DUM$=DUM$+' ',POS1,FLAG=0\A$=SUBSTR(DUM$,J,1),FLAG=(INDEX('; (',A$)),&
      POS1=J FOR J=1 UNTIL FLAG OR J>=LENGTH(DUM$)\DUM$=LEFT(DUM$,POS1-1),
      NUM$=LJUST(RJUST(DUM$))
4070 IF INDEX(DUM$,'$') THEN&
      GO TO 4070 WHERE POS1=INDEX(DUM$,'$'),DUM$=LEFT(DUM$,POS1-1)+&
        SUBSTR(DUM$,POS1+1)
4080 IF STACK(1)=NULL THEN&
      STRING STACK(NS):30:/DUM$/ WHERE NS=1 ELSE&
      STRING STACK(NS):30:/STACK,DUM$/ WHERE NS=NS+1
4100 NEXT K
4200 RETURN&

```

Fig. 2 (contd)

INITIATE PROCS  
 ADDSEG  
 APPEND  
 BUILDERRMSG  
 CALLCO  
 CKSUM  
 COMPCHECK  
 CONCAT  
 COND1  
 COND2  
 CONIN  
 CONOUT  
 CONX  
 DEVICE  
 EQUATE  
 HEXTOASCII  
 INITIATE  
 IOCHECK  
 KEY  
 LIST  
 LISTOUT  
 MESSAGE  
 MONITOR  
 NOCCINPUT  
 NULL  
 OPADD  
 PORT  
 PROMPTCALDISPLAY  
 PROMPTCFGDISPLAY  
 PROMPTERR1MSG  
 PROMPTERR2MSG  
 PROMPTERR3MSG  
 PROMPTERR5MSG  
 PROMPTOPRDISPLAY  
 SEGMSG  
 SEGOPMSG  
 SEND  
 SENDAVAIL  
 SENDSTATUS  
 SIMULATE  
 STACK  
 STARI  
 STARIN  
 STARO  
 STAROUT  
 STATUSSENDLIST  
 TIMEX  
 TOD  
 TTYO  
 XCONOUT  
 XENABLE  
 XKEY  
 XXCON

CONFIGURE PROCS  
 CONFIGURE  
 SEND  
 CONOUT  
 STACK  
 CHANNELCFG  
 XENABLE  
 STAROUT  
 PROMPTERR2MSG  
 PROMPTERR3MSG  
 HEXTOASCII  
 LISTOUT  
 XCONOUT  
 MONITOR  
 COND1  
 BUILDCFG  
 STARO  
 BUILDERRMSG  
 APPEND  
 TTYO  
 CALLCO  
 TOD  
 XXCON  
 COMPCHECK  
 STARIN  
 SEGMSG  
 KEY  
 SIMULATE  
 SENDSTATUS  
 NOCCINPUT  
 LIST  
 OPADD  
 COND2  
 EQUATE  
 MESSAGE  
 DEVICE  
 ADDSEG  
 CKSUM  
 STARI  
 CONIN  
 XKEY  
 PROMPTCFGDISPLAY  
 PROMPTCALDISPLAY  
 PROMPTOPRDISPLAY  
 SEGOPMSG  
 CONX  
 PROMPTERR1MSG  
 CONCAT  
 SENDAVAIL  
 STATUSSENDLIST  
 NULL  
 PROMPTERR5MSG  
 TIMEX

CALIBRATE PROCS  
 CALIBRATE  
 SEND  
 STARTCAL  
 ANALYZECAL  
 XENABLE  
 STAROUT  
 PROMPTERR2MSG  
 PROMPTERR3MSG  
 HEXTOASCII  
 CONOUT  
 STACK  
 EQUATE  
 CONCAT  
 ULCAL  
 DOWNLINK1CAL  
 DOWNLINK2CAL  
 ALLCAL  
 RNGDELAYBERTEST  
 STARO  
 BUILDERRMSG  
 LISTOUT  
 APPEND  
 XCONOUT  
 MONITOR  
 COND1  
 NULL  
 RVCALD1  
 SDACALD1  
 SDAACQD1  
 RVCALD2  
 SDACALD2  
 SDAACQD2  
 MESSAGE  
 DEVICE  
 TTYO  
 ADDSEG  
 CALLCO  
 TOD  
 XXCON  
 COMPCHECK  
 STARIN  
 SEGMSG  
 KEY  
 SIMULATE  
 SENDSTATUS  
 NOCCINPUT  
 LIST  
 OPADD  
 COND2  
 CKSUM  
 STARI  
 CONIN  
 XKEY  
 PROMPTCFGDISPLAY  
 PROMPTCALDISPLAY  
 PROMPTOPRDISPLAY  
 SEGOPMSG  
 CONX  
 PROMPTERR1MSG  
 SENDAVAIL  
 STATUSSENDLIST  
 PROMPTERR5MSG  
 TIMEX

OPERATE PROCS  
 OPERATE  
 STARTOPERATE  
 SEND  
 MISSIONOP  
 STACK  
 CONOUT  
 EQUATE  
 CONCAT  
 XENABLE  
 STAROUT  
 PROMPTERR2MSG  
 PROMPTERR3MSG  
 HEXTOASCII  
 OPERATORIN  
 MONITOR  
 COND1  
 LISTOUT  
 XCONOUT  
 NULL  
 APPEND  
 STARO  
 BUILDERRMSG  
 BUILDCFG  
 XCON  
 TOD  
 COMPCHECK  
 STARIN  
 SEGMSG  
 KEY  
 SIMULATE  
 SENDSTATUS  
 NOCCINPUT  
 LIST  
 OPADD  
 COND2  
 TTYO  
 CALLCO  
 ADDSEG  
 MESSAGE  
 DEVICE  
 CKSUM  
 STARI  
 CONIN  
 XKEY  
 PROMPTCFGDISPLAY  
 PROMPTCALDISPLAY  
 PROMPTOPRDISPLAY  
 SEGOPMSG  
 CONX  
 PROMPTERR1MSG  
 SENDAVAIL  
 STATUSSENDLIST  
 PROMPTERR5MSG  
 TIMEX

ORIGINAL PAGE IS  
 OF POOR QUALITY

Fig. 3. Typical output

PROCEDURES	INITIATE	CONFIGURE	CALIBRATE	OPERATE
ADDSEG	X	X	X	X
ALLCAL			X	
ANALYZECAL			X	
APPEND	X	X	X	X
BUILDCFG		X		X
BUILDERRMSG	X	X	X	X
CALIBRATE			X	
CALLCO	X	X	X	X
CHANNELCFG		X		
CKSUM	X	X	X	X
COMPCHK	X	X	X	X
CONCAT	X	X	X	X
COND1	X	X	X	X
COND2	X	X	X	X
CONFIGURE		X		
CONIN	X	X	X	X
CONOUT	X	X	X	X
CONX	X	X	X	X
DEVICE	X	X	X	X
DOWNLINK1CAL			X	
DOWNLINK2CAL			X	
EQUATE	X	X	X	X
HEXTOASCII	X	X	X	X
INITIATE	X			
LOCHECK	X			
KEY	X	X	X	X
LIST	X	X	X	X
LISTOUT	X	X	X	X
MESSAGE	X	X	X	X
MISSIONOP				X
MONITOR	X	X	X	X
NOCCINPUT	X	X	X	X
NULL	X	X	X	X
OPADD	X	X	X	X
OPERATE				X
OPERATORIN				X
PORT	X			
PROMPTCALDISPLAY	X	X	X	X
PROMPTCFGDISPLAY	X	X	X	X
PROMPTERR1MSG	X	X	X	X
PROMPTERR2MSG	X	X	X	X
PROMPTERR3MSG	X	X	X	X
PROMPTERR5MSG	X	X	X	X
PROMPTOPRDISPLAY	X	X	X	X
RCVCALD1			X	
RCVCALD2			X	
RNGDELAYBERTEST			X	
SDAACOD1			X	
SDAACOD2			X	
SDACALD1			X	
SDACALD2			X	
SEGMSG	X	X	X	X
SEGOPMSG	X	X	X	X
SEND	X	X	X	X
SENDAVAIL	X	X	X	X
SENDSTATUS	X	X	X	X
SIMULATE	X	X	X	X
STACK	X	X	X	X
STARI	X	X	X	X
STARIN	X	X	X	X
STARO	X	X	X	X
STAROUT	X	X	X	X
STARTCAL			X	
STARTOPERATE				X
STATUSSENDLIST	X	X	X	X
TIMEX	X	X	X	X
TOD	X	X	X	X
TTYO	X	X	X	X
ULCAL			X	
XCONOUT	X	X	X	X
XENABLE	X	X	X	X
XKEY	X	X	X	X
XXCON	X	X	X	X

Fig. 4. Summary table

ORIGINAL PAGE IS  
OF POOR QUALITY

D14

N79-22154

# Dual A/D Converter With Automatic DMA Block-Transfer Capability

D. E. Wallis

Communications Systems Research Section

*A PDP-11 computer-controlled UNIBUS analog-to-digital (A/D) converter has been designed and constructed for use in the DSN Planetary Radar Data Acquisition System. The converter is intended for synchronous quadrature-pair sampling and can be programmed to automatically transmit the sample values via direct memory access (DMA) to any desired blocks of memory locations. The article describes the converter in detail, and gives information on mechanical construction, data-transfer rates, self-test and calibration provisions, and programming.*

## I. Introduction

A PDP-11<sup>1</sup> computer-controlled UNIBUS analog-to-digital (A/D) converter has been designed and constructed for use in the DSN Planetary Radar Data Acquisition System at DSS 14. Immediate applications of the A/D converter will be in the measurement of CW total reflected spectra from celestial bodies such as Venus, Ganymede, Callisto, and various asteroids. The converter fills a need in gathering measurements for the computation of high-resolution spectra (FFTs of more than 512 points) in the bandwidth range 5-350 kHz.

Prior to the availability of this A/D converter, variable-clock A/D conversion could only be done using the multiplexed A/D converter of the SDS 930 computer. Quadrature-

pair sampling with the 930's A/D converter is not simultaneous and is limited to about 5 kHz bandwidth. Faster sampling can be done by the 512-channel correlator, but this limits the spectral resolution to 512 points. The available CSPI Spectrum Analyzer (Array Processor) at DSS 14 can compute spectra to 8K points, but requires a direct memory access (DMA) source of quadrature-pair samples having both adequate speed and the ability to load alternate banks (or blocks) of memory locations in order to obtain continuous spectrum computation. The new A/D converter meets these requirements in a very general way, and can work with types of processing equipment other than the CSPI Spectrum Analyzer.

The A/D converters commonly available on the market generally lack three design features deemed essential for planetary radar data-taking:

- (1) DMA block transfers of arbitrary length to arbitrary memory locations, with bank-switching to load data

<sup>1</sup>PDP and UNIBUS are registered trademarks of Digital Equipment Corporation, Maynard, Massachusetts.

alternately to two different banks of memory locations.

- (2) Simultaneous quadrature-pair sampling with minimal skew (order of 10 nanoseconds) using video-type high-speed sampling technology, and with sampling controlled by a variable-frequency external source.
- (3) Self-test and diagnosis provisions for computer-controlled testing.

It was, therefore, decided to design an A/D converter having the required features, and incorporating design concepts based on needs which have been identified over many years of experience in planetary radar data-taking. This new design is based on an existing type of video A/D converter module, which was then embedded into an appropriate mechanical package and DMA computer interface having the requisite data transfer and self-test functions.

## II. Description of Equipment

### A. General Description

The equipment (the "box") is a computer-controlled (PDP-11) dual A/D converter of 8-bit resolution. The two A/D converters are Computer Labs MATV-11 video types with 50-ohm inputs,  $\pm 2.5$ -volt input range, and 2's complement encoding. Sampling can be commanded directly by the computer program, using data-input instructions, and also the sampling can be controlled by an "external clock" input. When the external clock is enabled, the box will sample automatically, and will transfer the samples automatically to blocks of memory locations specified by the program. The box may be commanded to produce program interrupts at end-of-block. The box also provides for computer-controlled self-test. The logical complexity of the box is 105 integrated circuit packages plus three component headers. Mechanically, the box is an 3-1/2 in. (8.89 cm) rack-mounted drawer with internal forced-air blowers. Due to thick shielding plates, the box weighs approximately 36 kg (80 lb). The box is designed to be electromagnetically and thermally compatible with most Deep Space Station rack-mounted equipment installations. Figures 1 through 5 present photographs of the equipment.

### B. Data Transfer Rates

Data transfer rates are dependent on whether the computer and/or other peripherals are competing for data-bus usage. With other peripherals off, and with the PDP-11 computer in its WAIT state, the box can transfer pairs of 16-bit numbers at a pair-rate (or "bandwidth") of 270,000 pairs per second (540,000 words per second). These rates were observed with a PDP-11 having a relatively slow type of core memory.

The internal timing of the box has been designed to transfer at the theoretical maximum rate for NPR "DATO" transfers, 2.4 million words per second (into zero-delay memory, of course), but the timing is currently set about 5 percent slower. The operational scenario for which the box was designed, however, envisioned somewhat slower transfer clocking. For this reason, the box responds to the external clock by NPR (request), waiting for the computer's NPG (grant), doing one or two word transfers, and then dropping BBSY. Thus, the box is not designed to capture the data bus during an entire block transfer, and, therefore, cannot actually transmit at the theoretical maximum rate.

### C. Self-Test Provisions

The box is designed for computer-programmed self-test. The self-test features include:

- (1) Direct write-read tests of writable registers MARPA, PTC, MARPB and also the control bits CS 0, 1, 2, 3, 4, 6, 7.
- (2) Indirect write-read tests of MAR and TC, by setting CS 7 (SOFTINIT) and writing, respectively, to MARPB and PTC. The result is that the contents of MARPB and PTC can be read, respectively, from MAR and TC.
- (3) Verification of the hardwired interrupt vector (0170) by reading IVAD. Note: Because of other test provisions (see 4, below), either CS0 must have previously been cleared or both CS1 and CS2 must have previously been cleared, to prevent spurious NPR transfers from being triggered during testing.
- (4) Simulation of the "external clock," made available by having the program input ("move") data from IVAD, preferably using an available general register in the computer as the destination, for maximum speed. Output "moves" should not be used, due to artifacts of the computer. This simulated external clock is equivalent to an actual clock, and will produce NPR data transfers under the same rules as for the external clock (i.e., the GO conditions must be met).

### D. Calibration Provisions

The calibration potentiometers of the two MATV-11 video A/D converters are accessible from the rear of the box, and may be adjusted without opening the box. Calibration is conducted by connecting a precision voltage source to one of the A/D converter coaxial input jacks, and reading the converter under program control. In calibration, the potentiometers are adjusted to produce "flutter" in certain bit-combinations for various input voltages. The flutter statistics may, of course, be displayed by an appropriate computer program.

## E. Sampling Control

The two A/D converters can be caused to sample under the following stimuli:

- (1) *Input from Device Addresses 00, 04, and 20* which produce, respectively, the "real," "quadrature," and "both" samples. Under input, the box uses asynchronous technique to delay SSSYN response until the requested conversion is complete.
- (2) *Input or Output to Device Address 14*, when "GO" conditions are met. This action simulates an external clock and causes the automatic block transfer logic to trigger new A/D samples and to transmit them.
- (3) *External Clocks*. A TTL gate input (with 4.7K pullup to +5 volts) and an analog clock input are provided. The TTL gate input triggers the automatic block transfer logic on the fall of the input. This input should be left open-circuited when not in use. The analog clock input is 50 ohms (nominal) and is shunt zener protected. The analog signal is normally a zero-bias sinusoid obtained from a variable-frequency synthesizer, whose output is +13 dBm in 50 ohms (3 volts peak-peak). The analog signal is compared to zero by a  $\mu$ A 710 comparator, and the 710's TTL-compatible output triggers the automatic block transfer logic on the negative-going zero-crossing of the sinusoid. The 710 is wired with output-to-input positive feedback that induces a Schmitt-trigger type of action: When the analog signal crosses the trigger threshold (voltage), the 710 begins to change its output state. Feedback of this output state causes the threshold to move approximately 55 millivolts in that direction which enhances the change of state which was initiated by the threshold crossing. An unsymmetrical pair of thresholds are used: the threshold for the negative-going analog input is -5 millivolts which, considering the intrinsic 5 millivolt uncertainty of the 710, does not significantly affect the 710's ability to detect the negative-going zero-crossing. The threshold for the positive-going signal is, however, +50 millivolts, but with the same hysteresis characteristic.

## III. Programming

### A. Block Transfer Description

The box, when under control of the "external" (or simulated) clock, does real, quadrature, or real-quadrature pair sampling, and then transfers one or both conversion results (as numbers) to any desired block of contiguous addresses in the computer's memory system. On each external clock transition, the number of conversion words to be transferred (one or two)

is determined by the number of A/D converters enabled (CS1, CS2 in the control-status register). The number of word or word-pair transfers is controlled by the contents of PTC, which holds the two's complement of the number of such transfers that are to be accomplished. A block can consist of from 1 to 32,768-word or word-pair transfers. The addresses of the memory locations to which transfers will be made are specified by either of two base-address "preset" registers, MARPA and MARPB, and a moving address register, MAR, which increments from a preset value contained in either MARPA or MARPB. The MARPB preset address is used by default, but the box can be commanded to "cycle" two or more block transfers in which MARPB and MARPA are used, *alternately*, as base-address initialization. This cycling capability is used to load data into array-processing equipment such that while one block is being loaded by the box, the other block is being processed and vice versa.

### B. Block Transfer Control Under CS Bits 1, 2

CS Bit 1 enables the "quadrature" sampler hardware, and CS Bit 2 enables the "real" sampler hardware. The sequencing recognizes three cases of this pair of bits:

- (1) *None Enabled*. The box holds, same as GO released state.
- (2) *Either Enabled, But Not Both*. Whichever of the two samplers is enabled furnishes the word to be transferred. After the transfer, MAR (the "word" storage address) and TC increment. If TC has been in the carry state (TC = 0177777) during the transfer, then both MAR and TC will receive preset values as soon as the transfer is complete.
- (3) *Both Enabled*. The real sample is transferred first, and then MAR is incremented. Then, the quadrature sample is transferred, and then both MAR and TC increment. Thus, TC increments after a *quadrature-pair* has been transmitted. If the TC has been in the carry state during the transfer of the quadrature sample, then both MAR and TC will receive preset values as soon as the transfer is complete.

### C. Master Enabling (GO)

The box will do conversions under NPR and (if enabled) interrupts under BR, only when the following conditions (the "GO" conditions) all appear in the CS register:

- Bit 7 (Software-Controlled Initialization) released
- Bit 0 (GO) set
- Bit 1 or Bit 2 (Conversion Select/Enable) set

Otherwise, the box holds its position in its internal sequencing logic, and will "resume where it left off" when the running conditions are met. When the box is running NPR, it is possible that the box, as master, could address nonexistent storage. This error situation cannot be detected by the program, because the box has no NPR timeout to permit the CPU to reacquire the bus to command the box to hold (drop Bit 0, or drop both Bits 1 and 2) or to initialize (assert Bit 7), even though such control is available. NPR hang can, however, always be cleared by asserting bus INIT, which forces Bit 0 off (no-go), and cancels all NPR or BR activities. When the program succeeds in commanding no-go, the effect on the sequencing logic is benign, because the box cannot be bus master at such a time.

#### **D. Interrupt Logic**

The box can interrupt after the last data-word transmission of a block (as determined by TC = carry state), provided the interrupt is enabled (Bit 6 a "one"), with the box otherwise in

the running state. The interrupt guarantees that the entire block transmission is complete, and does not preclude further sampling and NPR transmissions while the interrupt is being processed by the program.

#### **E. Data Sampling Synchronization**

When "GO" conditions are all met, the next (subsequent) pulse from the external clock governs the actual sample time. The leading, negative going edge of the external clock produces the start-convert (ENCODE) command to the A/D hardware.

#### **F. Programmer's Reference Guide**

The Appendix gives a programmer's reference guide to the control and status registers of the A/D converter. The reference guide, prepared in the condensed form preferred by programmers, identifies the registers by name and low address bits, and gives descriptions of register and control bit functions.





activities are aborted "in a benign way." *Note:* The only other initialization available in the box is obtained by asserting unified-bus INIT, which aborts NPR/BR (abnormally, if these were active) and drops Bit 0 (placing the box in hold), guaranteeing a benign state for all drivers.

**Bit 6** – A "one" will enable the interrupt at the end of each data-block transfer. The bit is tested internally only when the logic is in the end-of-block state.

**Bit 5** – This read-only bit is a "one" when the box is using memory addresses initialized from MARPB, and can become a "zero" only in the cycling mode, when the box switches to the MARPA preset register. The "one" indicates that the use of the address sequence starting from MARPB is not finished, and the "zero" indicates similarly for the MARPA address sequence.

**Bit 4** – The program sets this bit to "one" to enable the external analog clock (3 volt peak-peak) input to control the sampler timing. This control was provided so that the external analog clock jack can be left open-circuited while testing is in progress.

**Bit 3** – A "one" will enable continuous cycling of the data block transmission, and causes presets of PTC to TC and MARPA or MARPB to MAR. MARPB is used if MAR was running from the MARPA value, and vice versa.

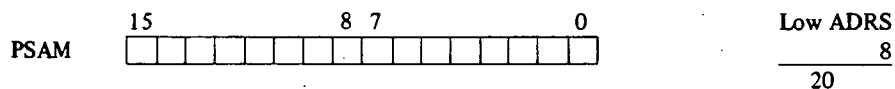
**Bit 2** – A "one" will enable the "REAL" sampler for automatic sampling synchronously to subsequent external clock pulses occurring after release of Bit 7 (initialization) and assertion of Bit 0 (GO).

**Bit 1** – A "one" will enable the "QUAD" sampler for automatic sampling, synchronously to subsequent external clock pulses (see description for Bit 2). Quadrature samples are obtained simultaneously with real samples when both quadrature and reals are enabled.

**Bit 0** – A "one" will enable the box's automatic NPR (and INTR, if enabled) sequencing when conditions on Bit 7, 2, and 1 are also met. A "zero" will cause the box to suspend operations, subject to resuming the sequencing at a later time, without loss of sequencing information or other control information. Bit 0 is cleared by unified-bus INIT, and automatically after the last word or word-pair transmission of a block, if cycling has not been enabled. When Bit 0 is commanded from set to clear, any sampling operation currently in progress will have been completed.

*Note:* The setting of Bit 0 to "one" cannot actually produce NPR sequencing unless Bit 7 was previously commanded to "zero," i.e., simultaneous clearing of Bit 7 and setting of Bit 0 will not produce "GO" conditions.

*Packed Quadrature and Real Sample*



This read-only register contains both the real and quadrature sample bytes packed into one 16-bit word. The left (high-order) byte contains the 8-bit 2's



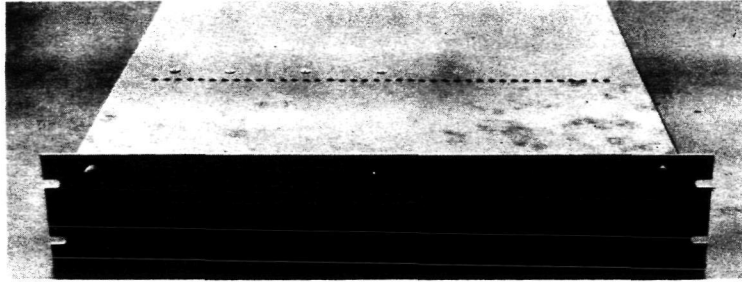


Fig. 1. Front view, showing 19 by 3-½ in. (48.26 by 8.89 cm) shielding grille and 5-volt power indicator LED

ORIGINAL PAGE 1  
OF POOR QUALITY

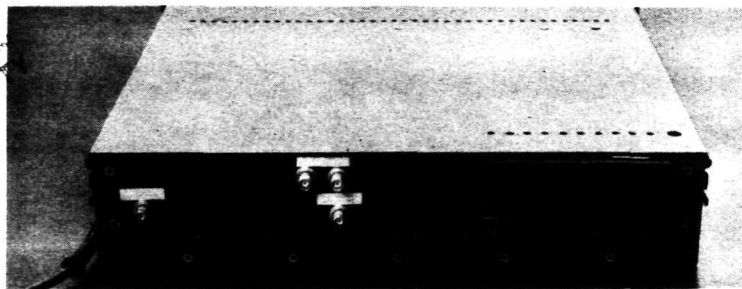


Fig. 2. Rear view, showing real and quadrature signal inputs, TTL and analog external clock inputs, UNIBUS connector, and converter module calibration access holes (at bottom)

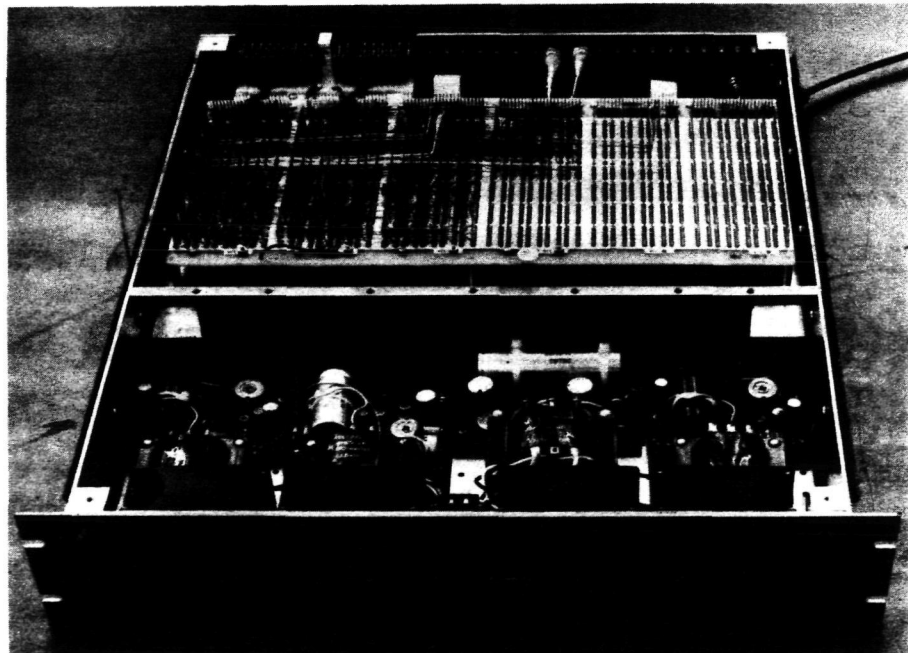


Fig. 3. Top cover removed for logic probing, showing power supplies and power-supply shield used as airflow divider

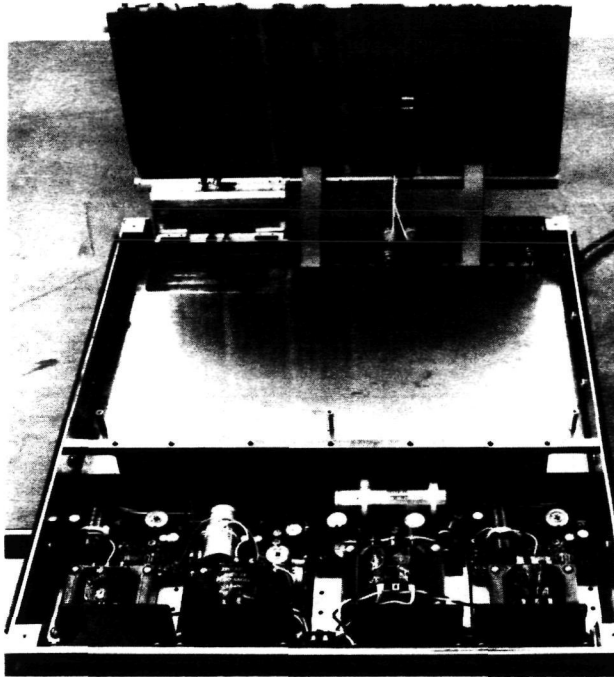


Fig. 4. Logic board folded upward on hinge for IC replacement, showing horizontal shield between logic circuits and A/D module compartment below; shield plate is also an air divider between compartments

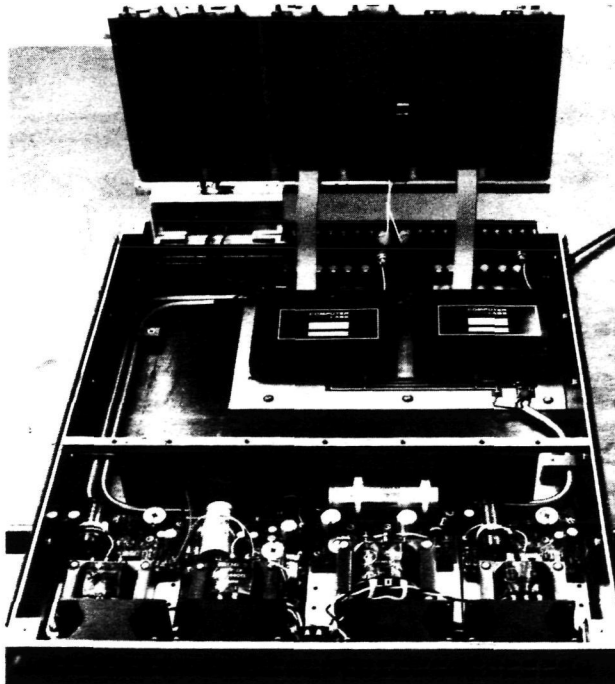


Fig. 5. Horizontal shield plate removed, revealing A/D converter modules on PC board

ORIGINAL PAGE IS  
OF POOR QUALITY

D15

## A Note on Digital Signatures

R. J. McEliece  
Consultant, Department of Mathematics  
University of Illinois

*This article demonstrates the fact that any one-way function can be used to generate unforgeable digital signatures in a conceptually simple and easily implementable manner.*

1. One of the most intriguing possibilities raised by Diffie and Hellman (Ref. 1) in their seminal paper on cryptography is that of devising digital signature systems. Until now, however, the only entirely satisfactory signature systems which have been generated using the Diffie-Hellman approach depend on the existence of a "trap door one-way permutation" — and apparently the only such function of this kind presently known is the number-theoretic mapping of Rivest, Shamir, and Adleman (Ref. 2). In this note, we will show that any one-way function (and one-way functions, in contrast to trapdoor one-way permutations, are quite easy to find) can be used to produce signature systems which are likely to be satisfactory for many applications.

2. Suppose a certain individual A wishes to transmit a sequence of  $n$  messages to another individual B. These messages will be transmitted digitally, and A wishes to be able to "sign" his messages in such a way that B will be certain that A actually was the sender. (For our purposes the actual content of the messages is unimportant; but, for example, the messages could be checks drawn against A's bank account at bank B.)

We suggest the following way for A to generate digital signatures. Let  $f$  be a "one-way" function with domain  $X$  and range  $Y$ . (This is an imprecise notion, but roughly it means

that for a given  $x \in X$ ,  $f(x)$  is easy to compute, but for a given  $y \in Y$ , the equation  $f(x) = y$  is overwhelmingly difficult to solve for  $x$ . We will give explicit examples in the next section.) Prior to the beginning of correspondence between A and B, A randomly selects  $n$  elements of  $X$ ,  $(x_1, x_2, \dots, x_n)$ . This list must be kept secret. He then computes  $y_i = f(x_i)$ ,  $i = 1, 2, \dots, n$ , and transmits the list  $(y_1, y_2, \dots, y_n)$  to B. This list need not be kept secret, and indeed in some circumstances it may be desirable to make it publicly known, in order to avoid later disputes. The signature attached to the  $i$ th message in the correspondence between A and B is simply  $x_i$ . B can verify that a given received signature  $x$  attached to what purports to be the  $i$ th message from A is authentic by computing  $f(x)$ ; the message is accepted if and only if  $f(x) = y_i$ .

In this scheme, the actual verification is computationally simple, since by assumption, given  $x$ ,  $f(x)$  is easy to compute. On the other hand, a potential forger who does not know the  $x_i$ 's would have to solve the equation  $f(x) = y_i$  for some  $i$  in order to attach a valid signature  $x_i$  to a message of his own. But since  $f$  is assumed to be a one-way function it would be computationally infeasible for him to do this. In the next section we discuss the selection of the function  $f$ .

3. It is easy to concoct horribly complicated functions  $f$  which might be one-way functions, but what is really needed is

a function  $f$  which is *provably* one-way. We can almost, but not quite rigorously, accomplish this by invoking the theory of *NP*-completeness. We cite only two examples, but many more could be given.

*Example 1.* Let  $C$  be an arbitrary  $N/2 \times N$  matrix with nonnegative integer entries. Let  $X$  be the set of  $N$ -dimensional vectors with entries 0 and 1. Then for  $x \in X$ , the function  $f(x) = Cx^T$  is, by the theory of *NP*-completeness, very likely to be a one-way function, provided  $N$  and the entries of  $C$  are large enough. For in the first place the function itself is quite easy to compute — it is a simple integer matrix-vector multiplication. On the other hand, the complexity of solving the

equation  $Cx^T = y$  is, by the theory of *NP*-completeness, almost surely an exponential function of  $N$ . (This is because the “integer programming” problem is *NP*-complete (Ref. 3).

*Example 2.* Let  $a = (a_1, \dots, a_N)$  be a list of large non-negative integers, and again let  $X$  be the set of  $N$ -dimensional 0-1 vectors. The function  $f(x) = \sum x_i a_i$ , where  $x = (x_1, \dots, x_N)$  is again likely to be one-way, because the corresponding combinatorial problem (solve  $a \cdot x = y$  for  $x$ ; the “knapsack” problem) is known to be *NP*-complete. Again, see Ref. 3 for details. (The knapsack problem was also used by Merkle and Hellman (Ref. 4) to design a public-key cryptosystem.)

## References

1. Diffie, W., and Hellman, M., “New Directions in Cryptography,” *IEEE Trans. Inform. Th.*, IT-22, pp. 144-654, 1976.
2. Rivest, R., Shamir, A., and Adleman, L., “A Method for Obtaining Digital Signatures and Public-Key Cryptosystems,” *Communications of the ACM*, 21, pp. 120-126, 1978.
3. Karp, R., “Reducibility Among Combinatorial Problems,” pp. 85-103, in *Complexity of Computer Computations*, Plenum Press, New York, 1972.
4. Merkle, R., and Hellman, M., “Hiding Information and Signatures in Trapdoor Knapsacks,” *IEEE Trans. Inform. Th.*, IT-24, pp. 525-530, 1978.

# A General Logic Structure for Custom LSI

M. W. Sievers

Communications Systems Research Section

*A designer of custom large-scale integrated circuits (LSI) should be primarily concerned with deriving a working chip as rapidly as is practical. Obtaining maximal usage of area or pushing a technology to its limit is best left for large producers of LSI who are able to recover the additional required expenditures of time and processing facilities by volume sales. Custom design may be greatly facilitated by a general template into which most circuitry can be built. This template must be both simple to use and reasonably conservative of area to be practical.*

*This paper describes a general structure that is being considered as a template candidate. Examples of circuits built in NMOS technology are shown. It is hoped this structure is suitable for building special-purpose devices such as correlators and FFT's as well as general-purpose controllers.*

## I. Introduction

This paper describes an integrated circuit structure suitable for implementing general combinatoric logic functions in custom LSI. The general logic structure (GLS) is similar to a programmed logic array (PLA) with additional features that enhance its flexibility. GLS was motivated by the storage logic structure described by Patil (Ref. 1).

Now the bad news. It can be expected that the mapping of an arbitrary logic function into a general structure is less efficient in use of area and probably slower than an optimized random logic design. However, in the realm of custom LSI, these factors may not be significant, especially if they may be traded for implementation ease and reduced cost. It should be noted further that this structure may not be suitable for

all possible circuitry. Some elements, most notably memory, pad drivers, and line receivers with Schmitt trigger inputs are best built outside of the GLS. The good news is that there are very few classes of these special circuits.

General structures are also attractive in fault tolerant designs. This is because once the failure mechanisms have been established for the structure, this information may be used to predict the reliability of functions mapped into it and to suggest design rules to increase fault and test coverage.

## II. GLS Description

An approximation of the logical equivalent of a GLS is shown in the example of Fig. 1. Each of the  $m$  column lines

may be formed into up to two NOR gates from two physically disjoint partitions of the  $n$  implicant rows. A gate is created by connecting pull-down transistors at desired implicant rows to a column and connecting the column to a pull-up resistor. The output of the NOR gate may be taken anywhere on the column segment on which the gate is built. Pull-up resistors are provided at both ends of each column. This permits a column to be cut and formed into two independent NOR gates.

A NOR gate output may be connected to any unused implicant row that it crosses. The connection is made by forming a contact point at the desired row-column intersection. Formation of multiple contact points allows transmitting the NOR output to different locations within the structure. Distribution of signals is further facilitated by connecting implicant rows directly to columns. In this way, an implicant carried at the "top" of the GLS may be brought to an implicant row at the "bottom."

Implicant rows may be cut into several segments. Each segment can be used for transmitting a different implicant. In this way, for example, an implicant row carrying an input term may be cut after the last pull-down transistor that uses it. The segment after the cut can then be reused to transmit a NOR output.

The example of Fig. 1 illustrates some of the flexibility of the GLS. Contact points are indicated by a dot and cuts by an  $x$ . NOR gate 1 forms the result  $A+B+C$ . The implicant row carrying input A is cut at Z and a contact point is created at Y. This connects gate 1 output to the implicant row freed by cut Z. Gate 1 output is now available as an input to NOR gate 3. Gate 3 output is connected to an unused implicant row which in turn is connected at T to a column. Contact W places the output of gate 3 on an implicant row, which makes it available to the input of gate 2.

Figure 2 continues the example of Fig. 1. Some of the abstraction used to depict the GLS in Fig. 1 has been elided here to more clearly represent its actual implementation. The implementation shown is based in NMOS technology.

Two types of rows are shown in Fig. 2. One row type transmits implicant terms and is drawn as a solid line. The other row type is connected to ground and is drawn as a dashed line. The reason for the two row types will become clearer in the discussion of Fig. 3. Columns are drawn as alternate dot-dashed lines.

Transistors are created at the intersection of a column and implicant row where the implicant is needed in the NOR function. Transistor channels provide a switchable path from

columns to the ground row. Pull-down transistors are enhancement mode devices. The channels of these transistors conduct when a positive gate-to-source voltage is present.

Pull-up resistors are implemented by depletion mode transistors that are shorted from gate to source. In this configuration, the transistor acts like a resistor with an impedance proportional to its length-to-width ratio.

When an implicant is high, it causes all transistors to which it is connected to conduct. This forces the corresponding columns to approximately the ground potential. When none of the implicants associated with a given column is high, the pull-up resistor brings the column to approximately the positive supply voltage; a NOR function.

The example of Fig. 1 is revisited one more time in Fig. 3. Figure 3 illustrates the stick diagram for an NMOS implementation of Fig. 1. In this figure, polysilicon is represented by a solid line, diffusion by a dashed line, metal by an alternating dot-dashed line, and implant by a thickened line.

When polysilicon crosses diffusion, a transistor is formed in which the polysilicon becomes the gate and diffusion the channel. This phenomenon is exploited in the GLS in the same manner as in an NMOS PLA. Polysilicon is used to transmit all implicant terms across the structure. Transistor channels, connecting metal columns to grounded diffusion rows are made to cross polysilicon rows of the implicants needed in the NOR to be formed. Formation of transistors in this manner necessitates an interleaving of polysilicon implicant rows and grounded diffusion rows.

The GLS illustrated in Figs. 1 thru 3 shows only two pull-up resistors per metal column. This restriction is unnecessary as shown in Fig. 4. The technique for providing additional pull-ups requires that the metal columns be periodically broken. The resulting gap is spanned by a diffusion cross-under. This diffusion is crossed by a metal carrying the positive supply voltage.

Three situations occur as represented by A, B, and C in Fig. 4. Situation A illustrates the method for providing pull-up resistors at column breaks. Polysilicon and implant are placed as shown to form depletion mode transistors. The poly gate is fed around to the transistor source and a contact point is made that connects the metal column, poly, and source. The drain side of the transistor channel is connected to the metal row carrying the positive supply voltage. Example B illustrates the formation of a communication path between two column pieces. The column pieces are connected by creating contact

points to the diffusion cross-under. Finally, example C shows that disjoint column pieces are made by simply omitting contact points from metal to the cross-under diffusion.

### III. Lower Bound on the Size of an NMOS GLS Binary Tree

An estimate of the lower bound on the size of a binary tree implemented in an NMOS GLS may be found with the aid of the binary NOR tree in Fig. 5. For this discussion, assume that the tree is complete; i.e., there exists an integer  $m$  such that the number of inputs  $n$ , is equal to  $2^m$ . This is the simplest tree that can be formed in the GLS because the GLS naturally forms NOR gates. Clearly, although any tree can be mapped into a binary NOR tree, trees with irregular structure require more space.

The complete  $n$  input binary NOR tree in Fig. 5 is formed from a total of  $n - 1$  NOR gates. Owing to the natural signal flow in the tree, it is best to build the tree exactly as shown in Fig. 5. That is, as a series of columns, each column containing a single level of gates. Since the depth of the tree is  $\log_2 n$ , that many columns are needed. Since the output of any gate may be placed on one of the implicant rows which drives the gate, no proliferation of implicant rows occurs. Therefore, at most,  $n$  implicant rows are needed. The tree requires  $n - 1$  gates so the total area occupied by the tree will be  $(n - 1)(G + P)$ , where  $G$  is the area of a gate and  $P$  is the area of the pull-up resistor.

Estimating the size of other trees formed in a GLS may be done by first determining the equivalent binary NOR tree. The total number of metal columns needed will be no less than the base 2 logarithm of the number of inputs; the number of rows will be no less than number of inputs, and the area will be at least one less than the number of inputs times the area of a gate and its pull-up.

### IV. Registers

In order for the GLS to be completely general it is necessary to demonstrate that it is feasible and practical to implement registers in it. One possible register is shown in Figs. 6a and 6b. Figure 6a shows the logical equivalent of a D flip-flop built with NOR gates. The storage element in this device is constructed from cross-coupled NOR gates. When both inputs of the flip-flop are low, the output remains unchanged. A high level signal to either input will force the output of the corresponding NOR gate low. Both outputs will go low if both inputs are high, but the state of the flip-flop is indeterminate if both inputs go low again simultaneously.

An input gating arrangement enables the data input to the flip-flop. When the clock is high, the flip-flop output will remain at its current state. When the clock goes low, the output of the flip-flop follows the input. Data is latched into the flip-flop when the clock returns to its high state.

An NMOS stick diagram of the register in Fig. 6a is shown in Fig. 6b. The line convention is the same as in Fig. 3.

This register fulfills the clocking requirements for testability established in Ref. 2. Complete compatibility with those requirements necessitates that all registers be shift registers. Placing a multiplexer (see Fig. 7 for an example of a multiplexer implemented in NOR gates) in front of the flip-flop is one possible method for building a shift register. The multiplexer selects data either from a previous register, the next register, a direct input, or the current data. In this configuration, the register may be continuously clocked. The multiplexer determines whether a left or right shift, load, or no operation is to occur on the next clock transition. A stick diagram of a two cell shift register is shown in Fig. 8.

### V. A Few Remarks on Optimality

A completely optimum design belongs in the same class of mythical creatures as unicorns, tax reform, and honest used car salesmen. It is possible to speculate on its existence, but it is impossible to achieve or recognize in any nontrivial situation. Some comments can be made, however, regarding "best" use of area when a GLS is compared with a PLA or gate array, and in "best" selection of architecture when a choice exists.

In a comparison of a PLA and GLS implementation of a given logical expression, it should be expected that the GLS will be more dense on the average. In a PLA, the concept of optimum design is restricted to finding the minimum set of implicants required to compute a given function. The GLS permits an added dimension by allowing a number of cut-and-paste operations that can be used to reclaim some of the area that would otherwise be lost in PLA designs. There will no doubt be functions that map as inefficiently into a GLS as a PLA. It is hoped that these are rarely encountered.

The density of functions mapped into gate arrays will also generally be less than that achievable with a GLS. This is because gate arrays are built from fully formed gates. These gates include additional large output drive transistors for supplying a specified fanout capability. In the GLS, these drive transistors are needed only at those outputs that must drive a large capacitance. The main savings therefore is in the area occupied by the drive transistors.

Choosing which architecture to use for a given function when a choice exists may be answered in part by timing considerations. For example, consider the two architectures in Figs. 9a and 9b for a four-bit parity encoder. The circuit in Fig. 9a is a two-level network, and Fig. 9b is a tree. Intuitively, it might seem reasonable to expect the circuit in Fig. 9a to have less delay from input to output than the circuit in Fig. 9b. This seems reasonable because there are fewer gates in the signal path of Fig. 9a than Fig. 9b. Unfortunately, this intuitive estimation is not always correct because the gates in Fig. 9a are larger and therefore slower than those in Fig. 9b.

Specifically, consider an NMOS GLS implementation of the circuits in Figs. 9a and 9b. A very crude approximation will be used to calculate the expected delays through these circuits. Assume it is possible to lump all capacitance seen by the drain of a transistor into a single term, which is designated  $c_p$ . This capacitance includes all parasitics due to increased metal length to accommodate the transistor, diffusion capacitance, Miller capacitance, etc. Additionally, assume that each pull-down transistor has a gate capacitance  $c_g$ . Define  $k$  as the ratio of pull-up resistor impedance to pull-down transistor impedance, and  $\tau$  as the transit time.

The capacitance and delay for each level in Figs. 9a and 9b are tabulated below, assuming an initial down transition at node 1.

9a		
Node	Capacitance	Delay
1	$5c_g + c_p$	$\tau(5c_g + c_p)/c_g$
2	$4c_g + c_p$	$k\tau(4c_g + c_p)/c_g$
3	$c_g + 4c_p$	$\tau(c_g + 4c_p)/c_g$
4	$c_g + 8c_p$	$k\tau(c_g + 8c_p)/c_g$

Total delay assuming an initial down transition at node 1 is:

$$\tau(6c_g + 5c_p)/c_g + k\tau(5c_g + 9c_p)/c_g$$

Similarly, the delay assuming an initial up transition at node 1 is:

$$k\tau(6c_g + 5c_p)/c_g + \tau(5c_g + 9c_p)/c_g$$

9b		
Node	Capacitance	Delay
1	$2c_g + c_p$	$\tau(2c_g + c_p)/c_g$
2	$c_g + c_p$	$k\tau(c_g + c_p)/c_g$
3	$c_g + 2c_p$	$\tau(c_g + 2c_p)/c_g$
4	$2c_g + 2c_p$	$2k\tau(c_g + c_p)/c_g$
5	$c_g + c_p$	$\tau(c_g + c_p)/c_g$
6	$c_g + 2c_p$	$k\tau(c_g + 2c_p)/c_g$
7	$c_g + 2c_p$	$\tau(c_g + 2c_p)/c_g$

Total delay assuming an initial down transition at node 1 is:

$$\tau(5c_g + 6c_p)/c_g + k\tau(4c_g + 5c_p)/c_g$$

The corresponding delay for an initial up transition at node 1 is:

$$k\tau(5c_g + 6c_p)/c_g + \tau(4c_g + 5c_p)/c_g$$

Assume  $c_p$  is on the order of  $c_g$  and that a typical value for  $k$  is 4. Then an examination of both sets of delays for both circuits reveals that Fig. 9a is always slower than Fig. 9b.

This is a very crude analysis intended only to show that the optimum choice of organizations based on delay is not always obvious. A rigorous analysis using actual layout parameters is the only way to accurately predict actual circuit delays. Performing such an analysis for several potential structures is only practical if an automated design system is available.

Another important factor to be considered when selecting the best architecture is topology. For example, the structure resulting from Fig. 9a will tend to have longer columns than Fig. 9b to accommodate the larger gates. However, Fig. 9b will tend to have longer implicant rows than Fig. 9a to accommodate more terms. A designer must decide which architecture best fits into the available area. As is the case for analyzing the timing of candidate architectures, determining dimensions of several structures is greatly facilitated by an automated design system.

## **VI. Comments Regarding an Automated Design System**

*It is possible to design an automated system for mapping functions into a GLS. This system is probably best implemented on an interactive color graphics system. In this system, a user could specify the function to be mapped, design guidelines, and analysis to be performed. By viewing the GLS created by the computer, or the results of an analysis, the user*

could suggest other mapping approaches or request changes be made.

The program might work by initially creating a copy of a clean GLS in memory. Cuts and contact points would be overlaid on this copy. An algorithm similar to printed circuit layout algorithms would be invoked to do the mapping iterations. The program would stop either when a desired set of requirements has been met or when no solution has been found after a time limit has been exceeded.

## **References**

1. Patil, S. S., and Williams, T., "An Approach to Using VLSI in Digital Systems," 5th Symp. Comp. Arch., 1978, pp. 139-143.
2. Eichelberger, E. B., and Williams, T. W., "A Logic Design Structure for LSI Testability," Proc. 14th Design Automation Conf., June 1977, pp. 462-467.

## **Bibliography**

Mead, C., and Conway, L., *Introduction to VLSI Systems* (text in preparation), 1978.

Sievers, M. W., "A General Logic Structure for Custom LSI," Jet Propulsion Laboratory IOM 331-78-109a, Oct. 5, 1978 (an internal document).

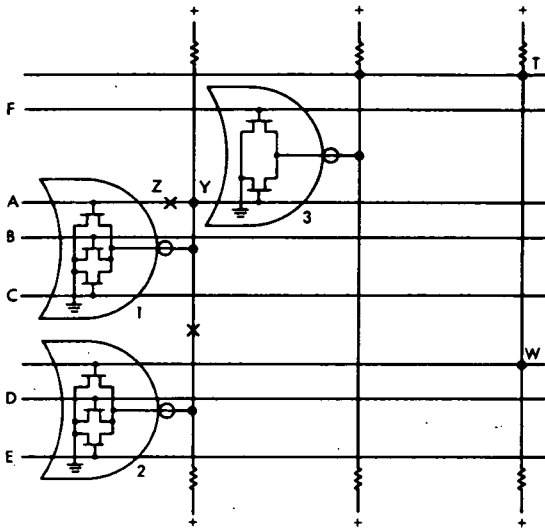


Fig. 1. Approximate logical equivalent of a GLS

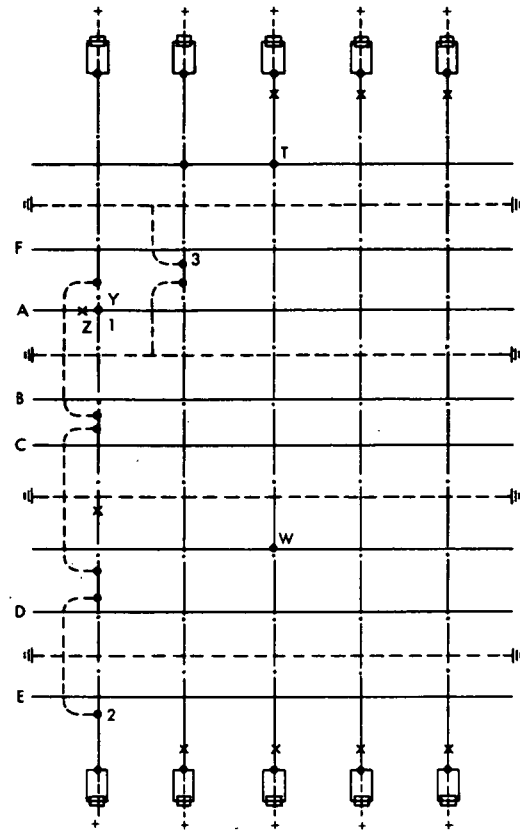


Fig. 3. NMOS stick diagram of GLS example

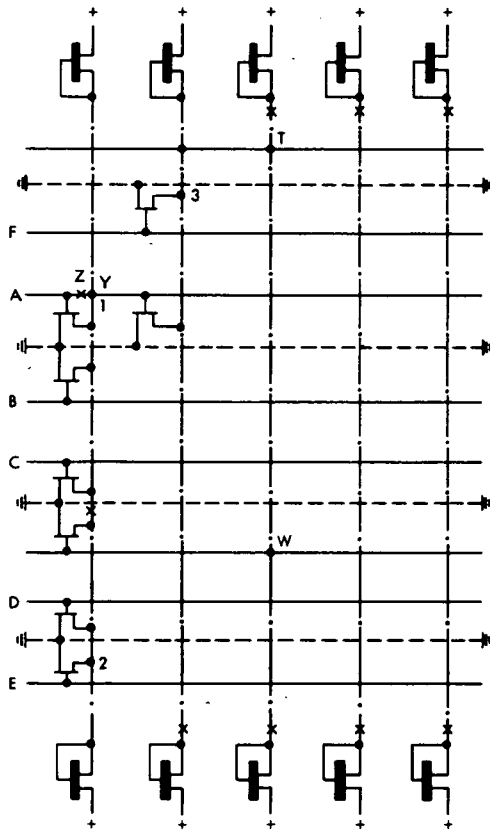


Fig. 2. Transistor level description of GLS example

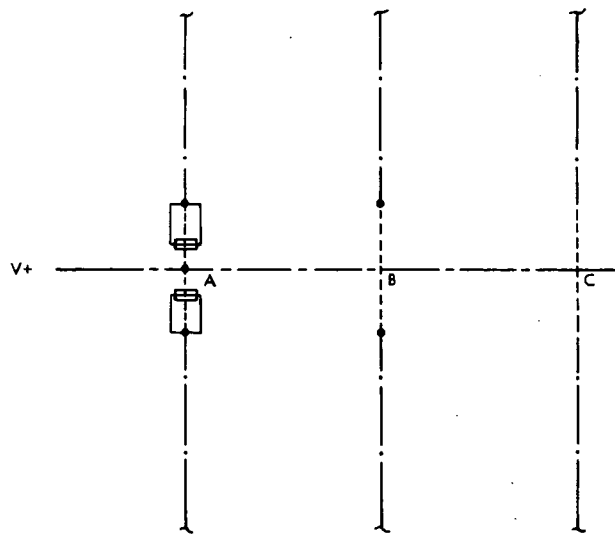


Fig. 4. Method for increasing number of pull-up resistors in column

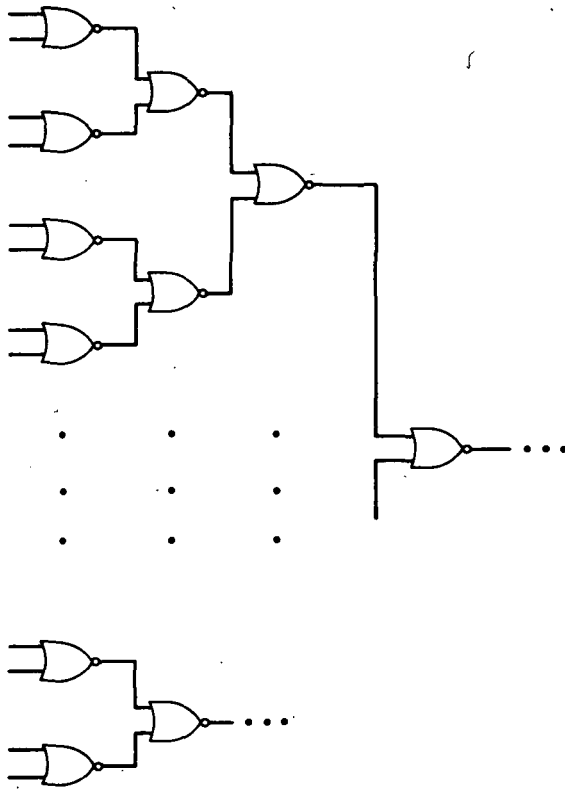


Fig. 5. Binary NOR tree

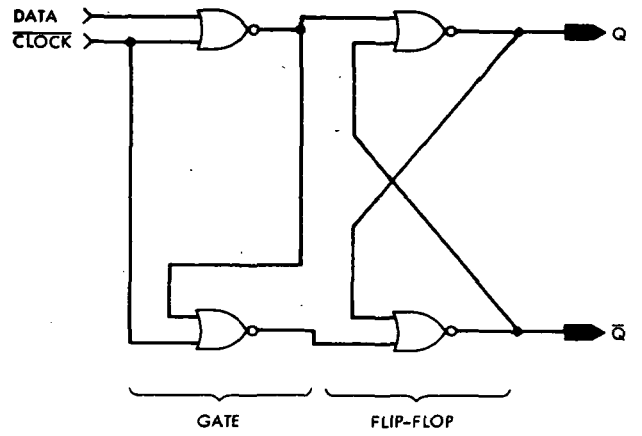


Fig. 6a. Logical equivalent of D flip-flop

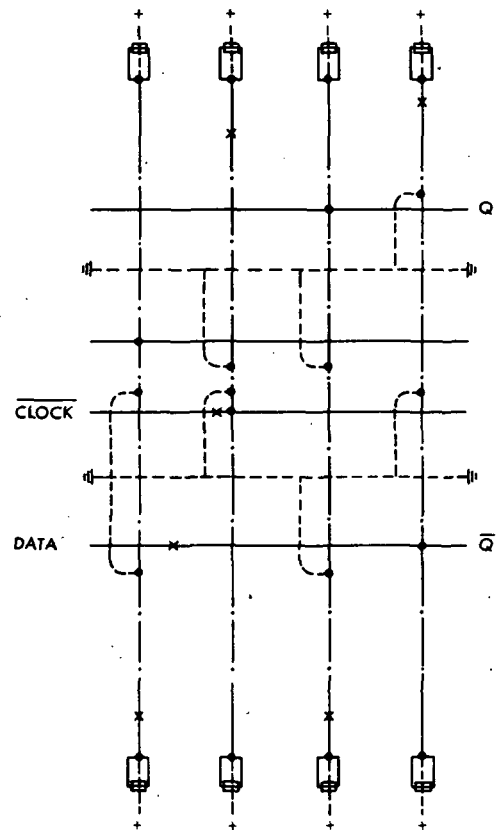


Fig. 6b. NMOS stick diagram of D flip-flop

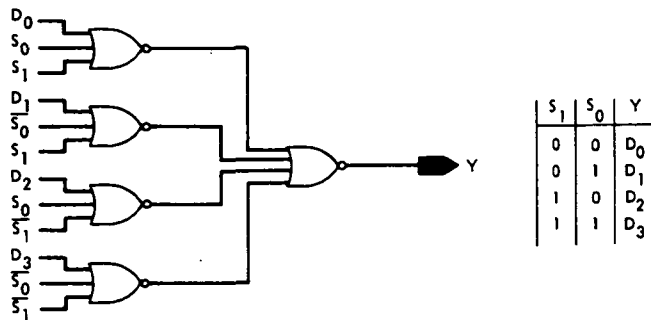


Fig. 7. Multiplexer implemented in NOR gates

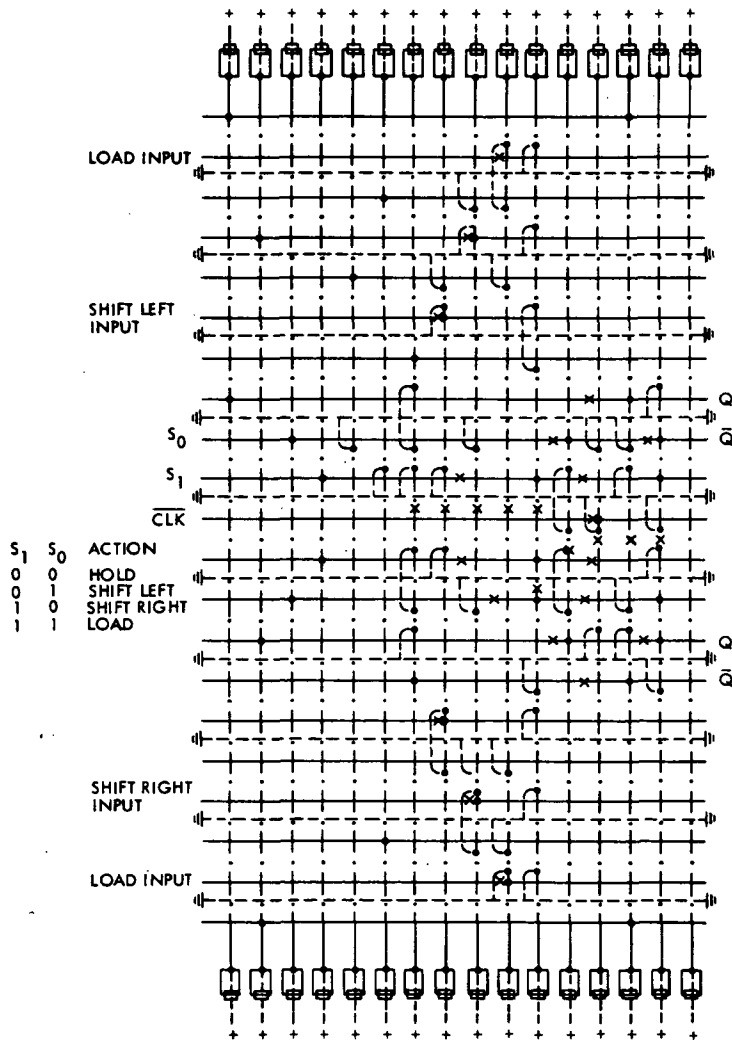


Fig. 8. Two cell shift register

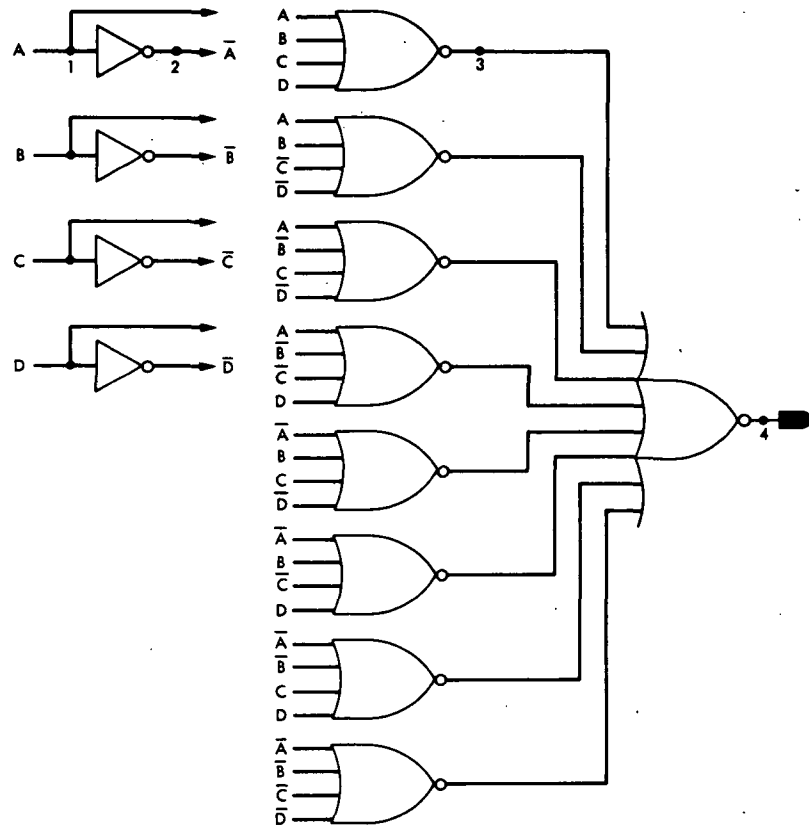


Fig. 9a. Two-level parity generator

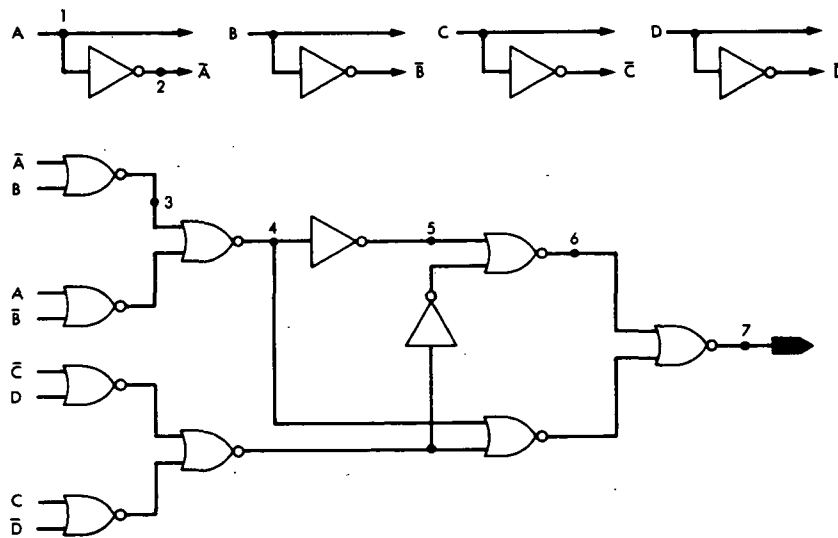


Fig. 9b. Parity generator tree

# An Efficient Soft Decision Decoding Algorithm for Block Codes

H. J. Greenberger

Communications Systems Research Section

*Nonoptimum decoding algorithms, which select a small set of candidate code words to be correlated with the received vector, can approach the performance of maximum likelihood decoders even at low signal-to-noise ratios. A decoding scheme based upon the best features of previously known algorithms of this type has been developed that can decode codes which have better performance than those in use today and yet not require an unreasonable amount of computation.*

## I. Introduction

An optimum decoder, for block codes transmitted over a memoryless channel, calculates the distance between the received vector and all possible code words and selects as the best estimate of the transmitted code word that one which is closest to it. Because of the amount of computation required, it is unreasonable to decode directly in this way all but the smallest codes, whose error correcting power is relatively weak. Many schemes have been suggested which reduce the computational complexity while maintaining the desired performance. The best of these algorithms are those which select a small subset of all possible code words, among which the best estimate of the full decoding algorithm has a high probability of being found. The selection of this subset uses the information provided by sorting the symbols of the received vector according to absolute magnitude so as to arrange them in order of their estimated probability of being correct. The algorithms of this class utilize this information and

the constraints of the parity check equations in different ways to generate the set of candidate code words.

One of the first algorithms of this kind was developed by D. Chase (Ref. 1). He suggested perturbing the hardlimited code word  $Y$  by adding to it, modulo 2, a test pattern  $T$  to obtain a new sequence  $Y'$ . This new sequence is decoded algebraically to find the unique code word (if one exists) within half the minimum distance of the code. The nonzero bits of the test patterns are selected by a combinatorial construction on the least reliable bits of the received vector (Ref. 2).

L. Baumert, R. McEliece and G. Solomon (Refs. 3 and 4) have done much work using sets of erasure patterns. In their technique, a set of bits equal to the number of redundant bits in the code is erased. A candidate code word is then generated by reconstructing these bits from the unerased ones. Each erasure pattern generates another candidate to be correlated

with the received vector. The reasoning behind using erasure patterns rather than error patterns is that the redundancy of binary codes is much greater than its error correcting power. On the other hand, to correctly decode a received word, this scheme must cover all hard decision errors. (Using Chase's algorithm, a number of errors, up to the correcting power of the code, may remain exposed.)

These algorithms can be combined into a hybrid scheme which uses a small number of erasure masks, a few bits of redundancy and consideration of error patterns of weight two or less. Such an algorithm is computationally more efficient than any one of its ancestors and is a possible competitor, in terms of complexity vs performance, to Viterbi decoding of convolutional codes (Ref. 5).

## II. An Efficient Hybrid Algorithm

This algorithm reduces the computational complexity by combining the best features of those mentioned in the previous section. Using the number of candidate code words required to achieve a given performance as a measure of efficiency, McEliece and Baumert's algorithm is the best. However, the amount of computation required to generate these candidates is much greater than for the other schemes. For each erasure mask the erased bits must be solved for in terms of the unerased ones. To reduce the number of times this computation must be done, errors of low weight are allowed in the unerased bits and redundancy is used to reduce the number of error patterns that need to be checked. A flow chart of the major sections of the algorithm is shown in Fig. 1.

The first step of the algorithm is to sort the symbols of the received code word according to their absolute magnitude, permute the columns of the parity check matrix and reduce it to standard form. Each erasure mask erases fewer bits than the number of parity check equations so not all of the unerased bits are independent. This dependency can be taken advantage of in order to determine which error patterns in the unerased bits are consistent with the parity equations, and only those patterns need be used to generate candidate code words. The number of such error patterns can be a small fraction of the total number of error patterns, greatly reducing the number of candidates required for a given level of performance.

Calculating the error patterns which will be consistent with the parity check equations can best be done by considering a portion of the syndrome and determining the error patterns, which when added to the initial estimate of the received vector will make that portion equal to zero. Since

a code word must satisfy  $[H]c = 0$ , it will also satisfy this equation for any subset of rows of  $[H]$ . Reducing the parity check matrix and partitioning  $[H]$  as:

$$\begin{bmatrix} P_1 & 0 \\ P_2 & 1 \end{bmatrix} \begin{bmatrix} c_1 \\ c_2 \end{bmatrix} = 0$$

$r$ -bits                       $(n-r)$  bits

it is seen that  $[P_1] c_1 = 0$ . Therefore, the first  $r$  bits of the code word must also be the solution of a set of homogeneous equations.

For an arbitrary received vector  $a$ , the product  $[H] a = s$  is called the syndrome and specifies the coset containing the possible error patterns in  $a$ . The same notion can be used when considering only the first  $r$  bits of the received word. Then  $[P_1] a_1 = s_1$ , where  $s_1$  is the partial syndrome which specifies the possible error patterns in  $a_1$ . Representing  $a_1$ , by  $c_1 + e_1$ , where  $e_1$ , is the partial error pattern corresponding to the partial code word  $c_1$

$$[P_1] [c_1 + e_1] = s_1$$

or

$$[P_1] e_1 = S_1$$

Given  $[P_1]$  and  $s_1$ , there are a large number of partial error patterns  $e_1$  that will satisfy this equation. However, for the decoding algorithm to be considered here, it is sufficient to consider patterns of 0, 1 or 2 errors. Note that even though the adjective "partial" is applied to  $a_1$ ,  $c_1$  and  $s_1$ , the remainder of the code word is completely determined from  $c_1$  by  $c_2 = [P_2] c_1$ . The advantage of this approach is that candidate code words are determined only by possible error patterns in the most reliable received bits  $a_1$ . The remaining received bits  $a_2$  do not enter at all into the calculation and can be considered erasures.

No errors as a possible error pattern can only occur if the partial syndrome equals zero; single errors can occur in those bits whose corresponding columns of  $[P_1]$  sum to  $s_1$ . In general, for an error pattern of weight  $w$  to be a possibility, the sum of the  $w$  corresponding columns of  $[P_1]$  must equal  $s_1$ .

Efficient algorithms have been developed for all the steps of Fig. 1 and are described in detail in Ref. 6. As an example consider the rate 1/2, (128,64) BCH code of minimum distance 22. This code's maximum likelihood coding gain, at a

bit probability of error of  $10^{-3}$ , is 1 dB better than the constraint length 7, rate 1/2 convolutional code which is in wide use today. The parameters for decoding this code using the algorithm developed here are:

- (1) Redundancy: 6 bits.
- (2) Number of masks: 20.

- (3) Mask weighing: see Fig. 2 (30 least reliable bits always erased).
- (4) Average Hamming distance between masks: 16.
- (5) All possible error patterns of weight 2 or less in un-erased bits checked.

The performance, using these parameters, is given in Fig. 3.

## References

1. Chase, D., "A Class of Algorithms for Decoding Block Codes with Channel Measurement Information," *IEEE Trans. Inform. Theory*, Vol. IT-18, Jan. 1972, pp. 170-182.
2. Chase, D., and Goldfein, H. D., "Long Block Codes Can Offer Good Performance," Information Theory International Symposium, Cornell, N.Y., Oct. 1977.
3. Baumert, L., McEliece, R., and Solomon, G., "Decoding With Multipliers," in *The DSN Progress Report 42-34*, Jet Propulsion Laboratory, Pasadena, Calif., May-June 1976, pp. 43-46.
4. Baumert, L., and McEliece, R., "Soft Decision Decoding of Block Codes," *The DSN Progress Report 42-47*, Jet Propulsion Laboratory, Pasadena, Calif., July-August 1978, pp. 60-64.
5. Forney, G. D., Jr., "The Viterbi Algorithm" *Proc. IEEE*, Vol. 61, Mar. 1973, pp. 268-276.
6. Greenberger, H., Ph.D. Thesis, University of Southern California, 1978.

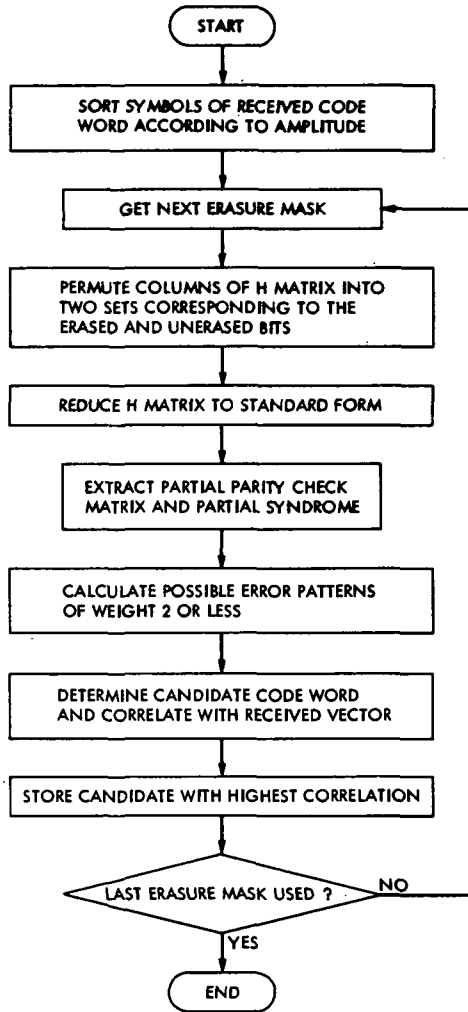


Fig. 1. Flow chart of soft decision decoding algorithm

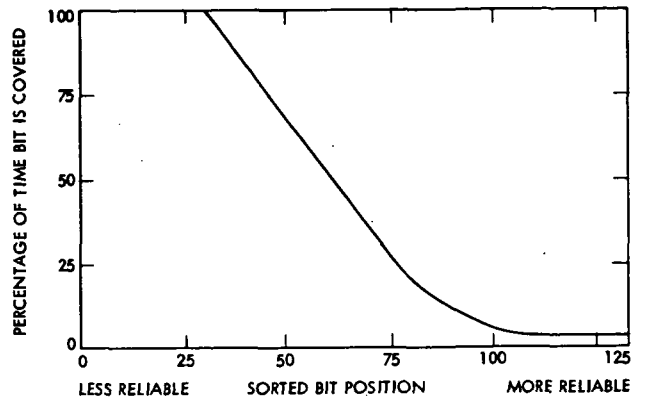


Fig. 2. Mask weighing function

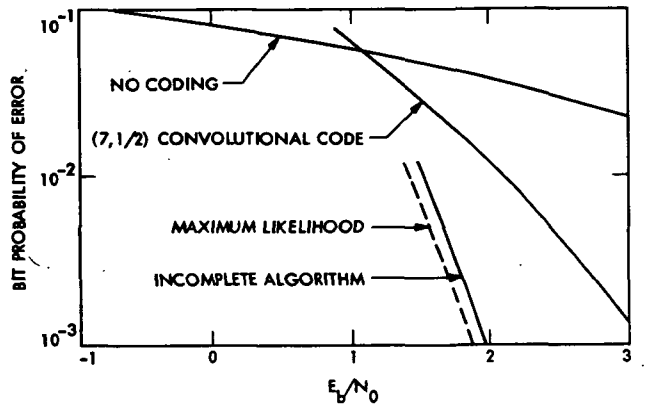


Fig. 3. Performance of the (128,64) BCH code

# Precise Extraction of Geometrical Dependence from Solar Wind Columnar Turbulence Measurements

A. L. Berman  
TDA Engineering Office

*Experimental solar wind columnar turbulence measurements have frequently been modelled as a function of a single geometrical parameter. Since columnar turbulence results from the signal path integration of an appropriate source function, hypothesized columnar turbulence models must be cast as a function of two independent geometrical parameters. This article quantifies the distortion which results from the attempt to extract and model the functional dependence of experimental columnar turbulence measurements via usage of a single geometrical parameter.*

*In the case of Doppler phase fluctuation data ( $\phi$ ), the net effect of usage of a single geometrical parameter is to translate the more accurate two parameter formulation:*

$$\phi(a, \beta) \cong K\beta a^{-1.3}$$

where:

$a$  = signal closest approach distance

$\beta$  = Earth-Sun-probe angle

to a less accurate one parameter expression of the form:

$$\phi(a) \approx Ka^{-1.5}$$

## I. Introduction

Precise determination of the functional (geometrical) dependence of solar wind columnar turbulence from experimental measurements is required by solar wind investigators for the validation of theoretical derivations. Directly, experimental turbulence measurements can be used to confirm the (hypo-

thesized) process by which such turbulence is generated; subsequently, by inverting this process, the measurements can be made to yield valuable information about the geometrical dependence of the most basic solar wind parameters, such as electron density and solar wind velocity. In the early days of solar wind research, it was understandable that solar wind turbulence would be measured solely as a function of the

dominant geometrical parameter — elongation angle (or, equivalently, Sun-Earth-probe angle or signal path closest approach distance). However, some recent work as well (Woo, Ref. 1; Callahan, Ref. 2) has continued to rely on a single (geometrical) parameter in the extraction of the geometrical dependence of solar wind columnar turbulence. Given today's more sophisticated measurement environment, more exact functional dependence determinations are highly desirable.

Ultimately, all measurements of columnar turbulence must be modelled as or mapped back to the signal path integration of some (possibly complex) solar wind parameter. There is as yet no consensus on the proper theoretical treatment which identifies such a parameter. However, excellent results have been obtained by empirically modelling columnar turbulence as the signal path integration of electron density (Berman, et al. Ref. 3). It has been shown (Berman, et al. Ref. 4) that the signal path integration of a power-law electron density model can be accurately described in closed form in terms of two geometrical parameters — Sun-Earth-probe angle  $\alpha$  and Earth-Sun-probe angle  $\beta$ . Significant "distortions" occur if one attempts to determine (power law) radial dependence of solar wind turbulence via usage of only one geometrical parameter, rather than the two that are required for a complete geometrical description. Such distortions mask the process whereby solar wind turbulence is generated, and can lead to erroneous inferences in regard to the functional dependence of the basic solar wind parameters (e.g., density and velocity).

This article will attempt to quantify the distortions induced via usage of an incomplete geometrical description. Included in the discussion are the cases of both close (spacecraft) and distant (natural) signal sources.

## II. Close Signal Sources

There is now considerable evidence that all measurements of columnar turbulence<sup>1</sup> strongly correlate with signal path integrated or in situ electron density; interplanetary scintillation examples are Erskine, et al. (Ref. 5), Chang (Ref. 6), and Houminer, et al. (Ref. 7); phase fluctuation examples are Berman, et al. (Ref. 3) and Berman (Refs. 8, 9, and 10); spectral broadening, Rockwell (Ref. 11). Since the indications for integrated electron density correlation are so obvious, the discussion here will be structured within such a framework. Were it to turn out, however, that columnar turbulence is really better represented by the signal path integration of a complex parameter related to but not identical to electron

<sup>1</sup>With the exception of angular broadening, which is not considered here due to an insufficiency of consistent data, and Faraday rotation, which measures the signal path integration of the product of electron density and the magnetic field.

density, the argument for a complete geometrical description would continue with equal validity.

A simple example serves to motivate an appreciation of the problem, when the (spacecraft) source is near the closest approach point (the "near-source" limit). At (different) times during 1975-1976 the Sun-Earth-probe angle  $\alpha$  and Earth-Sun-probe angle  $\beta$  for several spacecraft were as follows:

Spacecraft	$\alpha$ , deg	$\beta$ , deg
Helios 1	17.5	90
Viking	17.5	152
Pioneer 10	17.5	160

As is schematically illustrated in Fig. 1, all three spacecraft are at the identical Sun-Earth-probe angle of 17.5 deg (or signal closest approach distance of 65 solar radii), so that *all else being equal*, an experimenter relying solely on signal closest approach distance  $a$  might expect all (signals) to display a similar level of turbulence. However, since integrated density (as will be shown) scales with  $\beta$ , there will be a systematic difference of approximately 80% in the turbulence levels between the two extremes (the Helios 1 and Pioneer 10 cases). It is thus of interest to quantify in some manner the distortion induced via reliance on a single geometrical parameter.

In Ref. 12, Berman et al., have found a very large volume of Viking two-way S-band Doppler phase fluctuation data ( $\phi$ ) to be consistent with the signal path integration of  $Kr^{-2.30}$  for  $r \geq 5r_o$ , where  $r$  = radial distance and  $r_o$  = solar radius. This results in the following approximate expression (Ref. 4):

$$\phi(\alpha, \beta) \cong K\beta(\sin \alpha)^{-1.3} F(\alpha, \beta)$$

where:

$\phi$  = Doppler phase fluctuation

$K$  = constant

$\beta$  = Earth-Sun-probe angle

$\alpha$  = Sun-Earth-probe angle

$$F(\alpha, \beta) = 1 - 0.05 \left\{ \frac{\left( \beta - \frac{\pi}{2} + \alpha \right)^3 - \left( \alpha - \frac{\pi}{2} \right)^3}{\beta} \right\} - 0.00275 \left\{ \frac{\left( \beta - \frac{\pi}{2} + \alpha \right)^5 - \left( \alpha - \frac{\pi}{2} \right)^5}{\beta} \right\}$$

Since  $F(\alpha, \beta)$  is only a weak function of  $\alpha$  and  $\beta$ , one further approximates the above as:

$$\phi(\alpha, \beta) \cong K\beta\alpha^{-1.3}$$

where the (equivalent) signal closest approach distance  $a$  has been substituted for  $\sin \alpha$ . The important point of the above expression is that even starting with a power-law source function (in this case, density), the resulting integrated columnar turbulence departs significantly from power-law (with  $a$ ). An extreme example of the effect of changing  $\beta$  on turbulence which is modelled only as a function of  $a$  is the Helios data at approximately  $65 r_o$  as seen in Fig. 2. The large, nearly vertical, fall-off of the data at  $65 r_o$  is due to the rapid change in  $\beta$  as Helios 1 underwent perihelion, and not to any significant variation with  $a$ .

To be able to roughly compare results obtained through use of a single geometric parameter to those based on a complete (two-parameter) geometrical description, an approximate "total" radial dependence will be constructed by rewriting:

$$\phi(a, \beta) \cong K\beta a^{-1.3}$$

as:

$$\phi(a, \beta) \cong Ka^{-1.3 + \ln \beta / \ln a}$$

or

$$\phi(a) \approx Ka^{-1.3 + \ln(\beta_1/\beta_2) / \ln(a_1/a_2)}$$

where the subscripts 1 and 2 define the applicable (radial) span of data. Since the relationship between  $\beta$  and  $a$  is definitely *not* power law, consideration of the "total" (power law) radial dependence permits only a rough idea as to the expected distortion to be encountered in relying on a single geometric parameter.

Table 1 presents examples of the expected total radial dependence from the signal path integration of a  $Kr^{-2.30}$  electron density source, for actual spacecraft geometries during 1975-1976. From Table 1, it is apparent that one might expect to find a "total" radial dependence of:

$$\phi(a) \approx a^{-1.5}$$

from a typical set of such data.

### III. Distant Signal Sources

Distant signal sources require the same two-parameter geometrical description as do close signal sources. In this case though, it is Earth which approaches the signal closest approach point ("near-Earth" limit), rather than the source, as

discussed in section II. In either case, however, the effect is always most pronounced in the region where  $\beta \sim 90$  deg. The geometry for typical distant sources is schematically illustrated in Fig. 3. For the (extreme) range of geometry illustrated in Fig. 3, the expected approximate contribution ( $\Delta$ ) to the total power law radial dependence would be:

$$\begin{aligned} \Delta &\approx \frac{\ln\left(\frac{\beta_1}{\beta_2}\right)}{\ln\left(\frac{a_1}{a_2}\right)} \\ &= \frac{\ln\left(\frac{90}{153}\right)}{\ln\left(\frac{215}{96}\right)} \\ &= -0.7 \end{aligned}$$

so that one would expect the data to display a total radial dependence of  $\approx a^{-2.0}$ , under the assumption of a signal path integration of a  $Kr^{-2.3}$  source function. Possible interplanetary scintillation examples of this expected exaggerated steepening of the total radial dependence as  $\beta$  approaches  $90^\circ$  are the 81.5 MHz data of Fig. 3 in Rickett (Ref. 13), and the 73.8 MHz data of Fig. 1 in Coles, et al., (Ref. 14). The 81.5 MHz data from Rickett extend over the region  $117 r_o < a < 215 r_o$  and do in fact display a total radial dependence of  $\approx a^{-2.0}$ , according to the published fit line in Ref. 13.

For natural sources (interplanetary scintillation) only the "near-Earth" limit is a geometrical consideration, whereas in the case of man-made (spacecraft) sources, the geometry will be a combination of the "near-Earth" and "near-source" effects.

### IV. Application of the Total Radial Dependence Concept

To further explore the concept of "total" radial dependence, one can utilize the Doppler phase fluctuation (Doppler scintillation) data in Woo (Ref. 1). These data are for all intents and purposes the same as data published earlier in Berman, et al. (Ref. 4). Since Berman found these data compatible with the signal path integration of a  $Kr^{-2.3}$  source, one would expect Ref. 1 to find a total radial dependence of approximately  $a^{-1.5}$ . In Fig. 11 of Ref. 1 (reproduced here as Fig. 2), the data are shown with a fit line of  $a^{-1.45}$ , in reasonable accordance with expectations; however, the line is mislabeled as  $a^{-1.3}$ . Subsequently, Woo has republished (Ref. 15)

these data with a new, correct  $a^{-1.3}$  fit line (also reproduced here in Fig. 2). Visual inspection of the two fits seen in Fig. 2 clearly favors the original (mislabelled)  $a^{-1.45}$  fit.

## V. Discussion and Summary

Solar wind columnar turbulence results from the signal path integration of an appropriate solar wind parameter, and hence two independent geometrical parameters are required to provide a complete and accurate functional description. The two most appropriate geometrical parameters are the Sun-Earth-probe angle and Earth-Sun-probe angle. Attempts to model experimental measurements of solar wind columnar turbulence as a function of only a single geometrical parameter (e.g., Sun-Earth-probe angle, the dominant parameter) are inherently less accurate than using a complete geometrical description, and serve to mask the proper experimental relationship between columnar turbulence and the signal path integration of an appropriate source function.

Because of the preponderance of evidence linking columnar turbulence with the signal path integration of a power-law electron density model, this article has undertaken to quantify the distortion resulting from reliance on a single geometrical parameter, and to establish an approximate relationship between "total" radial dependence and the signal path integration of a power law source function. The net effect of reliance on a single geometric parameter is to (very approximately) translate the correct two parameter formulation:

$$\phi(a,\beta) \cong K \beta a^{-1.3} F(a,\beta)$$

into a considerably less accurate expression of the form:

$$\phi(a) \approx K a^{-1.5}$$

For future experimental measurement and modelling of solar wind columnar turbulence, usage of a two geometrical parameter model based on the signal path integration of a power law source function is clearly indicated.

## References

1. Woo, R., "Radial Dependence of Solar Wind Properties Deduced from Helios 1/2 and Pioneer 10/11 Radio Scattering Observations," in *The Astrophysical Journal* 219, January 15, 1978.
2. Callahan, P. S., "An Analysis of Viking S-X Doppler Measurements of Solar Wind Columnar Content Measurements," in *The Deep Space Network Progress Report 42-44*, Jet Propulsion Laboratory, Pasadena, California, 15 April 1978.
3. Berman, A. L., Wackley, J. A., and Hietzke, W. H., "The First Direct Comparison of Doppler Phase Fluctuation to Integrated Electron Density Over an Extensive Span of Signal Closest Approach Distance - A Brief Report," IOM ALB-78-35, March 10, 1978 (a JPL internal document).
4. Berman, A. L., and Wackley, J. A., "Doppler Noise Considered as a Function of the Signal Path Integration of Electron Density," in *The Deep Space Network Progress Report 42-33*, Jet Propulsion Laboratory, Pasadena, California, 15 June 1976.
5. Erskine, F. T., Cronyn, W. M., Shawhan, S. D., Roelof, E. C., and Gotwols, B. L., "Interplanetary Scintillation at Large Elongation Angles: Response to Solar Wind Density Structure," in *The Journal of Geophysical Research*, Volume 83, Number A9, September 1, 1978.
6. Chang, H., *Analysis of Dual-Frequency Observations of Interplanetary Scintillations Taken by the Pioneer 9 Spacecraft*, Doctoral Dissertation, Department of Electrical Engineering, Stanford University, May 1976.

7. Houminer, Z., and Hewish, A., "Correlation of Interplanetary Scintillation and Spacecraft Plasma Density Measurements," in *Planetary and Space Science*, Volume 22, Number 6, June 1974.
8. Berman, A. L., "Electron Density in the Extended Corona: Two Views," in *The Deep Space Network Progress Report 42-41*, Jet Propulsion Laboratory, Pasadena, California, 15 October 1977.
9. Berman, A. L., "Electron Density and Doppler RMS Phase Fluctuation in the Inner Corona," in *The Deep Space Network Progress Report 42-44*, Jet Propulsion Laboratory, Pasadena, California, 15 April 1978.
10. Berman, A. L., "Solar Wind Turbulence Models Evaluated via Observations of Doppler RMS Phase Fluctuation and Spectral Broadening in the Inner Corona," in *The Deep Space Network Progress Report 42-44*, Jet Propulsion Laboratory, Pasadena, California, 15 April 1978.
11. Rockwell, S. T., "An Empirical Spectral Bandwidth Model for Superior Conjunction," in *The Deep Space Network Progress Report 42-43*, Jet Propulsion Laboratory, Pasadena, California, 15 February 1978.
12. Berman, A. L., Wackley, J. A., Rockwell, S. T., and Kwan, M., "Viking Doppler Noise Used to Determine the Radial Dependence of Electron Density in the Extended Corona," in *The Deep Space Network Progress Report 42-38*, Jet Propulsion Laboratory, Pasadena, California, 15 April 1977.
13. Rickett, B. J., "Power Spectrum of Density Irregularities in the Solar Wind Plasma," in *The Journal of Geophysical Research*, Volume 78, Number 10, April 1, 1973.
14. Coles, W. A., Rickett, B. J., and Rumsey, V. H., "Interplanetary Scintillations," in *Solar Wind Three*, edited by Russell, C. T., published by the Institute of Geophysics and Planetary Physics, University of California, Los Angeles, California, July 1974.
15. Woo, R. "Errata," in *The Astrophysical Journal* 223, July 15, 1978.

**Table 1. Relationship of signal path integrated density model of radial (power law) index  $-(2 + \xi)$  to total (power law) radial dependence**

Spacecraft	Year	Data span of $(a/r_0)$	Data span of $\beta$ , deg	$\xi$	$\frac{\partial n(\beta_1/\beta_2)}{\partial n(a_1/a_2)}$	"Total" radial dependence
Pioneer 10	1975	17-170	174.8-121.4	0.3	-0.16	-1.46
Pioneer 11	1975	17-170	174.5-116.6	0.3	-0.18	-1.48
Helios 1	1975	12-60	171.5-102.7	0.3	-0.32	-1.62
Viking	1976	17-170	172.5-98.9	0.3	-0.24	-1.54
Average					-0.22	-1.52

$\alpha$  = CLOSEST APPROACH DISTANCE  
 $\alpha$  = SUN-EARTH-PROBE ANGLE  
 $\beta$  = EARTH-SUN-PROBE ANGLE

INTEGRATED DENSITY  
SCALES WITH  $\beta$

ALL SPACECRAFT AT SAME (SIGNAL) CLOSEST APPROACH DISTANCE:

SPACECRAFT	$\alpha$	$\beta$	RELATIVE INTEGRATED DENSITY
HELIOS 1	$17.5^\circ$	$90^\circ$	0.50
VIKING	$17.5^\circ$	$152^\circ$	0.84
PIONEER 10	$17.5^\circ$	$160^\circ$	0.89

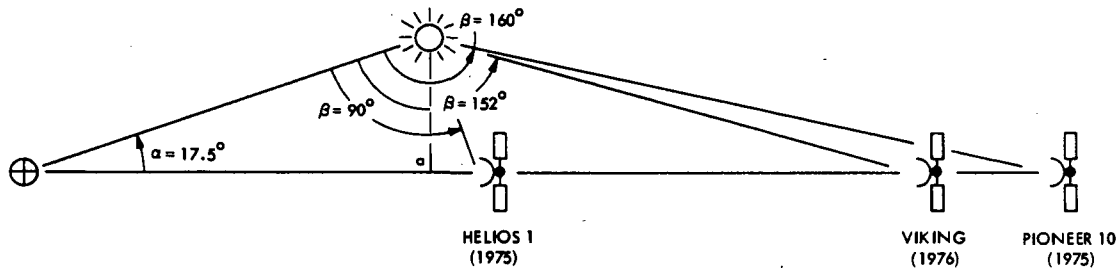


Fig. 1. Integrated density reduction for spacecraft due to "near-source" limit

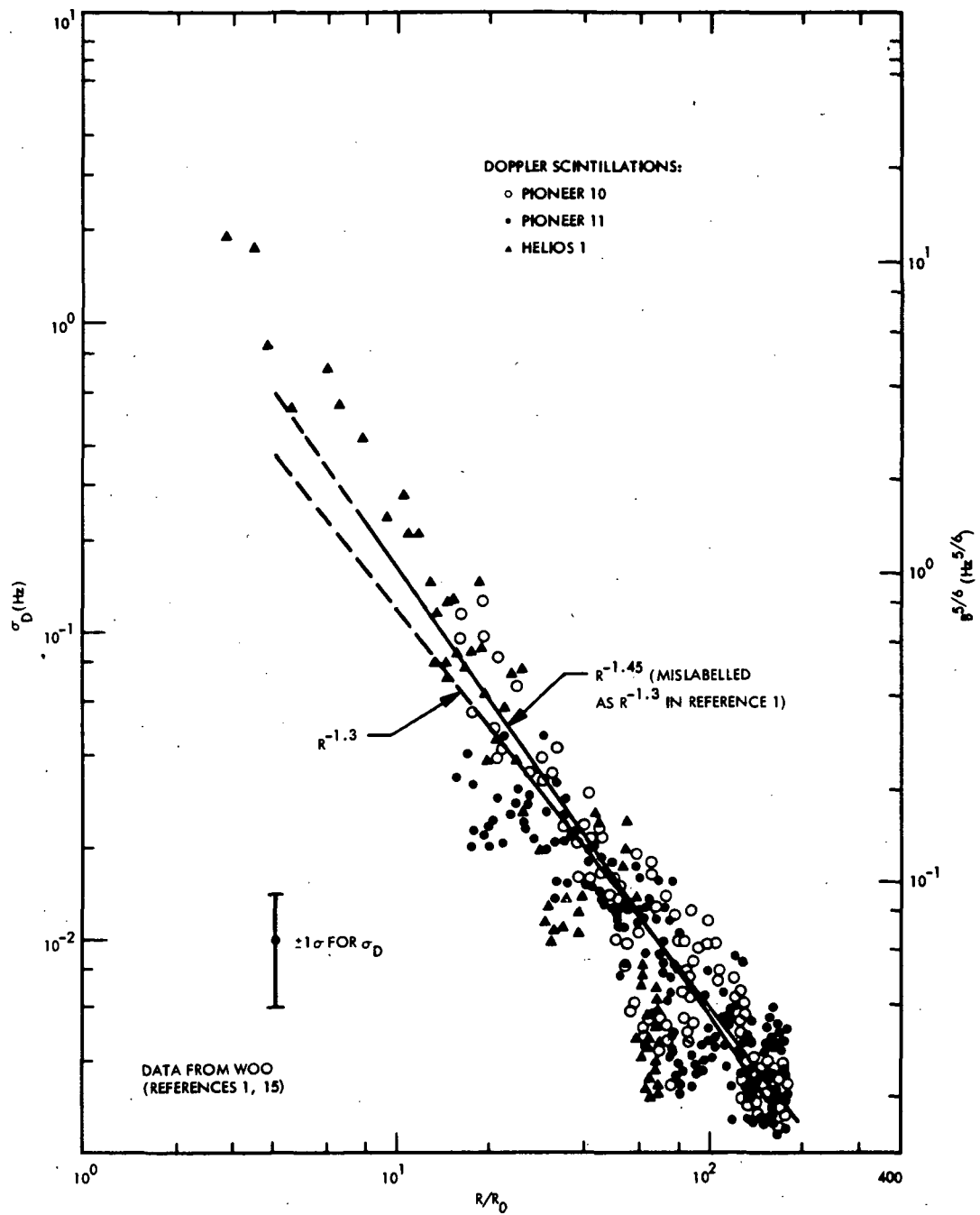
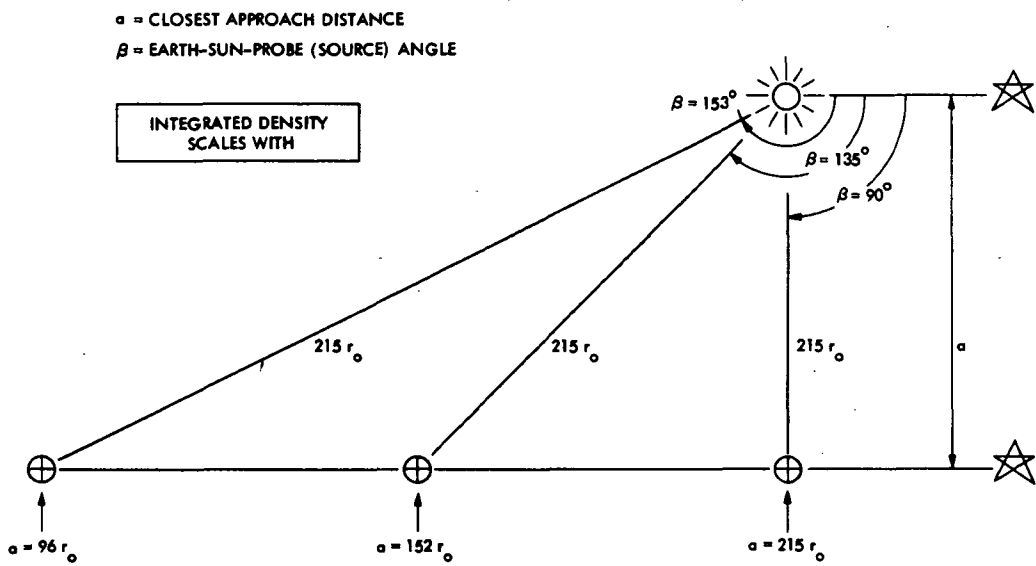


Fig. 2. Doppler phase fluctuation versus radial distance



**Fig. 3. Integrated density reduction for distant spacecraft and natural sources due to "near Earth" limit**

## A Reexamination of the Radial Dependence of Weak Interplanetary Scintillation

A. L. Berman  
TDA Engineering Office

*Recent investigations of weak interplanetary scintillation have found strong correlation between the scintillation index  $m$  and both in-situ and integrated electron density. A similar measure of solar wind columnar turbulence, doppler phase fluctuation, has been shown to be in excellent correspondence with the signal path integration of a specific, well-established mean electron density model -  $N_e(r) \cong Kr^{-2.3}$ , where  $N_e$  = electron density,  $K$  = constant and  $r$  = radial distance. It is thus natural to heuristically inquire whether  $m$  might not also correlate with the signal path integration of such an electron density model.*

*This article reexamines the power law radial dependence of  $m$  for weak interplanetary scintillation data published by various investigators during the last decade. The data are found to be consistent with the signal path integration of a power law electron density model of the form:*

$$N_e(r) \cong Kr^{-(2+\xi)}; 0.3 \leq \xi \leq 0.4$$

### I. Introduction

Recently Erskine et al. (Ref. 1) have determined strong correlation between interplanetary scintillation (the scintillation index  $m$ ) and near-earth, in-situ, solar wind electron density measurements. These findings confirm results obtained earlier by Chang (Ref. 2), wherein a linear relationship between integrated electron density and coherent signal intensity scintillation was determined via concurrent measurements of both using the Pioneer 9 spacecraft. Findings similar to Erskine were obtained for interplanetary scintillation by Houminer, et al. (Ref. 3).

The radial dependence of electron density in the extended corona (here defined to be  $r \geq 5r_0$ , where  $r$  = radial distance and  $r_0$  = solar radius) has been reviewed by Berman (Ref. 4), and is found by a variety of techniques to be well represented in the mean by the power law model  $Kr^{-2.3}$ . In addition, Berman (Ref. 5) and Berman, et al. (Refs. 6 and 7) have found excellent agreement between extended corona doppler phase fluctuation data obtained from the Helios, Pioneer, and Viking spacecraft and a signal path integrated electron density model of the form  $Kr^{-2.3}$ . Given the findings of Erskine, Chang, Houminer, and Berman, it is natural to inquire whether previous estimates of the radial dependence of (weak) inter-

planetary scintillation are consistent with the signal path integration of a power law electron density model of radial index approximately -2.3.

This article reviews radial dependence measurements obtained from weak interplanetary scintillation data over the last decade, and relates these measurements to the appropriate signal path integration of a power law source function. The determined radial dependence of weak interplanetary scintillation data is found to be in reasonable agreement with other experimental measurements of electron density and columnar turbulence, under the assumption of proportionality between weak interplanetary scintillation and signal path integrated electron density.

## II. Interplanetary Scintillation Measurements

Interplanetary scintillation refers to relatively high frequency ( $\geq 1$  Hz) fluctuations in received signal amplitude. The scintillation index is defined (Ref. 1) as:

$$m = \left( \int P(\nu) d\nu \right)^{1/2} = \Delta I / \langle I \rangle$$

where

$m$  = scintillation index

$P$  = power spectrum of signal intensity fluctuations

$\nu$  = fluctuation frequency

$\Delta I$  = rms intensity fluctuation

$\langle I \rangle$  = average source intensity

For natural (noncoherent) signal sources, the scintillation index correlates with columnar turbulence under conditions of low turbulence ("weak" scintillation). As columnar turbulence increases and the scintillation index approaches 1, saturation occurs, and further increases in columnar turbulence produce a sharp decrease in the scintillation index. Therefore, usage of the scintillation index in measuring the geometrical dependence of columnar turbulence is restricted to regions of weak scintillation (as determined by source frequency and elongation angle). There are no such restrictions with coherent (spacecraft) sources as saturation of the scintillation index does not occur.

Much of the analysis of interplanetary scintillation has indicated a total power law radial dependence of  $m(a) \cong Ka^{-1.5}$ , where  $K$  = constant and  $a$  = closest approach distance. Berman (Ref. 8) has shown that for correlation with

signal path integrated source functions, usage of a single geometrical parameter (e.g.,  $a$ ) can lead to significant distortions in modeling and interpretation. In the following section, previously obtained scintillation radial dependencies will be analyzed and mapped back to the signal path integration of an appropriate power law source function.

## III. Scintillation Index Radial Dependence

Following the method of Ref. 8 under the assumption that the radial dependence of the scintillation index is proportional to the signal path integration of a  $r^{-(2+\xi)}$  electron density model, one obtains

$$m(a, \beta) \cong K\beta a^{-(1+\xi)}$$

where

$K$  = constant

$\beta$  = Earth-Sun-source angle

$a$  = closest approach distance

However, all previously published determinations of the radial dependence of the scintillation index have been made as a sole power law function of closest approach distance (i.e., "total" radial dependence as in Ref. 8):

$$m(a) \cong Ka^x$$

again following the method of Ref. 8,  $m(a, \beta)$  is rewritten:

$$m(a, \beta) \cong Ka^{-(1+\xi)+\xi \ln \beta / \ln a}$$

and approximated as

$$m(a) \approx Ka^{-(1+\xi)+\xi \ln(\beta_1/\beta_2) / \xi \ln(a_1/a_2)}$$

where the subscripts 1 and 2 define the applicable (radial) span of data. As was noted in Ref. 8:

- (1) The term  $\xi \ln(\beta_1/\beta_2) / \xi \ln(a_1/a_2)$  can only be considered as an approximate indication of the possible (power law index) distortion in using a single geometrical parameter.
- (2) The distortion becomes most pronounced for data wherein  $\beta$  approaches  $90^\circ$ .

Table 1 presents the results of analyzing five published determinations of the radial dependence of the scintillation

index. The average total radial dependence of these five cases is (reestimated as):

$$m(a) \cong a^{-1.50}$$

The average correction  $\ln(\beta_1/\beta_2)/\ln(a_1/a_2)$  to account for variations of  $\beta$  is:

$$\ln(\beta_1/\beta_2)/\ln(a_1/a_2) \cong -0.16$$

so that in the aggregate these measurements would be consistent with the signal path integration of a mean electron density model of the form  $Kr^{-2.34}$ . Even should one allow that the distortion has been *overstated* by as large a factor as 2, the data would still be consistent with a mean electron density model of the form  $Kr^{-2.42}$ . It is therefore here concluded that the bulk of published interplanetary scintillation data is consistent with the signal path integration of an electron density model  $N_e$  in the extended corona of the form:

$$N_e(r) \cong Kr^{-(2+\xi)}; \quad 0.3 \leq \xi \leq 0.4$$

It is interesting to compare these results to a theoretical derivation of the expected radial dependence of the scintillation index given by Woo (Ref. 14) as follows:

$$m(a) \cong Ka^{0.5}\sigma_{n_e}(a)$$

where  $\sigma_{n_e}$  = rms electron density fluctuation. From Neugebauer (Ref. 15), one assumes:

$$\sigma_{n_e}(a) \propto N_e(a)$$

and from Ref. 4 one has:

$$N_e(a) \propto a^{-2.3}$$

so that one expects from the Woo expression:

$$m(a) \cong a^{0.5}a^{-2.3} = a^{-1.8}$$

or a value clearly inconsistent with the aggregate of published values as seen in Table 1. Looked at from the opposite point of view, the Woo expression and  $m \propto a^{-1.5}$  would require (under the assumption that  $\sigma_{n_e}(a) \propto N_e(a)$ ) an electron density radial dependence of  $r^{-2.0}$ . Such a radial index is less negative than any index reported in the thirteen electron density experiments documented in Table I of Ref. 4.

#### IV. Discussion and Summary

Previous work has demonstrated that electron density in the extended corona ( $r \geq 5r_0$ ) is well represented by the radial function  $Kr^{-2.3}$  and that doppler phase fluctuation data are in excellent agreement with the signal path integration of  $Kr^{-2.3}$ . In this article, it has been shown that previously published weak interplanetary scintillation data, which display a scintillation index *total* radial dependence of approximately  $a^{-1.5}$ , are consistent with the signal path integration of a power law electron density model of the form  $Kr^{-2.3}$  to  $Kr^{-2.4}$ . These results, in combination with previous doppler phase fluctuation results, suggest that most manifestations of columnar solar wind turbulence are or will be found to be proportional to signal path integrated electron density.

## References

1. Erskine, F. T., Cronyn, W. M., Shawhan, S. D., Roelof, E. C., and Gotwols, B. L., "Interplanetary Scintillation at Large Elongation Angles: Response to Solar Wind Density Structure," *J. Geophys. Res.*, Vol. 83, No. A9, Sept. 1, 1978.
2. Chang, H., *Analysis of Dual-Frequency Observations of Interplanetary Scintillations Taken by the Pioneer 9 Spacecraft*, Doctoral Dissertation, Department of Electrical Engineering, Stanford University, May 1976.
3. Houminer, Z., and Hewish, A., "Correlation of Interplanetary Scintillation and Spacecraft Plasma Density Measurements," *Planetary and Space Science*, Volume 22, Number 6, June 1974.
4. Berman, A. L., "Electron Density in the Extended Corona: Two Views," in *The Deep Space Network Progress Report 42-41*, Jet Propulsion Laboratory, Pasadena, Calif., Oct. 15, 1977.
5. Berman, A. L., and Wackley, J. A., "Doppler Noise Considered as a Function of the Signal Path Integration of Electron Density," in *The Deep Space Network Progress Report 42-33*, Jet Propulsion Laboratory, Pasadena, Calif., June 15, 1976.
6. Berman, A. L., and Wackley, J. A., "Viking S-Band Doppler Phase Fluctuations Used to Calibrate the Mean 1976 Equatorial Corona," in *The Deep Space Network Progress Report 42-38*, Jet Propulsion Laboratory, Pasadena, Calif., Apr. 15, 1977.
7. Berman, A. L., Wackley, J. A., and Hietzke, W. H., "The First Direct Comparison of Doppler Phase Fluctuation to Integrated Electron Density Over an Extensive Span of Signal Closest Approach Distance - A Brief Report," IOM ALB-78-35, March 10, 1978 (JPL internal document).
8. Berman, A. L., "Precise Extraction of Geometrical Dependence From Solar Wind Columnar Turbulence Measurements," in *The Deep Space Network Progress Report 42-50*, Jet Propulsion Laboratory, Pasadena, Calif., Apr. 15, 1979 (this volume).
9. Hewish, A., and Symonds, M. D., "Radio Investigation of the Solar Plasma," *Planetary and Space Science*, Vol. 17, 1969.
10. Readhead, A. C. S., "Interplanetary Scintillation of Radio Sources at Metre Wavelengths - II," in *The Monthly Notices of the Royal Astronomical Society*, 155, 1971.
11. Hewish, A., "Observations of the Solar Plasma Using Radio Scattering and Scintillation Methods," in *Solar Wind*, edited by Sonnett, C. P., Coleman, P. J., Jr., and Wilcox, J. M., published by National Aeronautics and Space Administration, Washington, D.C., 1972.
12. Rickett, B. J., "Power Spectrum of Density Irregularities in The Solar Wind Plasma," *J. Geophys. Res.*, Vol. 78, No. 10, April 1, 1973.
13. Coles, W. A., Rickett, B. J., and Rumsey, V. H., "Interplanetary Scintillation," in *Solar Wind Three*, edited by Russell, C. T., published by Institute of Geophysics and Planetary Physics, University of California, Los Angeles, Calif., July 1974.
14. Woo, R., "Measurements of the Solar Wind Using Spacecraft Radio Scattering Observations," in *Study of Travelling Interplanetary Phenomena*, edited by M. A. Shea, published by D. Reidel Publishing Company, Dordrecht, Holland, 1977.
15. Neugebauer, M., "Constancy of Relative Density Fluctuations in The Solar Wind (abstract)," in *EOS Transactions, American Geophysical Union 58*, page 1224, 1977.

**Table 1. Previously published weak interplanetary scintillation index data and indicated source function power law index**

Source	Year	Original published total radial dependence	Recalculated total radial dependence from data <sup>a</sup>	Data limits (of closest approach distance), AU	$\frac{\Omega(\beta_1/\beta_2)}{\Omega(a_1/a_2)}$	Indicated source function power law index
Hewish & Symonds (Ref. 9)	1969	-1.6	-1.57	0.12-1.0	-0.31	-2.26
Readhead (Ref. 10)	1971	-1.55	Same	0.05-0.83	-0.13	-2.42
Hewish (Ref. 11)	1971	-1.50	-1.52	0.04-0.9	-0.14	-2.38
Rickett <sup>b</sup> (Ref. 12)	1973	-1.6	-1.43		-0.15	-2.28
(2695 MHz)			-1.48	0.042-0.39	-0.06	-2.42
(611 MHz)			-1.42	0.12-0.48	-0.10	-2.32
(178 MHz)			-1.38	0.32-0.83	-0.28	-2.10
Coles <sup>c</sup> (Ref. 13)	1974		-1.42		-0.08	-2.34
(2695 MHz)			-1.50	0.045-0.15	-0.03	-2.47
(611 MHz)			-1.34	0.15-0.55	-0.12	-2.22
Average		-1.56	-1.50		-0.16	-2.34

<sup>a</sup>When possible, the total radial index was remeasured from published data (the fit line) and used where appropriate.

<sup>b</sup>These data were the measured fit lines in Fig. 3 (from Ref. 12) and include the 2695-, 611-, and 178-MHz data; the 81.5-MHz data were not used because the measured fit line was approximately -2.0. When the four slopes are averaged, a value close to the Ricketts value -1.6 is achieved.

<sup>c</sup>These data were the measured fit lines in Fig. 1 (from Ref. 13) and include the 2695- and 611-MHz data.

D26

N79-22160

# A Unified Observational Theory for Solar Wind Columnar Turbulence

A. L. Berman  
TDA Engineering Office

*Solar wind columnar turbulence measurements are possibly the most important tool in probing the solar corona and solar wind, if for no other reason than their abundant availability. Fundamental to the extraction and utilization of the full informational content of such measurements is the confident understanding of the proper relationship between columnar turbulence and the most basic solar wind parameters – solar wind velocity and electron density.*

*This article reviews investigations of the primary forms of solar wind columnar turbulence, including Doppler phase fluctuation, spectral broadening, weak interplanetary scintillation, and electron density. Based on the totality of these measurements, a unified, self-consistent, observational hypothesis for solar wind columnar turbulence is proposed as follows:*

- (1) *The dependence on radial distance  $r$  of solar wind mean electron density  $N_e$  is well represented by the power law model (with  $A$  and  $B$  fit coefficients):*

$$N_e(r) \cong Ar^{-6} + Br^{-2.3}$$

- (2) *To first order, all primary measurements of solar wind columnar turbulence are well represented by the signal path integration of the electron density model from (1) above ( $R$  = signal path):*

$$\text{Columnar turbulence} \propto \int N_e(r) dR$$

## I. Introduction

Solar wind columnar turbulence measurements constitute perhaps the most important overall experimental tool in probing the solar corona and solar wind, if for no other reason than the sheer abundance of such measurements. As an example, the Deep Space Network (DSN) automatically computes and records Doppler phase fluctuation data whenever a spacecraft

is being tracked for any purpose. The primary data types being considered here as columnar turbulence are spacecraft Doppler phase fluctuation, spacecraft carrier frequency spectral broadening, and signal intensity fluctuation (“interplanetary scintillation”) of both coherent (spacecraft) and noncoherent (natural) sources. Interplanetary scintillation of natural sources is further restricted to the region of “weak” scintillation.

Careful measurement and modelling of solar wind columnar turbulence can be ascribed to at least three major considerations, as follows:

- (1) The validation of the theoretical understanding of the mechanics of columnar turbulence generation.
- (2) The removal (via calibration) of columnar turbulence, which to varying degrees obscures many other radio science experiments.
- (3) The precise functional determination of more basic solar wind parameters, such as electron density and velocity, once the relationship between columnar turbulence and these parameters has become well understood.

This article reviews experimental measurements of electron density and the primary forms of solar wind columnar turbulence. Based on the totality of these observations, this article suggests a heuristic observational hypothesis for solar wind columnar turbulence, stated as follows:

- (1) The dependence on radial distance  $r$  of solar wind mean electron density  $N_e$  is well represented by the power law model (with  $A$  and  $B$  fit coefficients):

$$N_e(r) \cong Ar^{-6} + Br^{-2.3}$$

- (2) To first order, all primary measurements of solar wind columnar turbulence are well represented by the signal path integration of electron density ( $R$  = signal path):

$$\text{columnar turbulence} \propto \int N_e(r) dR$$

## II. Electron Density

Electron density radial dependence in the inner corona (here to be defined as  $r \leq 5r_o$ , where  $r$  is radial distance and  $r_o$  is the solar radius) has been frequently investigated via white light (eclipse) photometry analysis and K coronameter measurements. Examples of white light photometry analysis are van de Hulst (Ref. 1), and Blackwell (in Ref. 2), while examples of K coronameter measurements are Saito (Ref. 3), Hansen, et al. (Ref. 4), and Saito, et al. (Ref. 5). In general, usage of these techniques has resulted in a consistent determination of inner corona electron density which is well represented by the power law radial function:

$$N_e(r) \cong Ar^{-6}$$

In the extended corona (here to be defined as  $5r_o \leq r \leq 1\text{AU}$ ), a greater variety of techniques have been utilized to

determine the radial dependence of electron density. In addition to the techniques used for the inner corona, measurements in the extended corona have been made by radio interferometry (Muhleman, et al., Ref. 6), single frequency spacecraft range (Muhleman, et al., Refs. 7 and 8; Edenhofer, et al., Ref. 9), dual-frequency spacecraft range (Berman, et al., Ref. 10), pulsar time delay (Counselman, et al., Ref. 11, and Weisberg, et al., Ref. 12), and in situ spacecraft measurements (Ogilvie, et al., Ref. 13). The radial dependence (power law index) of electron density in the extended corona has been somewhat controversial, and estimates from various experiments have spanned the following rather large range of power law radial indices:

$$N_e(r) \cong Br^{-(2+\xi)}$$

$$0 \leq \xi \leq 0.5$$

In 1977, Berman (Ref. 14), reviewed the then available measurements of the radial dependence of electron density in the extended corona (Table 1 from Ref. 14). At that time the mean electron density power law exponent ( $r^{-(2+\xi)}$ ) from the experiments listed in Table 1 of Ref. 14 was:

$$\xi = 0.298$$

Table 1 from Ref. 14 is updated here with the following additional new entries:

Source	Year	$\xi$	Type of Measurement
Ogilvie	1978	0.5	in situ density, Mariner 10
Saito	1978	0.14	K coronameter
Berman	1978	0.3	S minus X range, Viking

The average of the sixteen experiments in Table 1 (of this article) is:

$$\xi = 0.301$$

with a 1 standard deviation ( $1\sigma$ ) of:

$$1\sigma = 0.13$$

Based on the contents of Table 1, it is concluded that:

$$N_e(r) \cong Ar^{-6} + Br^{-2.3}$$

continues as the best existing representation for mean electron density radial dependence in both the inner and extended corona. It should be stressed that confident knowledge of

the average radial dependence of electron density is fundamental to the evaluation of turbulence models, since electron density is clearly the key parameter.

An additional important feature of the mean electron density model is the very sharp "break" at approximately  $r \approx 4r_o$  between the  $Ar^{-6}$  and  $Br^{-2.3}$  terms. Analysis of columnar turbulence measurements in the region surrounding  $4r_o$  (signal closest approach distance) is most important in the process of validating columnar turbulence models.

### III. Doppler Phase Fluctuation

In 1975, Berman and Rockwell (Ref. 17), analyzed two-way S-Band Doppler noise (or phase fluctuation,  $= \phi$ ) from the 1975 solar conjunctions of Pioneer 10, Pioneer 11, and Helios 1, in terms of a geometrical parameter  $= \sin \alpha/\beta$ , where  $\alpha =$  Sun-Earth-probe angle and  $\beta =$  Earth-Sun-probe angle. A best fit to this parameter yielded:

$$\phi(\alpha, \beta) \approx K(\sin \alpha/\beta)^{-1.29}$$

Subsequently, Berman and Wackley (Ref. 18), showed that this same Doppler noise data provided a very good fit to the signal path integration of a nominal  $Kr^{-2.3}$  electron density model, except in the region  $a < 10r_o$ , where  $a =$  signal closest approach distance. When a term  $Ar^{-6}$  was added, a good fit was achieved over the entire span of data.

In 1976, Berman and Wackley (Ref. 19), showed that the signal path integration of  $Ar^{-6} + Br^{-2.3}$  provided a very good fit to the 1976 solar conjunction data of Helios 1 and 2, Pioneer 10 and Pioneer 11.

In 1976, Pioneer 11 underwent a solar conjunction in which the signal closest approach locus transversed very high ( $>80^\circ$ ) heliographic latitudes. Berman, et al. (Ref. 20), were able to show that Doppler noise dropped off sharply with increasing heliographic latitude, much as Saito (Ref. 3) and Counselman (Ref. 11) found for electron density.

In 1977, Berman, et al. (Ref. 15), analyzed a large volume (in excess of 800 pass-average data points) of two-way S-Band Doppler noise data accumulated during the Viking 1976 solar conjunction. A simultaneous, two parameter (coefficient and power law index) fit of these data to the signal path integrated electron density model  $Br^{-(2+\xi)}$  was performed; a best fit was obtained for  $\xi = 0.30$ .

In 1978, Berman (Refs. 21 and 22) showed that the combined set of all inner corona Doppler noise measurements obtained from Helios 1, Helios 2, and Viking, exhibited a very

sharp break at approximately  $a \approx 3r_o$ , exactly as does the signal path integration of the composite  $Ar^{-6} + Br^{-2.3}$  electron density model.

Finally, in 1978, Berman, et al. (Ref. 10), directly compared concurrent measurements of Viking two-way S-Band Doppler noise and Viking dual frequency (S-Band minus X-Band) range measurements; correspondence of these two parameters in Ref. 10 is seen to be excellent. Because of the tremendous volume of Viking Doppler noise and dual frequency range data utilized, and the very wide radial data span ( $2r_o - 160r_o$ ), it is here considered that this final comparison is incontrovertible evidence that to first order, Doppler phase fluctuation is well represented by the signal path integration of electron density.

### IV. Spectral Broadening

In 1978, Rockwell (Ref. 23), analyzed spacecraft carrier frequency spectral broadening (SB) between 2 and 20 Solar radii. (The data were primarily Helios data and had been originally provided by R. Woo.) Rockwell was able to demonstrate a good fit of these spectral broadening data to a signal path integration of  $Ar^{-6} + Br^{-2.3}$ . However, when Rockwell performed a simultaneous, two parameter fit to the data, he obtained a best fit for  $Ar^{-6} + Br^{-2.77}$ , which is a significantly steeper radial dependence than usually determined for the extended corona term. However, the most important feature of these spectral broadening data is that they clearly exhibit the sharp break at  $a \approx 3r_o$  (see, for instance, Berman, Ref. 22, Fig. 3), just as do the inner corona Doppler phase fluctuation data.

Based on the fact that spectral broadening data follow the sharp (integrated) density break in the transition from the inner to the extended corona, it is here concluded that spectral broadening data to first order are reasonably well represented by the signal path integration of electron density.

### V. Interplanetary Scintillation

Recently, Berman (Ref. 24), has suggested that the bulk of previously published determinations of the radial (power law) dependence of weak interplanetary scintillation data (the scintillation index) are reasonably consistent with the signal path integration of a power law electron density model of the form:

$$N_e(r) \approx r^{-(2+\xi)}$$

$$0.3 \leq \xi \leq 0.4$$

In addition, Chang (Ref. 25), has demonstrated proportionality between interplanetary scintillation of a coherent source

and integrated electron density via concurrent measurement of both using the Pioneer 9 spacecraft. Similar correlation between natural source weak interplanetary scintillation and in situ density measurements has been determined by Erskine, et al. (Ref. 26), and Houminer, et al. (Ref. 27). Based on the totality of these observations, it seems reasonable to infer that to first order, weak interplanetary scintillation is reasonably well represented by the signal path integration of electron density.

It is appropriate to note that this heuristic interpretation of weak interplanetary scintillation conflicts with the currently popular explanation for the observed radial dependence of the scintillation index. Greatly simplified, such an explanation allows:

$$m^2(a) \propto \int \sigma_{n_e}^2(r) dr$$

where:

$$\sigma_{n_e}(r) = \text{electron density fluctuation}$$

$$\approx Kr^{-\beta/2}$$

$$\beta \approx 4.1$$

so that:

$$m(a) \propto a^{-\left(\frac{\beta-1}{2}\right)} \approx a^{-1.55}$$

Recent papers which favor such an interpretation are Armstrong, et al. (Ref. 28), and Coles, et al. (Ref. 29).

However, the hypothesis advanced in this section is consistent with the earlier work of Little (Ref. 30), and implies the existence of a linear transverse fluctuation scale.

## VI. Discussion and Summary

This article has reviewed the relationship between signal path integration of electron density and observations of various forms of solar wind columnar turbulence. The salient points are briefly recapped as follows:

### (1) Electron density $N_e$ .

(a)  $N_e(r) \cong Ar^{-6} + Br^{-2.3}$  has been well established as

a mean model by a wide variety of experimental techniques.

### (2) Doppler Phase Fluctuation Data $\phi$ .

- (a)  $\phi$  is well represented by the signal path integration of  $Ar^{-6} + Br^{-2.3}$
- (b)  $\phi$  falls off with increasing heliographic latitude as does  $N_e$ .
- (c) A simultaneous 2 parameter fit of a very large volume of  $\phi$  to the signal path integration of  $Br^{-(2+\xi)}$  yields  $\xi = 0.30$ .
- (d)  $\phi$  exhibits a sharp break at  $a \approx 3r_0$ , exactly as does signal path integrated electron density.
- (e)  $\phi$  shows excellent correlation with concurrent measurements of signal path integrated electron density over a wide span of signal closest approach distances.

### (3) Spectral Broadening Data (SB).

- (a) SB is well represented by  $Ar^{-6} + Br^{-2.3}$ .
- (b) SB exhibits a sharp break at  $a \approx 3r_0$  as does Doppler phase fluctuation data and signal path integrated electron density.

### (4) Scintillation Index $m$ .

- (a)  $m$  is well represented by the signal path integration of a power law electron density model  $N_e(r) \approx Br^{-(2+\xi)}$ ;  $0.3 \leq \xi \leq 0.4$ .
- (b) Proportionality between  $m$  and signal path integrated electron density has been demonstrated via concurrent spacecraft measurements.

This article concludes that the above evidence provides a persuasive and cohesive picture in which all primary observations of solar wind columnar turbulence are seen to be well represented to first order by the signal path integration of a well established electron density model.

Finally, it is noted that this heuristic observational hypothesis conflicts with theoretical interpretations currently in favor. Nonetheless, earlier investigations predicted exactly such results as hypothesized in this article, based on the premise of a linear transverse fluctuation scale. Examples are Little (Ref. 30), Hollweg (Refs. 31 and 32), and Hollweg, et al. (Ref. 33).

## References

1. van de Hulst, H. C., "The Electron Density of the Solar Corona," *Bulletin of the Astronomical Institutes of The Netherlands*, Volume XI, Number 410, February 2, 1950.
2. Anderson, J. D., Esposito, P. B., Martin, W. L., Thornton, C. L., and Muhleman, D. O., "Experimental Test of General Relativity Using Time Delay Data from Mariner 6 and Mariner 7," in *The Astrophysical Journal*, Volume 200, August 15, 1975.
3. Saito, K., "A Non-Spherical Axisymmetric Model of The Solar K Corona of The Minimum Type," *Annals of the Tokyo Astronomical Observatory*, University of Tokyo, Second Series, Volume XII, Number 2, Mitaka, Tokyo, 1970.
4. Hansen, R. T., Garcia, C. J., Hansen, S. F., and Loomis, H. G., "Brightness Variations of the White Light Corona During the Years 1964-1967," in *Solar Physics* 7, 1969.
5. Saito, K., Poland, A. I., and Munro, R. H., "A Study of The Background Corona Near Solar Minimum," in *Solar Physics* 55, 1977.
6. Muhleman, D. O., Ekers, R. D., and Formalont, E. B., "Radio Interferometric Test of The General Relativistic Light Bending Near The Sun," *Physical Review Letters*, Volume 24, Number 24, 15 June 1970.
7. Muhleman, D. O., Anderson, J. D., Esposito, P. B., and Martin, W. L., "Radio Propagation Measurements of The Solar Corona and Gravitational Field: Applications to Mariner 6 and 7," in *Proceedings of the Conference on Experimental Tests of Gravitation Theories, Technical Memorandum 33-499*, edited by Davies, R. W., published by the Jet Propulsion Laboratory, Pasadena, California, 1 November 1971.
8. Muhleman, D. O., Esposito, P. B., and Anderson, J. D., "The Electron Density Profile of the Outer Corona and the Interplanetary Medium from Mariner 6 and Mariner 7 Time Delay Measurements," *The Astrophysical Journal*, 211, February 1, 1977.
9. Edenhofer, P., Esposito, P. B., Hansen, R. T., Lueneburg, E., Hansen, S. F., Martin, W. L., and Zygielbaum, A. I., "Time Delay Occultation Data of the Helios Spacecrafts and Preliminary Analysis for Probing the Solar Corona," in the *Journal of Geophysics* 42, 1977.
10. Berman, A. L., Wackley, J. A., and Hietzke, W. H., "The First Direct Comparison of Doppler Phase Fluctuation to Integrated Electron Density Over an Extensive Span of Signal Closest Approach Distance - A Brief Report," IOM ALB-78-35, March 10, 1978 (JPL Internal Document).
11. Counselman III, C. C., and Rankin, J. M., "Density of the Solar Corona from Occultations of NPO532," *The Astrophysical Journal*, Volume 175, August 1, 1972.
12. Weisberg, J. M., Rankin, J. M., Payne, R. R., and Counselman III, C. C., "Further Changes in the Distribution of Density and Radio Scattering in the Solar Corona," *The Astrophysical Journal*, Volume 209, October 1, 1976.
13. Ogilvie, K. W., and Scudder, J. D., "The Radial Gradients and Collisional Properties of Solar Wind Electrons," in *The Journal of Geophysical Research*, Volume 83, Number A8, August 1, 1978.
14. Berman, A. L., "Electron Density in the Extended Corona: Two Views," in *The Deep Space Network Progress Report 42-41*, Jet Propulsion Laboratory, Pasadena, California, October 15, 1977.

15. Berman, A. L., Wackley, J. A., Rockwell, S. T., and Kwan, M., "Viking Doppler Noise used to Determine the Radial Dependence of Electron Density in the Extended Corona," in *The Deep Space Network Progress Report 42-38*, Jet Propulsion Laboratory, Pasadena, California, 15 April 1977.
16. Newkirk, G., "Structure of the Solar Corona," in *The Annual Review of Astronomy and Astrophysics*, Vol. 5, 1967.
17. Berman, A. L., and Rockwell, S. T., "Analysis and Prediction of Doppler Noise During Solar Conjunctions", in *The Deep Space Network Progress Report 42-30*, Jet Propulsion Laboratory, Pasadena, California, 15 December 1975.
18. Berman, A. L., and Wackley, J. A., "Doppler Noise Considered as a Function of the Signal Path Integration of Electron Density," in *The Deep Space Network Progress Report 42-33*, Jet Propulsion Laboratory, Pasadena, California, 15 June 1976.
19. Berman, A. L., Wackley, J. A., and Rockwell, S. T., "The 1976 Helios and Pioneer Solar Conjunctions – Continuing Corroboration of the Link Between Doppler Noise and Integrated Signal Path Electron Density," in *The Deep Space Network Progress Report 42-36*, Jet Propulsion Laboratory, Pasadena, California, 15 December 1976.
20. Berman, A. L., Wackley, J. A., Rockwell, S. T., and Yee, J. G., "The Pioneer 11 1976 Solar Conjunction: A Unique Opportunity to Explore the Heliographic Latitudinal Variations of the Solar Corona," in *The Deep Space Network Progress Report 42-35*, Jet Propulsion Laboratory, Pasadena, California, 15 October 1976.
21. Berman, A. L., "Electron Density and Doppler RMS Phase Fluctuation in the Inner Corona," in *The Deep Space Network Progress Report 42-44*, Jet Propulsion Laboratory, Pasadena, California, 15 April 1978.
22. Berman, A. L., "Solar Wind Turbulence Models Evaluated Via Observations of Doppler RMS Phase Fluctuation and Spectral Broadening in The Inner Corona," in *The Deep Space Network Progress Report 42-44*, Jet Propulsion Laboratory, Pasadena, California, 15 April 1978.
23. Rockwell, S. T., "An Empirical Spectral Bandwidth Model for Superior Conjunction," in *The Deep Space Network Progress Report 42-43*, Jet Propulsion Laboratory, Pasadena, California, 15 February 1978.
24. Berman, A. L., "A Reexamination of the Radial Dependence of Weak Interplanetary Scintillation," in *The Deep Space Network Progress Report 42-50*, Jet Propulsion Laboratory, Pasadena, California, 15 April 1979 (this volume).
25. Chang, H., *Analysis of Dual-Frequency Observations of Interplanetary Scintillations Taken by the Pioneer 9 Spacecraft*, Doctoral Dissertation, Department of Electrical Engineering, Stanford University, May 1976.
26. Erskine, F. T., Cronyn, W. M., Shawhan, S. D., Roelof, E. C., and Gotwols, B. L., "Interplanetary Scintillation at Large Elongation Angles: Response to Solar Wind Density Structure," in *The Journal of Geophysical Research*, Volume 83, Number A9, September 1, 1978.
27. Houminer, Z., and Hewish, A., "Correlation of Interplanetary Scintillation and Spacecraft Plasma Density Measurements," in *Planetary and Space Science*, Volume 22, Number 6, June 1974.
28. Armstrong, J. W., and Coles, W. A., "Interplanetary Scintillations of PSR 0531+21 at 74 MHz," in *The Astrophysical Journal* 220, 15 February 1978.
29. Coles, W. A., and Harmon, J. K., "Interplanetary Scintillation Measurements of The

- Electron Density Power Spectrum in The Solar Wind," in *The Journal of Geophysical Research*, Volume 83, Number A4, April 1, 1978.
30. Little, L. T., "Small Scale Plasma Irregularities in The Interplanetary Medium," in *Astronomy and Astrophysics* 10, 1971.
  31. Hollweg, J. V., "A Statistical Ray Analysis of the Scattering of Radio Waves by the Solar Corona," in *The Astronomical Journal*, Volume 73, Number 10, Part 1, December 1968.
  32. Hollweg, J. V., "Angular Broadening of Radio Sources by Solar Wind Turbulence," in *The Journal of Geophysical Research, Space Physics*, Volume 75, Number 19, July 1, 1970.
  33. Hollweg, J. V., and Harrington, J. V., "Properties of Solar Wind Turbulence Deduced by Radio Astronomical Measurements," in *The Journal of Geophysical Research, Space Physics*, Volume 73, Number 23, December 1, 1968.

**Table 1. Electron density measurements of the form  $Br^{-(2+\xi)}$  in the solar corona**

Source	Reference	Year	$\xi$	Type of measurement
Ogilvie	13	1978	0.5	In Situ Density, Mariner 10
Saito	5	1978	0.14	K-Coronagraph
Berman	10	1978	0.3	S Minus X Range, Viking
Edenhofer	9	1977	0.2	S-Band Range, Helios 2
Berman	15	1977	0.30	S-Band Doppler Noise, Viking
Muhleman	8	1977	0.05	S-Band Range, Mariner 6
Muhleman	8	1977	0.08	S-Band Range, Mariner 7
Weisberg	12	1976	0.3 <sup>a</sup>	Pulsar Time Delay
Counselman	11	1972	0.4 <sup>b</sup>	Pulsar Time Delay
Muhleman	7	1971	0.41	S-Band Range, Mariner 6
Muhleman	6	1970	0.33	Radio Interferometry
Saito	3	1970	0.5	Photometry
Newkirk	16	1967	0.34 <sup>c</sup>	Compilation of Techniques
Blackwell	2	1967	0.33	Solar Eclipse
Blackwell	2	1967	0.33	Solar Eclipse
Blackwell	2	1966	0.3	Solar Eclipse

<sup>a</sup>One of several solutions; this solution is in best agreement with average in situ density values at 1 AU.

<sup>b</sup>One of several solutions; this solution included heliographic latitude.

<sup>c</sup>Computed between  $N_e(10r_\odot)$  and average in situ value ( $7.5 \text{ cm}^{-3}$ ) at 1 AU.

D<sub>21</sub>  
N79-22161

DSN Progress Report 42-50

January and February 1979

## Further Results on Fast Transforms for Decoding Reed-Solomon Codes Over $GF(2^n)$ for $n = 4,5,6,8$

I. S. Reed

Department of Electrical Engineering  
University of Southern California

T. K. Truong, R. L. Miller, and B. Benjauthrit  
Communications Systems Research Section

*In this article it is shown that Winograd's methods can be modified to compute Fourier-like transforms over  $GF(2^n)$ , where  $n = 4,5,6,8$ . Such transforms are used to encode and decode Reed-Solomon codes of block length  $2^n-1$ . With these transforms a Reed-Solomon decoder can be made faster and more efficient than a decoder that uses the conventional fast transforms over  $GF(2^n)$ .*

### I. Introduction

Fast transforms over the group  $(Z_2)^n$  were used first by Green (Ref. 1) of the Jet Propulsion Laboratory to decode the (32,6) Reed-Muller code (Ref. 2) in the Mariner and Viking space probes. In 1971, Mandelbaum (Ref. 3) proposed to decode Reed-Solomon (RS) codes by a transform technique. Recently Gore (Ref. 4) extended Mandelbaum's method to decode RS codes with a finite field transform over  $GF(2^n)$ . Later, Michelson (Ref. 5) implemented Mandelbaum's algorithm and showed that a transform decoder over  $GF(2^n)$  requires fewer multiplications than a more standard decoder (Refs. 6 and 7). The disadvantage of the transform method over  $GF(2^n)$  is that the transform length is an odd number, so that the most efficient FFT algorithm cannot be used. Recently, the authors in (Ref. 8) showed that RS codes can be decoded with a combination of a fast transform and continued fractions. This approach was used to decode RS codes over  $GF(2^{2^n})$  (Ref. 9), and over  $GF(32)$  and  $GF(64)$  (Ref. 10); Winograd's techniques were used to reduce the number of multiplications. In this paper we extend the results of Refs. 9 and 10 by providing a simple inspection technique to further cut down the number of multiplications.

Present plans for the space communication link for the Voyager mission (Ref. 11) include a 16-error-correcting, 255-symbol RS code, where each symbol has 8 bits. This RS code is concatenated with a Viterbi decoded convolutional code of constraint length 7, rate 1/2 or 1/3. Such a concatenated coding scheme can be used to reduce the signal-to-noise ratio required to meet a specified bit-error rate.

In order to decode a given received vector  $r = (r_0, r_1, \dots, r_{N-1})$  of such an RS code of length  $N$  by a transform technique, one first computes the syndromes (Ref. 8).

$$S_k = \sum_{i=0}^{N-1} r_i \gamma^{ki} = \sum_{i=0}^{N-1} (c_i + e_i) \gamma^{ki} = \sum_{i=0}^{N-1} e_i \gamma^{ki} = E_k$$

for  $k = 1, 2, \dots, 2t$  (1)

where

$t$  = maximum number of errors that can be corrected

$c = (c_0, c_1, \dots, c_{N-1})$  = transmitted RS code word

$e = (e_0, e_1, \dots, e_{N-1})$  = error pattern

and

$\gamma \in GF(2^n)$  is a primitive  $N$ th root of unity

The error locator polynomial is then determined from the syndromes and used to compute the remaining syndromes,  $E_{2t+1}, \dots, E_N = E_0$ . The corrected RS code word is then  $c = r - e$ , where  $e = (e_0, e_1, \dots, e_{N-1})$ , the error word is the inverse transform of  $E_k$  given by the relation:

$$e_l = N^{-1} \sum_{k=0}^{N-1} E_k \gamma^{-lk}, l = 0, 1, \dots, N-1$$
(2)

Observe that (1) as well as its inverse (2) are actually discrete Fourier-like transforms of the form:

$$A_j = \sum_{i=0}^{N-1} a_i \gamma^{ij}, 0 \leq j \leq N-1, \gamma^N = 1$$
(3)

Evidently, the computation of  $A_j$  in (3) directly involves  $N^2$  multiplications. By appropriate algebraic manipulations, it is shown in this paper that this number of multiplications can be reduced substantially.

Eq. (3) can be rewritten in matrix form as

$$\begin{pmatrix} A_0 \\ A_1 \\ \vdots \\ A_{N-1} \end{pmatrix} = \begin{pmatrix} \gamma^{00} & \gamma^{01} & \dots & \gamma^{0(N-1)} \\ \gamma^{10} & \gamma^{11} & \dots & \gamma^{1(N-1)} \\ \gamma^{20} & \gamma^{21} & \dots & \gamma^{2(N-1)} \\ \vdots & \vdots & \ddots & \vdots \\ \gamma^{(N-1)0} & \gamma^{(N-1)1} & \dots & \gamma^{(N-1)(N-1)} \end{pmatrix} \begin{pmatrix} a_0 \\ a_1 \\ \vdots \\ a_{(N-1)} \end{pmatrix}$$
(4)

or in abbreviated notation as

$$\bar{A} = W'\bar{a} \quad (5)$$

where  $W'$  is an  $N \times N$  matrix  $(\gamma^{ij})$ , and  $\bar{A}$  and  $\bar{a}$  are  $1 \times N$  column matrices  $(A_j)$  and  $(a_i)$ , respectively. Also let

$$A_j = a_0 + B_j \text{ for } j = 1, 2, \dots, N-1$$

where

$$B_j = \sum_{i=1}^{N-1} a_i \gamma^{ij}$$

or again in a short notation as

$$\bar{B} = W\bar{a} \quad (6)$$

where  $W$  is the  $(N-1) \times (N-1)$  matrix  $(\gamma^{ij})_{i,j \neq 0}$  and  $\bar{a}$ ,  $\bar{B}$  are the column matrices  $(a_i)$  and  $(B_j)$ , respectively. By factoring matrix  $W$  into a product of matrices  $W = W_1 W_2 \dots W_k$ , Gentleman (Ref. 12) was able to reduce the number of multiplications involved in this computation considerably.

In this paper, algorithms using the methods of Winograd (Refs. 13 and 14) are developed to compute the above transform over  $GF(2^n)$  for  $n = 4, 5, 6, 8$ . The idea behind this method is to first permute the entries of the matrix  $W$  into a cyclic block of submatrices. Then, using some variations of the ideas of Winograd, the total number of multiplications required to perform the transform are significantly reduced. Two cases need to be distinguished.

First, if  $N$  is a prime number  $p$ , then there exists  $\alpha \in GF(p)$ , which generates the cyclic multiplicative group of  $p-1$  elements. By applying the permutation  $\sigma(i) = \alpha^i$ ,  $i = 1, 2, \dots, p-1$ , the matrix  $W$  can be changed into a cyclic matrix  $\tilde{W}$  as follows:

$$B_{\sigma(j)} = \sum_{i=1}^{p-1} a_{\sigma(i)} \gamma^{\sigma(i)\sigma(j)} = \sum_{i=1}^{p-1} a_{\sigma(i)} \gamma^{\sigma(i+j)}, j = 1, 2, \dots, p$$

or

$$\tilde{B} = \tilde{W}\tilde{a} \quad (7)$$

where  $\tilde{W} = (\gamma^{\sigma(i+j)})$  and where  $\tilde{a} = (a_{\sigma(i)})$  and  $\tilde{B} = (B_{\sigma(i)})$  are column matrices.

Secondly if  $N$  is not a prime, then it can be factored into a product of relatively prime powers  $N = N_1 N_2 \dots N_k$ . Then by suitably applying the above technique for each  $N_i$ , the original  $\bar{B}$  can be reconstituted by using the Chinese Remainder Theorem and Winograd's approach. The above proposed transform algorithm over  $GF(2^n)$  generally requires fewer multiplications than the more conventional fast transform algorithm proposed by Gentleman (Ref. 12).

In the next section, methods for multiplying two polynomials by the cyclic convolution techniques are developed. Three examples, 3-, 5-, and 15-point cyclic convolutions, are provided to demonstrate the ideas involved. Section III contains technical results for simplifying computations over  $GF(2^n)$ . These results along with those in Section II about cyclic convolutions over  $GF(2^n)$  are used to obtain the finite field transforms of 7 and 9 points in Section IV. Transforms of length  $N = 3, 5$  and 17 points are given in Appendix B. In Section V finite field transforms of longer lengths, viz,  $N = 2^n - 1$ , where  $n = 4, 5, 6, 8$ , are obtained, using the results given in Section III. A comparison of the new algorithm and Gentleman's algorithm is made in Section VI. Finally a comparison of the two algorithms in terms of the complexity of transform decoding of Reed-Solomon codes over  $GF(2^n)$ ,  $n = 4, 5, 6, 8$  is provided in the last section of the paper.

## II. Cyclic Convolutions Over $GF(2^n)$

The computation of transforms over  $GF(2^n)$  will be based on fast cyclic convolutions. We first discuss a few techniques which are useful in obtaining fast cyclic convolutions.

Consider the multiplication of two polynomials  $x(u) = x_0 + x_1 u^m$  and  $y(u) = y_0 + y_1 u^m$  for  $m = 1, 2$  with coefficients in  $GF(2^n)$ . The product

$$\begin{aligned} x(u)y(u) &= (x_0 + x_1 u^m)(y_0 + y_1 u^m) \\ &= x_0 y_0 + [y_0(x_0 + x_1) + y_1(x_0 + x_1) + (x_0 y_0 + x_1 y_1)] u^m + x_1 y_1 u^{2m} \\ &= c_0 + c_1 u^m + c_2 u^{2m} \end{aligned} \quad (8)$$

where  $c_0 = x_0 \cdot y_0$ ,  $c_1 = (x_0 + x_1)(y_0 + y_1) + x_0 \cdot y_0 + x_1 \cdot y_1$  and  $c_2 = x_1 \cdot y_1$ . We see that only three multiplications are needed to perform (8), whereas a direct method would require four.

Now if  $x(u) = x_0 + x_1 u + \dots + x_{n-1} u^{n-1}$  and  $y(u) = y_0 + y_1 u + \dots + y_{n-1} u^{n-1}$  are two  $(n-1)$ th degree polynomials, then it is well known that the cyclic convolution  $T(u)$  of the coefficients of  $x(u)$  and  $y(u)$  is given by the coefficients of

$$T(u) \equiv x(u) y(u) \pmod{u^n - 1} \quad (9)$$

The direct method for computing the above cyclic convolution  $T(u)$  requires  $n^2$  multiplications. This number of multiplications can be reduced by the first factoring  $u^n - 1$  into distinct relatively prime factors

$$u^n - 1 = \prod_{i=1}^k m_i(u), \text{ when } n \text{ is odd} \quad (10)$$

Next compute the residues  $T_i(u)$  of  $T(u)$  as

$$T_i(u) \equiv T(u) \pmod{m_i(u)}, \quad i = 1, 2, \dots, k \quad (11)$$

Finally,  $T(u)$  can be reconstructed from the residues  $T_i(u)$  by the Chinese Remainder Theorem for polynomials (Ref. 15) as follows:

$$T(u) = T_1(u)M_1(u)M_1^{-1}(u) + \dots + T_k(u)M_k(u)M_k^{-1}(u) \pmod{u^n - 1} \quad (12)$$

where

$$M_i(u)M_i^{-1}(u) = 1 \pmod{m_i(u)} \text{ for } i = 1, \dots, k \quad (13)$$

Hence if the number of multiplications required to compute each  $T_i(u)$  can be reduced, the total number of multiplications needed for  $T(u)$  can also be reduced.

As an example, consider the cyclic convolution of 3 elements given in matrix form as

$$\begin{pmatrix} y_0 \\ y_1 \\ y_2 \end{pmatrix} = \begin{pmatrix} a_0 & a_1 & a_2 \\ a_1 & a_2 & a_0 \\ a_2 & a_0 & a_1 \end{pmatrix} \begin{pmatrix} x_0 \\ x_1 \\ x_2 \end{pmatrix} \quad (14)$$

When it is clear it is convenient to let  $[ ]^C$  represent the cyclic convolution of a matrix of the type shown in (14). Also let  $[ ]^T$  denote the transpose of a matrix. Then (14) can be rewritten as:

$$[y_0, y_1, y_2]^T = [a_0, a_1, a_2]^C [x_0, x_1, x_2]^T \quad (15)$$

The above convolution is obtained from the coefficients of

$$T(u) = (a_2 + a_0u + a_1u^2) \cdot (x_2 + x_1u + x_0u^2) \text{ mod } u^3 - 1 \quad (16)$$

Evidently a direct approach to compute (16) requires 9 multiplications. This number can be reduced to less than half as shown below.

To compute (16), factor  $u^3 - 1 = (u - 1)(u^2 + u + 1) = m_1(u)m_2(u) = m_1(u)M_1(u) = m_2(u)M_2(u)$  where  $m_1(u) = u - 1$  and  $m_2(u) = u^2 + u + 1$ . Here, the residues  $T_i(u) \equiv T(u) \text{ mod } m_i(u)$  are:

$$T_1(u) \equiv (a_2 + a_0 + a_1) \cdot (x_2 + x_1 + x_0) \text{ mod } (u - 1)$$

and

$$T_2(u) \equiv [(a_2 + a_1) + (a_0 + a_1)u] \cdot [(x_2 + x_0) + (x_1 + x_0)u] \text{ mod } (u^2 + u + 1)$$

Using the relations in (8),  $T_2(u)$  is given by

$$\begin{aligned} T_2(u) \equiv & (a_2 + a_1) \cdot (x_2 + x_0) + (a_0 + a_1) \cdot (x_1 + x_0) + [(a_2 + a_0) \\ & \cdot (x_2 + x_1) + (a_2 + a_1) \cdot (x_2 + x_0)] u \text{ mod } (u^2 + u + 1) \end{aligned}$$

Evidently 3 multiplications are needed to compute  $T_2(u)$ . From the Chinese Remainder Theorem for polynomials (Ref. 15),  $T(u)$  can be reconstructed from the residues  $T_1(u)$  and  $T_2(u)$  by the relation

$$T(u) \equiv T_1(u)M_1(u)M_1^{-1}(u) + T_2(u)M_2(u)M_2^{-1}(u) \text{ mod } (u^3 - 1) \quad (17)$$

where  $M_i^{-1}(u)$  uniquely satisfies the congruence  $M_i(u)M_i^{-1}(u) \equiv 1 \text{ mod } m_i(u)$  for  $i = 1, 2$ . These equations are satisfied by  $M_1^{-1}(u) = 1$  and  $M_2^{-1}(u) = u$ . Hence, from (17),

$$T(u) \equiv y_0 + y_1u + y_2u^2 \text{ mod } (u^3 - 1) \quad (18)$$

where  $y_0 = m_0 + m_1 + m_2$ ,  $y_1 = m_0 + m_2 + m_3$ ,  $y_2 = m_0 + m_3 + m_1$  and  $m_0 = (a_2 + a_0 + a_1) \cdot (x_2 + x_1 + x_0)$ ,  $m_1 = (a_2 + a_0) \cdot (x_2 + x_1)$ ,  $m_2 = (a_2 + a_1) \cdot (x_2 + x_0)$ ,  $m_3 = (a_0 + a_1) \cdot (x_1 + x_0)$ . From (18), only four multiplications are needed to perform (15).

Next, consider the cyclic convolution of 5 elements of  $GF(2^n)$ . Again such a convolution is represented in matrix form as

$$[y_0, y_1, y_2, y_3, y_4]^T = [a_0, a_1, a_2, a_3, a_4]^C [x_0, x_1, x_2, x_3, x_4]^T \quad (19)$$

where  $[ ]^T$  and  $[ ]^C$  denote the transpose and the cyclic matrices, respectively, and  $y_i, a_i, x_i \in GF(2^n)$  for  $i = 0, 1, 2, 3, 4$ . Again, this matrix equation can be obtained from the coefficients of

$$(a_4 + a_0u + a_1u^2 + a_2u^3 + a_3u^4) \cdot (x_4 + x_3u + x_2u^2 + x_1u^3 + x_0u^4) \pmod{(u^5 - 1)}$$

Since  $u^5 - 1 = (u - 1)(u^4 + u^3 + u^2 + u + 1) = m_1(u)m_2(u) = m_1(u)M_1(u) = m_2(u)M_2(u)$ , where  $m_1(u) = u - 1$  and  $m_2(u) = u^4 + u^3 + u^2 + u + 1$ , the system of congruences  $T_i(u) \equiv T(u) \pmod{m_i(u)}$  where  $i = 1, 2$  for this case is given by

$$T_1(u) \equiv (a_4 + a_0 + a_1 + a_2 + a_3) \cdot (x_4 + x_3 + x_2 + x_1 + x_0) \pmod{(u - 1)} \quad (20a)$$

and

$$\begin{aligned} T_2(u) \equiv & [(a_4 + a_3) + (a_0 + a_3)u + (a_1 + a_3)u^2 + (a_2 + a_3)u^3] \\ & \cdot [(x_4 + x_0) + (x_3 + x_0)u + (x_2 + x_0)u^2 \\ & + (x_1 + x_0)u^3] \pmod{(u^4 + u^3 + u^2 + u + 1)} \end{aligned} \quad (20b)$$

In order to compute (20b), let  $c_0 = (a_4 + a_3)$ ,  $c_1 = (a_0 + a_3)$ ,  $c_2 = (a_1 + a_3)$ ,  $c_3 = (a_2 + a_3)$ ,  $d_0 = (x_4 + x_0)$ ,  $d_1 = (x_3 + x_0)$ ,  $d_2 = (x_2 + x_0)$ ,  $d_3 = (x_1 + x_0)$ . Then,

$$\begin{aligned} T_2(u) \equiv & [c_0 + c_1u + c_2u^2 + c_3u^3] \cdot [d_0 + d_1u + d_2u^2 + d_3u^3] \\ \equiv & [(c_0 + c_1u) + u^2(c_2 + c_3u)] \cdot [(d_0 + d_1u) + u^2(d_2 + d_3u)] \\ \equiv & [A_0 + A_1u^2] \cdot [B_0 + B_1u^2] \pmod{(u^4 + u^3 + u^2 + u + 1)} \end{aligned} \quad (21)$$

where  $A_0 = c_0 + c_1u$ ,  $A_1 = c_2 + c_3u$ ,  $B_0 = d_0 + d_1u$  and  $B_1 = d_2 + d_3u$ . Now apply (8) at two levels, first to the expression  $(A_0 + A_1u^2)(B_0 + B_1u^2)$  and second to the expression of the form  $(A_0 + A_1) \cdot (B_0 + B_1) = [(c_0 + c_2) + (c_1 + c_3)u] \cdot [(d_0 + d_2) + (d_1 + d_3)u]$ , etc. By this means one can show that the set of coefficients of  $T_2(u)$  can be obtained with a total of only 9 multiplications. Finally, by the Chinese Remainder Theorem for polynomials (Ref. 15),  $T(u)$  is given by

$$T(u) = y_0 + y_1u + y_2u^2 + y_3u^3 + y_4u^4 \quad (22)$$

where

$$y_0 = m_0 + m_2 + m_9 + m_4 + m_5 + m_6,$$

$$y_1 = m_0 + m_1 + m_9 + m_4 + m_5 + m_7,$$

$$y_2 = m_0 + m_1 + m_9 + m_2 + m_5 + m_8,$$

$$y_3 = m_0 + m_1 + m_6 + m_7 + m_2 + m_8 + m_9 + m_3 + m_4,$$

$$y_4 = m_0 + m_1 + m_2 + m_3 + m_4 + m_5,$$

and

$$\begin{aligned}
m_0 &= (a_0 + a_1 + a_2 + a_3 + a_4) \cdot (x_0 + x_1 + x_2 + x_3 + x_4), \\
m_1 &= (a_0 + a_3) \cdot (x_3 + x_0), \quad m_2 = (a_1 + a_3) \cdot (x_2 + x_0); \\
m_3 &= (a_0 + a_2) \cdot (x_3 + x_1), \quad m_4 = (a_2 + a_3) \cdot (x_1 + x_0); \\
m_5 &= (a_4 + a_0 + a_2 + a_1) \cdot (x_4 + x_3 + x_2 + x_1); \\
m_6 &= (a_1 + a_2) \cdot (x_2 + x_1), \quad m_7 = (a_4 + a_0) \cdot (x_4 + x_3); \\
m_8 &= (a_4 + a_1) \cdot (x_4 + x_2), \quad m_9 = (a_4 + a_3) \cdot (x_4 + x_0).
\end{aligned}$$

Hence, by (22), the total number of multiplications required to perform (19) is 10.

We next consider the problem of computing the cyclic convolution of two sequences of  $l$  elements in  $GF(2^n)$  when  $l$  is not a prime number. This requires a result of Winograd (Ref. 13).

*Theorem 1:* Let  $s$  and  $t$  be relatively prime positive integers and  $A = (a_{ij})$  be the cyclic  $st \times st$  matrix (defined in Appendix A). Then there exists a permutation  $\pi$  such that  $B = (a_{\pi(i), \pi(j)})$  is partitioned into  $t \times t$  submatrices, where each submatrix is cyclic and the submatrices themselves form an  $s \times s$  cyclic matrix. For a proof see Ref. 14.

Now let  $l = l_1 \cdot l_2 \cdot \dots \cdot l_r$  where  $(l_i, l_j) = 1$  for  $i \neq j$ . By repeated applications of Theorem 1, it is readily seen that if the number of multiplications used to compute the cyclic convolution of  $l_i$  points is  $m_i$  for  $i = 1, 2, \dots, r$ , then the number of multiplications needed to compute an  $l$ -point cyclic convolution is equal to  $m_1, m_2, \dots, m_r$ .

Consider as an example the cyclic convolution of length 15 over  $GF(2^n)$ . By Theorem 1, one can permute the rows and columns of a  $15 \times 15$  cyclic matrix in such a way that this matrix forms a  $3 \times 3$  cyclic matrix with each matrix element being a  $5 \times 5$  cyclic submatrix as follows:

$$[E_0, E_1, E_2]^T = [A, B, C]^C [Y_0, Y_1, Y_2]^T \quad (23)$$

where  $E_0 = [y_0, y_6, y_{12}, y_3, y_9]^T$ ,  $E_1 = [y_{10}, y_1, y_7, y_{13}, y_4]^T$ ,  $E_2 = [y_5, y_{11}, y_2, y_8, y_{14}]^T$ ,  $A = [a_0, a_6, a_{12}, a_3, a_9]^C$ ,  $B = [a_{10}, a_1, a_7, a_{13}, a_4]^C$ ,  $C = [a_5, a_{11}, a_2, a_8, a_{14}]^C$ , and  $Y_i$  are the same as  $E_i$  with  $y_j$  replaced by  $x_j$ . By the same procedure used to compute the cyclic convolution of 3 elements, defined in (15), (23) becomes

$$E_0 = M_0 + M_1 + M_2, \quad E_1 = M_0 + M_2 + M_3, \quad E_2 = M_0 + M_3 + M_1 \quad (24)$$

where  $M_0 = (A + B + C) \cdot (Y_0 + Y_1 + Y_2)$ ,  $M_1 = (C + A) \cdot (Y_1 + Y_2)$ ,  $M_2 = (C + B) \cdot (Y_2 + Y_0)$ ,  $M_3 = (A + B) \cdot (Y_0 + Y_1)$ .

Clearly, (24) requires four  $(5 \times 5)$  cyclic matrix multiplications. To find  $M_i$  for  $i = 0, 1, 2, 3$ , one needs to multiply matrices of form  $(A + B + C)$ ,  $(C + A)$ ,  $(C + B)$ , and  $(A + B)$  by vectors  $(Y_0 + Y_1 + Y_2)$ ,  $(Y_1 + Y_2)$ ,  $(Y_2 + Y_0)$ , and  $(Y_0 + Y_1)$ , respectively. Again, with the same procedure that was used to compute the cyclic convolutions of 5 elements given in (19), one finally obtains the number of multiplications needed to perform  $M_i$  for  $i = 0, 1, 2, 3$ . Again each  $M_i$  can be obtained using 10 multiplications. Thus by (24) the total number of multiplications needed to compute the cyclic convolution of 15 elements in  $GF(2^n)$  is 40.

Finally, consider the cyclic convolutions of two sequences, where the number of points is a power of 2. For example, con-

sider the cyclic convolution of two 4-element sequences over  $GF(2^n)$ : Such a convolution can be represented in matrix form as

$$[y_0, y_1, y_2, y_3]^T = [a_0, a_1, a_2, a_3]^C [x_0, x_1, x_2, x_3]^T \quad (25)$$

By Theorem 1 in Appendix A, (25) can be rewritten as

$$[Y_1, Y_2]^T = [A, B]^C [X_1, X_2]^T$$

where

$$Y_1 = [y_2, y_1]^T, \quad Y_2 = [y_2, y_3]^T, \quad X_1 = [x_0, x_1]^T, \quad X_2 = [x_2, x_3]^T,$$

$$A = \begin{bmatrix} a_0 & a_1 \\ a_1 & a_2 \end{bmatrix}$$

and

$$B = \begin{bmatrix} a_2 & a_3 \\ a_3 & a_0 \end{bmatrix}$$

According to (9), we have  $Y_1 = D + E$  and  $Y_2 = D + F$ , where  $D = A \cdot (X_1 + X_2)$ ,  $E = (B - A) \cdot X_2$ , and  $F = (B - A) \cdot X_1$ , so that three matrix multiplications are needed. Observe that  $D, E$ , and  $F$  are also 2-point transforms of the form

$$\begin{pmatrix} a & b \\ b & c \end{pmatrix} \begin{pmatrix} x_1 \\ x_2 \end{pmatrix} = \begin{pmatrix} b(x_1 + x_2) + (a + b)x_1 \\ b(x_1 + x_2) + (b + c)x_2 \end{pmatrix} \quad (26)$$

With the above decomposition, one may compute  $D, E$ , and  $F$ , each with 3 multiplications. Thus, the total number of multiplications needed to perform the cyclic convolution of 4 elements is 9.

### III. The Computation of the Sum of Certain Elements of $GF(2^n)$ by Inspection

Sometimes, it is possible to show a priori that certain sums of elements of  $GF(2^n)$  actually lie in the ground field  $GF(2)$ . That is, if  $s$  is such a sum, then  $s = 0$  or  $s = 1$ . Hence multiplication by  $s$  need not be counted when considering the multiplicative complexity of an algorithm. This observation will be further studied in this section and utilized in the following sections. In this section, necessary and sufficient conditions are developed to determine when  $seGF(2^n)$  also lies in  $GF(2)$ . Moreover, if  $seGF(2)$ , it is shown how to evaluate it by inspecting a certain polynomial. This method will be used to simplify the complexity of the transforms in the next section.

*Theorem 2:* Let  $\alpha \in GF(2^n)$  be a primitive  $(2^n - 1)$ th root of unity. Let

$$\beta = \sum_{i \in I} \alpha^i$$

where  $I \subseteq \{0, 1, 2, \dots, 2^n - 1\}$ . Then  $\beta \in GF(2)$  if and only if  $2I = I$ , where the multiplication by 2 is taken mod  $(2^n - 1)$ .

*Proof:* Let  $\beta = \sum_{i \in I} \alpha^i$ . Then  $\beta^2 = \left( \sum_{i \in I} \alpha^i \right)^2 = \sum_{i \in I} \alpha^{2i}$

Since  $\beta \in GF(2)$  iff  $\beta^2 = \beta$ , it follows that  $\beta \in GF(2)$  iff  $\{2i \mid i \in I\} = I$  or  $2I = I$ .

*Example:* Let  $\alpha \in GF(2^3)$  be a primitive 7th root of 1. Then  $\alpha + \alpha^2 + \alpha^4 \in GF(2)$  since the set  $I = \{1, 2, 4\}$  is closed under multiplication by 2 (mod 7).

If  $\beta \in GF(2^n)$  satisfies the hypothesis of Theorem 2, one can determine whether  $\beta = 0$  or  $\beta = 1$ . This will be indicated in Theorem 3. First, however, note that if  $I \equiv \{0, 1, \dots, 2^n - 1\}$  has the property that  $2I = I$ , then one can express  $I = I_1 \cup I_2 \cup \dots \cup I_k$ , as a disjoint union of sets such that

(i)  $2I_j = I_j$  for  $j = 1, \dots, k$

and

(ii)  $I_j$  is minimal, i.e., if  $I_j \supseteq I_{j'}$  and  $2I_{j'} = I_{j'}$ , then either  $j = j'$  or  $I_{j'} = \emptyset$ .

In order to determine if

$$\beta = \sum_{i \in I} \alpha^i = 0 \text{ or } 1$$

first reduce the problem to sets  $I_j$  satisfying (ii) as well as (i). Then by set union, one can determine the general case when  $I = I_1 \cup \dots \cup I_k$ .

*Lemma:* Suppose  $|I_j| = d_j$ , where  $|I_j|$  denotes the number of elements in set  $I_j$  and suppose that  $2I_j = I_j$ , then  $I_j$  is minimal if and only if

$$I_j = \{i_0, 2i_0, \dots, 2^{d_j-1}i_0\}$$

for any  $i_0 \in I_j$ .

*Proof:* Suppose first that  $I_j$  is denoted as above. Since  $2I_j = I_j$ , it is clear that multiplication by 2 induces a cyclic permutation  $\pi$  on the elements  $i_0, 2i_0, \dots, 2^{d_j-1}i_0$ , with  $\pi^{d_j}(i_0) = i_0$ . Such a permutation is transitive; i.e., if  $a, b \in I_j$ , then there exists an integer  $s$ ,  $0 \leq s < d_j$  such that  $\pi^s(a) = b$ . Thus it is clear that  $I_j \neq I_k \cup I_l$  with  $I_k \cap I_l = \emptyset$ ,  $2I_k = I_k$ , and  $2I_l = I_l$ . Conversely, suppose  $I_j$  is minimal, and let  $i_0 \in I_j$ . Let  $s$  be the least positive integer such that  $\pi^s(i_0) = i_0$ . If  $s < d_j$ , then  $\{i_0, 2i_0, \dots, 2^{s-1}i_0\}$  is a proper subset of  $I_j$  closed under multiplication by 2. This contradicts the minimality of  $I_j$ . Thus  $s = d_j$ , hence

$$\{i_0, 2i_0, \dots, 2^{d_j-1}i_0\} = I_j$$

*Theorem 3:* Suppose  $\beta \in GF(2^n)$  and

$$\beta = \sum_{i \in I_j} \alpha^i,$$

where  $2I_j = I_j$  and  $I_j$  is minimal. Suppose also that  $|I_j| = d_j$ . Then  $\alpha^{i_0}$ , where  $i_0 \in I_j$  satisfies some irreducible polynomial

$$p(x) = x^{d_j} + a_{d_j-1} x^{d_j-1} + \dots + a_1 x + a_0$$

where  $a_k \in GF(2)$ , and furthermore,  $\beta = a_{d_j-1}$ .

*Proof:* Let  $i_0 \in I_j$ . Since  $I_j$  is minimal, it follows from the Lemma that

$$I_j = \{i_0, 2i_0, \dots, 2^{d_j-1} i_0\}$$

Let

$$p(x) = x^m + a_{m-1} x^{m-1} + \dots + a_1 x + a_0$$

be the minimal polynomial of  $\alpha^{i_0}$  over  $GF(2)$ . Then  $p(\alpha^i) = 0$  for all  $i \in I_j$ . Consequently,  $m = \deg p(x) = d_j$  and

$$p(x) = \prod_{k=0}^{d_j-1} (x - \alpha^{i_0 2^k})$$

By comparing the coefficients of  $x^{d_j-1}$  in  $p(x)$  it is readily seen that

$$\beta = a_{d_j-1}$$

*Example:* Let  $\alpha \in GF(2^n)$  satisfy  $x^3 + x^2 + 1 = 0$ . Then  $\alpha + \alpha^2 + \alpha^4 = 1$ , the coefficient of  $x^2$ .

#### IV. A Modified Winograd's Algorithm for Computing a Transform Over $GF(2^n)$ of $N$ Points for $N = 3, 5, 7, 9, 17$

In the introduction it was shown that a discrete Fourier transform defined in (3) can be appropriately rewritten via (5) and (6) in matrix form as shown in (7), namely,  $\tilde{B} = \tilde{W} \tilde{a}$  where  $\tilde{W}$  is an  $(N-1) \times (N-1)$  cyclic matrix. In this section, these  $N$ -point transforms are performed by the cyclic convolution approach described in Section II for  $N = 3, 5, 7, 9, 17$ . These short-length transforms are used in the next section to compute transforms of longer lengths of  $2^n - 1$  points, where  $n = 4, 5, 6, 8$ . Only the cases for  $N = 7$  and  $9$  are given explicitly in this section. The cases for  $N = 3, 5, 17$  are given more briefly in Appendix B.

Consider first the case  $N = 7$ . Let  $\gamma$  be a primitive 7th root of unity in  $GF(2^n)$ . The transform over  $GF(2^n)$  is expressible as

$$A_k = \sum_{i=0}^{7-1} a_i \gamma^{ik} \quad (27)$$

The permutation of  $\sigma$  for  $N = 7$  is given by  $\sigma(i) = 3^i \bmod 7$ . Applying this permutation to (6) one obtains a  $6 \times 6$  cyclic matrix equation. By Theorem 1 there exists a permutation  $\pi$  of rows and columns so that the  $6 \times 6$  cyclic matrix can be partitioned into a  $2 \times 2$  block matrix of  $3 \times 3$  cyclic matrices. This is accomplished as follows:

$$[B_3, B_5, B_6, B_4, B_2, B_1]^T = [\gamma^2, \gamma^1, \gamma^4, \gamma^5, \gamma^6, \gamma^3]^C [a_3, a_5, a_6, a_4, a_2, a_1]^T$$

or

$$[E_1, E_2]^T = [A, B]^C [X_1, X_2]^T \quad (28)$$

where  $E_1 = [B_3, B_5, B_6]$ ,  $E_2 = [B_4, B_2, B_1]$ ,  $A = [\gamma^2, \gamma^1, \gamma^4]^C$ ,  $B = [\gamma^5, \gamma^6, \gamma^3]^C$ ,  $X_1 = [a_3, a_5, a_6]^T$ ,  $X_2 = [a_4, a_2, a_1]^T$ . Using the 2-point cyclic convolution for the matrices in (28) yields

$$[E_1, E_2]^T = [D + E, D + F]^T$$

where  $D = (X_1 + X_2) \cdot A$ ,  $E = (B - A) \cdot X_2$ ,  $F = (B - A) \cdot X_1$ .

Since  $A$  and  $B$  are cyclic matrices, it is evident that the matrix  $B - A$  is also a cyclic matrix. Using the same procedure for computing the 3-point cyclic convolution in (14) one can compute  $D$ ,  $E$ , and  $F$ . Each of these quantities requires 4 multiplications. After some algebraic manipulations one finally arrives at the following expressions for the 7-point transform (27); namely,

$$\begin{aligned} A_0 &= m_0, A_1 = m_0 + m_1 + m_2 + m_3 + m_4 + m_5 + m_6; \\ A_2 &= m_0 + m_1 + m_7 + m_2 + m_4 + m_8 + m_5; \\ A_3 &= m_0 + m_1 + m_3 + m_7 + m_9 + m_{10} + m_{11}; \\ A_4 &= m_0 + m_1 + m_3 + m_7 + m_4 + m_6 + m_8; \\ A_5 &= m_0 + m_1 + m_7 + m_2 + m_9 + m_{11} + m_{12}; \\ A_6 &= m_0 + m_1 + m_2 + m_3 + m_9 + m_{12} + m_{10} \end{aligned} \tag{29}$$

where

$$\begin{aligned} m_0 &= 1 \cdot (a_0 + a_1 + a_2 + a_3 + a_4 + a_5 + a_6); \\ m_1 &= (\gamma^2 + \gamma^1 + \gamma^4 + 1) \cdot (a_3 + a_4 + a_5 + a_2 + a_6 + a_1); \\ m_2 &= (\gamma^2 + \gamma^1) \cdot (a_5 + a_2 + a_3 + a_4); \\ m_3 &= (\gamma^4 + \gamma^2) \cdot (a_6 + a_1 + a_5 + a_2); \\ m_4 &= 1 \cdot (a_3 + a_3 + a_6); \\ m_5 &= (\gamma^2 + \gamma^5 + \gamma^1 + \gamma^6) \cdot (a_5 + a_3); \\ m_6 &= (\gamma^4 + \gamma^3 + \gamma^2 + \gamma^5) \cdot (a_6 + a_5); \\ m_7 &= (\gamma^4 + \gamma^1) \cdot (a_6 + a_1 + a_3 + a_4); \\ m_8 &= (\gamma^4 + \gamma^3 + \gamma^2 + \gamma^5) \cdot (a_6 + a_3); \\ m_9 &= 1 \cdot (a_4 + a_2 + a_1); \end{aligned}$$

$$m_{10} = (\gamma^4 + \gamma^3 + \gamma^2 + \gamma^5) \cdot (a_1 + a_2);$$

$$m_{11} = (\gamma^4 + \gamma^3 + \gamma^1 + \gamma^6) \cdot (a_1 + a_4);$$

$$m_{12} = (\gamma^2 + \gamma^5 + \gamma^1 + \gamma^6) \cdot (a_2 + a_4);$$

Now factor  $x^7 - 1$  into a product of irreducible polynomials over  $GF(2)$ ; i.e.,  $x^7 - 1 = (x - 1)(x^3 + x + 1)(x^3 + x^2 + 1)$ . Let  $I = \{2, 1, 4\}$ . Then  $2I = I$ . By Theorem 2,  $(\gamma^2 + \gamma^1 + \gamma^4) = 0$  or  $1$ . Observe that  $I$  is minimal and  $|I| = 3$ . Next choose  $\gamma$  so that  $\gamma$  satisfies  $x^3 + x^2 + 1$ , then, by Theorem 3,  $\gamma^2 + \gamma^1 + \gamma^4 = 1$ . Thus  $m_1$ , in (29) is equal to zero. Hence, from (29), one observes that the number of multiplications needed to perform a 7-point transform over  $GF(2^n)$  is 9, excluding the multiplications by the unit  $\gamma^0 = 1$ . In what follows it will be necessary to consider a multiplication by the element  $\gamma^0$ . Hence, if one includes multiplications by the unit  $\gamma^0 = 1$ , the number of multiplications needed to perform the above transform is 12.

Next consider  $N_i = 3^2$ . Let  $\gamma$  be the 9th root of unity in  $GF(2^n)$ . The permutation of  $W$  as defined in (6) for a 9-point transform over  $GF(2^n)$  is given as follows:

$$\begin{pmatrix} b_2 \\ b_5 \\ b_8 \\ b_7 \\ b_4 \\ b_1 \\ b_3 \\ b_6 \end{pmatrix} = \begin{pmatrix} \gamma^4 & \gamma^8 & \gamma^7 & \gamma^5 & \gamma^1 & \gamma^2 & \gamma^3 & \gamma^6 \\ \gamma^8 & \gamma^7 & \gamma^5 & \gamma^1 & \gamma^2 & \gamma^4 & \gamma^6 & \gamma^3 \\ \gamma^7 & \gamma^5 & \gamma^1 & \gamma^2 & \gamma^4 & \gamma^8 & \gamma^3 & \gamma^6 \\ \gamma^5 & \gamma^1 & \gamma^2 & \gamma^4 & \gamma^8 & \gamma^7 & \gamma^6 & \gamma^3 \\ \gamma^1 & \gamma^2 & \gamma^4 & \gamma^8 & \gamma^7 & \gamma^5 & \gamma^3 & \gamma^6 \\ \gamma^2 & \gamma^4 & \gamma^8 & \gamma^7 & \gamma^5 & \gamma^1 & \gamma^6 & \gamma^3 \\ \gamma^3 & \gamma^6 & \gamma^3 & \gamma^6 & \gamma^3 & \gamma^6 & 1 & 1 \\ \gamma^6 & \gamma^3 & \gamma^6 & \gamma^3 & \gamma^6 & \gamma^3 & 1 & 1 \end{pmatrix} \begin{pmatrix} a_2 \\ a_5 \\ a_8 \\ a_7 \\ a_4 \\ a_1 \\ a_3 \\ a_6 \end{pmatrix} \quad (30)$$

The upper left 6x6 matrix of (30) is a cyclic matrix defined by

$$[Y_2, Y_5, Y_8, Y_7, Y_4, Y_1]^T = [\gamma^4, \gamma^1, \gamma^7, \gamma^5, \gamma^8, \gamma^2]^C \cdot [a_2, a_5, a_8, a_7, a_4, a_1]^T \quad (31)$$

By a procedure similar to that used to compute the matrix defined in (28), one obtains

$$\begin{aligned} Y_1 &= m_1 + m_2 + m_3 + m_4 + m_5 + m_6, & Y_4 &= m_1 + m_7 + m_2 + m_4 + m_8 + m_5; \\ Y_2 &= m_1 + m_3 + m_7 + m_9 + m_{10} + m_{11}, & Y_7 &= m_1 + m_3 + m_7 + m_4 + m_6 + m_8; \\ Y_5 &= m_1 + m_7 + m_9 + m_{11} + m_{12}, & Y_8 &= m_1 + m_2 + m_3 + m_9 + m_{12} + m_{10}; \end{aligned} \quad (32)$$

where

$$m_1 = (\gamma^4 + \gamma^1 + \gamma^7) \cdot (a_2 + a_7 + a_5 + a_4 + a_8 + a_1);$$

$$m_2 = (\gamma^4 + \gamma^1) \cdot (a_5 + a_4 + a_2 + a_7);$$

$$m_3 = (\gamma^7 + \gamma^4) \cdot (a_8 + a_1 + a_5 + a_4);$$

$$m_4 = (\gamma^4 + \gamma^1 + \gamma^7 + \gamma^5 + \gamma^8 + \gamma^2) \cdot (a_2 + a_5 + a_8);$$

$$m_5 = (\gamma^4 + \gamma^5 + \gamma^1 + \gamma^8) \cdot (a_5 + a_2);$$

$$m_6 = (\gamma^7 + \gamma^2 + \gamma^4 + \gamma^5) \cdot (a_8 + a_5);$$

$$m_7 = (\gamma^7 + \gamma^1) \cdot (a_8 + a_1 + a_2 + a_7);$$

$$m_8 = (\gamma^7 + \gamma^2 + \gamma^1 + \gamma^8) \cdot (a_8 + a_2);$$

$$m_9 = (\gamma^4 + \gamma^1 + \gamma^7 + \gamma^5 + \gamma^8 + \gamma^2) \cdot (a_7 + a_4 + a_1);$$

$$m_{10} = (\gamma^7 + \gamma^2 + \gamma^4 + \gamma^5) \cdot (a_1 + a_4);$$

$$m_{11} = (\gamma^7 + \gamma^2 + \gamma^1 + \gamma^8) \cdot (a_1 + a_7);$$

$$m_{12} = (\gamma^4 + \gamma^5 + \gamma^1 + \gamma^8) \cdot (a_4 + a_7).$$

If  $x^9 - 1$  is factored into a product of irreducible polynomials over  $GF(2)$ , one has  $x^9 - 1 = (x - 1)(x^2 + x + 1)(x^6 + x^3 + 1)$ . Let  $I = (4, 1, 7, 5, 8, 2)$ . Then  $2I = I$ . Observe that  $I$  is minimal and  $|I| = 6$ . For this case choose  $\gamma$  so that  $\gamma$  satisfies  $x^6 + x^3 + 1$ . Then, by Theorem 2 and Theorem 3  $(\gamma^4 + \gamma^1 + \gamma^7 + \gamma^5 + \gamma^8 + \gamma^2) = 0$  in (32). This implies  $m_4 = m_9 = 0$  in (32). From (32), one observes that the number of multiplications needed to perform (31) is exactly 10.

The last two columns of the matrix defined in (30) can be obtained by the following  $2 \times 2$  cyclic matrix

$$[x_1, x_2]^T = [\gamma^3, \gamma^6]^C [a_3, a_6]^T = [\gamma^3(a_3 + a_6) + (\gamma^3 + \gamma^6)a_6, \gamma^3(a_3 + a_6) + (\gamma^3 + \gamma^6)a_3]^T \quad (33)$$

But  $\gamma^3 + \gamma^6 = 1$ . Thus, (33) becomes

$$[x_1, x_2]^T = [\gamma^3(a_3 + a_6) + 1 \cdot a_6, \gamma^3(a_3 + a_6) + 1 \cdot a_1]$$

Similarly, the last two rows of the matrix defined in (30) can be obtained by computing the following cyclic matrix

$$\begin{aligned} [Z_1, Z_2]^T &= [\gamma^3, \gamma^6]^C [a_1 + a_4 + a_7, a_2 + a_5 + a_8]^T \\ &= [\gamma^3(a_1 + a_4 + a_7 + a_2 + a_5 + a_8) + 1 \cdot (a_2 + a_3 + a_8), \\ &\quad \gamma^3(a_1 + a_4 + a_7 + a_2 + a_5 + a_8) + 1 \cdot (a_1 + a_4 + a_7)]^T \end{aligned} \quad (34)$$

Note that one multiplication is needed to compute (33). Similarly (34) requires only 1 multiplication. Thus, the algorithm for computing the 9-point transform is

$$\begin{aligned}
b_0 &= 1 \cdot (a_0 + a_1 + a_2 + a_3 + a_4 + a_5 + a_6 + a_7 + a_8); \\
b_1 &= Y_1 + X_1 + 1 \cdot a_1, \quad b_2 = Y_2 + X_2 + 1 \cdot a_0, \quad b_3 = Z_1 + 1 \cdot (a_3 + a_6 + a_0); \\
b_4 &= Y_4 + X_1 + 1 \cdot a_0, \quad b_5 = Y_5 + X_2 + 1 \cdot a_0, \quad b_6 = Z_1 + 1 \cdot (a_1 + a_6 + a_0); \\
b_7 &= Y_7 + X_1 + 1 \cdot a_0, \quad b_8 = Y_8 + X_2 + 1 \cdot a_0.
\end{aligned} \tag{35}$$

From (35), the total number of multiplications needed to perform a 9-point transform is 12, excluding multiplications by the unit 1. Again, the algorithms for computing  $N$ -point transforms over  $GF(2^n)$  for  $N = 3, 5, 17$  are given in Appendix B.

## V. Transforms Over $GF(2^n)$ of $2^n - 1$ Points Where $n = 4, 5, 6, 8$

For  $N = N_1 N_2 \dots N_k$ , where  $(N_i, N_j) = 1$ , it was shown by Winograd in Refs. 13 and 14 that the transform matrix  $W'$  defined in (5) can be transformed into the product of  $W'_1, W'_2, \dots, W'_k$ , where  $W'_i$  is the matrix of an  $N_i$ -point discrete Fourier-like transform. Assume that  $m_i$  multiplications are needed to perform an  $N_i$ -point transform over  $GF(2^n)$  for  $1 \leq i \leq k$ . Then,  $m_1 m_2 \dots m_k$  multiplications are needed to compute the  $N$ -point transform.

Suppose  $N = 2^4 - 1 = 3 \times 5$ . Since the 15th roots of unity lie in  $GF(2^4)$ ,  $GF(2^4)$  is the appropriate domain for calculating the transform of 15 points using the algorithm described in the last paragraph of the previous section. The Chinese Remainder Theorem is used to represent each integer  $i$  ( $0 \leq i < 15$ ) by the pair  $(i_1, i_2) = (i \bmod 3, i \bmod 5)$ . Further, let  $\gamma_1, \gamma_2$ , and  $\gamma_3$  be the 3rd, 5th and 15th roots of unity in  $GF(2^4)$ , respectively. Then, the 15-point transform over  $GF(2^4)$  is

$$A_j = \sum_{i=0}^{14} a_i \gamma^{ij} \tag{36a}$$

After representing  $i$  and  $j$  by  $i = (i_1, i_2) = (i \bmod 3, i \bmod 5)$  and  $j = (j_1, j_2) = (j \bmod 3, j \bmod 5)$  respectively,

$$A_{(j_1, j_2)} = \sum_{i_1=0}^2 \left[ \sum_{i_2=0}^4 a_{(i_1, i_2)} \gamma_2^{i_2 \cdot i_2} \right] \gamma_1^{i_1 \cdot j_1} = \sum_{k_1=0}^2 a_{i_1}(j_2) \gamma_1^{i_1 \cdot j_1} \tag{36b}$$

where  $a_{i_1}(j_2)$  is the 5-point transform over  $GF(2^4)$  defined by

$$a_{i_1}(j_2) = \sum_{i_2=0}^4 a_{(i_1, i_2)} \gamma_2^{i_2 \cdot j_2}$$

Expressing (36b) in matrix notation, we have

$$(a_{i_1}(j_2)) = W'_2 \bar{a}_{i_1}$$

where

$$W'_2 = \begin{pmatrix} \gamma_2^0 & \gamma_2^0 & \gamma_2^0 & \gamma_2^0 & \gamma_2^0 \\ \gamma_2^0 & \gamma_2^1 & \gamma_2^2 & \gamma_2^3 & \gamma_2^4 \\ \gamma_2^0 & \gamma_2^2 & \gamma_2^4 & \gamma_2^1 & \gamma_2^3 \\ \gamma_2^0 & \gamma_2^3 & \gamma_2^1 & \gamma_2^4 & \gamma_2^2 \\ \gamma_2^0 & \gamma_2^4 & \gamma_2^3 & \gamma_2^2 & \gamma_2^1 \end{pmatrix}, \quad \bar{a}_{i_1} = \begin{pmatrix} a_{(i_1,0)} \\ a_{(i_1,1)} \\ a_{(i_1,2)} \\ a_{(i_1,3)} \\ a_{(i_1,4)} \end{pmatrix} \quad (37)$$

Thus (36) becomes

$$\bar{A}_{j_1} = \sum_{i_1=0}^2 \gamma_1^{i_1 j_1} W'_2 \bar{a}_{i_1} \quad \text{for } j = 0, 1, 2 \quad (38)$$

or

$$\begin{pmatrix} \bar{A}_0 \\ \bar{A}_1 \\ \bar{A}_2 \end{pmatrix} = \begin{pmatrix} W'_2 & W'_2 & W'_2 \\ W'_2 & W'_2 \gamma_1 & W'_2 \gamma_1^2 \\ W'_2 & W'_2 \gamma_1^2 & W'_2 \gamma_1 \end{pmatrix} \begin{pmatrix} \bar{a}_0 \\ \bar{a}_1 \\ \bar{a}_2 \end{pmatrix}$$

where  $\bar{A}_0$  is in terms of  $A_k$  as:

$$\bar{A}_0 = [A_{(0,0)}, A_{(0,1)}, A_{(0,2)}, A_{(0,3)}, A_{(0,4)}]^T = [A_0, A_6, A_{12}, A_3, A_9]^T \quad (39)$$

Similarly,  $\bar{A}_1 = [A_{10}, A_1, A_7, A_{13}, A_4]^T$ ,  $\bar{A}_2 = [A_5, A_{11}, A_2, A_8, A_{14}]^T$ , and  $\bar{a}_0$  through  $\bar{a}_2$  are obtained from the expressions for  $\bar{A}_0$  through  $\bar{A}_2$  on replacing each  $A_i$  by  $a_i$ . Using the 3-point transform (B-1) in Appendix B and making the correspondence,  $\gamma^0 \leftrightarrow W'_2$ ,  $\gamma^1 \leftrightarrow W'_2 \gamma_1$ ,  $\gamma^2 \leftrightarrow W'_2 \gamma_1^2$ , one obtains

$$\bar{A}_0 = M_0; \quad \bar{A}_1 = M_0 + M_1 + M_2; \quad \bar{A}_2 = M_0 + M_1 + M_3 \quad (40)$$

where  $M_0 = W'_2(\bar{a}_0 + \bar{a}_1 + \bar{a}_2)$ ,  $M_1 = W'_2(\gamma_1 + 1)(\bar{a}_1 + \bar{a}_2)$ ,  $M_2 = W'_2 \bar{a}_2$ ,  $M_3 = W'_2 \bar{a}_1$ . Thus, Eq. (40) requires four matrix multiplications.

Observe that all four matrix multiplications in (40) are 5-point transforms of exactly the same form as (B-2) in Appendix B. Thus one may compute  $M_j$  for  $j = 0, 1, 2, 3$  in (40) with a procedure similar to that used to compute the matrix defined in (B-2). The number of multiplications for computing an  $M_j$  for  $j = 0, 1, 2, 3$  in (40) is 5, excluding multiplication by  $\gamma^0$ . Thus, the total number of multiplications needed to compute a 15-point transform is  $4 \times 5 = 20$ .

Consider now a transform of  $N = 31$  points. Let  $\gamma$  be a 31st root of unity in  $GF(2^5)$ . Here the  $31 \times 31$  matrix is of the form given in (4) where  $N = 31$ . Now since  $N = 31$  is prime, the permutation  $\sigma$  is given by  $\sigma(i) = 3^i \bmod 31$ ,  $i = 1, 2, 3, \dots, 30$ . Using this permutation, one can permute the indices of  $B$ ,  $a$ ,  $W$  defined in (6) so that the matrix  $\tilde{W} = (\gamma^{\sigma(i)\sigma(j)})_{i,j \neq 0}$  is cyclic for  $i, j = 1, 2, \dots, 30$ . Next since  $N - 1 = 30 = 2 \times 15$ , then, by Theorem 1, the  $30 \times 30$  cyclic matrix  $\tilde{W}$  can be first partitioned into  $15 \times 15$  submatrices where each submatrix is a  $2 \times 2$  cyclic matrix. By (26), only three matrix multiplications are needed to

perform these  $2 \times 2$  cyclic matrices. Also by (23), the number of multiplications needed to compute a  $15 \times 15$  cyclic matrix is 40. Thus, the total number of multiplications needed to perform a 31-point transform is  $3 \times 40 = 120$ .

Next consider the finite field  $GF(2^6)$ . Since  $N = 2^6 - 1 = 63 = N_1 \cdot N_2 = 7 \cdot 9$ , by Winograd's algorithm one needs to compute an  $N_i$ -point transform over  $GF(2^6)$  for  $N_i = 7$  and 9. It was shown in the previous section that the number of multiplications needed to perform a 7-point transform over  $GF(2^6)$  is 12, including the multiplications by the unity  $\gamma^0 = 1$ , and that the number of multiplications needed to perform a 9-point transform is 12, excluding multiplications by the unity  $\gamma^0 = 1$ . By the same procedure used to compute a 15-point transform over  $GF(2^4)$  in (36a), the total number of multiplications needed to perform a 63-point transform over  $GF(2^6)$  is  $12 \times 12 = 144$ .

Consider now the transform over  $GF(2^8)$  of 255 points. Since  $N = 255 = 3 \cdot 5 \cdot 17 = N_1 \cdot N_2 \cdot N_3$ , by Winograd's algorithm one needs to compute an  $N_i$ -point transform over  $GF(2^8)$  for  $N_i = 3, 5, 17$ . An  $N_i$ -transform over  $GF(2^8)$  for  $N_i = 3, 5$  and 17 is computed in Appendix B. With the procedure used to compute the 15-point transform over  $GF(2^4)$  in (36a), the total number of multiplications needed to perform a 255-point transform over  $GF(2^8)$  is  $4 \times 10 \times 57 = 2180$  multiplications.

## VI. Comparison of New Algorithm With Gentleman's Algorithm

If  $N = 2^n - 1 = N_1 \cdot N_2 \cdot \dots \cdot N_k$ , where  $(N_i, N_j) = 1$  for  $i \neq j$ , Gentleman showed (Refs. 5 and 12) that an  $N$ -point transform  $N$  requires  $N(N_1 + N_2 + \dots + N_k - k + 1)$  multiplications. The present algorithm for computing the  $(2^n - 1)$ -point transform for  $n = 4, 5, 6, 8$  and Gentleman's algorithm are compared in Table 1. The number of multiplications needed to perform these algorithms is given in both cases. Evidently for  $n = 4, 5, 6, 8$  the new algorithm for computing the  $(2^n - 1)$ -point transform requires considerably fewer multiplications than Gentleman's algorithm.

## VII. Transform Decoding of Reed-Solomon Codes

Let  $N$  be the block length of an RS code over  $GF(2^n)$ . Also let  $d = 2t + 1$  be the minimum distance of the code, where  $t$  is the number of allowable errors. It was shown in Ref. 5 that a finite field transform over  $GF(2^n)$  can be used to compute the syndrome and error magnitudes. It follows from Refs. 15 and 16 that the number of multiplications required to perform the syndrome and error magnitude calculations for the standard decoder is approximately  $(N - 1)(d - 1) + t^2$ .

For a  $(2^n - 1, d)$  RS code where  $d = 2t + 1$ , the number of multiplications needed to compute the syndrome and the error magnitudes is given in Table 2 for  $n = 4, 5, 6, 8$ . For comparison, the corresponding number of multiplications required by Gentleman's algorithm and by the standard algorithm are also given in the table.

## Appendix A

*Definition:* An  $n \times n$  matrix  $A = (a_{ij})$  ( $0 \leq i, j \leq n - 1$ ) is cyclic if  $a_{ij} = a_{i+1, j-1}$ , where the indices are computed mod  $n$ .

*Theorem 1:* Let  $A$  be any  $n \times n$  cyclic matrix, and suppose  $n = a \times b$ , where  $(a, b) \neq 1$ . Then  $A$  can be partitioned into a cyclic  $a \times a$  matrix whose entries are themselves  $b \times b$  submatrices.

*Proof:* Omitted.

## Appendix B

This Appendix presents a brief summary of the transform algorithm of  $N$  points for  $N = 3, 5, 17$ . For  $N = 3$ , let  $\gamma$  be the 3rd root of unity in  $GF(2^n)$  such that  $\gamma$  satisfies the irreducible polynomial  $x^2 + x + 1$ . The transform over  $GF(2^n)$  is

$$A_k = \sum_{n=0}^2 a_n \gamma^{nk} \quad \text{for } k = 0, 1, 2 \quad (\text{B-1})$$

Let  $m_0 = 1 \cdot (a_0 + a_1 + a_2)$ ,  $m_1 = (a_1 + a_2) \cdot \gamma^1$ ,  $m_2 = (\gamma^2 - \gamma^1) \cdot a_1 = 1 \cdot a_1$ , and  $m_3 = (\gamma^2 - \gamma^1) \cdot a_2 = 1 \cdot a_2$ . Thus,  $A_0 = m_0$ ,  $A_1 = m_0 + m_1 + m_2$ , and  $A_2 = m_0 + m_1 + m_3$ . Hence, the total number of multiplications needed to perform the above transform is 4, including multiplications by the unit 1.

Next consider the case  $N = 5$ . Let  $\gamma$  be a 5th root of unity in  $GF(2^n)$  such that  $\gamma$  satisfies the irreducible polynomial  $x^4 + x^3 + x^2 + x + 1$ . The 5-point transform is

$$A_k = \sum_{n=0}^{5-1} a_n \gamma^{nk} \quad \text{for } k = 0, 1, 2, 3, 4 \quad (\text{B-2})$$

Let  $A_0 = \gamma^0(a_0 + a_1 + a_2 + a_3 + a_4 + a_5)$ , and also let  $\sigma(i) = 2^i \bmod 5$ . Equation (B-2) becomes

$$\tilde{B} = [B_2, B_4, B_3, B_1]^T = [\gamma^4, \gamma^3, \gamma^1, \gamma^2]^C [a_2, a_4, a_3, a_1]^T \quad (\text{B-3})$$

By a procedure similar to that used to compute the cyclic convolution of 4 elements of  $GF(2^n)$  in (25), one may compute (B-3). Thus, after some algebraic manipulations on (B-2) and (B-3) one arrives at the following expressions for the 5-point transform:

$$\begin{aligned} A_0 &= m_0, A_1 = S_2 + m_5 + m_9, A_2 = S_1 + m_2 + m_6; \\ A_3 &= S_1 + m_5 + m_8, A_4 = S_2 + m_4 + m_7. \end{aligned} \quad (\text{B-4})$$

where  $m_0 = \gamma^0 \cdot (a_0 + a_1 + a_2 + a_3 + a_4)$ ,  $m_1 = (\gamma^0 + \gamma^3) \cdot (a_1 + a_2 + a_3 + a_4)$ ,  $m_2 = (\gamma^3 + \gamma^4) \cdot (a_2 + a_3)$ ,  $m_3 = (\gamma^1 + \gamma^3) \cdot (a_1 + a_4)$ ,  $m_4 = (\gamma + \gamma^4) \cdot (a_1 + a_3)$ ,  $m_5 = (\gamma + \gamma^4) \cdot (a_2 + a_4)$ ,  $m_6 = 1 \cdot a_1$ ,  $m_7 = 1 \cdot a_3$ ,  $m_8 = 1 \cdot a_4$ ,  $m_9 = 1 \cdot a_2$ ,  $S_1 = m_0 + m_1 + m_2$ ,  $S_2 = m_0 + m_1 + m_3$ .

If again one includes multiplications by the unit 1, it follows from the algorithm in (B-4) that the number of integer multiplications needed to perform a 5-point transform is 10. If multiplications by 1 are excluded, only 5 multiplications are needed.

Now consider the case  $N = 17$ . The permutation  $\sigma$  is  $\sigma(i) = 5^i \bmod 17$ . Applying this permutation to (6) one obtains a  $16 \times 16$  cyclic matrix. By Theorem 2, the cyclic matrix can be partitioned into blocks of  $4 \times 4$  matrices so that the blocks form a  $4 \times 4$  cyclic matrix. This has the form

$$[T_2, T_4, T_3, T_1]^T = [A, B, C, D]^C [S_2, S_4, S_3, S_1]^T \quad (\text{B-5})$$

where  $T_2 = [b_5, b_8, b_6, b_{13}]^T$ ,  $T_4 = [b_{14}, b_2, b_{10}, b_{16}]^T$ ,  $T_3 = [b_{12}, b_9, b_{11}, b_4]^T$ ,  $T_1 = [b_3, b_5, b_7, b_1]^T$ .

$$A = \begin{pmatrix} \gamma^8 & \gamma^6 & \gamma^{14} & \gamma^{13} \\ \gamma^6 & \gamma^{13} & \gamma^{14} & \gamma^2 \\ \gamma^{13} & \gamma^{14} & \gamma^2 & \gamma^{10} \\ \gamma^{14} & \gamma^2 & \gamma^{10} & \gamma^{16} \end{pmatrix}, \quad B = \begin{pmatrix} \gamma^2 & \gamma^{10} & \gamma^{16} & \gamma^{12} \\ \gamma^{10} & \gamma^{16} & \gamma^{12} & \gamma^9 \\ \gamma^{16} & \gamma^{12} & \gamma^9 & \gamma^{11} \\ \gamma^{12} & \gamma^9 & \gamma^{11} & \gamma^4 \end{pmatrix}$$

$$C = \begin{pmatrix} \gamma^9 & \gamma^{11} & \gamma^4 & \gamma^3 \\ \gamma^{11} & \gamma^4 & \gamma^3 & \gamma^{15} \\ \gamma^4 & \gamma^3 & \gamma^{15} & \gamma^7 \\ \gamma^3 & \gamma^{15} & \gamma^7 & \gamma^1 \end{pmatrix}, \quad D = \begin{pmatrix} \gamma^{15} & \gamma^7 & \gamma^1 & \gamma^5 \\ \gamma^7 & \gamma^1 & \gamma^5 & \gamma^8 \\ \gamma^1 & \gamma^5 & \gamma^8 & \gamma^6 \\ \gamma^5 & \gamma^8 & \gamma^6 & \gamma^{13} \end{pmatrix}$$

and  $S_1$  through  $S_4$  are obtained from the expressions for  $T_1$  through  $T_4$  on replacing each  $b_i$  by  $a_i$ .

By a procedure similar to that used to compute the cyclic matrix of 4 elements in (25), we obtain

$$\begin{aligned} T_2 &= V_1 + N_4 + N_6, & T_4 &= V_2 + N_4 + N_7, \\ T_3 &= V_1 + N_5 + N_8, & T_1 &= V_2 + N_5 + N_9, \end{aligned} \tag{B-6}$$

where

$$\begin{aligned} N_1 &= B(S_1 + S_2 + S_3 + S_4), & N_2 &= (A + B) \cdot (S_2 + S_3), \\ N_3 &= (C + B) \cdot (S_1 + S_4), & N_4 &= (C + A) \cdot (S_3 + S_1), \\ N_5 &= (C + A) \cdot (S_2 + S_4), & N_6 &= E \cdot S_1, \\ N_7 &= E \cdot S_3, & N_8 &= E \cdot S_4, & N_9 &= E \cdot S_2 \end{aligned} \tag{B-7}$$

and

$$V_1 = N_1 + N_2, \quad V_2 = N_1 + N_3,$$

where  $E = A + B + C + D$ . Note that (B-7) requires nine  $(4 \times 4)$  matrix multiplications. Observe that  $N_i$  for  $i = 1, 2, \dots, 9$  in (B-6) can all be put in the form,

$$\begin{pmatrix} b_1 \\ b_2 \\ b_3 \\ b_4 \end{pmatrix} = \begin{pmatrix} \gamma^1 & \gamma^2 & \gamma^3 & \gamma^4 \\ \gamma^2 & \gamma^3 & \gamma^4 & \gamma^5 \\ \gamma^3 & \gamma^4 & \gamma^5 & \gamma^6 \\ \gamma^4 & \gamma^5 & \gamma^6 & \gamma^7 \end{pmatrix} \begin{pmatrix} a_1 \\ a_2 \\ a_3 \\ a_4 \end{pmatrix} \tag{B-8}$$

To compute (B-8), write it as

$$\begin{pmatrix} F_0 \\ F_1 \end{pmatrix} = \begin{pmatrix} J & K \\ K & L \end{pmatrix} \begin{pmatrix} E_0 \\ E_1 \end{pmatrix} = \begin{pmatrix} U_1 + U_2 \\ U_1 + U_3 \end{pmatrix} \quad (\text{B-9})$$

where  $U_1 = (E_0 + E_1) \cdot K$ ,  $U_2 = (J + K) \cdot E_0$ ,  $U_3 = (L + K) \cdot E_0$  are three  $(2 \times 2)$  matrix multiplications.

The matrix  $U_1$  in (B-9) is given by the relationship

$$\begin{aligned} U_1 &= \begin{pmatrix} u_0 \\ u_1 \end{pmatrix} = \begin{pmatrix} \gamma^3 & \gamma^4 \\ \gamma^4 & \gamma^5 \end{pmatrix} \begin{pmatrix} a_1 + a_3 \\ a_2 + a_4 \end{pmatrix} \\ &= \begin{pmatrix} (a_1 + a_3 + a_2 + a_4) \cdot \gamma^4 + (\gamma^3 + \gamma^4) \cdot (a_1 + a_3) \\ (a_1 + a_3 + a_2 + a_4) \cdot \gamma^4 + (\gamma^4 + \gamma^5) \cdot (a_1 + a_3) \end{pmatrix} \end{aligned}$$

The matrices  $U_2$  and  $U_3$  in (B-9) can also be obtained in a similar manner.

Now, let

$$\begin{aligned} M_1 &= \gamma^4 \cdot (a_1 + a_2 + a_3 + a_4), & M_2 &= (a_1 + a_3) \cdot (\gamma^3 + \gamma^4); \\ M_3 &= (\gamma^4 + \gamma^5) \cdot (a_1 + a_3), & M_4 &= (\gamma^2 + \gamma^4) \cdot (a_1 + a_2); \\ M_5 &= (\gamma^4 + \gamma^6) \cdot (a_1 + a_2), & M_6 &= (\gamma^1 + \gamma^3 + \gamma^2 + \gamma^4) \cdot a_1; \\ M_7 &= (\gamma^2 + \gamma^4 + \gamma^3 + \gamma^5) \cdot a_1, & M_8 &= (\gamma^3 + \gamma^5 + \gamma^4 + \gamma^6) \cdot a_1; \\ M_9 &= (\gamma^4 + \gamma^6 + \gamma^5 + \gamma^7) \cdot a_1. \end{aligned} \quad (\text{B-10})$$

Thus,

$$\begin{aligned} b_1 &= M_1 + M_2 + M_4 + M_6, & b_2 &= M_1 + M_3 + M_4 + M_7; \\ b_3 &= M_1 + M_2 + M_5 + M_8, & b_4 &= M_1 + M_3 + M_5 + M_9 \end{aligned} \quad (\text{B-11})$$

From (B-11), the total number of multiplications needed to perform (B-8) is 9.

To compute  $N_i$  for  $i = 1, 2, 3, 4, 5$ , defined in (B-7), the same procedure can be used that was used above for (B-8). The number of multiplications for comparing each of these  $M_j$ 's is 9. To compute  $N_i$  for  $i = 6, 7, 8, 9$ , for example, consider  $N_6 = E \cdot S_1$ ,

$$N_6 = \begin{pmatrix} n_1 \\ n_2 \\ n_3 \\ n_4 \end{pmatrix} = \begin{pmatrix} \gamma^8 + \gamma^2 + \gamma^9 + \gamma^{15}, \gamma^6 + \gamma^{10} + \gamma^{11} + \gamma^7, \gamma^{13} + \gamma^{16} + \gamma^4 + \gamma^1, \gamma^{14} + \gamma^{12} + \gamma^3 + \gamma^5 \\ \gamma^6 + \gamma^{10} + \gamma^{11} + \gamma^7, \gamma^{13} + \gamma^{16} + \gamma^4 + \gamma^1, \gamma^{14} + \gamma^{12} + \gamma^3 + \gamma^5, \gamma^2 + \gamma^9 + \gamma^{15} + \gamma^8 \\ \gamma^{13} + \gamma^{16} + \gamma^4 + \gamma^1, \gamma^{14} + \gamma^{12} + \gamma^3 + \gamma^5, \gamma^2 + \gamma^9 + \gamma^{15} + \gamma^8, \gamma^{10} + \gamma^{11} + \gamma^7 + \gamma^6 \\ \gamma^{14} + \gamma^{12} + \gamma^3 + \gamma^5, \gamma^2 + \gamma^9 + \gamma^{15} + \gamma^8, \gamma^{10} + \gamma^{11} + \gamma^7 + \gamma^6, \gamma^{16} + \gamma^4 + \gamma^1 + \gamma^{13} \end{pmatrix} \begin{pmatrix} a_3 \\ a_{15} \\ a_7 \\ a_1 \end{pmatrix} \quad (\text{B-12})$$

By a procedure similar to that used to compute the cyclic matrix defined in (B-8), one obtains

$$M_1 = (\gamma^{14} + \gamma^{12} + \gamma^3 + \gamma^5) \cdot (a_3 + a_{15} + a_7 + a_1);$$

$$M_2 = (\gamma^{13} + \gamma^{16} + \gamma^4 + \gamma^1 + \gamma^{14} + \gamma^{12} + \gamma^3 + \gamma^5) \cdot (a_3 + a_7);$$

$$M_3 = (\gamma^{14} + \gamma^{12} + \gamma^3 + \gamma^5 + \gamma^2 + \gamma^9 + \gamma^{15} + \gamma^8) \cdot (a_3 + a_7);$$

$$M_4 = (\gamma^6 + \gamma^{10} + \gamma^{11} + \gamma^7 + \gamma^{14} + \gamma^{12} + \gamma^3 + \gamma^5) \cdot (a_3 + a_{15});$$

$$M_5 = (\gamma^{14} + \gamma^{12} + \gamma^3 + \gamma^5 + \gamma^{10} + \gamma^{11} + \gamma^7 + \gamma^6) \cdot (a_3 + a_{15});$$

$$M_6 = (\gamma^8 + \gamma^2 + \gamma^9 + \gamma^{15} + \gamma^6 + \gamma^{10} + \gamma^{11} + \gamma^7 + \gamma^{13} + \gamma^{16} + \gamma^4 + \gamma^1 + \gamma^{14} + \gamma^{12} + \gamma^3 + \gamma^5) \cdot a_3;$$

$$M_7 = (\gamma^6 + \gamma^{10} + \gamma^{11} + \gamma^7 + \gamma^{13} + \gamma^{16} + \gamma^4 + \gamma^1 + \gamma^{14} + \gamma^{12} + \gamma^3 + \gamma^{15} + \gamma^2 + \gamma^9 + \gamma^{15} + \gamma^8) \cdot a_3;$$

$$M_8 = (\gamma^{13} + \gamma^{16} + \gamma^4 + \gamma^1 + \gamma^{14} + \gamma^{12} + \gamma^3 + \gamma^5 + \gamma^2 + \gamma^9 + \gamma^{15} + \gamma^8 + \gamma^{10} + \gamma^{11} + \gamma^7 + \gamma^6) \cdot a_3;$$

$$M_9 = (\gamma^{14} + \gamma^{12} + \gamma^3 + \gamma^5 + \gamma^2 + \gamma^9 + \gamma^{15} + \gamma^8 + \gamma^{10} + \gamma^{11} + \gamma^7 + \gamma^6 + \gamma^{16} + \gamma^4 + \gamma^1 + \gamma^{13}) \cdot a_3;$$

and

$$n_1 = M_1 + M_2 + M_4 + M_6, \quad n_2 = M_1 + M_3 + M_4 + M_7;$$

$$n_3 = M_1 + M_2 + M_5 + M_8, \quad n_4 = M_1 + M_3 + M_5 + M_9$$

Now, factor  $x^{17} - 1$  into a product of irreducible polynomials, i.e.,  $x^{17} - 1 = (x - 1) \cdot (x^8 + x^7 + x^6 + x^4 + x^2 + x + 1) \cdot (x^8 + x^5 + x^4 + x^3 + 1)$ . If one chooses  $\gamma$  such that  $\gamma$  satisfies  $x^8 + x^7 + x^6 + x^4 + x^2 + x + 1$ , then, by Theorem 2 and Theorem 3,  $\gamma^6 + \gamma^{10} + \gamma^{11} + \gamma^7 + \gamma^{14} + \gamma^{12} + \gamma^3 + \gamma^5$  and  $\gamma^{14} + \gamma^{12} + \gamma^3 + \gamma^5 + \gamma^{10} + \gamma^{11} + \gamma^7 + \gamma^6$  are equal to zero and  $\gamma^6 + \gamma^{10} + \gamma^{11} + \gamma^7 + \gamma^{15} + \gamma^{16} + \gamma^4 + \gamma^1 + \gamma^{14} + \gamma^{12} + \gamma^3 + \gamma^5 + \gamma^2 + \gamma^9 + \gamma^{15} + \gamma^8 = 1$ . These identities are used to reduce the  $M_k$ 's; e.g.,  $M_4 = 0$ , etc. After this reduction it can be shown that the total number of multiplications needed to perform (B-12) is 7, including multiplications by  $\gamma^0$ . If multiplications by  $\gamma^0$  are excluded, evidently only 3 multiplications are actually needed. In a similar fashion, matrices  $N_7$ ,  $N_8$ , and  $N_9$  in (B-7) can be computed. After combining the above results, it is seen that the total number of multiplications needed to perform a 17-point transform over  $GF(2^n)$  is  $5 \times 9 + 4 \times 3 = 57$ , excluding multiplications by  $\gamma^0$ . To include multiplications by  $\gamma^0$ , the total number of multiplications is  $5 \times 9 + 4 \times 7 + 1 = 74$ .

## Acknowledgment

The authors wish to thank Dr. S. A. Butman, Manager of Communications Systems Research Section and Dr. N. A. Renzetti, Manager of Tracking and Data Acquisition Engineering, Jet Propulsion Laboratory, for their encouragement of the research which led to this paper.

## References

1. Green, R. R., "Analysis of a Serial Orthogonal Decoder," *Space Programs Summary 37-53*, Vol. III, pp. 185-187, Jet Propulsion Laboratory, Pasadena, Calif., 1968.
2. Reed, I. S., "A Class of Multiple-Error-Correcting Codes and the Decoding Scheme," *IRE Trans.*, PGIT-4, 1954, pp. 38-49.
3. Mandelbaum, D., "On Decoding Reed-Solomon Codes," *IEEE Trans. Inform. Theory*, Vol. IT-17, No. 6, pp. 707-712, Nov. 1971.
4. Gore, W. C., "Transmitting Binary Symbols with Reed-Solomon Code," Johns Hopkins EE Report No. 73-5, Apr. 1973.
5. Michelson, A., "A New Decoder for the Reed-Solomon Codes Using a Fast Transform Technique," Systems Engineering Technical Memorandum No. 52, Electronic Systems Group, Eastern Division, GTE Sylvania, Aug. 1975.
6. Peterson, W. W., *Error-Correcting Codes*, MIT Press, Cambridge, Mass., pp. 168-169, 1961.
7. Lin, S., *An Introduction to Error-Correcting Codes*, Prentice-Hall, Englewood Cliffs, N.J., 1970.
8. Reed, I. S., Scholtz, R. A., Truong, T. K., and Welch, L. R., "The Fast Decoding of Reed-Solomon Codes Using Fermat Theoretic Transforms and Continued Fractions," *IEEE Trans. Inform. Theory*, Vol. IT-24, No. 1, pp. 100-106, Jan. 1978.
9. Reed, I. S., Truong, T. K., and Benjauthrit, B., "Transform Decoding of Reed-Solomon Codes over  $GF(2^n)$  Using the Techniques of Winograd," in *The Deep Space Network Progress Report 42-43*, pp. 141-163, Jet Propulsion Laboratory, Pasadena, Calif., Feb. 15, 1978.
10. Reed, I. S., Truong, T. K., and Benjauthrit, B., "On Decoding of Reed-Solomon Codes over  $GF(32)$  and  $GF(64)$  Using the Transform Techniques of Winograd," in *The Deep Space Network Progress Report 42-44*, pp. 139-171, Jet Propulsion Laboratory, Pasadena, Calif., Apr. 15, 1978.
11. Odenwalder, J., et al., "Hybrid Coding Systems Study Final Report," Linkabit Corp., NASA CR 114, 486, Sept. 1972.
12. Gentleman, W. M., "Matrix Multiplication and Fast Fourier Transforms," *Bell System Technical Journal*, 1968, pp. 1099-1103.
13. Winograd, S., "On Computing the Discrete Fourier Transform," *Proc. Nat. Acad. Sci. USA*, 1976, 73, pp. 1005-1006.

14. Winograd, S., "On Computing the Discrete Fourier Transform," Research Report, Math. Science Dept., IBM Thomas J. Watson Research Center, Yorktown Heights, New York, 10592.
15. Berlekamp, E. R., *Algebraic Coding Theory*, New York, McGraw Hill, 1968.
16. Forney, G. D., "On Decoding BCH Codes," *IEEE Trans. Inform. Theory*, Vol. IT-11, Oct. 1965.

**Table 1. The complexity of transform over  $GF(2^n)$  for  $n = 4,5,8$**

$N = 2^n - 1$	Factors $N_1 \cdot N_2 \dots N_k$	No. Mult. of New Algorithm	No. Mult. of Gentleman's Algorithm $N(N_1 + N_2 + \dots + N_k - k + 1)$
$2^4 - 1$	$3 \times 5$	$4 \times 5 = 20$	$15(3 + 5 - 1) = 105$
$2^5 - 1$	31	120	961
$2^6 - 1$	$7 \times 9$	$12 \times 12 = 144$	$63(7 + 9 - 1) = 945$
$2^8 - 1$	$3 \times 5 \times 17$	$4 \times 10 \times 57 = 2280$	$255(3 + 5 + 17 - 2) = 5865$

**Table 2. The complexity of decoding RS of  $2^n - 1$  points for  $n = 4,5,8$**

$N$	Factors $N_1, N_2, \dots, N_k$	No. Mult. of New Algorithm	No. Mult. of Gentleman's Algorithm $2N(N_1 + N_2 + \dots + N_k - k + 1)$	No. Mult. of Standard Algorithm $(N - 1)(d - 1) + t^2$
15	$3 \times 5$	$2 \times 20 = 40$	$2 \times 105 = 210$	$14 \times 8 + 4^2 = 128$
31	31	$2 \times 120 = 240$	$2 \times 961 = 1922$	$30 \times 16 + 8^2 = 544$
63	$7 \times 9$	$2 \times 132 = 264$	$2 \times 945 = 1890$	$62 \times 30 + 15^2 = 2085$
255	$3 \times 5 \times 17$	$2 \times 2280 = 4560$	$2 \times 5862 = 11724$	$254 \times 32 + 16^2 = 8384$

## Wideband Data Error Rates

J. P. McClure  
DSN Data Systems Section

*Data on the error and outage characteristics of the Ground Communications Facility's wideband data circuits have been gathered and analyzed. Most error blocks occur one at a time, whereas missing blocks are grouped into strings (outages) having a median length of about 10 blocks.*

Most ground communications digital transmission channels are subject to two problems — they cause bit errors and they occasionally fail, generating outages. Over the years the Ground Communications Facility (GCF) has measured and analyzed these impediments in the high-speed data and wideband data transmission circuits (see Refs. 1-6).

The GCF digital transmission circuits have changed greatly since they were first used by the DSN. Originally, all overseas circuits were derived from HF radio, with a slow transition to underseas cables in the late 1960s. Most of the overseas (and some domestic) circuits are now routed via commercial communications satellites. Circuit quality has continuously improved.

In early 1977, it was realized that measurement of the current wideband impediments would be needed in order to design an efficient wideband error control system. Accordingly, the GCF developed a measurement and analysis configuration in the Central Communications Terminal in JPL Building 230. This configuration is illustrated in Fig. 1.

The configuration utilized two status outputs from the subsystem's Coded Multiplexer:

(1) Data Block Detected: This lead carries a pulse each

time the Coded Multiplexer recognizes a data block. Lack of such a pulse implies a missing block.

(2) Block Error Detected: This lead pulses only when a recognized block contains an error.

The two status leads were electrically isolated from their other loads and connected to external interrupt inputs of a MODCOMP II minicomputer (the future EDC 4, to be exact). A real-time program processed the pulses using time, block size, and circuit bit rate to determine the sequence of good, error, and missing blocks. These sequences were recorded on disc.

The configuration was used by GCF Operations to record approximately 200 passes of Viking Telemetry (2400 bit block size). Some of the "passes" were very short, some were not properly terminated, some contained inappropriate rates, etc. These faulty passes were deleted during off-line editing of the data.

The resulting edited tape contained usable data from 143 tracking passes — a total of about 1290 hours (54 days) of real-time wideband data. The data was about equally divided between the three 64-m DSSs (14, 43, and 63). It was

considered a good random sample of inbound wideband circuit operation.

The raw data on the tape consisted of counts of consecutive good, error, or missing blocks, along with the time when the sequence ended. As an example:

Time	Good	Error	Missing
083215	4395	—	—
083215	—	2	—
083216	—	—	13
083226	105	—	—

This sequence shows that 4395 good blocks were received, followed by 2 blocks each containing bit errors, then 13 missing blocks (an outage), then 105 more good blocks, etc. No attempt was made to tell where the error(s) occurred in a block nor the causes of the error or missing blocks.

The first analysis program basically consisted of a dump of the taped data. Visual inspection showed that most of the DSS 43 errors were systematic — every  $690 \times N$  blocks there was one block in error.  $N$  ranged from one to five. Since DSS 43 was using a line rate of 27.6 kbps and a 2400-bit block, the 690 figure translated to exactly 1 minute. NASCOM (the NASA agency which provides circuits to the GCF) was advised of the problem. They determined that timing signals were not being properly synchronized within their network. Several months were spent remedying the situation. DSS 43's data was then clean until the very end of the recording period, when the same problem reoccurred.

The second analysis program omitted the 21 DSS 43 passes which contained systematic errors. The balance of the passes were processed to yield the data shown in Table 1.

In all cases the block missing rate in Table 1 is much larger than the block error rate. This correlates with earlier measurements of HSD and WBD performance. The combined error and missing rate, 0.00280, represents approximately 1.75 min of

outage/error per average (10.5 h) tracking pass. Unfortunately, these 1.75 min are widely scattered through the pass, occurring, typically, only a few blocks at a time. The error plus missing block rate runs considerably higher for the overseas stations, averaging 149 blocks per hour for all stations.

An event, as used herein, is a single set of like blocks. For example, 4395 good blocks followed by 2 error blocks, 13 missing blocks and 105 good blocks represent 2 good events, 1 error event and 1 missing event. As shown in Table 1, the event rates are also much higher for the overseas DSSs, and average 9.9 per hour throughout the net. Paraphrasing, there is an average of 9.9 "gaps" in each hour's worth of wideband data. Each such gap is a subject for recall after the pass.

Figure 2 shows the distribution of the lengths of the error and missing events for all of the stations. As an example of how to read the curves, there were approximately 440 error events which contained four to seven consecutive error blocks. There were 107 missing events containing 64 to 127 consecutive missing blocks.

Examination of these curves and their data shows:

- (1) Most error events contained only a single block in error. (Actually, 78% have only a single block in error.)
- (2) Long strings of error blocks just don't occur. (The longest error event was 28 blocks long.)
- (3) Consecutive missing blocks (missing events) can be quite long. The longest in this set of tests was, in fact, 9083 blocks, about 13.2 min.
- (4) The median length of the missing events is around 10 blocks; i.e., the typical outage is about 10 blocks long.
- (5) An error correction scheme which could span a 1000 block error/outage period would probably correct more than 99% of the gaps.

Various algorithms for wideband error correction are being modeled against the actual test data. Results of these studies will be presented in a future report.

## References

1. Nightingale, D., "High-Speed Data System Performance and Error Statistics at 4800 bps", in *The Deep Space Network*, Technical Report 32-1526, Vol. IV, pp. 154-159, Jet Propulsion Laboratory, Pasadena, Calif., Aug. 15, 1971.
2. McClure, J. P., "Madrid-to-JPL 50 kbits/s Wideband Error Statistics," in *The Deep Space Network*, Technical Report 32-1526, Vol. IX, pp. 177-184, Jet Propulsion Laboratory, Pasadena, Calif., June 15, 1972.
3. McClure, J. P., "Ground Communications Facility 50-kbps Wideband Data Error Rate Test," in *The Deep Space Network*, Technical Report 32-1526, Vol. VI, pp. 149-157, Jet Propulsion Laboratory, Pasadena, Calif., Dec. 15, 1971.
4. McClure, J. P., "High Speed Data Block Bursts," in *The Deep Space Network Progress Report 42-20*, pp. 149-153, Jet Propulsion Laboratory, Pasadena, Calif., Apr. 15, 1974.
5. McClure, J. P., "High Speed Data Throughput," in *The Deep Space Network Progress Report 42-23*, pp. 74-77, Jet Propulsion Laboratory, Pasadena, Calif., Oct. 15, 1974.
6. McClure, J. P., "4800 bps High Speed Data Error Statistics," in *The Deep Space Network Progress Report 42-24*, pp. 108-114, Jet Propulsion Laboratory, Pasadena, Calif., Dec. 15, 1974.

**Table 1. Wideband data performance statistics**

Parameter	Station			Total
	14	43	63	
Number of passes	46	25	48	119
Tracking hours	611	230	431	1272
Block error rate	0.000095	0.000470	0.000553	0.000319
Block missing rate	0.000693	0.003772	0.004313	0.002484
Combined rate	0.000788	0.004241	0.004866	0.002800
Error + missing rate, blocks/hour	58 blks/h	174 blks/h	212 blks/h	149 blks/h
Error events	1715	3234	6488	11437
Missing events	210	296	607	1113
Error + missing rate, events per hour	3.15 Ev/h	15.3 Ev/h	16.5 Ev/h	9.9 Ev/h
Max consecutive error blocks	11	28	22	28
Max consecutive missing blocks	5530	3635	9083	9083

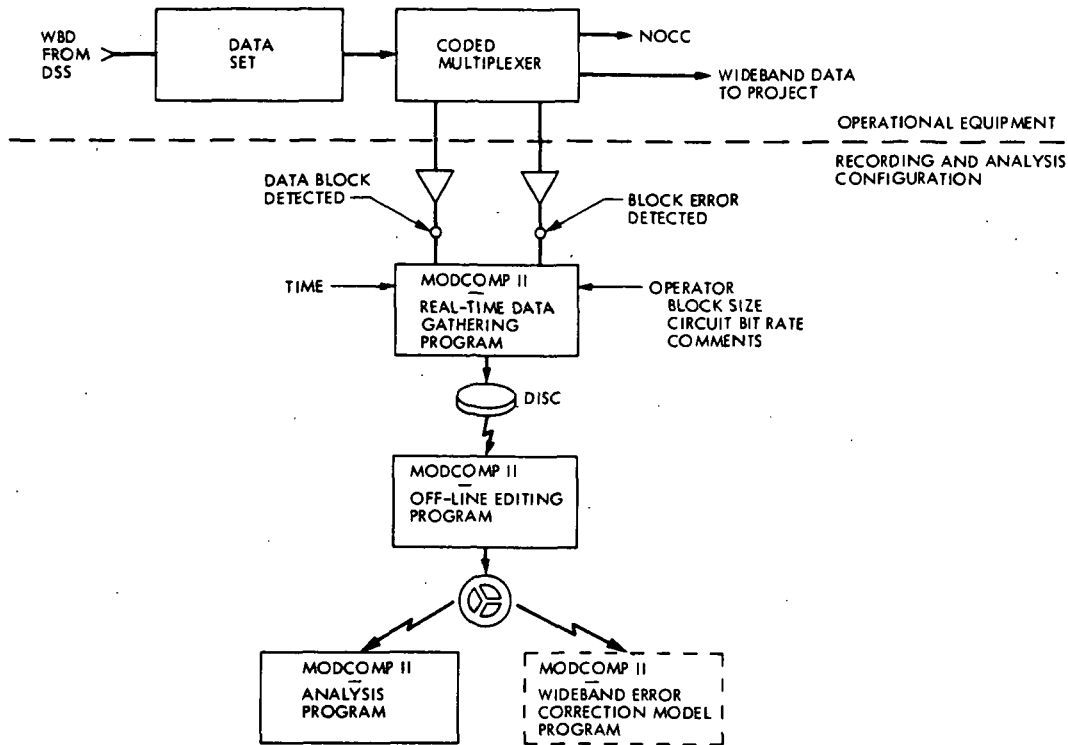


Fig. 1. Recording and analysis configuration

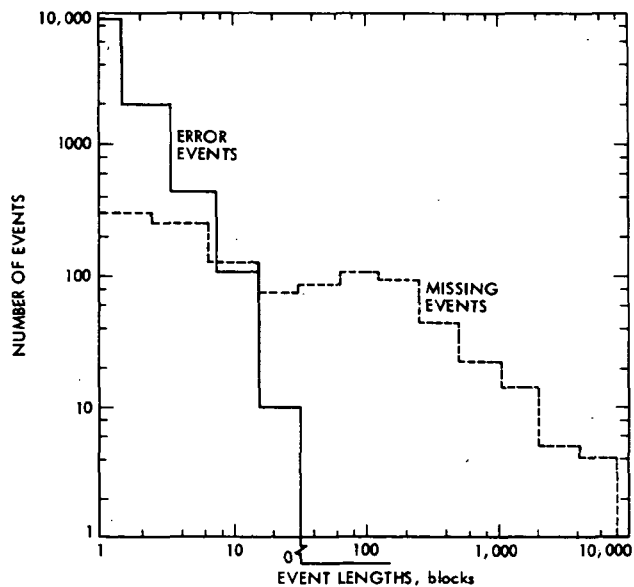


Fig. 2. Distribution of error and missing event lengths (all stations)

## Computerized Simulation and Parameterization of a New High-Performance Tubular Solar Collector

F. L. Lansing and C. S. Yung  
DSN Engineering Section

*This work is the second of two reports describing the thermal analysis, computerized performance, simulation and performance sensitivity of the new General Electric vacuum tube solar collector. The collector is considered a potential candidate for future DSN solar heating and cooling applications. The first report presented details of the two-dimensional thermal model of the solar collector at steady state. In this report, the second phase of the study is presented to include the computer simulation and the performance parameterization. Comparison of the simulated performance with the manufacturer's test data showed good agreement at wide ranges of operating conditions. The effects of nine major design and performance variables on the performance sensitivity were presented. The results of this parameterization study were supportive in detecting the areas of design modifications for performance optimization.*

### I. Introduction

The high-performance low-concentration tubular solar collector recently manufactured by General Electric Company has been under investigation in the DSN Engineering Section for possible use in future heating/cooling applications at the ground stations. The thermal performance of this collector was not sufficiently reported by the manufacturer, although high performance was claimed. Details of the in-house two-dimensional thermal analysis and the mathematical model were previously reported in Ref. 1 as a first phase of the investigation.

In order to support the second phase of the investigation, which is the parameterization of the collector and the numerical evaluation of its performance, an in-house computer pro-

gram has been written using the mathematical model developed in Ref. 1. Appendix A gives the details of the computational sequence followed. Furthermore, in order to validate the performance, improve the present design, and search for the dominant parameters that affect the performance, a sensitivity analysis is needed. This article focuses on the second phase of the study and reports on the results obtained from this sensitivity analysis.

Only few experimental data were supplied by the manufacturer (see Refs. 2 and 3), and therefore the results of the performance simulation will be compared against these test data only. Some unknown material properties, physical dimensions and boundary conditions were assumed in this work to complete the modelling process as will be described in detail later.

## II. Collector Description

Two versions of the collector design have been manufactured by G.E. Both versions have the same basic features, with the exception of a few differences explained as follows. The detailed description of the basic features of the collector was given in Ref. 1, but is briefly mentioned here for convenience. The collector module consists of a number of heat collection units: 10 in the first version and 8 in the second. The units are mounted in parallel with a highly reflective back reflector. The back reflector is a V-shaped surface in the first version as shown in Fig. 1. In the second version, the back reflector is a double cusp (parabolic shape) as shown also in Fig. 1. Each unit contains a U-shaped copper tube and the tubes of the units are connected in series to form a serpentine. Each collector unit consists of two coaxial cylindrical glass tubes with evacuated annular space in between.

The first (outer) cylinder serves as a "window," and the second (inner) cylinder is selectively coated on the outer surface to serve as the "absorber." The heat is transferred through the second glass tube to a conforming cylindrical metallic shell made of copper. The latter transfers the heat to the working fluid passing through the U-tube. To allow for thermal expansion, one side of the U-tube is attached to the copper shell while the other side is left free to move as shown in Fig. 1. The thermal model, however, considers that both sides of the U-tube are in contact with the copper shell.

Although the second version of the collector design was made public after the mathematical model was established in Ref. 1, the first design will still be analyzed. The differences between the two designs, namely, the shape of the back reflector and the number of units per module, will not be changed in the thermal model.

## III. Additional Assumptions

In addition to the assumptions and idealizations that were made to simplify the collector simulation in Ref. 1, the following assumptions are added in the second phase of the study for completeness.

- (1) The outer surface of the second glass tube is assumed to be selectively coated, instead of coating the outer surface of the metallic shell. This will reduce the outward long-wave radiation losses to the first glass tube.
- (2) The deformation, due to lateral thermal expansion of the U-shape tubing, is assumed to be insignificant and not to cause any glass breakage. Also, the present slit suggested by the manufacturer in the metallic shell is assumed to be narrow enough to keep the cold and hot fluid tubing always in contact with the shell. This

assumption is made to increase the fin efficiency and improve the heat transfer between the fluid and the copper shell.

The above assumptions, together with the thermal model presented in Ref. 1, were used to construct a computer program as shown in Appendix A. An illustrative example on the use of the computer program in determining the various performance characteristics is given in Appendix B.

## IV. Comparison with Experimental Tests

In order to provide a cross-checking on the computer program validity, a comparison is made of some simulated performance results against the manufacturer test data. The dotted line in Fig. 2 was provided by the manufacturer (in Ref. 3), based on experimental tests made in 1978 at Desert Sunshine Exposure Tests, Inc., and Florida Solar Energy Center, using a collector module of the first design version. The X points in Fig. 2 are the simulated results of some arbitrarily selected operating conditions having different inlet fluid temperature  $T_c(0)$ , ambient temperature  $T_A$ , and solar intensity  $I$ . The abscissa in Fig. 2,  $[T_c(0) - T_A]/I$ , is commonly chosen to compare solar collectors of different optical and thermal characteristics. The coordinates of Fig. 2 also fit Eq. (A-36), in Appendix A, where the ordinate intercept represents the optical efficiency and the curve slope is an indication of the thermal losses to the ambient.

The collector characteristic equation can be expressed, from Fig. 2, by the approximate formula:

$$\eta_{\text{module}} = 0.640 - 2.0669 \frac{T_c(0) - T_A}{I} \quad (1)$$

where the temperatures  $T_A$  and  $T_c(0)$  are in degrees Celsius and  $I$  is in  $\text{W}/\text{m}^2$ .

The good agreement between the computer simulation results and the experimental tests, indicated in Fig. 2, provided the validation needed for the computer program. Consequently, the performance sensitivity to nine major variables was done next using a baseline set of operating conditions. The numerical example presented in Appendix B gives the magnitude of this set of variables used as a baseline. The flow rate of a collector module (10 collector units) was chosen to be 50 kg/h (instead of 5 kg/h used in Appendix B) to follow the manufacturer's specification. The simulated module efficiency, at the reference conditions, is 49.47%, corresponding to (1) a solar radiancy  $I$  of  $630.7 \text{ W}/\text{m}^2$ , (200 Btu/h ft<sup>2</sup>), (2) a wind speed  $W$  of 4.47 m/s, (3) an ambient temperature  $T_A$  of 4.4°C

(40°F), (4) a reflectivity of absorber shell  $b$  of 0.5, (5) a second glass tube emissivity,  $\epsilon_s$  of 0.2, (6) a reflectivity of back reflector  $\rho_v$  of 0.9, (7) a U-tube size of 6 mm (1/4 in.) nominal diameter, (8) a fluid mass flow rate  $M$  of 50 kg/h, and (9) an inlet fluid temperature to the first collector unit  $T_c(0)$ , of 48.89°C (120°F). The selection of these reference conditions was made using explicit and implicit data provided by the manufacturer.

## V. Performance Parameterization

The performance of the collector is mainly determined by the above nine major variables. Each variable is set to change in value around the preselected reference state, and the results of one collector module (10 units) are discussed in the following subsections.

### A. Effect of Solar Radiancy Variations

The performance sensitivity to the solar radiancy  $I$  is plotted as shown in Fig. 3. A nonlinear relationship is evident between the radiancy vs the fluid temperature gain or the collector efficiency. An increase of the solar intensity by 50%, for example, will improve the fluid temperature gain by 63.8% and the collector efficiency by 9.21%. On the other hand, a 50% reduction of the solar intensity will lower the fluid temperature gain by 60.9% and the collector efficiency by 27.9%. This behavior can be best explained by using the efficiency expression Eq. (A-36) in Appendix A. The efficiency of one collector unit given in Eq. (A-36) is divided into two terms. The first term

$$\left[ F\lambda \left( \alpha_{a,e} + \alpha_{f,e} \frac{B_4}{B_7} + \alpha_{s,e} \frac{B_6}{B_7} \right) \right]$$

which is independent of the intensity  $I$ , represents the optical efficiency of the collector at zero thermal losses. The second term, namely,

$$FB_0 [T_c(0) - T_A] / I$$

herein called the thermal loss factor, is proportional to the temperature difference  $(T_c(0) - T_A)$  and inversely proportional to the intensity  $I$ . This finding explains the nonlinear relationship of the efficiency vs the intensity as illustrated in Fig. 3. In addition, Eq. (A-36) can be used to interpret the increase of collector efficiency when the solar intensity increases.

### B. Effect of Wind Speed Variations

The convective loss coefficient,  $H_{fA}$  between the first (outer) glass tube and ambient air is solely a function of the wind speed as given by Eq. (A-12) in Appendix A. Two extreme values of the wind speed were assumed to take place around the reference state. The first is a no-wind condition and the second is a wind speed of 8.94 m/s (20 mph), which is double the reference speed of 4.47 m/s (10 mph). The results are plotted in Fig. 4. It is evident from Fig. 4 that the effect of wind speed variations on efficiency and fluid temperature gain is small. At the no-wind condition, for example, the wind velocity decreased by -100% compared to the reference point and caused an increase in the efficiency by only 1.8%. On the other hand, at double the reference wind speed, an efficiency decrease of 0.4% was found. These findings lead to the conclusion that the collector performance has a very small sensitivity to variations in wind speed.

### C. Effect of Ambient Temperature Variations

The effect of ambient temperature was investigated by varying the ambient temperature from -23.33°C (-10°F) to 48.89°C (120°F) around the reference state, which is 4.4°C (40°F), keeping all other parameters the same. The results are plotted in Fig. 5, showing the effects on the collector efficiency and the fluid temperature gain.

Increasing the ambient temperature causes an increase in the collector efficiency due to the reduction of the thermal losses and vice versa. These thermal losses are proportional to the temperature difference  $(T_c(0) - T_A)$  as given by Eq. (A-36). An increase of the ambient temperature from 4.4°C (40°F) to 48.89°C (120°F), i.e., an increase of the absolute temperature by 16%, caused an increase in the thermal efficiency by about 28%. This is equivalent to a sensitivity of about 1.75. On the other hand, a decrease of the ambient temperature from 4.4°C (40°F) to -23.33°C (-10°F), i.e., a decrease of the absolute temperature by 10%, caused a decrease in the thermal efficiency by about 12%. Again, the sensitivity to ambient temperature is 1.2, which shows the important role that the ambient temperature plays in the performance.

### D. Effect of Absorber Shell Reflectivity $b$

The optical properties of the metallic shell and the second (inner) glass tube should be carefully selected in the design in order to yield a good collector performance. The mechanism by which the solar energy is absorbed, converted into heat, and transmitted to the working fluid can be one of two types.

The first heat transfer mechanism could be achieved by adopting a heat-absorbing glass material for the second glass tube to act as the "absorber" from which the net absorbed heat is conducted to the metallic shell that holds the fluid tubing. This mechanism is already used by the manufacturer, and it requires that the first (outer) glass tube function only as a "window" for minimizing the outward infrared radiation losses.

Another heat transfer mechanism is envisioned in which both the first and second glass tubes act as a double-paned "window" made of common clear glass with negligible heat absorbing capability. The major portion of solar energy will be absorbed at the outer surface of the metallic shell, thus acting as the "absorber". In these two mechanisms, the reflection coefficient  $r$  for the first glass tube outer and inner surfaces, and that for the outer surface of the second tube, do not play a significant role. The reflection coefficient  $r$  is known to be a function only of the incident angle and the refraction index of glass.

The absorption coefficients  $a$  (for the first glass tube) and  $\bar{a}$  (for the second glass tube) depend on the glass extinction coefficient  $\phi$  and thickness  $t$  (Ref. 5) such that

$$\left. \begin{aligned} a &= e^{-\phi t_f} \\ \bar{a} &= e^{-\bar{\phi} t_s} \end{aligned} \right\} \text{or} \quad (2)$$

In general, the percentage of ferrous oxide ( $F_2O_3$ ) in glass is important since iron accounts for most of the absorption. Reference 6 gives the extinction coefficient  $\phi$  for the three different types of clear, medium-heat-absorbing and high-heat-absorbing glass panels as  $6.85 \text{ m}^{-1}$ ,  $129.92 \text{ m}^{-1}$ , and  $271.26 \text{ m}^{-1}$ , respectively.

The reflectivity of the metallic shell  $b$ , on the other hand, affects the balance of heat absorbed, reflected, or transmitted to and from the second glass tube. The metallic shell outer surface can be either polished or coated to change the value of  $b$ , which will be shown next to be an important factor.

Several variations of the reflection coefficient  $b$  were made in the program using the above three different types of second glass tube material. Both  $T_c(0)$  and  $T_A$  were set equal to isolate the effects of thermal losses and to focus on the collector optical efficiency alone. The results were plotted as shown in Fig. 6. Since the details of the optical properties of the collector components were not given by the manufacturer, the baseline collector properties were selected arbitrarily to be having a medium-heat-absorbing second glass tube ( $\bar{\phi} = 129.92$

$\text{m}^{-1}$ ), a polished copper shell ( $b = 0.5$ ), and a clear first glass tube ( $\phi = 6.85 \text{ m}^{-1}$ ).

It can be observed from Fig. 6 that reducing the shell reflectivity  $b$  always improves the optical efficiency with any type of second glass-material. The percentage improvement is large at small extinction coefficients. The collector efficiency for the first mechanism of heat transfer was found always higher than that for the second mechanism when both mechanisms have the same coefficient  $b$ . At small values of  $b$ , or at high shell absorptivity, the effect of  $\phi$  becomes diminishing, and the collector optical efficiency reaches about 80%. This last result leads to the recommendation that high absorptivity or black coating is necessary for the metallic shell in order to achieve the highest performance, whether or not a heat-absorbing glass is used.

### E. Effect of Second Glass Tube Outer Surface Emissivity

If a "selective" coating is used on the outside surface of the second (inner) glass tube, it will reduce the outward infrared radiation losses, thus improving the performance. Different emissivity values were tested in the parameterization study, ranging from 0.05 to 0.9, with a reference value at 0.2, which is also "selective." The results are plotted as shown in Fig. 7. The strong relationship between the efficiency and the emissivity  $\epsilon_s$  is clearly indicated in Fig. 7. The overall thermal loss coefficient  $B_0$  is dominantly dependent on the "equivalent" radiation coefficient  $B_4$ , which is given in Eqs. (A-26) and (A-35). Smaller emissivity values cause smaller overall thermal loss coefficient, resulting in higher collector efficiency. If the infrared emissivity drops from the reference "selective" value ( $\epsilon_s = 0.2$ ) to a lesser emissivity value of 0.05, for example, i.e., a decrease of 75%, the overall thermal loss coefficient  $B_0$  for the first collector unit will be decreased by 72% and the collector module efficiency will be improved by 24.1%. This is equivalent to a sensitivity of  $-0.32$  for the collector module efficiency and  $+0.96$  for the coefficient  $B_0$ . On the other hand, an increase of the emissivity ( $\epsilon_s$ ) from 0.2 (selective) to 0.9 (flat black), i.e., an increase of 350% causes an increase in the loss coefficient  $B_0$  for the first collector unit by 269% i.e., a loss coefficient sensitivity of 0.77. The corresponding module efficiency will drop to a low value of 10.4% i.e., a decrease of 78.9% compared to the reference state. The efficiency sensitivity in the latter case is equivalent to  $-0.22$ .

It can be concluded from the above discussion that "selective" coatings having an infrared emissivity in the order of 0.2 or less are recommended to achieve higher performance. Coating instability due to temperature recycling, aging, or operation at high temperatures and the associated increase in collector operation and maintenance cost, should be traded off against the improvement in collector performance.

C-3

## F. Effect of the Back Panel Reflectivity

The back reflector used, whether it is a V-shape or a cusplike shape, is necessary in order to enhance concentration of the solar flux on the glass tubes. Equation (A-11) gives the relationship between the augmentation factor  $\lambda$  and the units spacing  $S$ , outer glass tube diameter  $D_{f,o}$ , and the back surface reflectivity ( $\rho_v$ ). Equation (A-11) assumes that for both the V and cusp-back reflector types, the solar energy falling on the unshaded areas of the back reflector is reflected totally, with no loss, upon the external surface of the first glass tube. The higher the reflectivity  $\rho_v$  is, the higher the augmentation factor, and the higher the efficiency will be. The results of varying  $\rho_v$  are plotted in Fig. 8. The baseline design assumes a highly reflective mirrorlike material that is used for the back panel with  $\rho_v$  of 0.9. If a polished aluminum rack with  $\rho_v$  of 0.5, for example, is used, it means a drop in the reflectivity by 44.4%. The resulting drop in module efficiency is found to be 16.7%. This is equivalent to an efficiency sensitivity of about 0.38, which is not insignificant.

## G. Effect of Tubing Size

The size of the copper serpentine tube carrying the fluid is set using the manufacturer data to be a 6 mm (1/4 in.) nominal diameter. With a fluid flow of 50 kg/h, an inside diameter  $D_{t,i}$  of 10 mm, and an outside diameter  $D_{t,o}$  of 14 mm, the Reynolds number is computed as 6121, which lies in the transition region. Given a fixed mass flow rate, the effect of varying the tube diameter on the efficiency was studied for two different tube sizes. The first tubing has a nominal diameter of 1/8 in. ( $D_{t,i} = 7.2$  mm,  $D_{t,o} = 10.2$  mm) and the second tubing, has a nominal diameter of 3/8 in. ( $D_{t,i} = 12.6$  mm,  $D_{t,o} = 17.2$  mm). The resulting efficiencies were 49.50, 49.47, and 49.41%, corresponding to the nominal diameters of 1/8, 1/4, and 3/8 in., respectively.

The effect of tubing size could be considered, therefore, practically negligible. The slight improvement noticed above when a small tubing is used is contributed by the increased convective heat transfer coefficient  $H_{ah}$  caused by the higher fluid velocities attained. The effect of the latter on performance was somewhat counterbalanced by the corresponding smaller heat transfer surface area.

## H. Effect of Fluid Mass Flow Rate

The choice of the operating mass flow rate is important if the collector efficiency needs to be improved and the pump horsepower to be decreased. Several references in the literature, including Ref. 7, have indicated a practical range from 24.4 kg/h-m<sup>2</sup> (5 lb/h-ft<sup>2</sup>) to 97.7 kg/h-m<sup>2</sup> (20 lb/h-ft<sup>2</sup>) to

trade off between collector efficiency and pump horsepower. A recommended rate of 48.8 kg/h-m<sup>2</sup> (10 lb/h-ft<sup>2</sup>) was given in Ref. 7. The flow rate recommended by the manufacturer for the 10-unit collector module is 50 kg/h or 34.2 kg/h-m<sup>2</sup> based on 1.464 m<sup>2</sup>/module, which lies in the above practical range.

Increasing the fluid mass flow rate always increases the heat transfer between the copper tubing and the fluid, therefore increasing the extracted heat rate and the collector efficiency. On the other hand, for a given inlet fluid temperature, increasing the flow rate reduces the fluid exit temperature. Apart from the fact that a tradeoff analysis needs to be done with the feed pump horsepower, the "quality" of the extracted heat should be investigated from a thermodynamic availability viewpoint. If a reversible engine is connected to the collector and made to operate utilizing the collector extracted heat as if the latter is taken from a finite heat reservoir at the exit temperature  $T_h(0)$ , the availability  $A$  will be as sketched in Fig. 9(a).  $A$  is defined as the maximum useful mechanical work that could be obtained from the above collector-reversible engine system.  $A$  is written for a constant specific heat fluid as

$$A = Q_{ext} - T_A MC_w \ln \frac{T_h(0)}{T_c(0)} \quad (3)$$

where

$$Q_{ext} = MC_w [T_h(0) - T_c(0)] \quad (4)$$

For a module with 10 units, the temperature  $T_c(0)$  is taken at the entrance of the first unit and  $T_h(0)$  is taken at the exit of the 10th unit. The relationship between the availability  $A$  and the mass flow rate at given fluid inlet temperature  $T_c(0)$  and ambient temperature  $T_A$  has the same trend as sketched in Fig. 9(b). The values of peak availability  $A_m^*$  at the optimum mass flow rate  $M^*$  are plotted at different inlet fluid temperatures (Fig. 10). Figure 10 indicates that for given inlet fluid temperature and ambient temperature, there exists an optimum mass flow rate  $M^*$  that corresponds to a maximum thermodynamic availability  $A_m^*$ . These findings are highly important in optimizing the collector operating conditions for solar-thermal-electric applications as will be shown in the next section.

## I. Effect of Inlet Fluid Temperature

The results of changing the cold fluid temperature at the entrance of the first collector unit are plotted as shown in Fig. 11. Increasing the temperature  $T_c(0)$  causes an increase of the thermal losses from the collector surface since these losses are proportional to the temperature difference between the

collector operating temperature and ambient air. The correlation between  $T_c(0)$  and the module efficiency tends to deviate from the approximate straight line form due to the increasing effect of the radiation losses at higher fluid temperatures. Although increasing the inlet fluid temperature causes a setback in the collector efficiency; the resulting increase of the outlet fluid temperature may be favored, especially when the heat is converted to mechanical work via engines. In order to find the optimum inlet fluid temperature at which the production of mechanical work is maximum, the thermodynamic availability  $A$  is introduced as in Eqs. (3) and (4). For a given mass flow rate, the availability  $A$  was computed at different inlet temperatures, keeping all other variables unchanged. The peak availability  $A_T^*$  and the optimum temperature  $T_c^*(0)$  were registered at the given mass flow rate. The results were plotted as shown in Fig. 12. It is indicated from Fig. 12 that the maximum availability  $A_T^*$ , corresponding to the optimum inlet temperature, stays approximately constant if the flow rate is beyond 50 kg/h. The latter matches the flow rate recommended by the manufacturer. From Fig. 12, at a flow rate of 50 kg/h, the availability  $A_T^*$  is maximum at an inlet fluid temperature of 69°C (156.2°F) and equal to 74.33 watts/module. On the other hand, entering the optimum fluid temperature (69°C) into Fig. 10, the optimum flow rate corresponding to a maximum availability  $A_m^*$  is about 140 kg/h, where  $A_m^*$  is about 74 watts/module. In general, maximizing the availability using the optimum inlet fluid temperature

approach rather than the optimum mass flow rate approach is found convenient since the first gives more practical values of flow rates compared to the second approach.

## VI. Summary

In order to evaluate, in detail, the recently manufactured high-performance tubular collector by General Electric, a parameterization analysis was made. An in-house computer program was written for this purpose, following the thermodynamic analysis presented in Ref. 1 and the computational sequence in Appendices A and B. Comparison of simulated results and manufacturer's test data showed good agreement at a wide range of operating conditions. The comparison is considered a validation method for the computer program. Nine design and performance parameters were investigated to evaluate the performance sensitivity to their changes. The parameters considered were (1) solar radiancy, (2) wind speed, (3) ambient temperature, (4) reflectivity of metallic shell, (5) second tube outer surface emissivity, (6) reflectivity of back reflector, (7) fluid tubing size, (8) fluid mass flow rate, and (9) inlet fluid temperature to first collector unit. The results of this parameterization study shed some light onto variables of insignificant effects and others that need to be modified in the design in order to yield a higher performance than the present one.

## Definition of Terms

<i>A</i>	thermodynamic availability	<i>W</i>	wind speed, m/s
<i>a, ā</i>	glass absorption coefficient	$\alpha$	absorptivity
<i>b</i>	"absorber" reflection coefficient	$\rho$	reflectivity
<i>B<sub>0</sub>-B<sub>8</sub></i>	thermal conductance, W/m <sup>2</sup> °C	$\tau$	transmissivity
<i>C</i>	specific heat, W/kg°C	$\lambda$	augmented radiation factor
<i>C<sub>0</sub>, C<sub>1</sub></i>	constants	$\eta$	collector efficiency
<i>D</i>	diameter	$\delta$	parameter, °C/m
<i>E<sub>1</sub>-E<sub>6</sub></i>	energy flux, W/m <sup>2</sup>	$\epsilon$	emissivity
<i>F</i>	flow factor	$\mu$	viscosity
<i>G</i>	heat capacity = $MC_w/D_{f,o}$	$\phi$	extinction coefficient
<i>H</i>	convective heat transfer coefficient, W/m <sup>2</sup> °C		
<i>I</i>	solar flux, W/m <sup>2</sup>		Subscripts
<i>K</i>	thermal conductivity, W/m°C	<i>A</i>	ambient air
<i>L</i>	collector-unit length, m	<i>a</i>	"absorber" metallic shell
<i>M</i>	fluid mass flow rate, kg/h	<i>c</i>	cold fluid
<i>N</i>	number of collector units per module	<i>e</i>	effective
<i>n</i>	characteristic constant, m <sup>-1</sup>	<i>f</i>	first (outer) glass tube
<i>Q</i>	heat rate, W	<i>h</i>	hot fluid
<i>R</i>	equivalent radiation heat transfer coefficient, W/m <sup>2</sup> °C	<i>i</i>	inside
<i>r</i>	glass reflection coefficient	<i>o</i>	outside
<i>S</i>	spacing between 2 consecutive collector units, m	<i>s</i>	second (inner) glass tube
<i>T</i>	temperature, K	<i>t</i>	serpentine tube
<i>t</i>	thickness, m	<i>u</i>	insulation
<i>x</i>	distance, m	<i>v</i>	V-shape reflector
		<i>w</i>	working fluid (hot or cold)

## References

1. Lansing, F. L., and Yung, C. S., "A Two Dimensional Thermal Analysis of a New High Performance Tubular Solar Collector," in *The Deep Space Network Progress Report 42-49*, Jet Propulsion Laboratory, Pasadena, Calif., Feb. 15, 1979.
2. "SOLARTRON TC-100 Vacuum Tube Solar Collector – Commercial and Industrial Installation Manual," Document No. 78SDS4214A, General Electric Advanced Energy Programs, Philadelphia, Pa., Nov. 1978.
3. "SOLARTRON TC-100 Vacuum Tube Solar Collector – Commercial and Industrial Application Guide," Document No. 78SDS4215A, General Electric Advanced Energy Programs, Philadelphia, Pa., Nov. 1978.
4. Duffie, J. A., and Beckman, W. A., *Solar Energy Thermal Processes*, Wiley Interscience Publication, New York, N.Y., 1974.
5. Kreith, F., *Principles of Heat Transfer*, Third Edition, Intext Educational Publishers, New York, 1973.
6. Threlkeld, J. L., *Thermal Environmental Engineering*, Prentice-Hall, Inc., Englewood Cliffs, N.J., 1962.
7. Hewitt, H. C., and Griggs, E. I., "Optimal Mass Flow Rates Through Flat Plate Solar Collector Panels," ASME Publication 76-WA/SOL-19, presented at ASME Winter Annual Meeting, New York, N.Y., Dec. 1976.

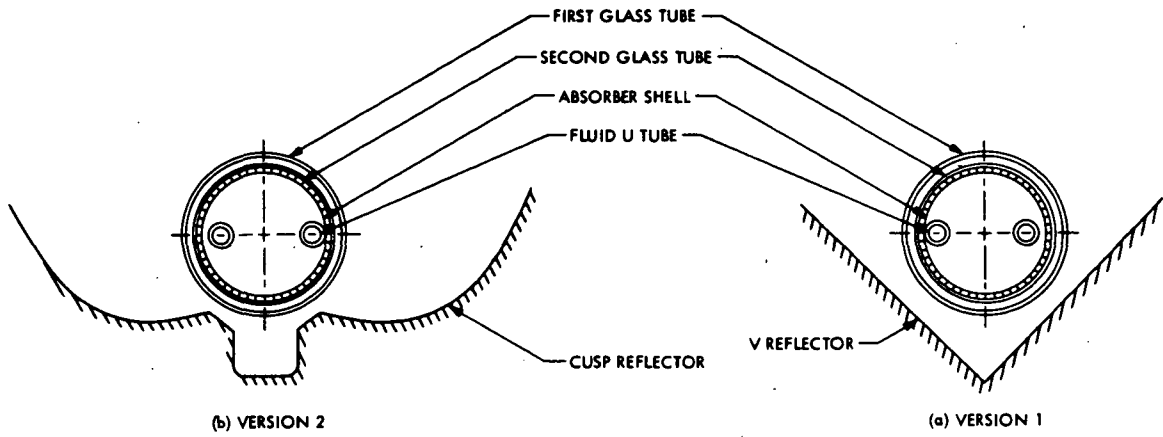


Fig. 1. Two versions of a collector unit

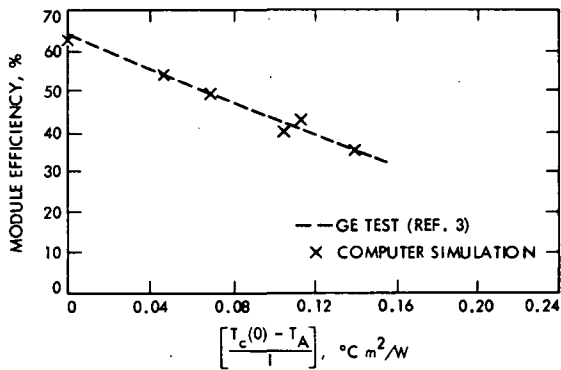


Fig. 2. Performance comparison between some simulated and experimental data

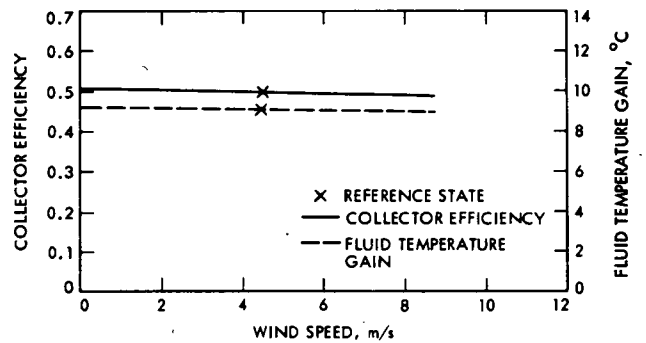


Fig. 4. Effect of wind speed variations

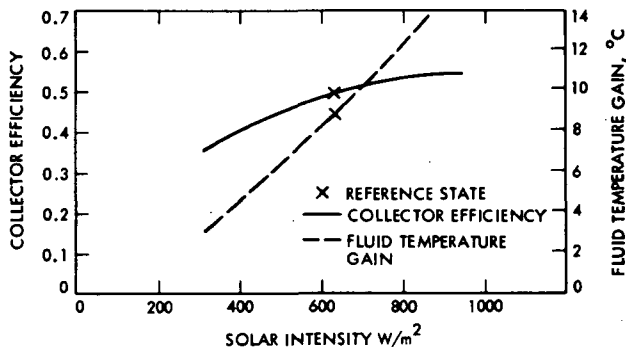


Fig. 3. Effect of solar intensity variations

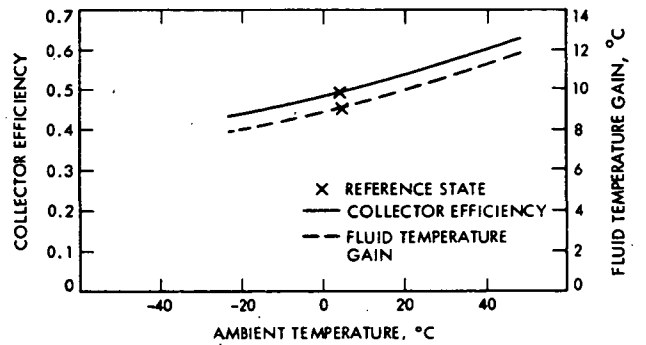


Fig. 5. Collector performance vs ambient temperatures

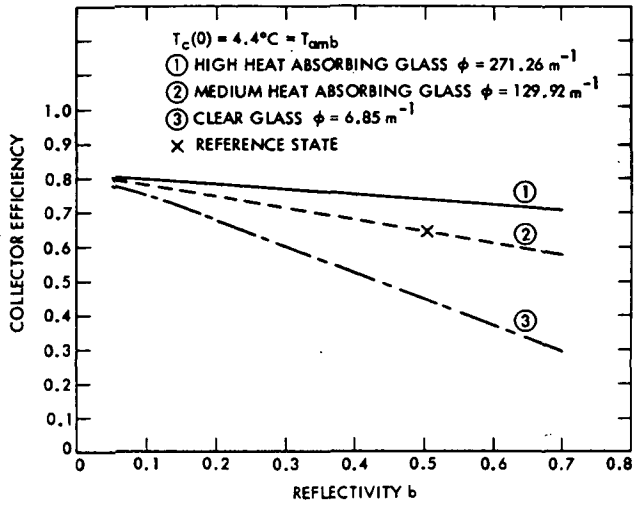


Fig. 6. Effect of metallic shell reflectivity  $b$  on efficiency

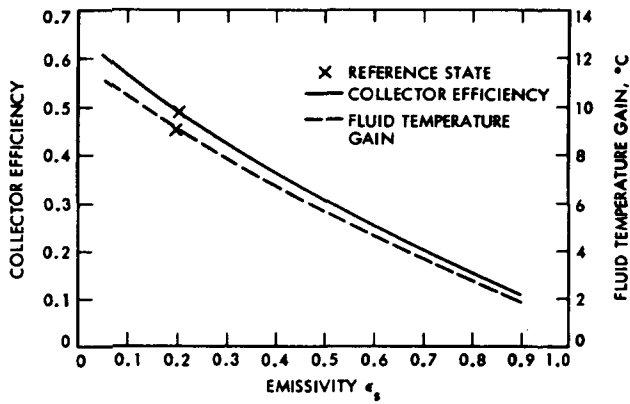


Fig. 7. Effect of second glass surface emissivity  $\epsilon_s$

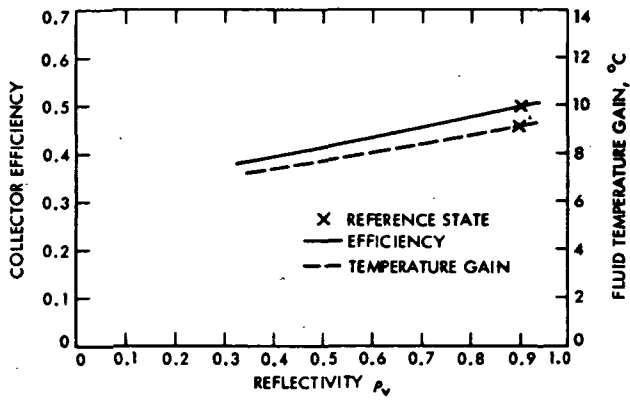


Fig. 8. Effect of the reflectivity  $\rho_v$  of the back V-shape reflector

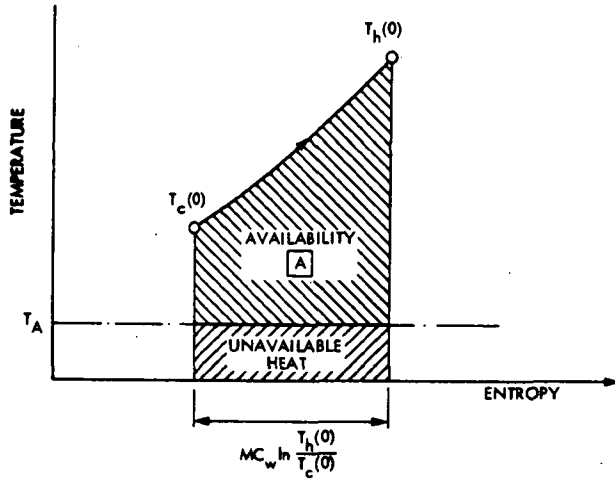


Fig. 9a. Thermodynamic availability for the collector extracted heat

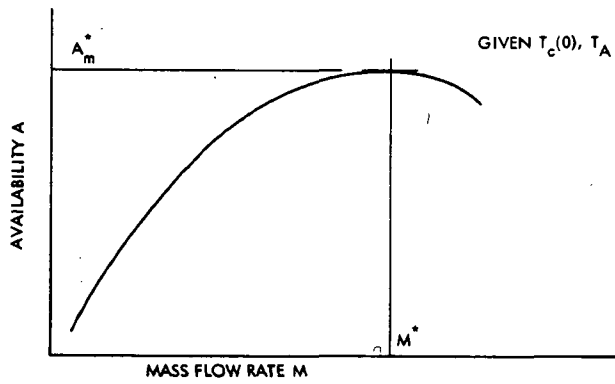


Fig. 9b. Sketch of thermodynamic availability vs the mass flow rate for a given inlet and ambient temperature.

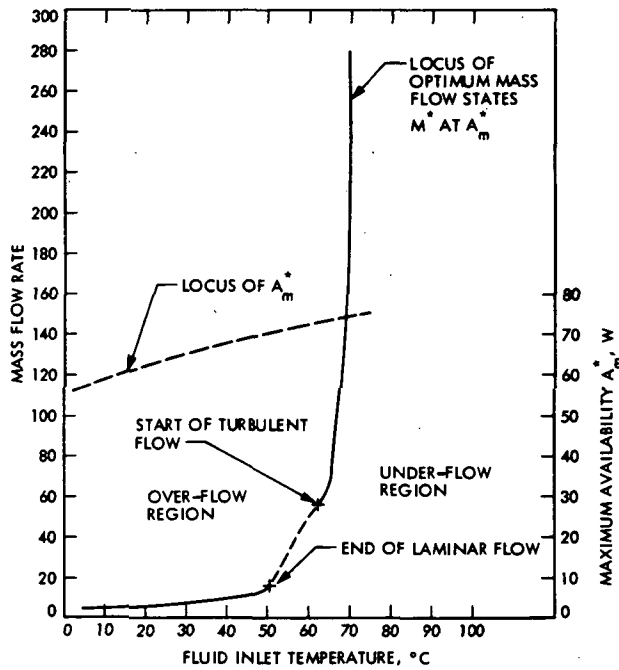


Fig. 10. Fluid inlet temperature effect on optimum mass flow rate

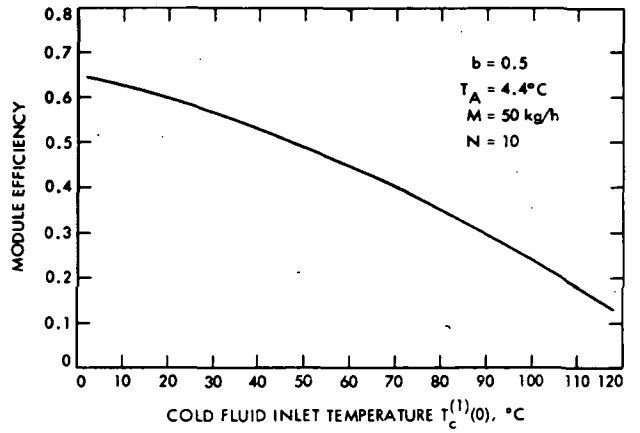


Fig. 11. Effect of inlet fluid temperature on module efficiency

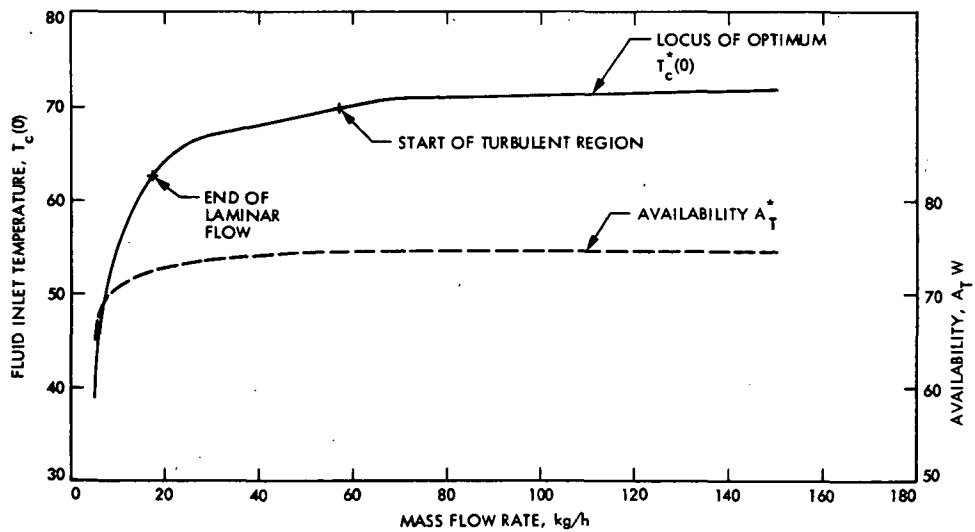


Fig. 12. Optimum fluid inlet temperature at various mass flow rates

## Appendix A

### Details of the Computer Model

#### I. Introduction

A computer program is written using the thermal model and analytic equations given in the first phase of this study (Ref. 1). The program is divided into several parts described in detail next.

#### II. Program Input Data

The following data need to be provided by the user in order to complete the program execution.

##### A. Optical Properties

Glass reflection coefficient	$r$
First glass tube absorption (or extinction coefficient)	$a$ (or $\phi$ )
Second glass tube absorption (or extinction) coefficient	$\bar{a}$ (or $\bar{\phi}$ )
Reflectivity of absorber shell	$b$
Reflectivity of back reflector	$\rho_v$
Emissivity of first glass tube surfaces	$\epsilon_f$
Emissivity of second glass tube outer surface	$\epsilon_s$

##### B. Collector Dimensions

Spacing between collector units	$s$
Inner diameter of first glass tube	$D_{f,i}$
Outer diameter of first glass tube	$D_{f,o}$
Inner diameter of second glass tube	$D_{s,i}$
Outer diameter of second glass tube	$D_{s,o}$
Inner diameter of metallic shell	$D_{a,i}$
Outer diameter of metallic shell	$D_{a,o}$
Inner diameter of fluid tubing	$D_{t,i}$
Outer diameter of fluid tubing	$D_{t,o}$
Length of one side of the U-tube of a collector unit	$L$
Thickness of insulation at the open end	$t_u$
Number of collector units per module	$N$

##### C. Thermodynamic Properties

Working fluid viscosity	$\mu_w$
Working fluid specific heat	$C_w$
Working fluid thermal conductivity	$K_w$
Thermal conductivity of second glass tube	$K_s$
Thermal conductivity of absorber metallic shell	$K_a$
Thermal conductivity of open-end insulation	$K_u$

##### D. Operating Conditions

Fluid flow rate	$M$
Fluid temperature at the entrance of the first collector unit	$T_c(0)$

##### E. Weather

Solar radiancy	$I$
Ambient temperature (dry bulb)	$T_A$
Wind speed	$W$

#### III. Program Sequence

The following equations are listed in the same order of calculations sequence. Reference should be made to Ref. 1 for more details.

##### A. Optical Properties

1. The transmissivity, absorptivity, and reflectivity of the first glass tube are  $\tau_f$ ,  $\alpha_f$  and  $\rho_f$ , respectively, where

$$\tau_f = \frac{a(1-r)^2}{1-a^2r^2} \quad (\text{A-1})$$

$$\alpha_f = \frac{(1-r)(1-a)}{1-ar} \quad (\text{A-2})$$

$$\rho_f = r + \frac{ra^2(1-r)^2}{1-a^2r^2} \quad (\text{A-3})$$

where  $r$  and  $a$  are the reflection and absorption coefficients, respectively, for the first glass tube.

2. The absorptivity ( $\alpha_B$ ) of the bottom surface of the second glass tube alone is given by

$$\alpha_B = \frac{\bar{a}(1-b)(1-r)}{1-\bar{a}^2br} \quad (\text{A-4})$$

Also, the absorptivity  $\alpha_s$  and reflectivity  $\rho_s$  of the second glass tube are given by

$$\alpha_s = \frac{(1-r)(1-\bar{a})(1+\bar{a}b)}{1-\bar{a}^2br} \quad (\text{A-5})$$

$$\rho_s = r + \frac{\bar{a}^2b(1-r)^2}{1-\bar{a}^2br} \quad (\text{A-6})$$

where  $\bar{a}$  and  $r$  are the absorption and reflection coefficients of the second glass tube, and  $b$  is the reflectivity of the absorber shell surface.

3. The effective properties  $\alpha_{a,e}$  of the metallic absorber shell  $\alpha_{f,e}$  and  $\rho_{f,e}$  of the first glass tube and  $\alpha_{s,e}$  of the second glass tube, are given by

$$\alpha_{a,e} = \frac{\alpha_B \tau_f}{1 - \rho_f \rho_s} \quad (\text{A-7})$$

$$\alpha_{f,e} = \alpha_f + \frac{\alpha_f \tau_f \rho_s}{1 - \rho_f \rho_s} \quad (\text{A-8})$$

$$\alpha_{s,e} = \frac{\alpha_s \tau_f}{1 - \rho_f \rho_s} \quad (\text{A-9})$$

$$\rho_{f,e} = \rho_f + \frac{\rho_s \tau_f^2}{1 - \rho_f \rho_s} \quad (\text{A-10})$$

4. Augmentation factor  $\lambda$  is given by

$$\lambda = \left[ 1 + \rho_v \left( \frac{s}{D_{f,o}} - 1 \right) \right] \quad (\text{A-11})$$

## B. Heat Transfer Coefficients

1. Convection coefficient between tubes and ambient. The convective heat transfer coefficient between the outer glass

tube and surrounding air,  $H_{fA}$  in  $\text{W/m}^2\text{C}$ , is given approximately in Ref. 4 as a linear function of the wind speed  $W$

$$H_{fA} = 5.7 + 3.8W \quad (\text{A-12})$$

where  $W$  is in m/sec. Eq. (A-12) is also used to determine the film coefficients between the inner surface of "absorber" shell and the still air core  $H_{aA}$ , also between the end insulation and the air core  $H_{uA}$ . The coefficients are obtained by setting  $W$  equal to zero in Eq. (A-12). Accordingly,

$$H_{aA} = H_{uA} \cong 5.7 \quad (\text{A-13})$$

2. Radiation coefficient. Two "effective" radiation heat transfer coefficients are calculated for the present model, namely,  $R_{sf}$  and  $R_{fA}$ . The coefficient  $R_{sf}$  represents the radiation exchange between the inner surface of the first (outer) glass tube and the outer surface of the second (inner) glass tube. Hence,

$$R_{sf} = \frac{\sigma (T_s^4 - T_f^4)}{\left[ (T_s - T_f) \left( \frac{1}{\epsilon_s} + \left( \frac{1}{\epsilon_f} - 1 \right) \frac{D_{s,o}}{D_{f,i}} \right) \right]} \quad (\text{A-14})$$

The coefficient  $R_{fA}$  represents the radiation exchange between the first (outer) glass tube and the ambient air and is given by

$$R_{fA} = \frac{\epsilon_f \sigma (T_f^4 - T_A^4)}{(T_f - T_A)} \quad (\text{A-15})$$

A convergent iterative process is used for each collector unit whereby average temperatures of each of the first glass tubes are assumed. These averages give the first estimate of the coefficients  $R_{sf}$  and  $R_{fA}$  to determine the temperature distribution  $T_f(x)$  and  $T_s(x)$  which in turn are used to modify the radiation coefficients. The iteration process is completed for a given collector unit before proceeding to the next unit in the module and so on.

3. Convection between the working fluid and tubes. The present model incorporates all the equations needed to calculate the forced convection heat transfer coefficient between the working fluid and the copper tubing at any one of the three flow regions: laminar, transition, and turbulent. The laminar region is characterized by a Reynolds number ( $Re$ ) less than 2100 for circular tubes. For the turbulent flow case, the Reynolds number is greater than 7000. References 4 and 5

were used to determine the Nusselt number ( $Nu$ ) for laminar and turbulent flow regions. For laminar flow

$$Nu = 4.64 + \frac{0.067 D_{t,i} Re Pr/l}{1 + 0.04 \left( \frac{D_{t,i}}{l} Re Pr \right)^{2/3}} \quad (\text{A-16})$$

where  $D_{t,i}$  is the inner tube diameter,  $l$  is the total tube length and  $Pr$ ,  $Re$  and  $Nu$  are Prandtl, Reynolds, and Nusselt numbers, respectively. The dimensionless numbers are written as follows:

$$\left. \begin{aligned} Re &= \frac{4M}{\pi D_{t,i} \mu_w} \\ Pr &= \frac{C_w \mu_w}{K_w} \\ Nu &= \frac{H_{ah} D_{t,i}}{K_w} \end{aligned} \right\} \quad (\text{A-17})$$

For turbulent flow inside tubes, the Nusselt number  $Nu$ , is given by

$$Nu = 0.023 Re^{0.8} Pr^{0.3} \quad (\text{A-18})$$

In the metastable transition region, no reliable expression has been found in the literature to express the Nusselt number. Accordingly, a linear interpolation is used in this work as a first approximation of the fluid transition from laminar to turbulent regions, i.e., in the range where  $2100 < Re < 7000$ . The approximate equation used is

$$Nu_{(\text{transition})} = Nu_{2100} + (Re - 2100) \left( \frac{Nu_{7000} - Nu_{2100}}{7000 - 2100} \right) \quad (\text{A-19})$$

where  $Nu_{2100}$  is the Nusselt number computed from Eq. (A-16) at  $Re$  equal to 2100 and  $Nu_{7000}$  is the Nusselt number computed from Eq. (A-18) at  $Re$  equal to 7000.

The fluid thermal properties used in the above equations were taken at some preselected average bulk temperature and were assumed to be constant during operation. The working fluid used in the modelling exercise was the ethylene glycol-water solution with a volumetric ratio of 50/50 as recommended by the manufacturer. Pure water was not selected because of its inadequacy at working temperatures below  $0^\circ\text{C}$  ( $32^\circ\text{F}$ ) or above  $100^\circ\text{C}$  ( $212^\circ\text{F}$ ).

### C. Absorbed Energy Flux $E$ Coefficients

The energy flux terms ( $E$ 's), discussed in detail in Ref. 1, are rewritten here to complete the program sequence.

1. The fraction of solar energy that is absorbed by the "absorber" shell  $E_1$  is given by

$$E_1 = \alpha_{a,e} \lambda I \quad (\text{A-20})$$

2. The fraction of solar energy that is absorbed by the first (outer) glass tube  $E_2$  is expressed by

$$E_2 = \alpha_{f,e} \lambda I \quad (\text{A-21})$$

3. The fraction of solar energy that is absorbed by the second (inner) glass tube  $E_3$  is written as

$$E_3 = \alpha_{s,e} \lambda I \quad (\text{A-22})$$

### D. "Equivalent" Heat Transfer Coefficients ( $B$ 's)

The  $B$  coefficients are herein called "equivalent" since they represent the "equivalent" heat transfer coefficients for a plate-to-plate heat exchange giving the same heat transfer of the present circular geometry. The  $B$  coefficients were previously discussed in Ref. 1 and are rewritten here, briefly, for completion.

1. The "equivalent" conduction coefficient  $B_1$  between the "absorber" shell and second (inner) glass tube is given by

$$B_1 = \frac{2\pi/D_{f,o}}{\left[ \frac{\ln(D_{s,o}/D_{s,i})}{K_s} + \frac{\ln(D_{a,o}/D_{a,i})}{K_a} \right]} \quad (\text{A-23})$$

2. The coefficient  $B_2$  represents the "equivalent" heat loss coefficient from the central air core to the ambient air through the open and closed ends of the collector. Figure A-1 shows a sketch of the location of film coefficients used in deriving the  $B_2$  expression for one collector unit having one end insulated and the other using double hemispheres with vacuum in between. One can prove that

$$B_2 = \frac{1}{\left[ \frac{D_{f,o}}{\pi h_{aA} (D_{a,i} + 2D_{t,o})} + \frac{1}{PA_c} \right]} \quad (\text{A-24})$$

where  $P$  and  $A_c$  are given by

$$P = \frac{2}{\frac{1}{H_{aA}} + \frac{1}{R_{sf}} + \frac{2r_s}{K_s} + \frac{1}{H_{fA}}} + \frac{1}{\frac{1}{H_{uA}} + \frac{r_u}{K_u} + \frac{1}{H_{fA}}}$$

$$A_c = \frac{\pi D_{a,i}^2}{4}$$

3. The "equivalent" convection coefficient between the absorber shell and the fluid ( $B_3$ ) is given by

$$B_3 = \pi (D_{t,i}/D_{f,o}) H_{ah} \quad (\text{A-25})$$

4. The "equivalent" radiation coefficient between the first glass and second glass tubes is given by

$$B_4 = \pi R_{sf} (D_{s,o}/D_{f,o}) \quad (\text{A-26})$$

5. The "equivalent" combined radiation and convection coefficient between the first glass tube and ambient is written as

$$B_5 = \pi (H_{fA} + R_{fA}) \quad (\text{A-27})$$

### E. Overall Heat Loss Coefficient $B_0$

The coefficients  $B_1$ ,  $B_2$ ,  $B_4$ , and  $B_5$  represent, by analogy to electric circuits, the thermal conductances between the "absorber" shell, glass tubes and ambient air as shown in Fig. A. The thermal resistances  $1/B_1$ ,  $1/B_4$ , and  $1/B_5$  are connected in series and their resultant is connected in parallel with the resistance  $1/B_2$ . The overall thermal conductance of this circuit is herein called the overall heat loss coefficient  $B_0$  given by

$$B_0 = B_2 + \frac{1}{\frac{1}{B_1} + \frac{1}{B_4} + \frac{1}{B_5}}$$

### F. Temperature Distribution

The hot and cold temperatures  $T_h(x)$  and  $T_c(x)$ , respectively, at any position  $x$  from the open end of one collector unit, are obtained from

$$T_h(x) = \frac{\delta}{C_1 - C_0} - \left[ \frac{\delta}{C_1 - C_0} - T_c(0) \right] \frac{n \cosh n(L-x) - (C_1 - C_0) \sinh n(L-x)}{n \cosh nL + (C_1 - C_0) \sinh nL} \quad (\text{A-28})$$

$$T_c(x) = \frac{\delta}{C_1 - C_0} - \left[ \frac{\delta}{C_1 - C_0} - T_c(0) \right] \frac{n \cosh n(L-x) + (C_1 - C_0) \sinh n(L-x)}{n \cosh nL + (C_1 - C_0) \sinh nL} \quad (\text{A-29})$$

where the constants  $n$ ,  $c_0$ ,  $c_1$  and  $\delta$  are computed in sequence from the following equation:

$$\left. \begin{aligned} n &= \sqrt{C_1^2 - C_0^2} \\ C_0 &= B_3^2 / (GB_8) \\ C_1 &= \frac{B_3}{GB_8} (B_8 - B_3) \\ \delta &= B_3 E_6 / GB_8 \end{aligned} \right\} \quad (\text{A-30a})$$

where

$$\left. \begin{aligned} E_6 &= E_1 + B_2 T_A + \frac{B_1 E_5}{B_7} \\ E_5 &= E_3 \frac{B_6}{B_1} + E_4 \frac{B_4}{B_1} \\ E_4 &= E_2 + B_5 T_A \\ B_8 &= B_2 + 2B_3 + \frac{B_4 B_5}{B_7} \\ B_7 &= B_6 + \frac{B_4 B_5}{B_1} \\ B_6 &= B_4 + B_5 \end{aligned} \right\} \quad (\text{A-30b})$$

and

$$G = \frac{M C_w}{D_{f,o}} \quad (\text{A-30d})$$

The "absorber" shell temperature  $T_a(x)$  is given by

$$T_a(x) = \frac{\{E_6 + B_3 [T_h(x) + T_c(x)]\}}{B_8} \quad (\text{A-31})$$

The second glass tube temperature  $T_s(x)$  is given by

$$T_s(x) = \frac{[E_5 + B_6 T_a(x)]}{B_7} \quad (\text{A-32})$$

Also, the first glass tube temperature  $T_f(x)$  is given by

$$T_f(x) = \frac{[E_4 + B_4 T_s(x)]}{B_6} \quad (\text{A-33})$$

### G. Performance Factors

The flow factor  $F$  is defined by

$$F = \frac{GD_{f,o}}{SL B_0} \left[ \frac{2 \sinh nL}{\frac{B_3}{nG} \cosh nL + \sinh nL} \right] \quad (\text{A-34})$$

where  $B_0$  is the overall heat loss coefficient given in Sec. A.3.5. by

$$B_0 = B_2 + \frac{B_4 B_5}{B_7} = B_2 + \frac{1}{\frac{1}{B_1} + \frac{1}{B_4} + \frac{1}{B_5}} \quad (\text{A-35})$$

The unit collector instantaneous efficiency, based on the solar radiancy falling on the projected area  $SL$  is given by

$$\eta_{unit} = \frac{MC_w [T_h(0) - T_c(0)]}{ISL}$$

or

$$\eta_{unit} = F \left[ \lambda \left( \alpha_{a,e} + \alpha_{f,e} \frac{B_4}{B_7} + \alpha_{s,e} \frac{B_6}{B_7} \right) - B_0 \frac{T_c(0) - T_A}{I} \right] \quad (\text{A-36})$$

where  $SL$  is the projected area of a collector unit. For a collector module that consists of  $N$  collector units in series, the module efficiency is given by

$$\eta_{module} = \frac{MC_w [T_h^{(N)}(0) - T_c^{(1)}(0)]}{ISLN} \quad (\text{A-37})$$

where  $T_h^{(N)}(0)$  is the fluid temperature at the exit of the  $n$ th unit and  $T_c^{(1)}(0)$  is the fluid temperature at the entrance of the first collector unit.

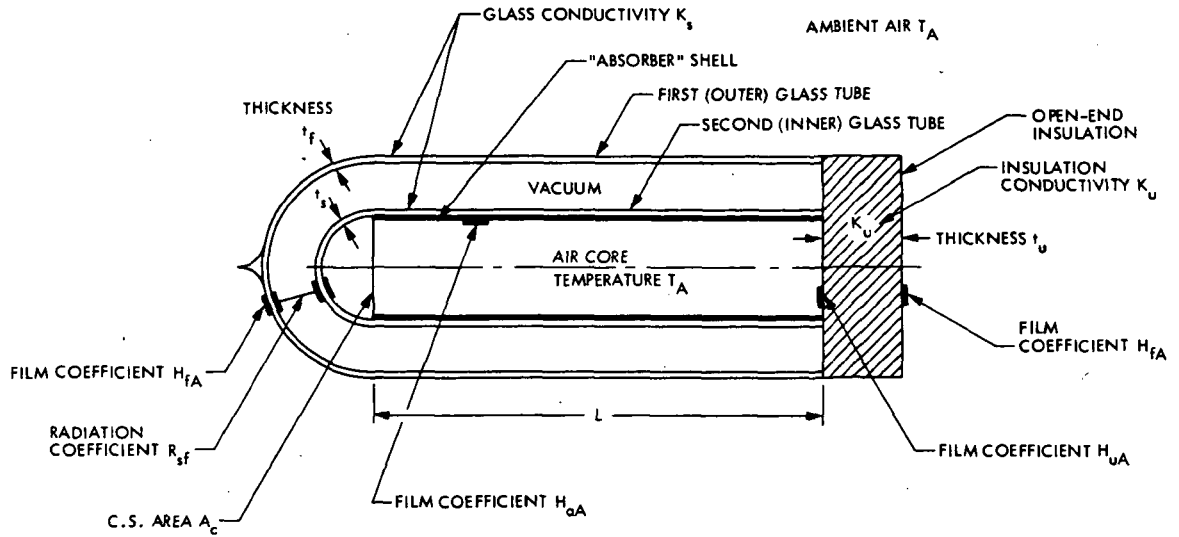


Fig. A-1. Film coefficients used for the determination of the "equivalent" coefficient  $B_2$

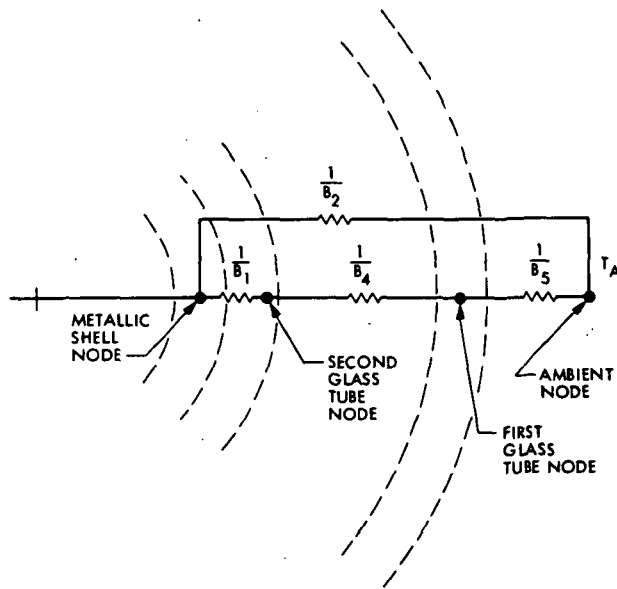


Fig. A-2. Overall heat loss coefficient  $B_0$

## Appendix B

### Numerical Example

As an illustration of the use of the computer program described in Appendix A, a numerical example is given next to show the sequence followed. For convenience, the performance of only one collector unit will be computed. The performance of a module with  $N$  units in series can be computed by repetition, following the same sequence of calculations of a single unit.

#### I. Input Variables

The following input variables are entered in the program where some were based on information provided by the manufacturer and the rest were estimated from past experience. The input data are grouped in order similar to Section II of Appendix A.

##### A. Optical Properties

Glass reflection <sup>1</sup> coefficient $r$	0.043
First glass tube extinction <sup>2</sup> coefficient $\phi$	$6.85 \text{ m}^{-1}$
Second glass tube extinction <sup>3</sup> coefficient $\phi$	$129.92 \text{ m}^{-1}$
Reflectivity <sup>4</sup> of metallic shell $b$	0.5
Reflectivity <sup>5</sup> of back V-reflector $\rho_v$	0.9
Emissivity of first glass tube surfaces $\epsilon_f$	0.9
Emissivity <sup>6</sup> of second glass tube surface $\epsilon_s$	0.2

##### B. Collector Dimensions

Spacing <sup>7</sup> between two consecutive collector units $S$	0.12 m
Inner diameter <sup>8</sup> of first glass tube $D_{f,i}$	0.076 m
Outer diameter <sup>8</sup> of first glass tube $D_{f,o}$	0.082 m
Inner diameter <sup>8</sup> of second glass tube $D_{s,i}$	0.058 m
Outer diameter <sup>8</sup> of second glass tube $D_{s,o}$	0.064 m
Inner diameter <sup>8</sup> of metallic shell $D_{a,i}$	0.056 m

Outer diameter <sup>8</sup> of metallic shell $D_{a,o}$	0.058 m
Length of one <sup>8</sup> side of U-tube $L$	1.22 m
Thickness <sup>8</sup> of insulation at the open end $t_u$	0.004 m

##### C. Thermodynamic Properties

Type of working fluid: ethylene glycol-water (50/50) by volume	
Fluid viscosity <sup>9</sup> $\mu_w$	1.04 kg/m h
Fluid specific heat <sup>9</sup> $C_w$	1.0122 Wh/kg°C
Fluid thermal conductivity <sup>9</sup> $K_w$	0.4 W/m°C
Glass thermal conductivity $K_g$	0.7 W/m°C
Thermal conductivity of shell $K_a$	380.16 W/m°C
Thermal conductivity of open-end insulation $K_u$	0.319 W/m°C

##### D. Operating Conditions

Fluid flow rate, m	5.0 kg/h
Inlet fluid temperature $T_c(0)$	48.89°C (120°F)

##### E. Weather

Solar radiancy $I$	630.7 W/m <sup>2</sup> (200 Btu/h ft <sup>2</sup> )
Ambient temperature $T_A$	4.4°C (40°F)
Wind speed $W$	4.47 m/s (10 mph)

## II. Output Results

The following is a partial list of the output results obtained from running the computer program using Sec. B.1 data.

##### A. Optical Properties

$\alpha_f$ (Eq. A-2)	0.0203
$\alpha_{f,e}$ (Eq. A-8)	0.0251
$\alpha_s$ (Eq. A-5)	0.4176
$\alpha_{s,e}$ (Eq. A-9)	0.3833

<sup>9</sup>Taken as an average from 4°C to 120°C.

<sup>1</sup> Taken at zero incidence angle and a glass refraction index of 1.526.

<sup>2</sup> Assumed made of clear glass (Refs. 2 and 3).

<sup>3</sup> Assumed made of a medium heat absorbing glass.

<sup>4</sup> For polished copper surface.

<sup>5</sup> For silvered aluminum surface.

<sup>6</sup> Assumed for a selective coating.

<sup>7</sup> See Refs. 2 and 3.

<sup>8</sup> Estimated from sketches in Refs. 2 and 3.

$\alpha_B$ (Eq. A-4)	0.3273
$\alpha_{a,e}$ (Eq. A-7)	0.3004
$\lambda$ (Eq. A-11)	1.4171

### B. Heat Transfer Coefficients

Reynolds number Re	612.1 (laminar)
Prandtl number Pr	2.632
Nusselt number Nu	4.748
Fluid heat transfer coefficient $H_{ah}$	189.9 W/m <sup>2</sup> °C
"Equivalent" coefficient $B_1$	544.5117 W/m <sup>2</sup> °C
"Equivalent" coefficient $B_2$	0.1336 W/m <sup>2</sup> °C
"Equivalent" coefficient $B_3$	72.7588 W/m <sup>2</sup> °C
"Equivalent" coefficient $B_4$	3.1424 W/m <sup>2</sup> °C
"Equivalent" coefficient $B_5$	85.1437 W/m <sup>2</sup> °C
Overall loss coefficient $B_0$	3.1473 W/m <sup>2</sup> °C

### C. Temperature Distribution

The temperature profile along each collector tube is plotted as shown in Fig. B-1 at the above input conditions. The arithmetic average of the tube temperatures are as follows: 6.58°C for the first glass tube; 58.57°C for the second glass tube; 58.24°C for the metallic shell; 53.05°C for the cold fluid and 57.38°C for the hot fluid. The actual fluid temperature gain  $[T_h(0) - T_c(0)]$  is computed as 8.6996°C using Eqs. (A-28) and (A-29).

In addition to the above results, the flow factor  $F$  is computed as 0.6401 and the collector efficiency is found to be 47.68%.

### III. Temperature Trends for Hot and Cold Fluids

The hot and cold fluid temperatures  $T_h(x)$  and  $T_c(x)$  were given in Appendix A by Eqs. (A-28) and (A-29), respectively. The useful temperature gain  $[T_h(x) - T_c(x)]$  at any position  $x$  from the open end can be written as

$$[T_h(x) - T_c(x)] = \left[ \frac{\delta}{C_1 - C_0} - T_c(0) \right] \left[ \frac{2(C_1 - C_0) \sinh n(L-x)}{n \cosh nL + (C_1 - C_0) \sinh nL} \right] \quad (B-1)$$

To find the location of any maximum or minimum fluid temperatures along the collector length, Eqs. (A-28), (A-29), and (B-1) are differentiated with respect to  $(x)$  keeping all other parameters constant. One can prove mathematically that neither the cold temperature  $T_c(x)$  nor the useful temperature gain  $[T_h(x) - T_c(x)]$  can ever possess any maximum or minimum value. In spite of this finding, the hot fluid temperature  $T_h(x)$  possesses one peak value at some location  $\bar{X}$  (measured from the open end) given by

$$\bar{X} = L - \frac{1}{n} \tanh^{-1} \left( \frac{C_1 - C_0}{n} \right) \quad (B-2)$$

$\bar{X}$  can be either within the collector tube or theoretically outside  $0 \leq x \leq L$  depending on the constants  $C_1, C_0$ . The corresponding temperature difference  $[T_h(\bar{X}) - T_c(\bar{X})]$  can be proven to be smaller than that at the open end ( $x=0$ ) at all times. The conclusion is that the rate of energy extracted from the collector is maximum at the open end and is unaffected by the internal temperature peaks. The optical stability of selective coatings, on the other hand, is related to the highest temperature attained, and therefore needs this investigation.

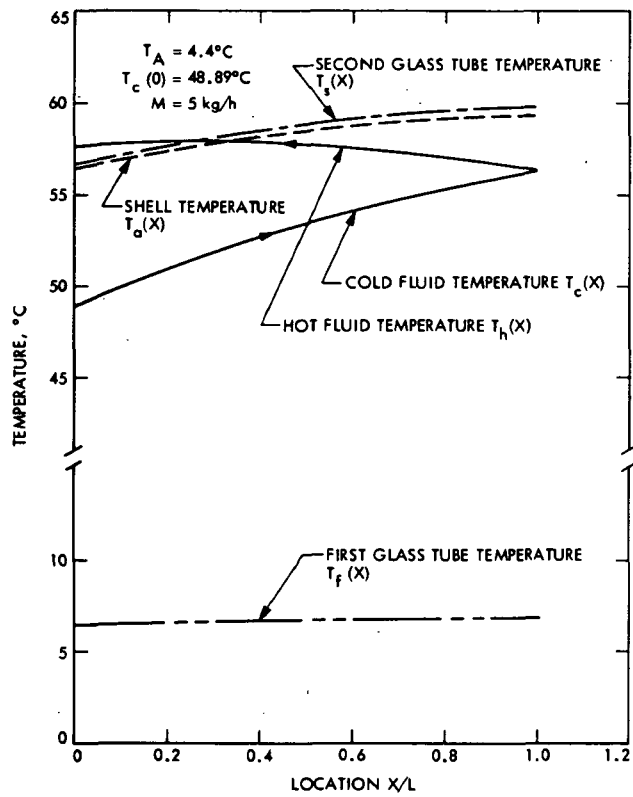


Fig. B-1. Temperature distribution along a collector unit

# DOMSAT CW Transmission Bent Pipe Investigation: Initial Phase Noise Measurements via RCA SATCOM Link

M. H. Brockman

Telecommunications Science and Engineering Division

C. E. Jones

Radio Frequency and Microwave Subsystems Section

*A preliminary investigation of a DOMSAT link using a SATCOM stationary Earth satellite and ground station has provided initial phase noise data for continuous-wave radio frequency transmission which is applicable to a bent pipe technique.*

## I. Introduction

An initial phase noise investigation has been made for continuous wave (CW) transmission from the RCA SATCOM station at Goldstone, California, up to a SATCOM stationary Earth satellite and retransmission back to the same Goldstone station. This investigatory test was conducted to provide initial information for a study for a proposed bent pipe concept for Galileo mission support.

2225-MHz) transmitted from the Earth satellite provided an output CW signal from the SATCOM ground station at approximately 73 MHz. Bandpass filters with 1-MHz half-power bandwidths were utilized at the input to and output from the SATCOM ground equipment to effectively eliminate any interference to and from other users. Uplink power was set by RCA so as to provide a downlink nominal carrier-to-noise power ratio of +11.4 dB in the 1-MHz half-power bandwidth for the ~73-MHz output signal.

## II. Configuration for Phase Noise Investigation

### A. General

The test configuration used for the CW phase noise investigation is shown in Fig. 1. For this investigation, a 73-MHz CW signal was provided to the RCA SATCOM ground station which resulted in an uplink CW signal at 6208 MHz to the SATCOM Earth satellite. The downlink signal (6208 minus

Operating frequencies for the elements of the test configuration shown in Fig. 1 were chosen so as to make use of available hardware as described later in this report. Translation of the ~73-MHz signal to 9.56 MHz provides a carrier-to-noise power ratio of +33.8 dB in a 6-kHz noise bandwidth at the output of the bandpass filter shown in Fig. 1 due to receiver noise. This 9.56-MHz signal plus noise provides an input to a sinusoidal phase detector which is an element of the phase-locked-loop shown in Fig. 1. The phase-locked-loop provides a

means for comparing the phase of the ~73-MHz output signal from the SATCOM ground equipment with the 73-MHz signal provided for uplink transmission. The receiver noise discussed above, which is input to the sinusoidal phase detector, appears as 0.83 degrees rms at baseband in a 3-kHz noise bandwidth at the output of the phase detector. The widest closed loop bandwidth of the phase-locked-loop is chosen so that any effect introduced on the 0.83 degrees rms due to receiver noise is small (about 0.5%). Any phase differences due to frequency translation, oscillator instability, and intermodulation effects in the SATCOM link will then appear at the output of the phase detector in a 3-kHz noise bandwidth superimposed on the receiver noise discussed above. These phase differences, if present, will represent those components that the phase-locked-loop cannot follow (track out) and consequently will be a function of the closed loop noise bandwidth. For this initial investigatory test, the phase-locked-loop shown in Fig. 1 had three selectable bandwidths with two-sided design values of 10, 50 and 250 Hz. The actual measured two-sided closed loop noise bandwidths were 9.3, 47, and 267 Hz.

## B. Equipment Description

To minimize hardware and engineering costs the test equipment used for the SATCOM phase stability measurements consisted of, for the most part, commercial equipment and components available at JPL. The uplink 73-MHz signal and the 63.44-MHz used within the phase-locked-loop were generated by Hewlett-Packard 5100A frequency synthesizers (refer to Fig. 1). The 24-MHz VCO used within the loop was a Block III receiver type. The reference frequency used for translating the downlink 73 MHz to 9.56 MHz was generated by a Fluke 644A synthesizer. All mixers were commercial double-balanced mixers including the loop phase detector.

Because of their inability to operate up to the required system frequencies, all synthesizers were set at one-half of the desired frequency, and then each output was frequency-multiplied, utilizing commercial frequency doublers followed by lab-constructed bandpass filters to ensure clean output spectra. Selection of 9.56 MHz for the translated downlink signal was dictated by an available narrow-band (~6 KHz) bandpass filter (FL1) centered at that frequency.

In order to duplicate the expected behavior of the test equipment using the SATCOM communication link, a lab test setup was made as shown in Fig. 2. The noise level was adjusted for a 11.4-dB signal-to-noise power ratio at the output of the 73-MHz bandpass filter (Point B); then the output spectrum of the 9.56-MHz filter (Point A) was photographed and is shown in Fig. 3. Comparison of Figs. 3 and 6 (described in Section III) shows similarity between the lab test

setup and the actual SATCOM spectrum at the 9.56-MHz filter output.

Figure 4 shows the loop dynamic phase error for 267-Hz bandwidth operation when locked to a test input CW signal plus noise with a signal-to-noise ratio of +11.4 dB in a 1-MHz bandwidth. Again, a close similarity between test and SATCOM measurements is noted by comparison of Figs. 4 and 7c (described in Section III).

## III. Measured Performance

Figures 5a and 5b show the ~73-MHz carrier signal plus receiver noise voltage spectrum at the output of the 1-MHz bandwidth bandpass filter for the downlink signal described in the preceding section for two different spectrum analyzer swept frequency ranges. Figure 6 shows the corresponding 9.56-MHz carrier signal plus receiver noise spectrum at the output of the 6-kHz bandwidth bandpass filter (input to the phase detector) over a smaller frequency interval. The measured values of phase noise at the output of the phase detector were 0.88, 0.85 and 0.83 deg rms respectively for the closed loop noise bandwidths of 9.3, 47, and 267 Hz. Figures 7a, 7b, and 7c are oscilloscope pictures of the phase noise at the output of phase detector for the corresponding measured 0.88, 0.85 and 0.83 deg rms values. Note that separate tests (see Section II-B) with a +11.4-dB carrier-to-noise ratio in the 1-MHz bandwidth at ~73 MHz provided the same carrier plus receiver noise spectrum as shown in Fig. 6 and a measured noise level of 0.83 deg rms at the output of the phase detector. Figure 8 shows phase noise plotted as a function of the phase-locked-loop two-sided noise bandwidth with a curve drawn through the measured data points. It is interesting to note that the measured phase noise (0.83 deg rms) for operation with 267-Hz closed loop noise bandwidth is the same as the expected value due to receiver noise as discussed earlier (Section II-A).

In explanation of this for the condition in which the 0.83 deg rms is essentially due to receiver noise, the measured 0.88 deg rms for 9.3-Hz closed loop selection includes additional phase noise of 0.29 deg rms due to the SATCOM two-way link. This results from the receiver noise and satellite link noise being statistically independent. The 0.85 deg rms measured for 47-Hz closed loop selection then includes additional phase noise of 0.18 deg rms due to the SATCOM link. If the assumption is made that the carrier-to-noise power ratio was actually 1 dB higher than described in Section II-A, then receiver noise would be 0.74 deg rms. The additional phase noise due to the SATCOM link would then be 0.48 deg rms for 9.3-Hz closed loop selection, 0.42 degrees rms for 47-Hz selection and 0.38 deg rms for 267-Hz selection.

During this CW phase noise investigation, another signal was observed in the SATCOM receiver about 1.5 MHz higher in frequency than the CW signal being observed herein. Later investigation by RCA revealed that this signal, which was transmitted from a station along the Alaskan pipeline, had its polarization (linear) improperly set and it should not have been present in the SATCOM transponder that contained the CW transmission considered here. It should be noted that subsequent polarization adjustment at the station in Alaska to orthogonal linear removed the signal from the transponder being utilized for this investigation. This signal (~1.5 MHz higher in frequency) appeared to be about 12 dB lower in peak level than the CW transmission. Observation of its on-off modulation pattern on a spectrum analyzer in the SATCOM ground station in conjunction with the phase error observed on the oscilloscope (see Fig. 7) indicated that a small portion (~1 deg peak to peak) of this modulation pattern appeared at the output of the phase detector in the phase-locked-loop discussed above (see Fig. 1).

#### IV. Summary and Conclusion

This initial phase noise investigation with CW transmission indicated that phase instabilities due to the SATCOM link are at relatively low frequencies about the radio frequency carrier. Providing that a phase noise investigation over wider bandwidths that will accommodate a telemetry modulation spectrum confirms this, a bent pipe technique utilizing such a link should introduce a very small telemetry signal-to-noise degradation for operation into a DSN station facility operating with radio frequency closed loop noise bandwidths of 10 Hz or greater. The test configuration described in this report can be expanded to include telemetry modulation which encompasses a correspondingly wider bandwidth. With such a configuration, a simulated telemetry transmission test conducted in conjunction with a facility such as CTA-21 would provide initial data on telemetry signal-to-noise ratio loss due to phase noise for a bent pipe technique.

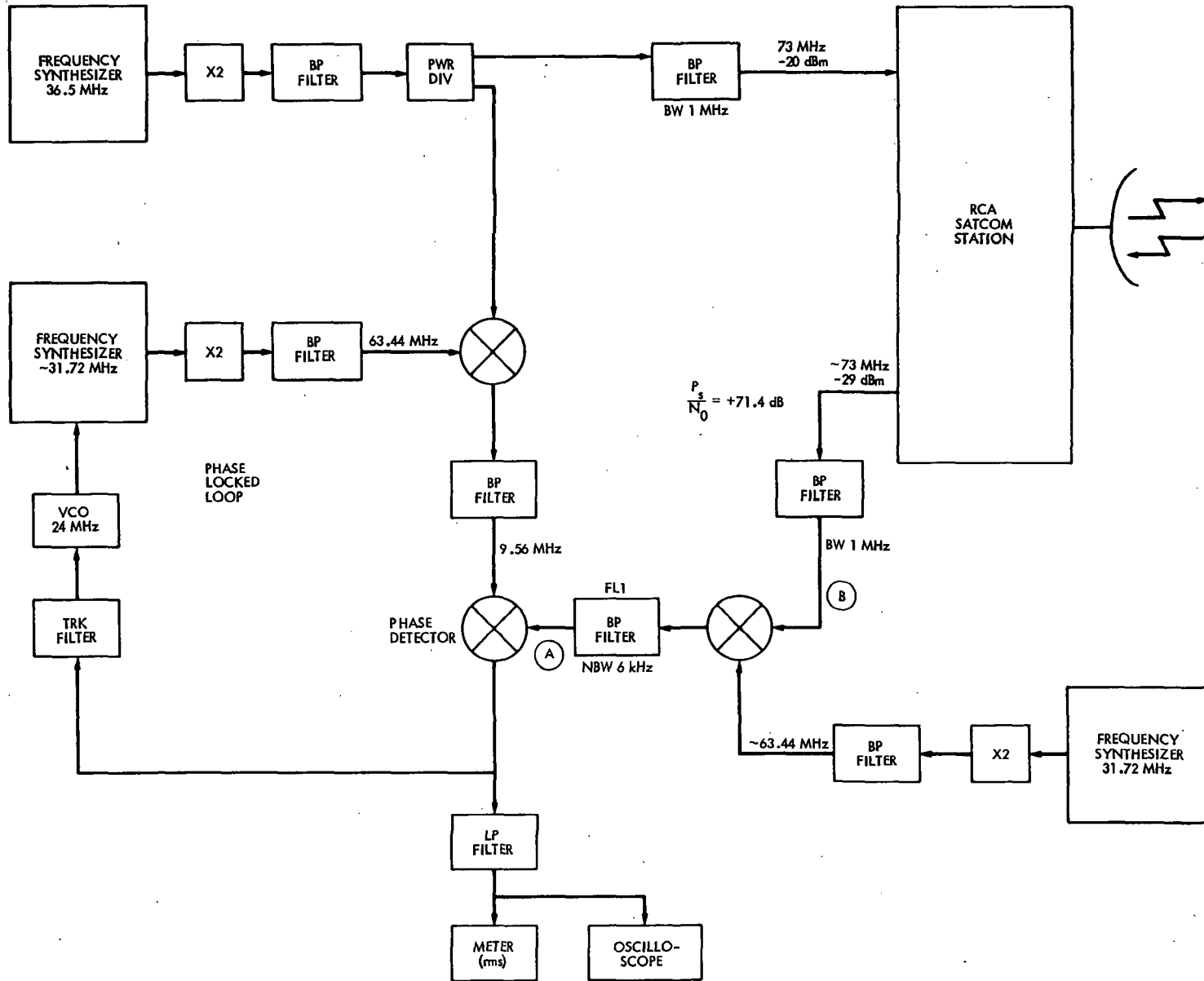


Fig. 1. Test Configuration for initial phase noise measurement CW transmission via SATCOM link

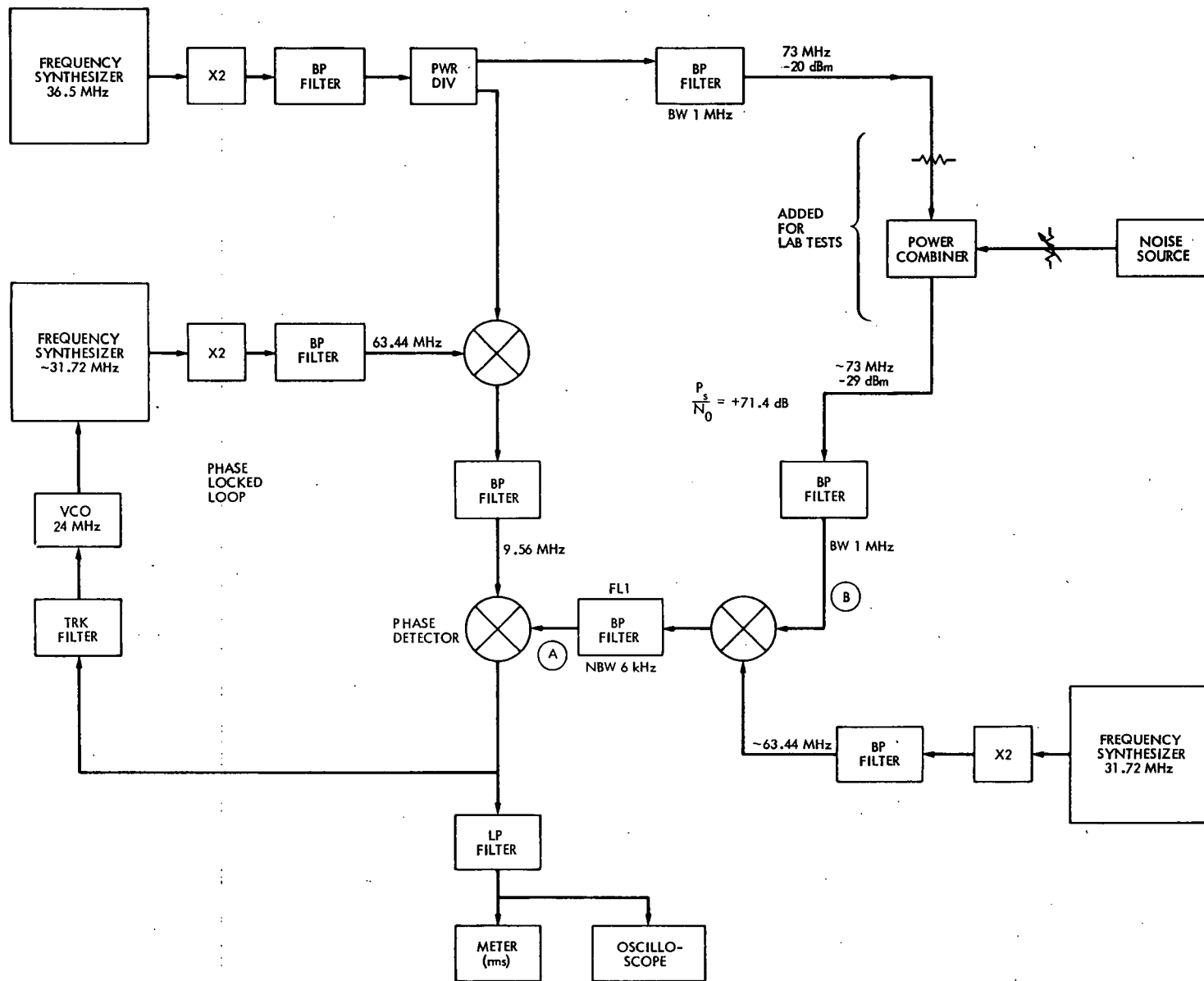


Fig. 2. Equipment configuration for laboratory calibration

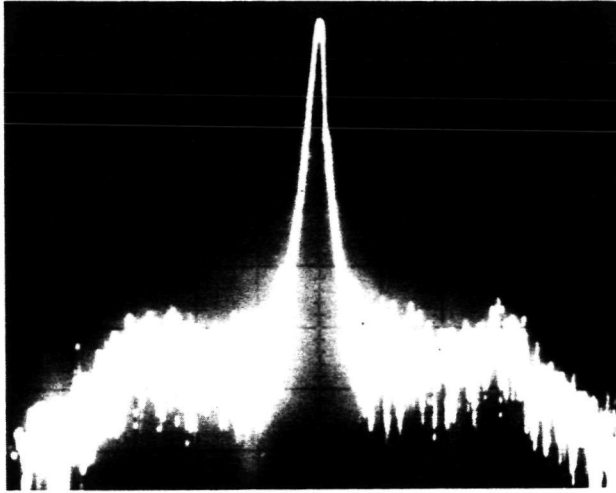


Fig. 3. 9.56-MHz lab calibration spectrum at 6 kHz-bandwidth filter output. Horizontal scale = 1 kHz/div; vertical scale = 10 dB/div (SNR) = +33.8 dB)

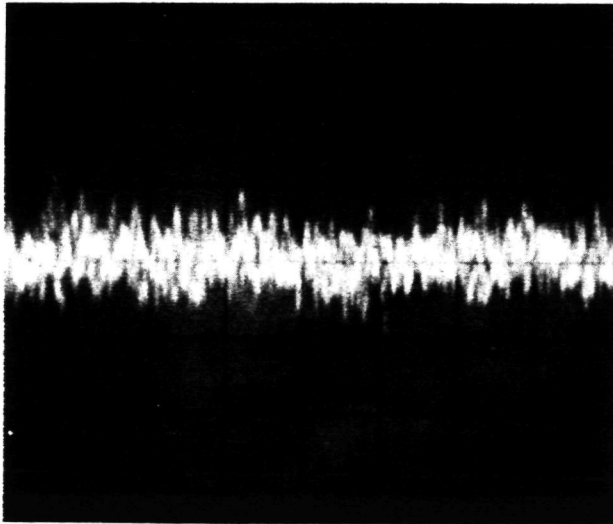


Fig. 4. Lab calibration 3-kHz bandwidth baseband noise. Horizontal sweep = 2 ms/div; vertical scale = 1.5 deg peak/div

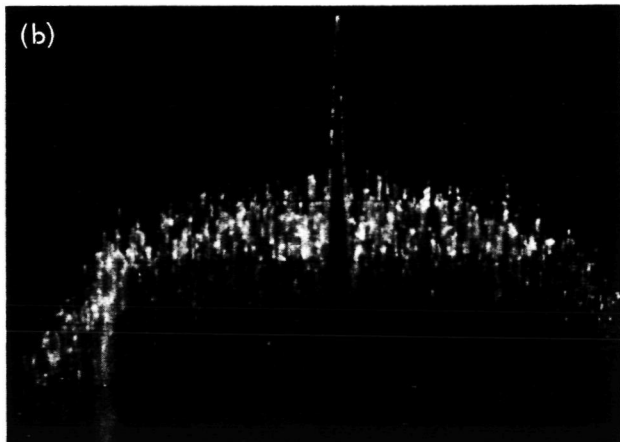
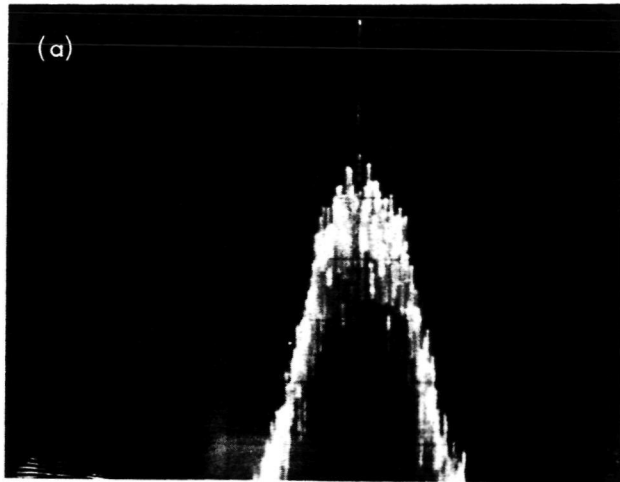
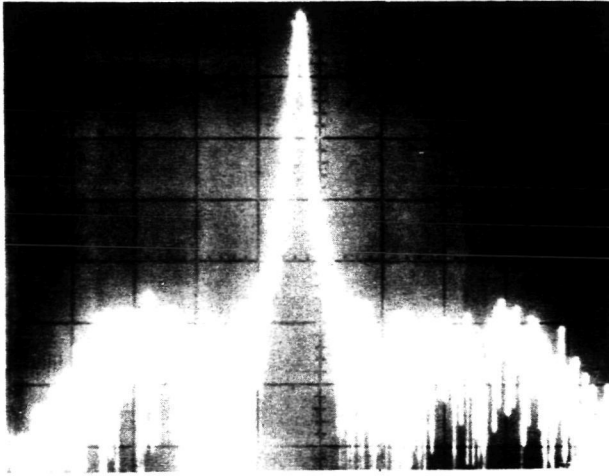


Fig. 5. 73-MHz received spectrum at 1-MHz bandwidth filter output (SNR = +11.4 dB)

- (a) Horizontal scale = 1 MHz/div; vertical scale = 10 dB/div
- (b) Horizontal scale = 0.2 MHz/div; vertical scale = 10 dB/div

ORIGINAL PAGE IS  
OF POOR QUALITY



ORIGINAL PAGE IS  
OF POOR QUALITY

Fig. 6. 9.56 MHz received spectrum at 6 kHz bandwidth filter output. Horizontal scale = 1 kHz/div; vertical scale = 10 dB/div (SNR = +33.8 dB)

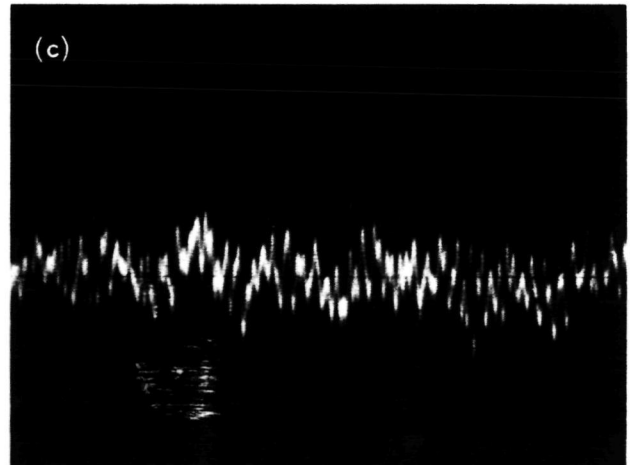
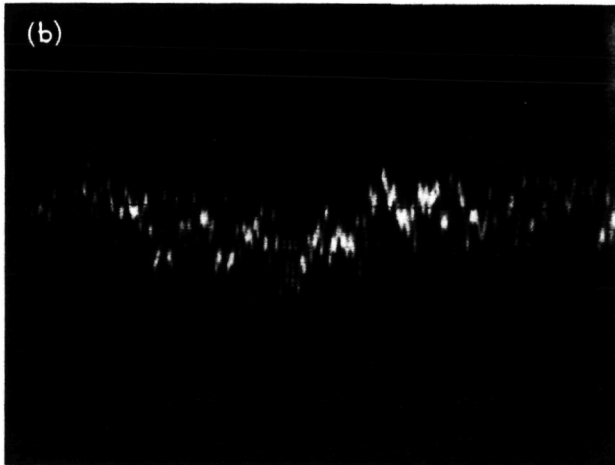
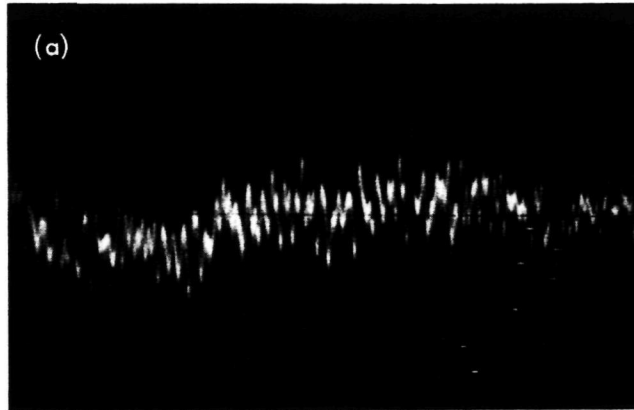
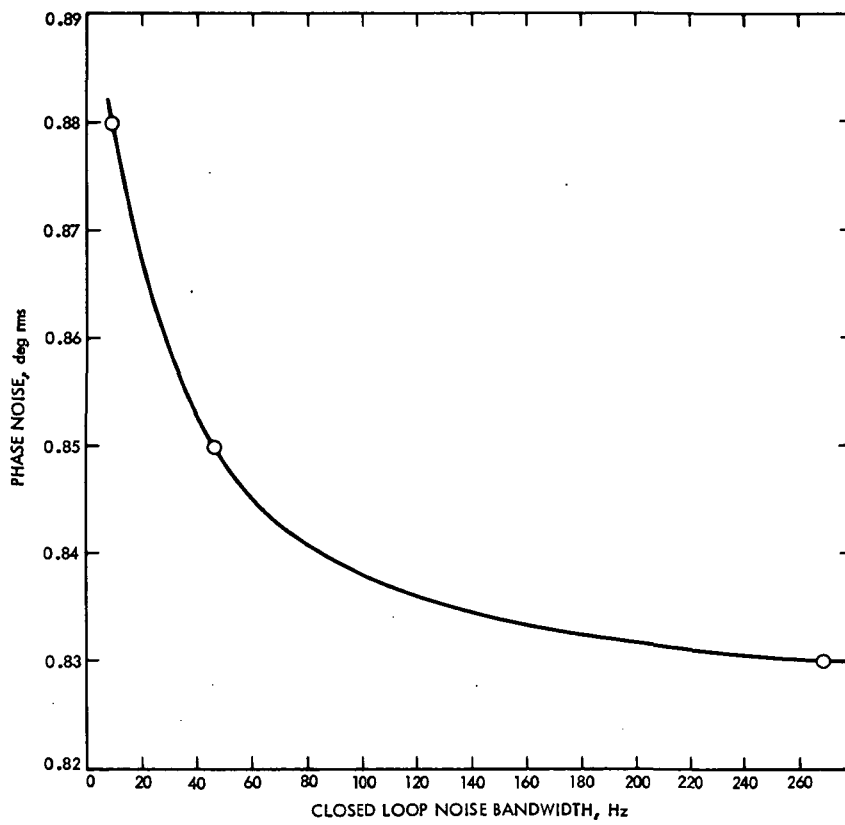


Fig. 7. Received 3-kHz bandwidth baseband noise. Horizontal sweep = 2 ms/div; vertical scale = 1.5 deg peak/div  
(a) 9.3-Hz phase-locked-loop bandwidth (b) 47-Hz phase-locked-loop bandwidth (c) 267-Hz phase-locked-loop bandwidth



**Fig. 8. Initial phase noise measurement RCA SATCOM link - CW transmission test**

## DSN VHF Transmitting Array Backup Command Uplink for Voyager 2

R. M. Dickinson

Radio Frequency and Microwave Subsystems Section

*As a result of the failure of the Voyager 2 primary S-band receiver and the failed component in the remaining receiver, JPL is evaluating the feasibility and cost of an alternate command uplink in the low VHF band around 40 MHz, by utilizing the planetary radio astronomy experiment receiver aboard the spacecraft. The design considerations, tentative specifications and one preliminary mechanization for the requisite ground transmitting facility are presented. The magnitude of the transmitting requirement is on the order of 120 dBm EIRP, achievable with a 183-m diameter phase steered beam array with 250-kW output power. Preliminary results of tests conducted to date employing the Stanford 46-m diameter steerable parabolic antenna and 300-kW CW VHF transmitter at 46.72 MHz are reviewed.*

### I. Introduction

The remaining Voyager 2 spacecraft command receiving capability is degraded, and there is concern on the continued operations of the primary S-band receiver even in its degraded mode. In order to enhance completing the assigned mission to Saturn and to, perhaps, preserve the capability of a flyby of Uranus, an investigation was undertaken to evaluate alternate command techniques other than via the normal S-band uplink or stored program capabilities on board the spacecraft for Voyager 2.

The planetary radio astronomy (PRA) experiment instrument was identified as a possible redundant command receiver in September 1973 by the PRA experiment project scientist because the PRA receiver output has a direct connection to the spacecraft Flight Data System (FDS). In concept, the VHF

uplink signal to the PRA receiver from the Earth would be suitably modulated, along with having the FDS previously modified so that its software programming would properly interpret the PRA instrument outputs as command logic signals to be routed to the Central Control and Sequencer (CC&S) for ultimate issuance to the appropriate spacecraft subsystem. The data rate would probably not be as high as the existing S-band uplink (16 bps) in order to afford the same bit error probability in the PRA non-phase locked or incoherent receiver, which is basically a broadband (200 kHz) power detector.

Because of the incoherent receiver, the low gain of the experiment antennas, the VHF operating frequencies and the long transmission ranges (Saturn 10 AU, Uranus 20 AU), a new ground-based transmitting facility would be required.

## II. Transmitting Array Specifications

For assistance in deriving the approximate requirements of the ground transmitter, it was necessary to estimate the PRA performance characteristics, taking into consideration the configuration and environment aboard the spacecraft. Because of on-board RFI from switching power supply harmonics and other electronics noise, the PRA receiver signal-to-noise ratio (SNR) is better at the upper end (greater than 40 MHz) of the receiver capability. The receiver is limited to less than 50 MHz by amplifier bandpass and image filtering design limitations. Also, from realistic considerations of the chances for obtaining a long term "emergency" RF spectrum uplink frequency assignment at VHF, the higher the frequency, the less the disruption to established users, and thus the greater the chance of obtaining a carrier assignment.

The galactic background noise level in this region of the RF spectrum dominates the receiver input noise, and has a frequency to the minus 2.7 ( $f^{-2.7}$ ) power characteristic that would also favor the upper end of the PRA instrument capability.

The PRA experiment antennas consist of a pair of 10-m long whips that are orthogonal to each other and as orthogonal as possible to the other spacecraft appendages (magnetometer and RTG booms). The resulting placement is such that the plane of the whips is swept back at about 35 degrees to the Earth-spacecraft line. The whip output signals are processed through RF circuitry that results in simultaneous right and left circularly polarized (RCP and LCP) outputs. The degree of crossed polarized discrimination in the actual spacecraft environment is unknown at VHF, but is estimated to be about 8 to 10 dB. The net result is a multilobed antenna pattern at VHF of somewhat unknown polarization characteristics whose spatial disposition, magnitude and frequency sensitivity are also unknown. Nevertheless, for purposes of link analysis, the assumption of a receiving gain equal to that of a simple dipole was selected, with the real state of effective gain to be determined (TBD).

The project scientist and JPL Division 33 personnel performed a preliminary link analysis and determined that the approximately 120-dBm effective isotropic radiated power (EIRP) may yield on the order of 8 bps at Jupiter (5 AU), 1/2 bps at Saturn (10 AU) and 1/32 bps at Uranus (20 AU) with a bit error probability of about  $5 \times 10^{-5}$ . The proposed modulation technique would be to switch between RCP and LCP.

Extensive spacecraft computer reprogramming, along with replanning of command sequences and sequence selection, would be necessary to accommodate the low data rates. It

should be pointed out that the reprogramming can only be effected initially via the surviving (hopefully) S-band command uplink. If the S-band link fails before the reprogramming is complete, the PRA outputs will not be accepted as legitimate commands.

It was further assumed for planning purposes that a single VHF ground transmitting facility would be employed, and that it must provide a minimum continuous period of two hours of transmitting time with the power beam pointed in the ecliptic plane.

## III. VHF Transmitter Options

A survey of existing VHF high-power transmitters and antenna installations was conducted in order to determine if any current facilities could meet the combined VHF frequency, EIRP, beam pointing and modulation requirements. Table 1 lists the candidates considered and brief notes concerning their technical limitations. All candidates were unsatisfactory on the basis of either EIRP limitations or pointing limitations, and polarization modulation diversity, which was not unexpected. However, it was noted that the Stanford facility was the most satisfactory near-term capability and was strongly recommended to the project to be employed in reducing the uncertainties in link design by conducting initial measurements of the receiving SNR at current range using the interrupted CW (ICW) modulation technique instead of polarization switching.

The longer term transmitter option of modifying or supplementing one of the existing facilities was felt to be not desirable when it was pointed out that dedicated, exclusive use of the facility may be required during track times and for verification testing of performance prior to critical mission phases. This priority or exclusive use (perhaps with configuration control) for upwards of five or more years would not be incompatible with a dedicated DSN facility if it turned out to be the *only* command uplink to the spacecraft.

The above considerations, when taken in connection with the required command verification and transmission elements, led to consideration of a site at Goldstone to make use of existing DSN facilities.

## IV. Transmission Facility Configurations

The 120-dBm EIRP capability may be achieved with various combinations of transmitter power and antenna gain. The simplest VHF uplink in concept is a single large transmitter and a steerable paraboloid, as generating large amount of power at these frequencies is not difficult generally. Nevertheless, if an antenna diameter of 100 meters is assumed, then on

the order of one megawatt of RF power must be radiated, CW. Feed breakdown and transmission line limitations are serious problems. Thus, in order to reduce the feed problems, an array of elements is desired, with the total radiated power divided between the elements. An obvious tradeoff exists between large, high-gain array elements that are steerable mechanically and electrically phased versus smaller elements that are fixed, requiring only electrical phase steering, at low RF power levels. High-power, continuous phase shifters are to be avoided.

As a result of the uncertainties in the required link performance and in the link location, and in order to provide maximum flexibility in the tracking time beam steering requirement, it was decided to employ simple crossed dipoles as the antenna elements, with solid state RF power amplifier modules at each element. If it were known for certain that only a two-hour tracking capability was required, then higher gain or shaped beam radiating elements could be employed. The ease of added growth and the fail soft character of the many element dipole array were added bonus factors to consider in the overall facility design.

To provide a point design for purposes of establishing the costs of a 120-dBm EIRP,  $\pm 15$  degree tracking VHF transmitting capability, which was also potentially capable of being implemented in less than a year, the system shown in Fig. 1 and the block diagram of Fig. 2 were selected for detailed consideration.

## V. An Array Point Design

A 1000 crossed-dipole element array with 250 W per element employing switched circular polarization modulation was selected to achieve the 120-dBm EIRP at 40 MHz. An unobstructed view to the south on a hillside tilted at latitude for an approximately 183-m (600-ft) diameter flat area with an access road and approximately one megawatt of primary power was desired.

An electrically bonded ground screen was required in order to yield a known and controlled ground plane. Square mesh with openings not much larger than  $1/3$  meter is desired for the circular polarization capability. The bonds are required to be continuous in both directions, as shown in the subarray drawing of Fig. 3.

Paralleled GaAs FET device output solid state RF power amplifiers of 125 W each, driving each orthogonal pair of dipoles at an element, driven in phase quadrature, would have their input drive signals switched by 180 degrees RF phase to achieve the polarization modulation.

The block diagram of Fig. 2 shows the array element phase shifters located within the proposed (unmanned) local control building. The low level signals would then be routed to the appropriate radiating element via double shielded coaxial lines buried beneath the ground screen or via solid outer conductor coax. Very high quality shielding is necessary to prevent feedback oscillations in the power amplifiers.

To enhance the capability for alternate uses of the facility after project completion or in the event the single remaining S-band receiver continues to successfully operate, a non-simultaneous receiving capability is shown. The receiving function could be employed to verify the transmit beam pointing location via monostatic radar bounces from the moon.

The bandwidth for the transmitter and antenna elements need be only that necessary to pass the modulation of the very low bit rate commands when operating. However, to the degree that there exists any uncertainties in the spacecraft antenna patterns as a function of frequency, and bandwidth may be allocated for any frequency latitude in that event, then added bandwidth capability may be required. Obviously, the alternate uses of the facility are enhanced by having large bandwidths, but at obvious increased expense. The narrow band array should achieve well over 70 percent aperture efficiency.

As it may be desirable to reduce the array antenna pattern sidelobe level during reception, a separate amplitude tapered aperture distribution combiner may be employed, which is switched in only during receiving operations. However, there is no good reason to taper the aperture distribution when transmitting commands, as the maximum on-axis gain that results is desired and simply achieved.

Bent, thinwall electrical conduit stuffed with rope to damp the wind driven vortex shedding oscillations was suggested for the radiating dipole elements. All four conductors could be grounded to the bonded ground screen at the element mounting base. Orthogonal wings of the dipoles could be fed in quadrature phase at the bends to yield circular polarization.

As the second harmonic of the array is near resonance of a standing person, and the site, if at Goldstone, is expected to be unmanned, then a personnel exclusion fence and warning signs and lights were proposed for alerting intruders to the RF hazard. The peak flux density on axis in the power beam is calculated to be about  $5 \text{ mW/cm}^2$  at a range of slightly less than a kilometer. The average flux density in the aperture is only about  $1.2 \text{ mW/cm}^2$ , but the peak, localized density in and around the dipoles with a body present is such as to be avoided if possible.

The threshold for producing instabilities in the ionosphere with the high-power VHF beam was calculated based upon thermal self-focusing. The 183-m diameter, uniformly distributed aperture, 250-kW array beam is about 10 dB below the threshold, and difficulties are not expected, except possibly in conjunction with severe solar activity.

## VI. Alternate Utilization

During the survey of existing facilities and in connection with discussions of the array with others, the alternate uses to which the array facility could be employed (listed in Table 2) were encountered. The SPS power beam ionospheric heating simulation application would actually benefit by a higher total flux density in certain regions of the ionosphere. Hence, an even larger area, more powerful facility would be mutually beneficial to DOE and NASA. Close coordination with the radio science and radar astronomy community as well as the National Science Foundation is advised if further detailed consideration of the capability is anticipated.

## VII. VHF Uplink Experiments

After the initial array design investigations, Stanford University was requested to participate formally in a test of the uplink in order to gain information for reducing the range of uncertainties in the estimated link performance and to determine if the spacecraft PRA receiver could be successfully commanded to a range of receiving frequencies higher than its nominally designed 40.5 MHz. Also, the on-board RFI environment was to be sampled in and around the compromise 46.72-MHz operating frequency for Stanford, which was recommended by the DSN frequency allocation group after considering the assigned government band edges in the Palo Alto area, while keeping in mind the severe tuning limitations of the quarter wave (at 49.8 MHz) stub-supported open-wire transmission lines on the dish of the Stanford antenna.

The Stanford group restored and retuned the transmitter facility to operational readiness on short notice in order to support the first test on September 13, 1978.

300 kW was transmitted from the 46-m (150 ft) diameter antenna for 6-minute, 24-second periods with a 50 percent transmit duty cycle, time tagged for later correlation by the PRA experiment team at the University of Colorado.

The Stanford signal, because of the greater than minus 25-dB SNR, was detected with difficulty in the PRA experiment output. The experiment provided a greater than 1000 to 1 probability against incorrect detection, but the results were about 4.3 dB down  $\pm 2$  dB one-sigma variation from the expected signal level. This result was well within the range of the TBD's, however. The on-board RFI appears not to be excessive from 40.5 MHz up to the highest frequency the PRA receiver was commanded to operate at, which was 49.152 MHz. An unresolved issue was that the on-board PRA instrumentation recorded receipt of the sense of circular polarization opposite that which was transmitted from the Stanford antenna.

An attempt was made to repeat the experiment again on November 18, 1978; however, one of the coaxial transmission lines carrying the high-power RF failed.

## VIII. Conclusions and Recommendations

The PRA VHF uplink to Voyager 2 is technically feasible given that the FDS can be reprogrammed to interpret the experiment receiver output as legitimate commands when properly interfaced with the spacecraft CC&S. Depending upon the desired bit error probability and bit rate for the commands, a transmitting array larger than 183-m diameter and/or a radiated RF output power of greater than 250 kW may be required.

If the decision is made to pursue this alternate command link, then more detailed studies should be made of the optimum command sequences, stored command selection, the best allowed operating frequency, the spacecraft antenna patterns and polarization, the optimum modulation scheme, and the best location and implementation configuration for the VHF transmit array.

**Table 1. 40-MHz uplink capabilities**

Requirements Summary:		
(1) EIRP 120 dBm at ~40 MHz		
(2) 2-h tracking, minimum		
(3) Switched circular polarization modulation		
(4) Capable of ~9 mo implementation, 1985 end of life		
Candidates considered	Latitude	Capabilities
Arecibo	18.5° N	92 m (300 ft) useful at 40% $\eta_A = 27$ dB (93 dBm = 2 MW, feed, power amplifier and rotary joint required)
Stanford*	37° N	46 m (150 ft) at 50% $\eta_A = 22.7$ dB, 300 kW = 84.7 dBm (-12.6 dB and feed) (designed for 49.8 MHz)
Platteville	40.18° N	10-element ring-dot array $\approx 19$ dB, 2 MW = 93 dBm (-8 dB, 25-30 MHz)
Sunset	40.18° N	29-dB manual-steerable, linear-polarization, 5-kW average (steering and power limits)
Goldstone DSS 14 mod	35.16° N	64 m at 40% $\eta_A = 24$ dB (96 dBm = 4 MW, feed, power amplifier required)
Turnstile array	35.16° N	1000 turnstiles for 36 dB, 250 W per subarray, $\pm 23\text{-}1/2^\circ \times \pm 15^\circ$ scan
Jicamarca	12.5° S	1/2° beam, 6 MW peak, 49.98 MHz, manual phased
Alternative designs: Shaped beam subarrays, folded dipole radiators, mechanically steered, high-gain subarrays, manually phased declination, high-power phase shifter		
*Recommended to reduce link design uncertainty by measuring SNR at current range.		

**Table 2. 40-MHz uplink alternate utilization**

Solar corona radar
SPS power beam ionospheric heating simulation
Stratosphere-mesosphere coherent scatter radar
Pulsar receiver array
Earth and planetary Faraday rotation effects
Radio astronomy sky mapping

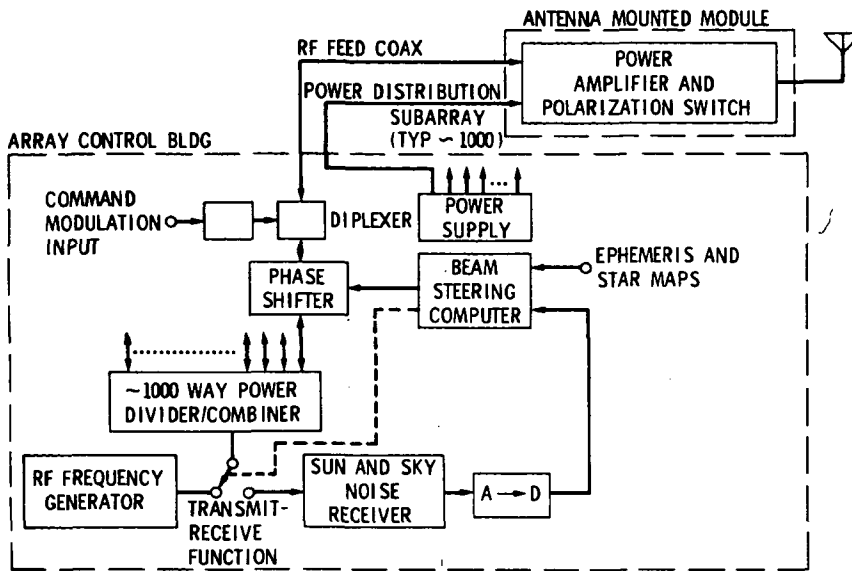


Fig. 1. 40-MHz uplink crossed dipole array

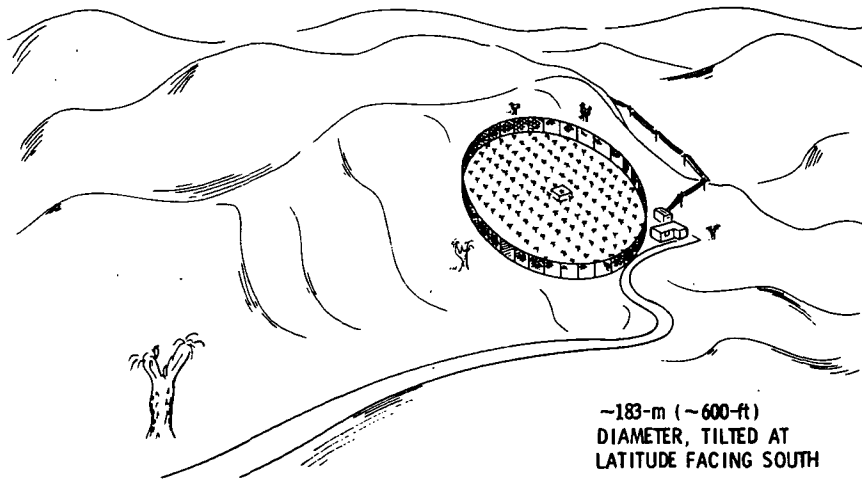


Fig. 2. 40-MHz uplink system block diagram

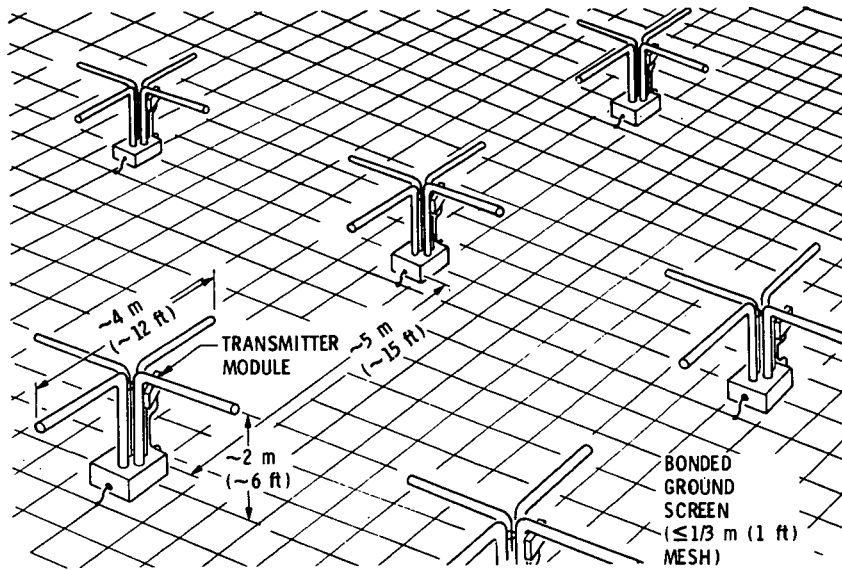


Fig. 3. 40-MHz uplink subarrays

## X-3060 Klystron Design Improvement Program Status

A. Goldfinger  
Varian Associates, Inc.

M. A. Gregg  
Radio Frequency and Microwave Subsystems Section

*The X-3060 klystron, a 100 kW continuous wave amplifier klystron, was introduced in the DSN in 1965. Questions have arisen since its introduction regarding its field performance record but its operational performance has been difficult to assess. An early design defect was corrected in 1974 by rebuilding all tubes with an improved potted heater design and only one failure has been recorded since that time. However, due to early "start up" failures, age of the present units, and efforts to establish the most reliable performance possible, a study program was begun to evaluate the klystron design. This article describes the results of Phase I (Study Definition) and Phase II (Design Improvement) of a four-phase program. Phase I revealed certain weaknesses and design features that conflict with ultrareliable klystron performance. Phase II has produced a new paper design that overcomes the deficiencies and unreliable features shown by the Phase I effort.*

### I. Introduction

The study program was originally directed toward the eventual redesign of the X-3060 and X-3075 S-band klystrons. At the conclusion of Phase I (Study Definition), however, the decision was made at JPL to direct the remaining effort of the study program toward improvement of the X-3060 klystron only. The evaluation was completed in October, 1977. Results of the analysis were presented to JPL in a design review meeting on 27 October 1977. This critical examination of the X-3060 design revealed certain weaknesses and design features which conflicted with ultrareliable klystron performance. The findings and recommendations of the Phase I evaluation are summarized in Table 1.

The primary goal of the study program (Phase II) was to produce a new paper design for the X-3060 klystron which would overcome the deficiencies and undesirable features shown by the Phase I evaluation. A fundamental requirement of the new design is increased reliability. A secondary effort is directed toward increasing the efficiency of the X-3060, but only insofar as it does not compromise reliability. Although Phase II primarily concerns itself with computer designs and analysis, detailed layout and outline drawings have been generated to present a more complete comparison between the new and the old designs. The design improvements, discussed in the following paragraphs, are presented in two parts: electrical design improvements and mechanical design improvements.

## II. Electrical Design Improvements

The electrical design improvements, as a result of Phase II of the study, deal with redesign of the electron gun and RF structure of the klystron.

### A. Electron Gun

Redesign and analysis of the existing X-3060 klystron electron gun have shown that a considerable gain can be made in lowering the voltage gradients in the electron gun. This will certainly provide a marked improvement in tube performance with regard to gun arcing. Additionally, lengthening of the electron gun envelope insulator may be incorporated as an option in the new design if it is desired, to eliminate the oil-filled socket tank. Assuming that the changes are consistent with the requirements of field applications, removal of the modulating anode is highly recommended.

Because the preliminary findings (Phase I) indicated that substantial voltage gradient improvement could be made by removing the modulating anode, a new physical design has been generated to accomplish this improvement. Figure 1 is the physical layout of the existing X-3060 electron gun. Figure 2 shows, for comparison, the physical arrangement of the new design.

In addition to the modulating anode removal, lengthening of the ceramic insulator enclosing the electron gun should be considered. This lengthening was not considered or discussed during the Phase I investigation and is introduced here as a suggestion only. Such lengthening will not affect the electron optics or the internal voltage gradients of the gun, but will lower the external voltage gradients to permit reliable operation in air. In future systems installations, this could eliminate the very costly oil-filled socket tank now used.

Upon completion of the new physical layout, computer analysis was made for the voltage gradients and electron optics of the new design. Figure 3 shows comparative voltage gradients between the old and new designs. As predicted from the Phase I estimates, the highest gradients were substantially reduced, and the highest gradient calculated in the new design was 100 kV/cm (254 kV/in.).

### B. RF Structure

Computer analysis shows that by lengthening the RF structure and rearranging the RF design parameters, significant improvement can be made to three important operational parameters (i.e., gain, bandwidth, and efficiency). Importantly, no far-out or "state of the art" techniques need be employed to obtain these results. Following present-day good design practice is all that is required. Actual predicted perfor-

mance is summarized in Table 2 and the original design is compared to performance results obtained from an X-3060 built recently (May 1978).

During the investigation of the present X-3060 RF design, a number of deficiencies were noted. These deficiencies are a natural result of designing a klystron with a wide tuning range (i.e., 2114 to 2388 MHz). In particular, drift tube gap spacing and gap-to-gap drift tube distances are often compromised to satisfy operation at both ends of the frequency tuning range. In fact, the output cavity drift tube gap in the present X-3060 design is far too long to provide optimum efficiency at either 2114 MHz or 2388 MHz, but it is designed this way to provide low gap capacitance, a requirement of wide tuning range cavities. It is also worth repeating that wide range tuning mechanisms (cavity tuners) in high power klystrons have traditionally compromised high reliability. Typical disadvantages are:

- (1) The tuner is normally subjected to high RF fields, the consequence of which is high RF loss and subsequent thermal stress.
- (2) Because of size limitations at high frequencies, coolant passages within the tuner are necessarily small and subject to blockage.
- (3) The tuner can easily be subjected to mishandling and mistuning accidents caused by inexperienced personnel.
- (4) Because of the inherent fragility and complexity, the tuner presents a problem with regard to its vacuum integrity during both initial construction and subsequent rebuilding operations.

Naturally, if system requirements dictate wide-range operation, nothing can be done to avoid the design compromises, and unfortunately, state of the art wide range tuner designs offer no improvement over what already exists in the X-3060. Present JPL requirements are unique, however, in that operation is confined to a few discrete frequencies at the extremities of the 2114 to 2388 MHz frequency range. It was suggested in the Phase I final report that the wide tuning range requirement be eliminated and that two tubes be developed, each electrically optimized for its particular frequency, one at 2114 MHz and the other at 2388 MHz. These tubes would have narrow range trim tuners only, to permit initial factory tune-up. This is the design philosophy used throughout the Phase II effort. The two tubes are mechanically interchangeable, using a common focusing magnet.

Two completely new designs have been developed. The first will operate at 2388 MHz and is referred to in the remainder of this article as the X-3060A. The second tube will operate at 2114 MHz and is referred to as the X-3060B. Both designs will

be electrically similar to the 5K70SG klystron. The 5K70SG was used as the basic model because it has demonstrated a highly efficient performance, with reliability in numerous field applications for a period exceeding ten years.

Computer programs (Klystron Design Calculation Program) were used to translate the 5K70SG design criteria to the operational conditions of the X-3060A and X-3060B. Computer analysis showed that the X-3060B (2114 MHz) would have to be 10.16 cm (4 in.) longer than the existing X-3060 to satisfy the 5K70SG design criteria, and the X-3060A would have to be approximately 5.08 cm (2 in.) longer. Although this added length is not particularly desirable, its introduction into the next series of calculations (Gain-Bandwidth Computer Program) produced a larger than expected increase in the small-signal gain. This additional gain is not a requirement of the improvement program, but the gain can be traded off for additional bandwidth. Greater bandwidth will greatly improve the operational stability, particularly at the band edges (2384 MHz and 2392 MHz in the X-3060A, 2110 MHz and 2118 MHz in the X-3060B). Because of this worthwhile stability improvement, a new target bandwidth of 12 MHz was established (present requirements are 8 MHz), and the Gain-Bandwidth Programs were used to accomplish this new goal. The computer predicted performance exceeds even the new 12 MHz goal by a comfortable safety margin.

The calculations discussed above have established the preliminary operational parameters to be analyzed by the Varian LSCEX2 large-signal computer program. The large-signal program takes into account the space-charge debunching forces in the electron beam from the lowest level of RF drive power to the highest RF drive level required to obtain saturation (maximum) power output. During this final analysis phase, the preliminary design parameters may be readjusted slightly to obtain the ultimate goal which in this case is maximum efficiency consistent with electron beam stability.

Because the basic design parameters are essentially scaled from a klystron that performs well (5K70SG), no adjustment of drift tube diameters, gap spacings, or drift distances was required. Tens of iterations were used, however, to determine two parameters in particular: the output cavity  $Q_L$  (primarily the external coupling factor) and the frequency placement of the penultimate cavity. The interdependence of these two parameters was very thoroughly analyzed because of the many combinations that can be used to obtain a highly efficient performance and the markedly different effect each combination has on the action of electrons in or near the output cavity gap.

A combination is chosen that satisfies requirements of gain and efficiency. But more importantly, a parameter combina-

tion must be chosen that does not permit electrons to stop, reverse their direction in the output gap, and return toward the input cavity. This is accomplished by selecting a sufficiently high minimum velocity for the slowest electrons found in the output gap.

### III. Mechanical Design Improvements

The following paragraphs deal entirely with the mechanical redesign as applied to the new RF designs. The approach used to describe the mechanical changes is a comparative one, using the existing X-3060 as a model so that the merit of the new design can be seen relative to the old design.

#### A. Diaphragm Trim Tuner

For the purpose of this discussion, it is assumed that the present wide range tuning requirement can be eliminated and that a two-tube approach can be used to cover the present operational frequencies. This assumption permits the introduction of a simple and reliable diaphragm tuner, many versions of which have been used in very high power applications.

The proposed trim tuner to be used in the X-3060A or X-3060B, and the wide-range tuner presently used in the X-3060, are shown in Fig. 4. Casual observation will show the complexity of the old tuner design as compared to the new trim tuner. Not so obvious in the old design are the six vacuum-to-water and three vacuum-to-air brazing joints used in the present X-3060 tuner. In addition to the large number, many of the brazing joints are blind; that is, they can neither be inspected nor repaired after the final braze pass. This type of assembly severely compromises reliability and rebuildability. Compared to this, the trim tuner design has only two vacuum-to-air brazing joints and no vacuum-to-water joints. Neither of the vacuum-to-air joints is blind, and both are easily repairable.

In addition to these mechanical advantages, the trim-tuner diaphragm is relatively far removed from the high RF fields at the drift tube gap center and will therefore be subjected to far less RF heating than the present X-3060 capacitive paddle. The diaphragm is thermally coupled by large cross-sectional areas of copper to the massive water cooled copper cavity walls. In Fig. 4A, a water cooled post is shown joined to the diaphragm face. This is a contingent plan only, and it is expected that this cooling can be eliminated.

In the authors' opinion, replacement of the complex wide range tuner with the simpler trim tuner is one of the most important steps that can be taken in redesign of the X-3060. If this recommendation cannot be followed, and wide frequency range operation is an absolute requirement, the present

X-3060 tuner must be completely redesigned mechanically, as recent experience has shown it to be almost unbuildable. At best, however, the wide range tuner will never compare in reliability to the proposed diaphragm trim tuner.

### **B. Extended Tailpipe Elimination**

As described in the Phase I final report, the most significant deficiency of the present X-3060 klystron is the extended tailpipe design. The tailpipe is that region of the klystron just beyond the output cavity drift tube gap.

The extended tailpipe configuration shown in Fig. 5 was first introduced in the X-3060 klystron in 1965. Its purpose was to minimize the asymmetry normally caused by the exit path of the output waveguide through the focusing magnet, and to reduce to an absolute minimum body current interception caused by the magnetic asymmetry. Mechanical considerations, however, created an extended tailpipe section that is exposed to a rapidly expanding electron beam just beyond the output gap. This extended section has created both indirectly and directly related failures in the X-3060 klystron. The problem is caused by the fact that the electron beam expands in that region faster than was predicted at the time of the design introduction, and additionally, secondary electrons return from the collector to impinge on the tailpipe surfaces.

For the above reasons, and because the tailpipe is electrically part of the klystron body, the body current readings for the X-3060 have been recorded as high as 10% of the total beam current. This tailpipe current (reading as body current) completely masks body current interception in any other part of the RF structure and is unacceptable because it requires that body current protective circuit trip levels be set too high (1.0 amp). This removes the protection required in the remainder of the RF structure which may suffer damage from relatively low quantity (0.050 amp) but high velocity electrons. Under these circumstances, protection cannot be provided for the following common field conditions:

- (1) Low or incorrectly adjusted magnetic field.
- (2) Incorrect tuning.
- (3) Overdrive.
- (4) Stray magnetic fields (gun region).
- (5) Disturbance of the main magnetic field by accidental introduction of ferrous materials (screwdrivers, wrenches, etc.).

Elimination of the extended tailpipe design is not only recommended, it is a mandatory condition for reliability. Figure 6 shows the new design to be employed in the X-3060A/B klystrons. As shown, the new design provides

adequate clearance for the expanding beam and transfers tailpipe interception current to the collector where it is properly metered as collector current. With this configuration, body current readings will return to normal values in the order of 0.050 amp to 0.075 amp, and the RF structure can be properly protected with body current protective trips set at 0.100 amp.

One additional design change has been made. A reentrant output polepiece has been introduced to create a peak in the magnetic field near the output gap. Recent designs have shown that this peaked magnetic field is very beneficial in terms of reducing beam interception in the output region of the klystron. This reentrant design is shown in Fig. 6.

### **C. Cavity/Body Construction**

It was found, during the investigation of the X-3060, that the rigidity of the RF structure was somewhat lacking and structural stiffeners were promised for proposed new designs. That will be the case, but in addition, recent tests of an X-3060 (May 1978) showed thermal drift attributable to cavity detuning, indicating a need for additional cavity cooling.

The proposed new design for the X-3060A/B will incorporate relatively massive copper cavities which have a wall thickness in the order of three times the wall thickness of the present X-3060. Not only will this create a rugged RF structure, it will permit the passage of water through the cavity walls to insure greater thermal stability. Comparative views of the present cavity structures and the proposed design are shown in Figs. 7 and 8. In addition to increased cavity wall thickness and cooling, cavity end walls and drift tubes will have increased thermal cross section to provide the best possible thermal stability.

In short, the RF structure will have construction closely paralleling a 450 kW klystron (X-3070) known to be operationally stable at the highest frequency of concern (i.e., 2388 MHz).

## **IV. Summary**

The end product of the Phase II segment of the present study contract is the presentation of a new paper design which eliminates the deficiencies of the present X-3060 klystron. Below is a list of the major modifications involved in creating the new design:

- (1) Gun ceramic lengthened to permit operation in air.
- (2) Modulating anode removed to reduce voltage gradients.

- (3) Increased drift tube and cavity wall cross section for improved thermal stability.
- (4) Incorporation of cavity wall cooling for thermal stability.
- (5) Modified gap and drift tube spacings for greater efficiency.
- (6) Elimination of complex wide range tuner and replacement with simple trim tuner.
- (7) Elimination of complex extended tailpipe design and replacement with conventional waveguide output circuit.
- (8) Replacement of long taper waveguide with Tchebycheff step transition to maintain waveguide flange interface plane.
- (9) Modification of collector to incorporate conventional flytrap design (replaces extended tailpipe).
- (10) Modification of magnet to interface new tube design.

**Table 1. X-3060 design evaluation summary**

Parameter	Rating/ comments	Recommendations
<b>A. Electron gun</b>		
1. Cathode filament	Good	Maintain
2. Cathode loading	Excellent	Maintain
3. Voltage gradients	Fair	Redesign
4. Modulating anode	Unnecessary	Eliminate
<b>B. Klystron body</b>		
1. Tailpipe	Unacceptable	Redesign
2. Tube/Magnet alignment	Marginal	Redesign (accomplished)
3. Tuners	Disadvantageous	Redesign
4. Higher efficiency	Practical	Redesign
5. RF design parameters	Fair	Redesign
6. Mechanical rigidity	Marginal	Redesign
<b>C. Magnet</b>		
1. Tube/magnet alignment	Marginal	Redesign (accomplished)
2. Individual coil control		Recommended
3. Magnet assembly	Not compatible (new tailpipe design)	Redesign

**Table 2. Predicted performance (X-3060A and X-3060B) versus performance of existing X-3060**

Parameter	Units	Existing	X-3060	X-3060A	X-3060B
Frequency	MHz	2388	2114	2388	2114
Beam voltage	(kV)	36.0	36.0	36.0	36.0
Beam current	(A)	7.7	7.7	6.96	6.96
Power output	(kW)	115	112	125	132
Efficiency	%	41.4	40.4	50	52.7
Saturation gain	dB	56.6	54.7	59	59.3
Saturation BW	MHz	10.58	10.4	16.7	16.7
Small signal gain	dB	59.63	58.0	61	61
Small signal BW	MHz	6.1	6.4	14	13.8

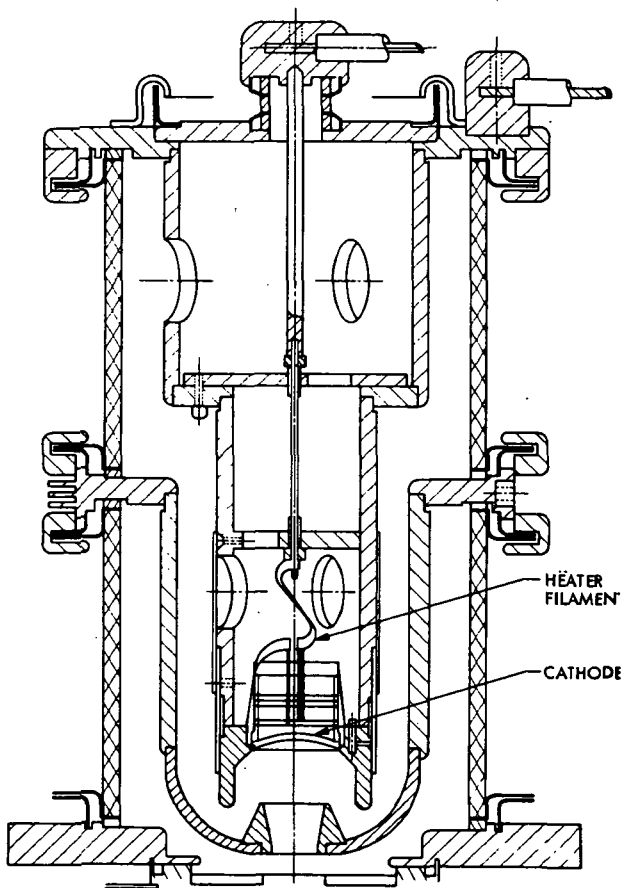


Fig. 1. Existing X-3060 electron gun layout

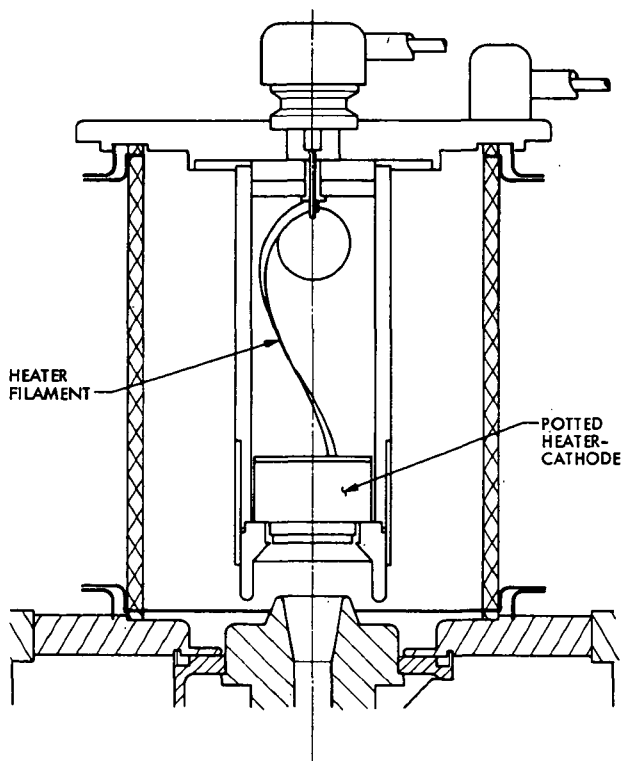


Fig. 2. New design X-3060 electron gun layout

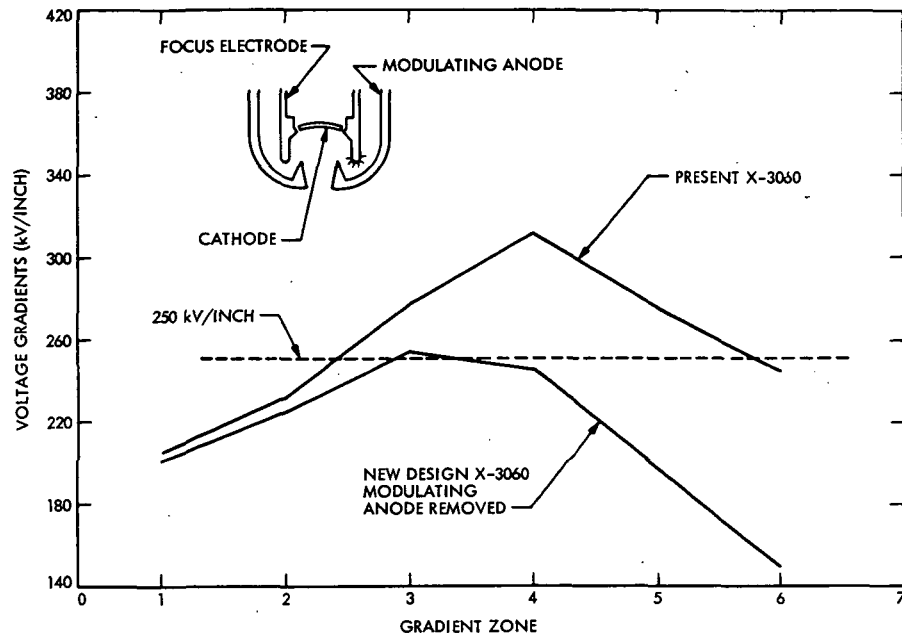


Fig. 3. Gradient comparison: new vs. old design

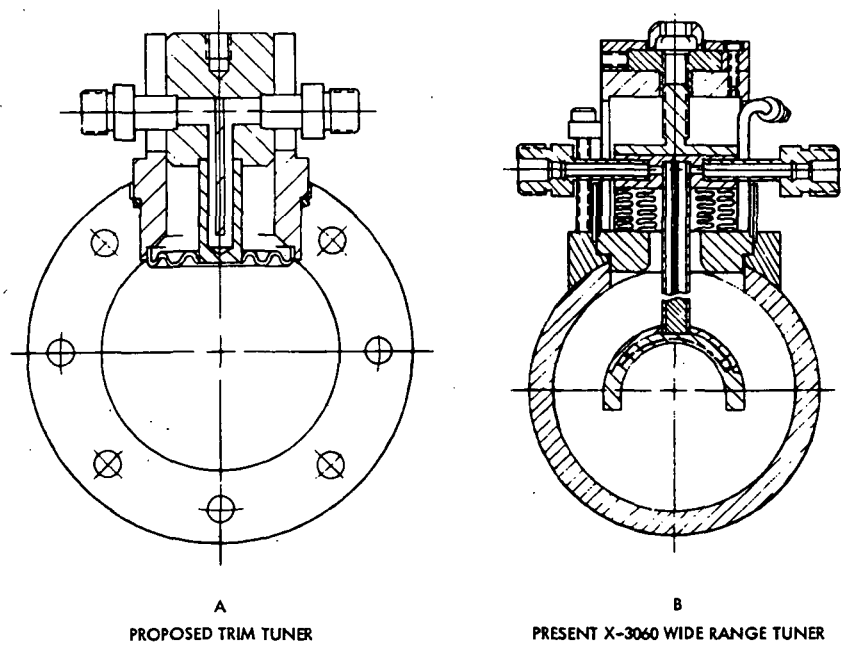


Fig. 4. Tuner designs

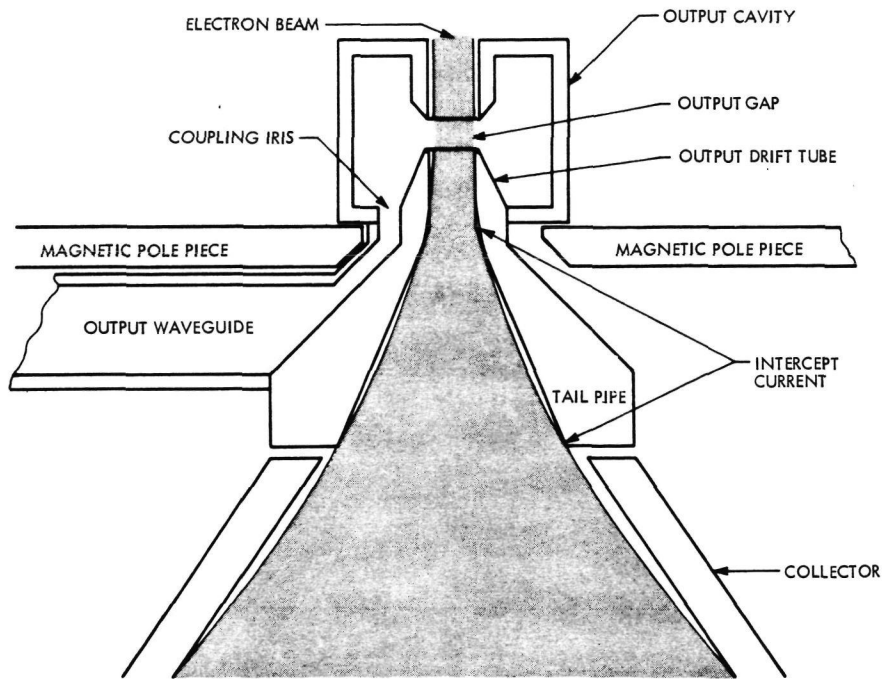


Fig. 5. X-3060 output circuit showing extended tailpipe

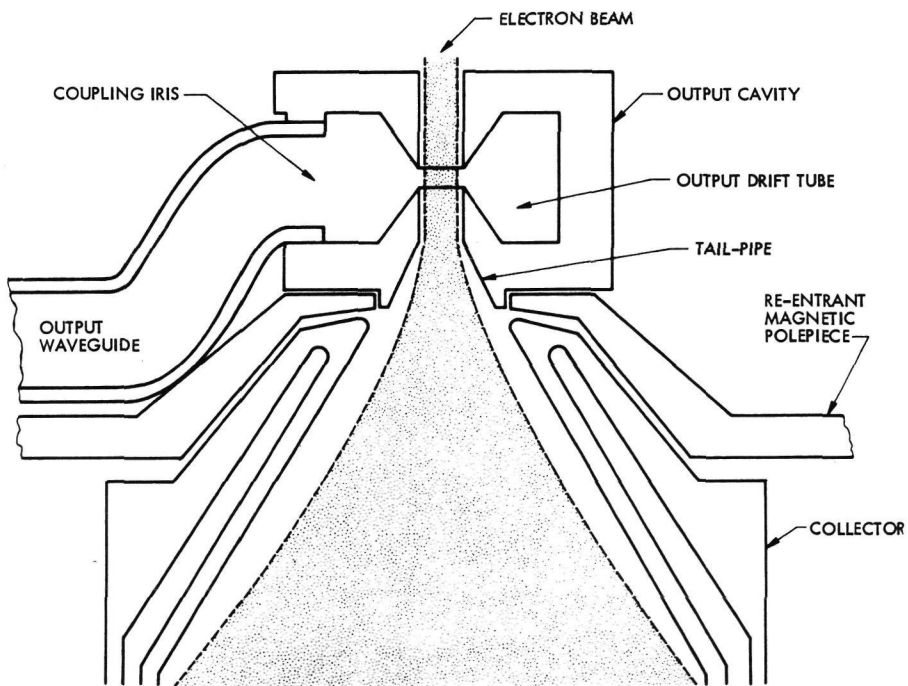


Fig. 6. New design X-3060A/B output circuit

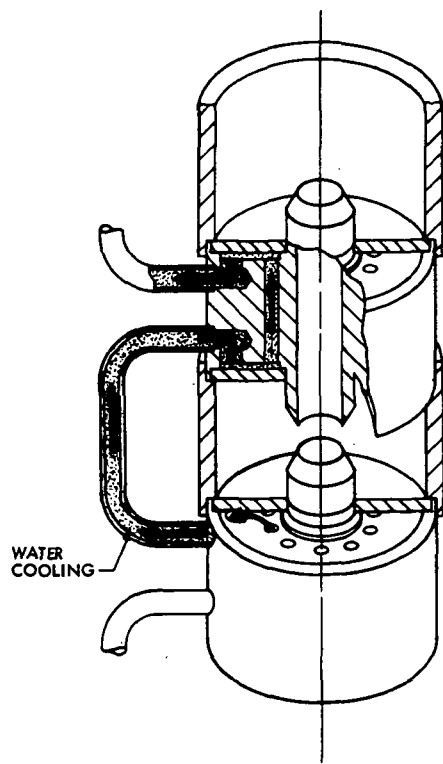


Fig. 7. Present cavity structure, X-3060

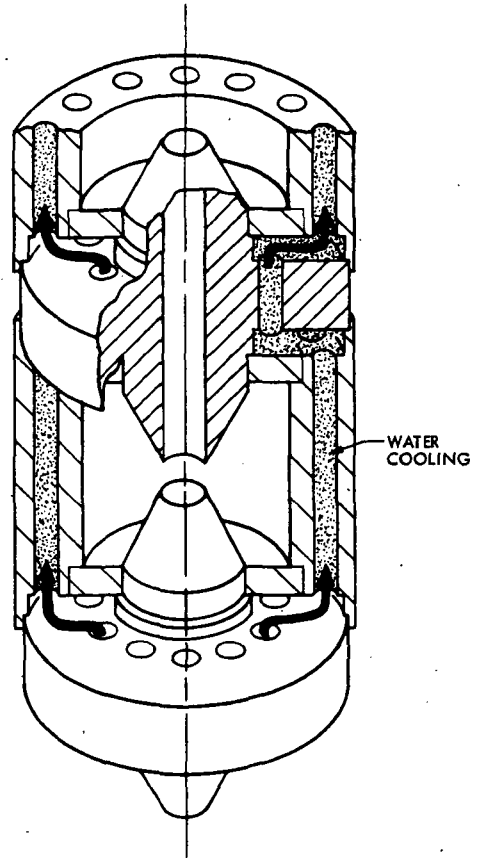


Fig. 8. Proposed cavity structure, X-3060A/B

D27  
N79-22167

## Radio Frequency Carrier Arraying

R. Lay

Radio Frequency and Microwave Subsystems Section

*Carrier arraying of receiving systems provides an improvement in the signal-to-noise ratio relative to a single receiving system. Measurements using arrays of up to four receiving systems have been conducted to verify the predicted signal-to-noise ratio improvement. The measured signal-to-noise ratio improvement agrees with the predicted within 0.2 dB.*

### I. Introduction

The increase in the sensitivity of radio frequency reception obtained by the technique of carrier arraying has been determined in the analysis presented in Ref. 1. Measurements made to verify the predicted signal-to-noise ratio improvement obtained by carrier arraying over that of a single receiving system are described in this article. These measurements include arraying combinations of two, three, and four receivers.

DSN Block III receivers were used for these carrier array measurements. As discussed in Ref. 1, the reference receiver (receiver 1) was in the standard configuration with the first local oscillator in the phase tracking loop, as shown in Fig. 1. This local oscillator was shared by all receivers. Array receivers (2, 3, and 4) were used with the second local oscillator in the phase tracking loop. For the carrier array measurements a design bandwidth of 152 Hz was used in the reference receiver, while 1-Hz design bandwidth was used in the array receiver. This fulfilled the requirement that the bandwidth of the array receivers be much smaller than the bandwidth of the reference receiver. The RF carrier signals of the array receivers were

combined with the reference receiver at IF in the summing junction of the reference receiver.

In the following material the method of calculating the predicted improvement is presented for one of the array combinations and is discussed first. This is followed by the measured signal-to-noise ratio improvement for each of the arraying combinations of two, three, and four receivers. The measured values are then compared to the predicted values.

### II. Predicted Performance for Carrier Arraying

#### A. General

In Ref. 1 the predicted improvement performance is calculated in two steps. First, the improved performance of the reference receiver is determined, neglecting the contribution of phase noise from the array receivers. Then a correction is made to include the degradation due to the addition of phase noise from the array receivers.

Neglecting the phase noise of the array receivers, the pre-detection signal-to-noise ratio improvement  $\eta$  of the reference

receiver when combined with array receivers 2, 3 and 4, using Eq. (19) of Ref. 1, is given by:

$$\eta = \frac{(1 + \beta_2 \gamma_2 + \beta_3 \gamma_3 + \beta_4 \gamma_4)^2}{1 + \beta_2^2 + \beta_3^2 + \beta_4^2}$$

where

$\gamma_2^2, \gamma_3^2, \gamma_4^2$  = the ratio of the carrier power-to-noise spectral density of each of the array receivers 2, 3 and 4 compared to the carrier power-to-noise spectral density of the reference receiver.

$\beta_2, \beta_3, \beta_4$  = the carrier voltage of the IF signal from each of the array receivers 2, 3 and 4 compared to the carrier voltage of the IF signal of the reference receiver at the output of the summing junction.

The contribution of phase noise from the array receivers can now be included using Eq. (22) of Ref. 1. This is presented later in more detail in Section II-D of this article when a sample calculation of the carrier signal-to-noise ratio improvement resulting from arraying four receivers is discussed.

As noted above, both  $\beta$ 's and  $\gamma$ 's are significant parameters and must be determined for each test condition. The method of measurement and adjustment of these two parameters is discussed below.

## B. Carrier Power-to-Noise Spectral Density Ratio $\gamma^2$

The absolute value of the carrier power-to-noise spectral density ratio for each receiver is not required to predict the improvement in signal-to-noise ratio that can be obtained when combining one or more array receivers with the reference receiver. It is sufficient to know the relative magnitude of carrier power and noise spectral density between each array receiver and the reference receiver. This is discussed in the following paragraphs.

To obtain the relative magnitude of carrier power, a test signal was distributed to each of the four receivers through power dividers (Fig. 2). The relative level of the signals at the output of the power dividers (P1, P2, P3 and P4) was determined by sequentially connecting the outputs of the power dividers to the reference receiver through cable C1, using the reference receiver gain control system as a carrier voltage level detector. In the MGC configuration the relative signal level measurements can be made with an accuracy of better than 0.1 dB.

To obtain the relative magnitude of the noise spectral density, measurements of the noise temperature were made on each receiver, including cables C1, C2, C3 and C4 (Fig. 2). Results of the relative signal level measurements and the noise temperature measurements are tabulated in Table 1. The carrier power-to-noise spectral density ratio  $\gamma^2$  can then be obtained from the following expression:

$$\gamma_N^2 = \frac{V_N^2 T_{n1}}{V_1^2 T_{nN}}$$

where

$V$  = the relative input signal level in volts

$T_n$  = the input noise temperature in kelvins

1 = reference receiver

$N$  = array receiver 2, 3 or 4

From the measurements listed in Table 1, the following are the values of  $\gamma^2$  that apply to all the array measurements.

$$\gamma_2^2 = 0.906$$

$$\gamma_3^2 = 0.961$$

$$\gamma_4^2 = 0.981$$

## C. IF Carrier Power Ratio $\beta$

Here again, the absolute levels of the IF carrier of each receiver is not required. What is needed is the ratio of the IF carrier voltage of the array receivers relative to the reference receiver when each of the array receivers is combined with the reference receiver in the summing junction. The gain control system of the reference receiver was again used to measure the increase in IF voltage when each of the array receivers was combined with the reference receiver. The accuracy of these measurements is also about 0.1 dB. These measurements are tabulated in Table 2.

## D. Sample Calculation

The configuration selected for the sample calculation is the one using an array of four receivers where

$$\beta_2 = 0.75$$

$$\beta_3 = \beta_4 = 0.65$$

as identified in Table 2.

The phase noise of the reference receiver alone was measured to obtain an initial reference point. The relative receiver input signal level corresponding to this receiver phase noise measurement is obtained from Eq. (16) of Ref. 1, which gives the value of phase noise as a function of the relative signal level. Since this equation is used several times, a plot (Fig. 3) has been made. From this plot the initial reference receiver phase noise ( $\sigma_{\phi_{n1}}$ ) of 14.9 deg rms corresponds to a relative signal level of 12.1 dB above the reference receiver design threshold.

The predetection signal-to-noise ratio improvement of the reference receiver when summed with array receivers 2, 3 and 4, neglecting the phase noise contribution of receivers 2, 3 and 4 is

$$\eta = \frac{(1 + \beta_2 \gamma_2 + \beta_3 \gamma_3 + \beta_4 \gamma_4)^2}{1 + \beta_2^2 + \beta_3^2 + \beta_4^2}$$

$$10 \log_{10} \eta = 5.71 \text{ dB}$$

This represents an improvement in the reference receiver predetection signal-to-noise ratio of 5.71 dB, equivalent to a relative signal level of 17.8 dB above design threshold. Again, from Fig. 3 this corresponds to reference receiver phase noises

$$\sigma_{\phi_{n1 \Sigma 1,2,3,4}} = 8.00 \text{ deg rms} = 0.140 \text{ rad rms}$$

The next step is to calculate the contribution of phase noise from each of the array receivers. From the expression defining receiver phase noise as a function of relative signal level above design threshold, the phase noise of each of the array receivers can be determined knowing the relative signal level above design threshold for each of the array receivers. The relative signal level above design threshold of the array receivers differs from the reference receiver due to three factors:

- (1) The ratio of design loop noise bandwidths. This factor is

$$\frac{2B_{L0}(\text{reference receiver})}{2B_{L0}(\text{array receiver})}$$

- (2) The ratio of the carrier power-to-noise spectral  $\gamma^2$
- (3) The reduction in the carrier signal voltage in the array receivers due to the added noise of the first local oscillator derived from the reference receiver. From Ref. 1, this factor is

$$1 - \frac{\sigma_{\phi_{n1 \Sigma 1,2,3,4}}^2}{2}$$

Adding these three factors to the value of the relative signal level above design threshold of the reference receiver (12.1 dB), the relative signal level above the design threshold for array receivers 2 becomes

$$12.1 + 10 \log_{10} \frac{2B_{L0}(\text{reference})}{2B_{L0}(\text{array})} + 10 \log_{10} \gamma_2^2 + 10 \log_{10} \left[ 1 - \frac{\sigma_{\phi_{n1 \Sigma 1,2,3,4}}^2}{2} \right]^2 = 33.4 \text{ dB}$$

From Fig. 4, this is equivalent to a contribution of phase noise from array receiver 2 of

$$\sigma_{\phi_{n2 \Sigma 1,2,3,4}} = 4.32 \text{ deg rms}$$

In a similar manner, for array receivers 3 and 4

$$\sigma_{\phi_{n3 \Sigma 1,2,3,4}} = 4.25 \text{ deg rms}$$

$$\sigma_{\phi_{n4 \Sigma 1,2,3,4}} = 4.25 \text{ deg rms}$$

The total phase noise of the reference receiver, from Eq. (22) of Ref. 1, is

$$\sigma_{\phi_{\eta}} = \left[ \sigma_{\phi_{n1 \Sigma 1,2,3,4}}^2 + \left( \frac{\beta_2 \sigma_{\phi_{n2 \Sigma 1,2,3,4}}}{1 + \beta_2} \right)^2 + \left( \frac{\beta_3 \sigma_{\phi_{n3 \Sigma 1,2,3,4}}}{1 + \beta_3} \right)^2 + \left( \frac{\beta_4 \sigma_{\phi_{n4 \Sigma 1,2,3,4}}}{1 + \beta_4} \right)^2 \right]^{1/2}$$

$$\sigma_{\phi_{\eta}} = 8.55 \text{ deg rms}$$

From Fig. 3 this corresponds to a relative signal level above design threshold of 17.2 dB. This represents a 5.1-dB improvement over the initial reference point of 12.1 dB relative signal level above design threshold. These calculations for all the array combinations are tabulated in Table 2.

### III. Measured Performance of Carrier Arraying

The most significant parameter available to measure the improvement in performance when more than one receiver is

arrayed is the signal-to-noise ratio (rms phase noise) of the receiver loop output signal. Since the receiver loop output signal is used as the doppler signal, the rms phase noise of the doppler output was used to measure the receiver performance. By comparing the doppler phase noise of the reference receiver when combined with the array receivers to the doppler phase noise of the reference receiver alone, the improvement in performance can be determined directly by using the plot of receiver phase noise vs relative signal level of Fig. 5. An example using this plot is shown in Fig. 5 for the first measurement

listed in Table 2, which resulted in a 2.6-dB improvement when one array receiver was combined with the reference receiver.

Measurements of radio frequency carrier signal-to-noise ratio improvements have been made by arraying combinations of two, three, and four receivers. These measurements were made with different voltage couplings  $\beta$  at the summing junction. These measurements are tabulated in Table 2 and do not differ by more than 0.1 dB from predicted values.

## Reference

1. Brockman, M. H., "Radio Frequency Carrier Arraying for High Rate Telemetry Reception," in *The Deep Space Network Progress Report 42-45*, pp. 209-223, Jet Propulsion Laboratory, Pasadena, Calif., June 15, 1978.

**Table 1. Relative input signal level and receiver noise temperature measurements**

	Relative input signal level, V	$T_n$ , K
Receiver No. 1	1.000	3170
Receiver No. 2	0.948	3147
Receiver No. 3	0.979	3161
Receiver No. 4	0.987	3147

**Table 2. Carrier signal-to-noise ratio improvement due to carrier arraying of receiver systems**

Receiver	$\beta$	Measured phase noise, deg rms	Carrier S/N improvement	
			Measured, dB	Calculated <sup>a</sup> dB
Receiver No. 1		14.9		
Receivers Nos. 1, 2	$\beta_2 = 0.75$	11.3	2.6 <sup>b</sup>	2.6
Receiver Nos. 1, 2, 3	$\beta_3 = 0.65$	9.6	4.1	4.2
Receiver Nos. 1, 2, 3, 4	$\beta_4 = 0.65$	8.5	5.0	5.1 <sup>c</sup>
Receiver No. 1		16.9		
Receiver Nos. 1, 2	$\beta_2 = 0.80$	12.6	2.6	2.7
Receiver Nos. 1, 2, 3	$\beta_3 = 0.95$	10.6	4.2	4.2
Receiver Nos. 1, 2, 3, 4	$\beta_4 = 0.85$	9.6	5.1	5.2
Receiver No. 1		16.9		
Receiver Nos. 1, 2	$\beta_2 = 1.00$	12.6	2.6	2.7
Receiver Nos. 1, 2, 3	$\beta_3 = 0.95$	10.6	4.2	4.2
Receiver Nos. 1, 2, 3, 4	$\beta_4 = 1.00$	9.4	5.2	5.2

<sup>a</sup>These calculated SNR Improvements were obtained using  $\gamma_2 = 0.95$ ,  $\gamma_3 = 0.98$ , and  $\gamma_4 = 0.99$ .

<sup>b</sup>The method of determining the measured improvement in carrier SNR is shown on Fig. 5 for this one measurement.

<sup>c</sup>A sample calculation for this test condition is discussed in Section II-D.

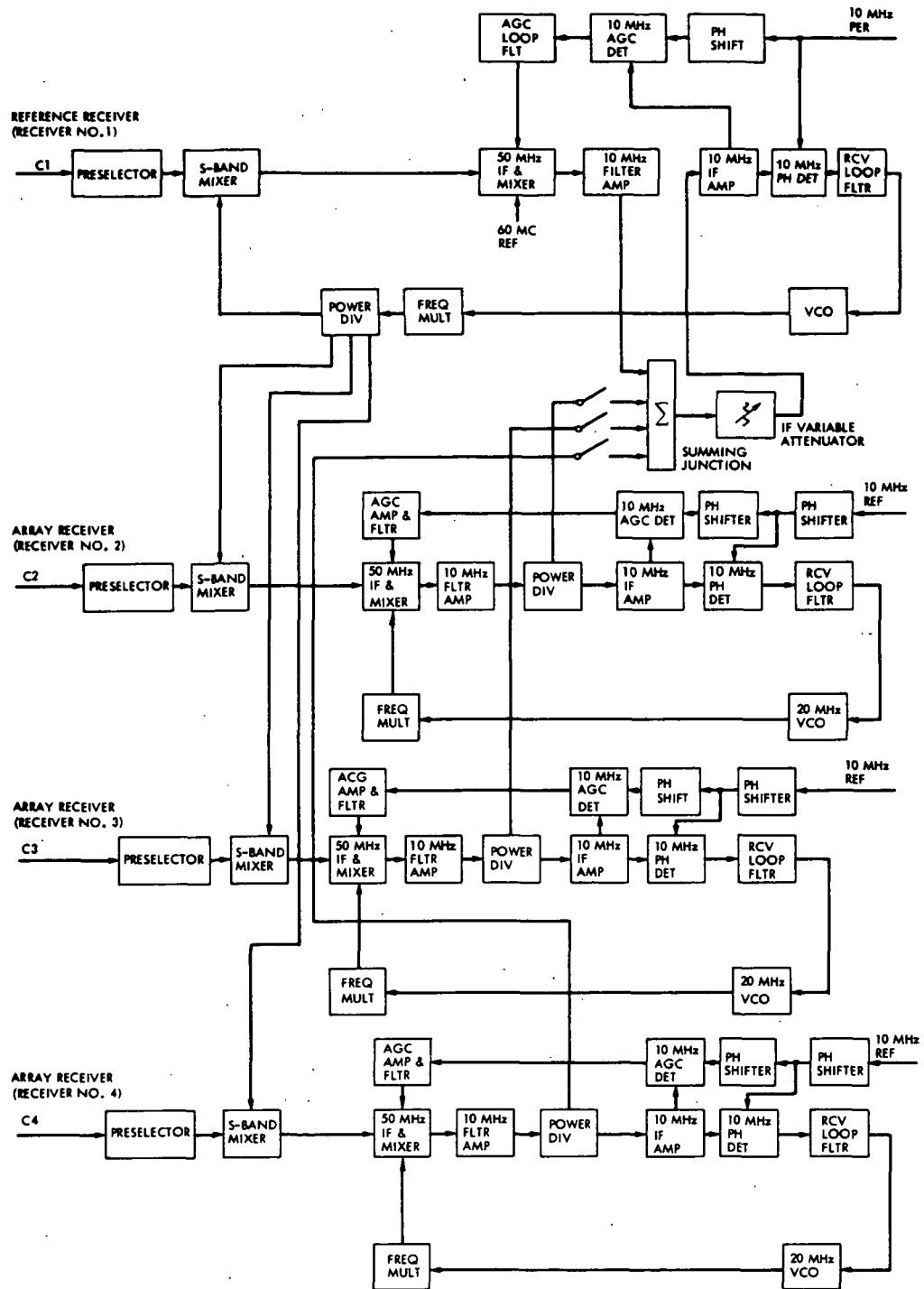


Fig. 1. Block diagram of carrier array of four receiving systems

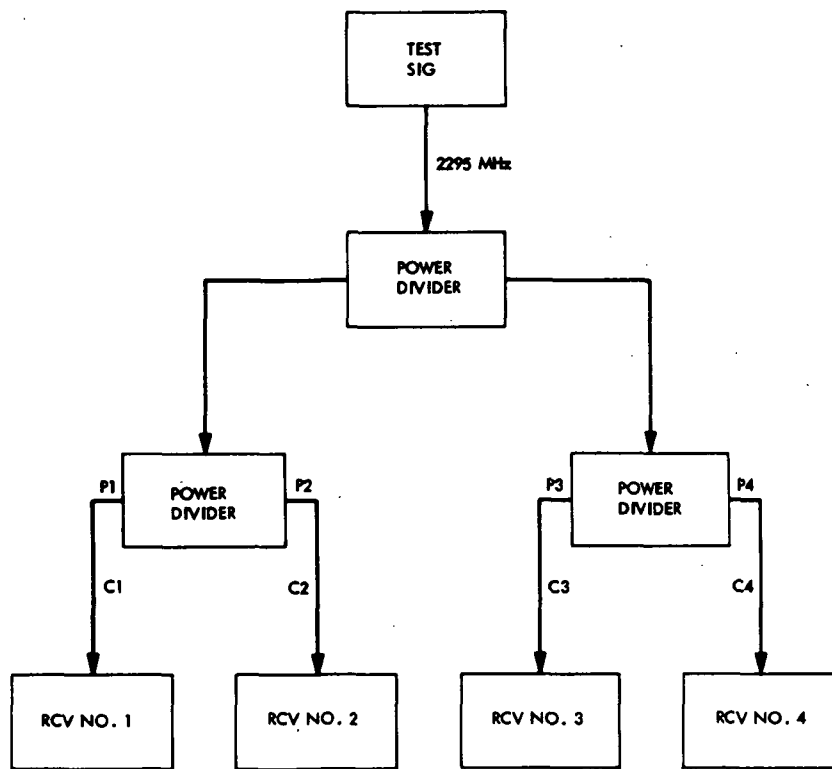
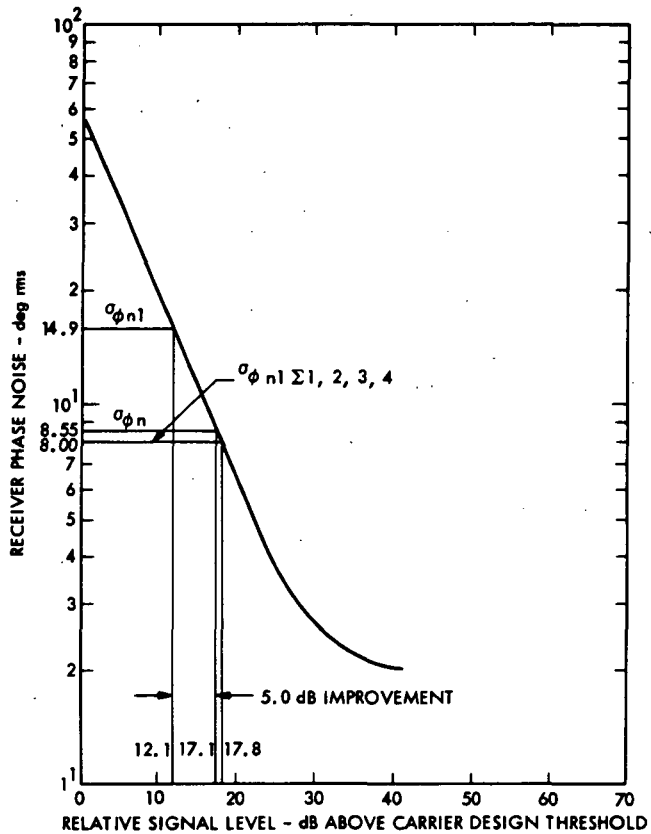


Fig. 2. Signal distribution for carrier array tests



NOTE:  $\sigma_{\phi n1}$  = PHASE NOISE OF RECEIVER 1, BEFORE ARRAYED WITH RECEIVERS 2, 3, AND 4

$\sigma_{\phi n1 \Sigma 1, 2, 3, 4}$  = PHASE NOISE OF RECEIVER 1, AFTER ARRAYED WITH RECEIVERS 2, 3, AND 4 NEGLECTING THE PHASE NOISE CONTRIBUTION FROM RECEIVERS 2, 3, AND 4

$\sigma_{\phi n}$  = PHASE NOISE OF RECEIVER 1, AFTER ARRAYED WITH RECEIVERS 2, 3, AND 4 WITH THE CONTRIBUTION IN PHASE NOISE FROM RECEIVERS 2, 3, AND 4

Fig. 3. Receiver phase noise vs RF carrier level, reference receiver 1

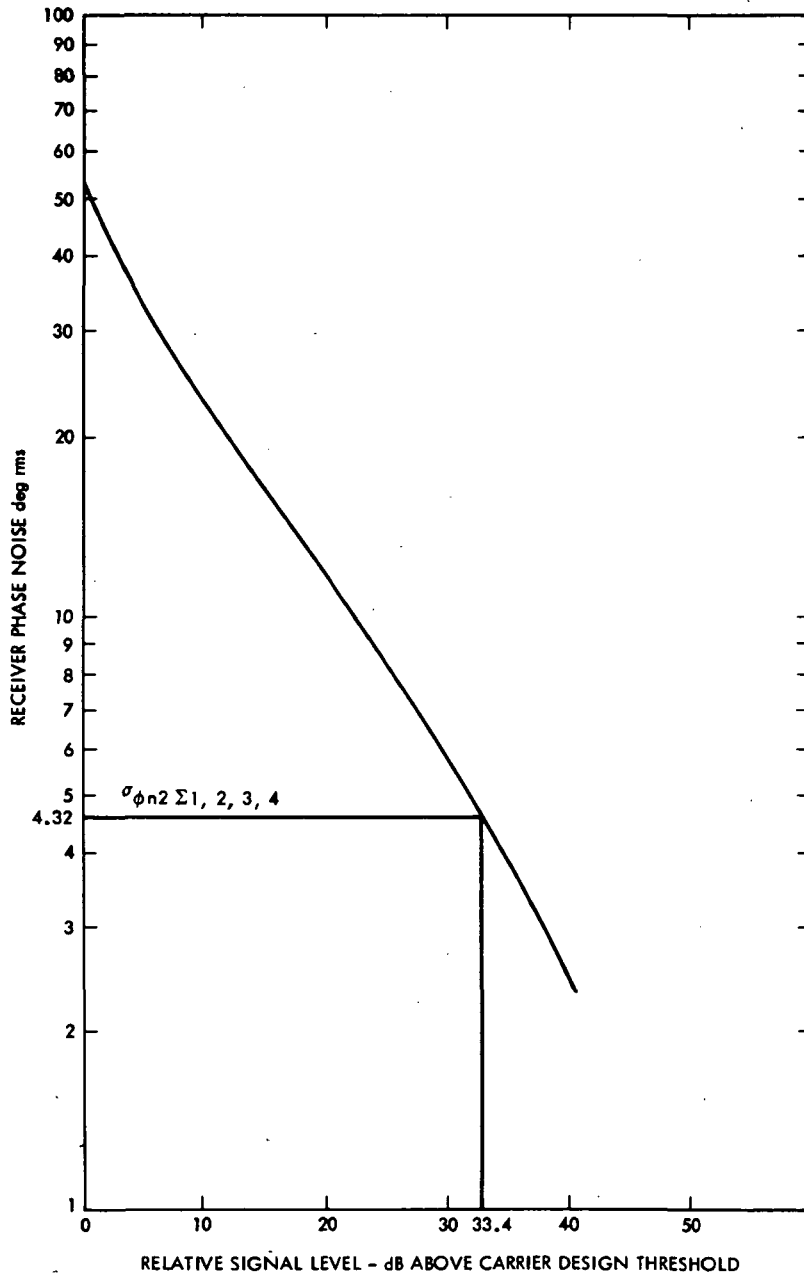


Fig. 4. Receiver phase noise vs RF carrier level, array receivers 2, 3, and 4

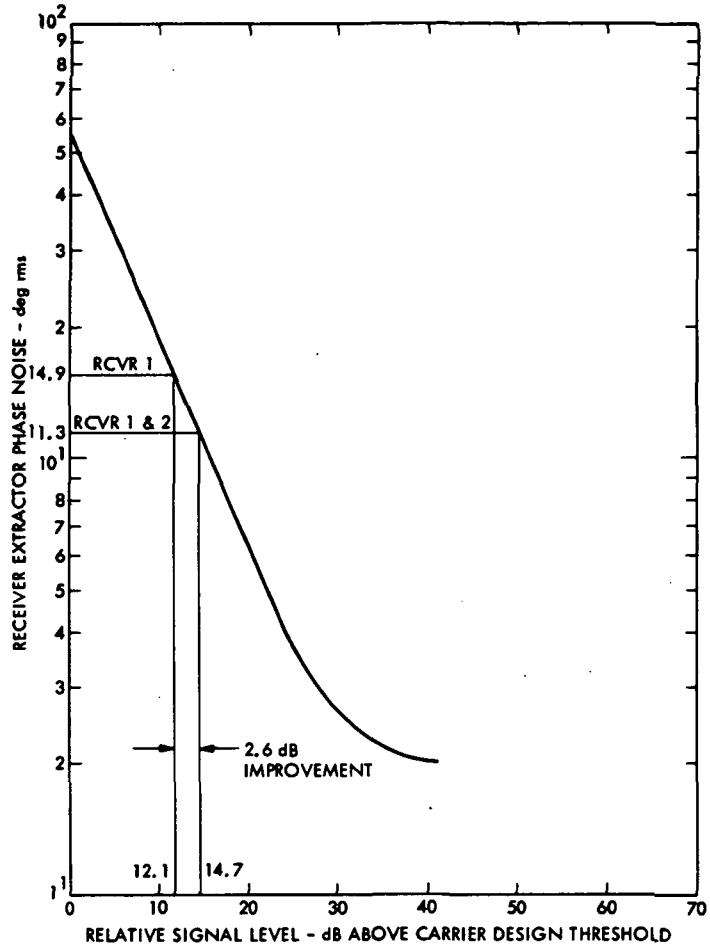


Fig. 5. Receiver phase noise vs RF carrier level, reference receiver 1

P  
DSS

N79-22168

## Spectral Signal Indicator Progress Report

B. Chaney, H. Cooper, and B. Crow  
Radio Frequency and Microwave Subsystems Section

*The Spectral Signal Indicator was designed as a receiver acquisition aid for the Pioneer Venus Probe entry in December 1978. A description of the Pioneer Venus SSI operation is given, as well as future implementation plans.*

The design of the Spectral Signal Indicator (SSI) was begun in the second quarter of 1977. Its function was to aid in the acquisition of the Pioneer Venus (P-V) probes which were to enter the Venusian atmosphere in December 1978. For the P-V encounter, the SSI system consisted of three racks of equipment linked by an interface panel (located in one of the three racks, see Fig. 1). Since DSS 14 and DSS 43 were to monitor the entry, a SSI system was supplied to each station.

Owing to the mission profile, it was probable that two (and possibly three) probes would enter the Venusian atmosphere simultaneously; therefore, three analyzers at each station were required (two analyzers plus a "hot spare"). Each analyzer consisted of (1) a spectrum analyzer, (2) a spectrum translator, (3) a frequency synthesizer, (4) a spectrum display, (5) an alpha/numeric display, (6) a RF input selector switch, (7) a controller, and (8) an interface panel.

Two elements of the SSI which deserve special mention are the controller and interface panel. The controller was designed to (1) automatically coordinate the controls of the spectrum analyzer, translator, and synthesizer, (2) perform frequency calculations to calculate closed-loop acquisition frequencies, (3) control the remote printer and alpha/numeric display, and (4) perform a self-test of the SSI assembly. The interface panel provided a means whereby the open-loop receiver synthesizer

settings and the closed-loop receiver rest VCO settings could be inputted to the controller for use in the acquisition frequency calculations.

A typical P-V operation of the SSI is described in the following example: During the mission precalibration, the operator sets the open-loop receiver synthesizer and the closed-loop receiver rest VCO frequencies into the interface panel. Next, the operator presses the Test switch on the controller, and the controller then performs a self-test of the SSI Assembly. This self-test feature consists of injecting a test signal into the analyzer. The SSI Controller directs the adjustment of all analyzer, synthesizer and translator controls to position the test signal in the middle of the analyzer display. Equipment malfunction and/or incorrect control settings are displayed on the alpha/numeric display.

The open-loop receiver to be monitored is selected on the RF input switch. The operator monitors the spectrum display screen until a signal appears, at which time the cursor is positioned over the signal and the print button is pushed. The controller then computes the S-band probe frequency based on the open-loop receiver synthesizer setting and known configuration. The controller also computes the closed-loop receiver POCA setting. This data is displayed on the alpha/numeric monitor and is also sent to a remote printer located

near the closed-loop receiver operator. The closed-loop receiver operator then sets the computed values into the POCA for quick acquisition.

The P-V configuration was a mission-peculiar design to solve an immediate problem. Now, a more long-range, multi-mission approach is being pursued. This new design (called Phase II SSI development) is shown in Fig. 2. Phase II implementation is scheduled to be completed in late 1979, at which time the SSI will consist of one rack of equipment (one analyzer), which will be controlled through the Star Switch Controller by the DST. At that time DSS 14, 43 and 63 will each have one operational SSI plus a set of spares.

The Phase II SSI will be configurable for multimission support for Radio Science and RFI applications. All operation of the SSI will be from the DST operator position. A remote

display/cursor assembly will allow the DST operator to view the spectral display and control the analyzer cursor position. Signal input, analysis parameters and receiver configuration data will be input to the SSI via the DST. The SSI will supply to the DST operator tuning information for the closed-loop receivers to aid in the acquisition of signals displayed on the display/cursor assembly. The DST operator will have high-level commands at his disposal to scan the analyzer through a range of frequencies, stop when an interesting signal is observed, center the signal in the analysis bandwidth and narrow the analysis bandwidth to get a more detailed picture of the signal.

An interim configuration is being assembled for DSS 14 only, to assist in the Voyager Jupiter Encounter in July of 1979. The SSI will be configured to send spectral data to a remote SSI display located at NOCC via commercial telephone lines.

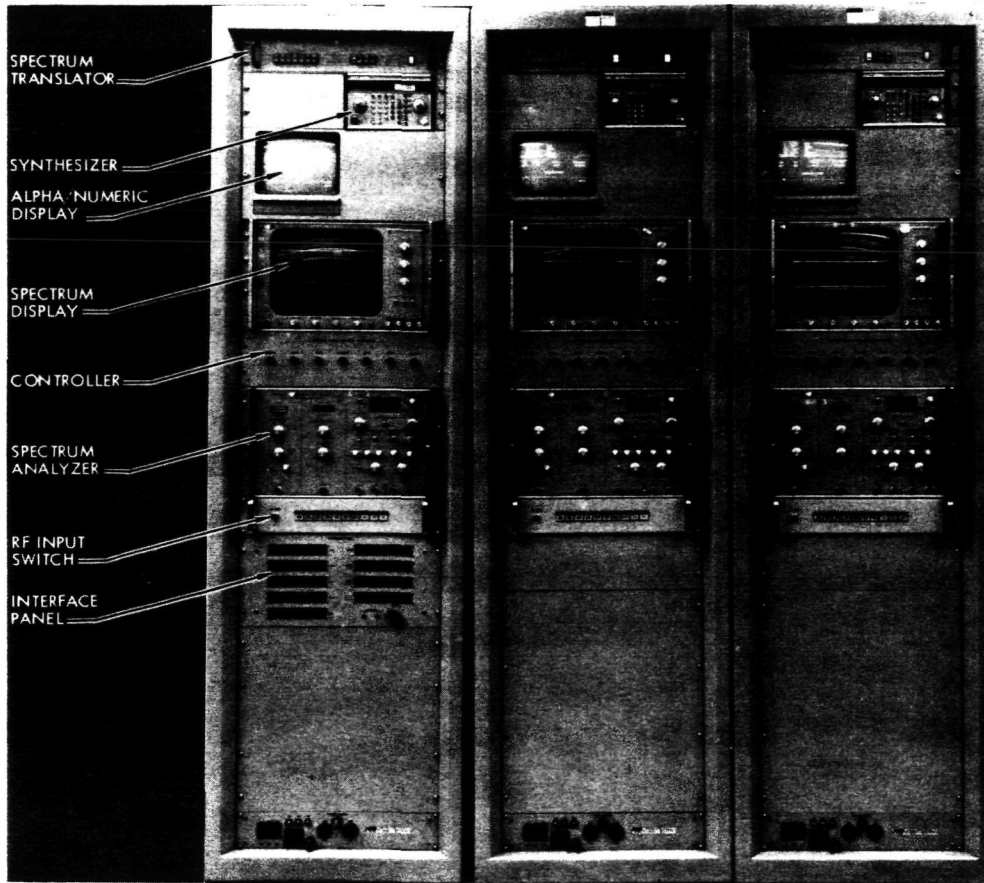


Fig. 1. Spectral Signal Indicator System

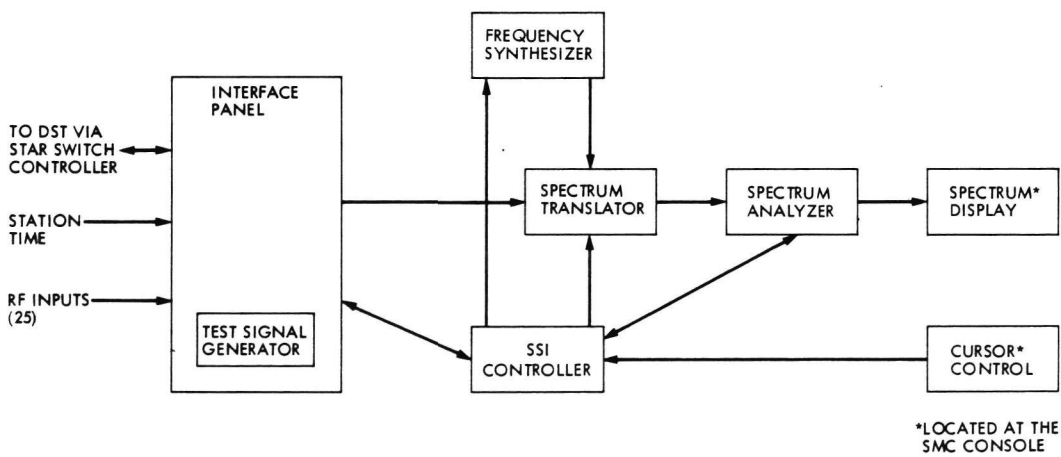


Fig. 2. Phase II SSI assembly

## S-X 34-Meter Conversion Receiver and Microwave Performance

H. R. Buchanan

Radio Frequency and Microwave Subsystems Section

*The S-X 34-meter conversion provides for upgrading a subnet of three stations to a 34-meter antenna aperture and adding X-band receive capability. This subnet will consist of DSSs 12, 42, and 61. Implementation of DSS 12 was completed in October 1978. A description of the conversion as applied to the antenna microwave and receiver subsystems is given. Performance requirements and test results are included.*

### I. Introduction

The conversion of the first 26-meter station, DSS 12, to a 34-meter aperture with X-band receive capability added to the existing S-band uplink and downlink has now been completed. The additional antenna gain afforded by the enlarged aperture increases the usefulness of the station to the Voyager mission and other outer planet missions and enhances the capability of the 34-meter station to offload the 64-meter subnet during cruise modes. The X-band receive capability is needed to provide adequate data returns from the outer planets and improve immunity from the increasing incidences of radio frequency interferences that have been occurring at S-band. Two additional 26-meter stations, DSS 42 (Australia) and DSS 61 (Spain), will be completed in May 1980.

### II. Description

The principal modifications involved in the S-X conversion project are in the antenna mechanical, the antenna microwave, and receiver-exciter subsystems. The microwave and receiver-exciter subsystems are the subject of this report. An overall

description of the program is given by Ref. 1. A block diagram of the RF subsystems is shown in Fig. 1.

The antenna microwave subsystem (UWV) modifications subdivide into three prime areas:

- (1) The microwave S/X-band feed assembly.
- (2) The X-band maser and associated instrumentation.
- (3) A new microwave switch configuration assembly.

During the initial phase of the S-X 34-meter conversion program, a significant effort was expended in studying the optimum feed system configuration, the RF optics design, and the predicted gain and noise temperature performance of the 34-meter antenna. The outcome of this study was the choice of a previously developed and demonstrated dual-band feed system employing separately located feeds combined in a reflex-dichroic reflector arrangement. A particularly compact design was chosen, minimizing aperture blockage for optimum performance. The details of the design study are given in Ref. 2.

At the conclusion of the design study, the detail arrangement of the dual-frequency feed cone (SXD) was initiated. Two detailed progress reports have been previously given for the SXD cone assembly in Refs. 3 and 4. The latter report includes a description of the high-powered diplexing tests conducted at the microwave test facility at Goldstone, and the test results measured there. The performance requirements for the microwave portion of the S-X 34-meter conversion are given in Table 1.

A new X-band maser and supporting instrumentation have been added as a part of the S-X 34-meter conversion. The amplifying portion of the X-band maser is identical to the operational maser which has been reported previously in Ref. 5. The maser includes a superconducting magnet for improved gain and phase stability. The closed cycle cryogenic system is identical to that used previously. The maser amplifier assembly has been repackaged, however, to afford a more compact and flexible packaging arrangement. Several new instrumentation features have been incorporated, which include a serial communication link for ground-to-antenna controls and monitoring signals, a new type of X-band monitor receiver, and a built-in X-band test signal source for adjustment and calibration of the maser amplifier. A more detailed progress report will be issued on the S-X 34-meter conversion maser system at an early date. The performance requirements for the X-band maser are given in Table 2.

The UWV switch control group for the 34-meter S-X conversion has been completely redesigned to be compatible with centralized station control and monitoring. This group of equipment establishes the RF signal routing within the antenna microwave subsystem. Waveguide and coaxial switches are commanded to the desired configuration, while interlock switches associated with equipment and personnel protection prevent the application of beam voltage to the transmitters until all safety conditions are established. Once beam voltage is applied, further movement of critical microwave switches is automatically prevented.

The control and monitoring of the microwave switches and transmitter interlocks are accomplished from either the DSS Data System Terminal assembly (DST) or a local control keyboard within the switch control equipment. A local graphics display is also provided for the local operator. A number of permanent standard configurations are available from the switch control equipment. Each configuration is identified by a standard alphanumeric name. The graphics display presents a detailed block diagram associated with the selected configuration. The configuration name and various monitor

functions are also displayed. Figure 2 shows a typical configuration display entitled "MITRK."

Manual pushbuttons have been provided in the antenna electronics room for local control of each individual microwave switch. This provision is useful for servicing, maintenance and other manual switch operations. Reference 6 provides more details of the microwave switch control equipment. A progress report on this portion of the system is planned for the near future.

The addition of an X-band receive capability at the 34-meter antenna stations requires the addition of another microwave element, a fourth harmonic filter. This element is actually a part of the transmitter subsystem. The purpose of this filter is to highly attenuate the fourth harmonic output from the S-band klystron amplifier. This harmonic signal is near the amplifying frequency range of the X-band maser and must be suppressed to prevent interference with the normal X-band reception performance.

The most cost-effective method of providing X-band receive capability was determined to be the addition of an X- to S-band down converter inserted in front of the existing Block III receiver. The coherent reference for the down converter is obtained through appropriate frequency multipliers and dividers which are driven from the exciter synthesizer. As can be seen from Fig. 1, each Block III receiver may select either an S-band signal from the S-band maser or an X-band signal which has been down converted to S-band.

In addition to the X- to S-band down converter, the S-X 34-meter conversion also included the addition of an X/S-band translator to provide either S-band or X-band coherent test signals and the addition of the doppler extractors, as shown in Fig. 1. The performance requirements, specifications, and test data associated with the S-band receiver are given in Table 3. A more detailed discussion of the receiver conversion is presented in Ref. 7.

### III. Installation

The S-X 34-meter conversion at DSS 12 was completed in October 1978. Post-installation test results are indicated in Tables 1, 2, and 3. With the exception of the X-band gain performance, all RF test results demonstrate that the design requirements have been successfully met. The X-band antenna gain performance is still being investigated with the primary emphasis on the condition of surface panels of the main reflector. This investigation is being pursued as station scheduling time permits.

## References

1. Lobb, V. B., "26-Meter S-X Conversion Project," in *The Deep Space Network Progress Report 42-39*, pp. 157-167, Jet Propulsion Laboratory, Pasadena, Calif., June 15, 1977.
2. Nixon, D. L., and Bathker, D. A., "S-/X-Band Microwave Optics Design and Analysis for DSN 34-Meter-Diameter Antenna," in *The Deep Space Network Progress Report 42-41*, pp. 146-165, Jet Propulsion Laboratory, Pasadena, Calif., Oct. 15, 1977.
3. Hartop, R. W., "Dual-Frequency Feed System for 26-Meter Antenna Conversion," in *The Deep Space Network Progress Report 42-40*, pp. 146-149, Jet Propulsion Laboratory, Pasadena, Calif., Aug. 15, 1977.
4. Hartop, R. W., "Dual-Frequency Feed Cone Assemblies for 34-Meter Antennas," in *The Deep Space Network Progress Report 42-47*, pp. 85-88, Jet Propulsion Laboratory, Pasadena, Calif., Oct. 15, 1978.
5. Buchanan, H. R., Hartop, R. W., Leflang, J. G., Loreman, J. R., and Trowbridge, D. L., "Operational X-Band Maser System," in *The Deep Space Network Progress Report 42-26*, pp. 175-182, Jet Propulsion Laboratory, Pasadena, Calif., Apr. 15, 1975.
6. *Configuration Control Group (34-Meter Antenna) DSS 12 and 42*, Technical Manual 512181, Jet Propulsion Laboratory, Pasadena, California, Dec. 1, 1978 (JPL internal document).
7. Weller, R. E., "S-X Conversion for the Block III Receiver-Exciter," in *The Deep Space Network Progress Report 42-42*, pp. 141-148, Jet Propulsion Laboratory, Pasadena, Calif., Dec. 15, 1977.

**Table 1. SXD cone assembly performance requirements and test data**

Parameter	S-band		X-band	Notes
	Transmit	Receive	Receive	
Frequency, MHz	2110 ± 10	2285 ± 15	8420 ± 20	
Gain, dBi				
Required	55.3 ± 0.7	56.1 <sup>+0.3</sup> -0.9	66.9 <sup>+0.3</sup> -0.9	
Test	Note 1	56.2	65.7	See Note 2
Diplexed system noise temperature, K				
Required		27.5 ± 2.5	25.0 ± 3.0	
Test		Note 3	24.0	See Note 4
Listen only system noise temperature, K				
Required		21.5 ± 2.5	-	
Test		21.6	-	
System noise increment 30° elevation to zenith, K				
Required		-	5.0	
Test		-	4.0	See Note 5

Notes:

1. Transmit antenna gain has not been verified by test.
2. X-band receive gain is still under investigation. The reflector surface panels are to be reset in the near future.
3. Adequate test data are not yet available.
4. It is expected that further refinement of the X-band system temperature to 23 K may result as more test data become available.
5. Measured increment of 4 K is based upon limited amount of test data.

**Table 2. X-band maser performance requirements and test data**

Parameter	Requirements	Test
Frequency, MHz	8420 ± 20	8420 ± 20
-1 dB bandwidth, MHz	40	53
Gain stability, dB peak-to-peak		
Short term, 10 seconds	0.06	0.04
Long term, 12 hours	1.0	<1.0
Moving, 0.2 deg/s max	1.0	0.6
Equivalent noise temperature, K	8 ± 2	7.7 at 8400 7.7 at 8420 9.9 at 8440

**Table 3. Receiver performance requirements, specifications, and test data**

Parameter	Requirements	Specifications	Test
Frequency range	8.4-8.44 GHz	8.4-8.44 GHz	8.4-8.43 GHz <sup>a</sup>
Noise figure	<10 dB	<10 dB	8.0 dB
Doppler phase error noise	<12 deg	<12 deg	8 deg
Doppler shift during mission lifetime	80 km/s	80 km/s (X = 4.51 MHz) (S = 1.267 MHz)	X>4.6 MHz S>4.6 MHz
Doppler shift during single pass	1.0 km/s	1.0 km/s (X = 56.3 kHz) (S = 15.4 kHz)	150 kHz
Doppler rate near Earth	100 m/s <sup>2</sup>	100 m/s <sup>2</sup> (X = 5630 Hz/s) (S = 1540 Hz/s)	5630 Hz/s with 32-deg phase error
Doppler rate planetary encounter or orbit	0.1 m/s <sup>2</sup> (<10° error when 10 dB above receiver 12-Hz threshold)	0.1 m/s <sup>2</sup> (X = 5.63 Hz/s) (S = 1.54 Hz/s)	<10-deg phase
Doppler stability 5 × 10 <sup>4</sup> second averaging	0.4 m	0.4 m X = 8100 deg	625 deg <sup>b</sup>
Group delay	1.4 m	1.4 m (9.3 ns)	0.5 ns <sup>b</sup>
X-band translator output	-50 dBm min	-50 dBm min	-34 dBm

<sup>a</sup>8.43 – 8.44 GHz noncoherent mode.

<sup>b</sup>Added instability due to S-X conversion over  $\Delta T$  of 5°C.

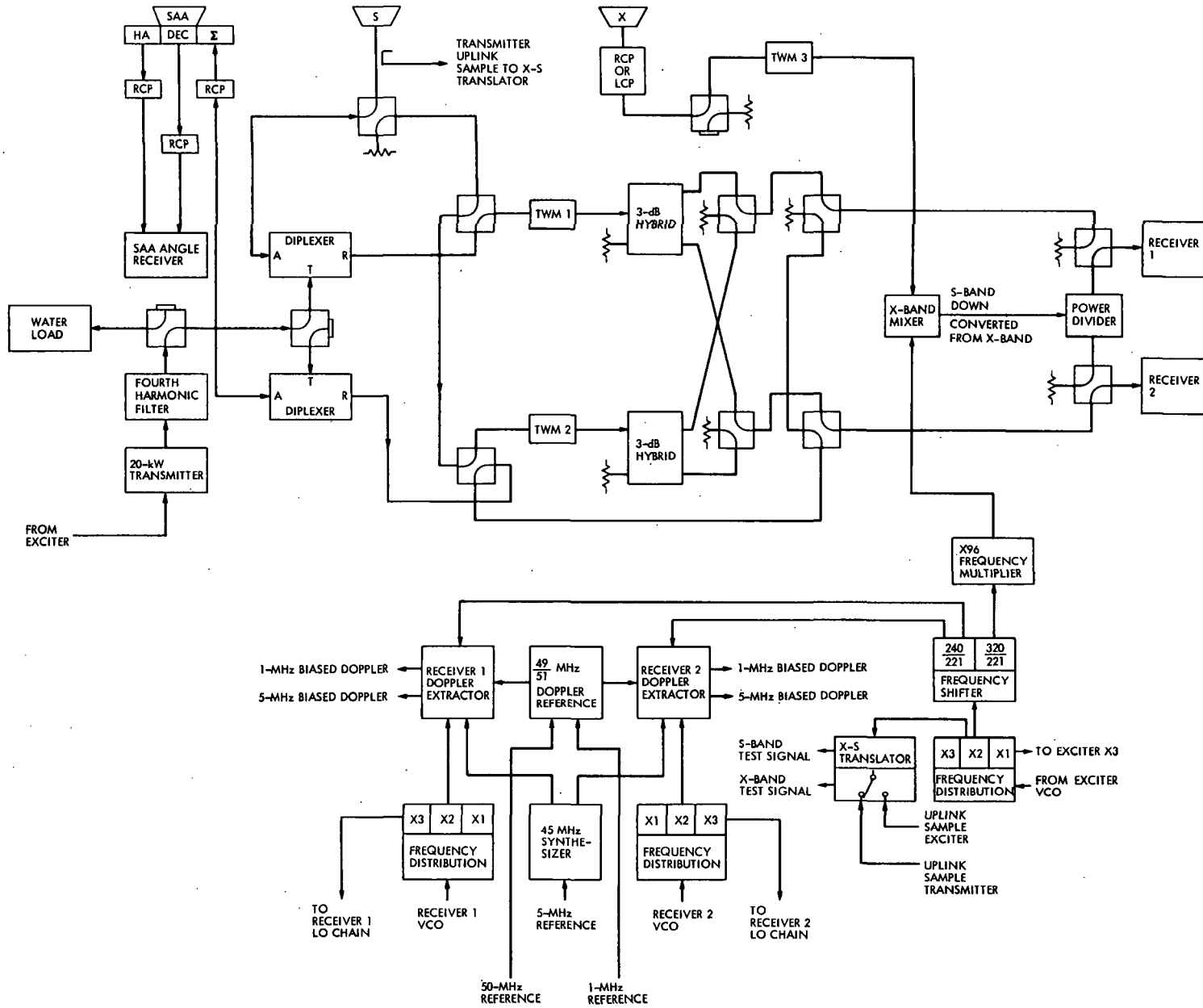


Fig. 1. RF subsystems simplified block diagram

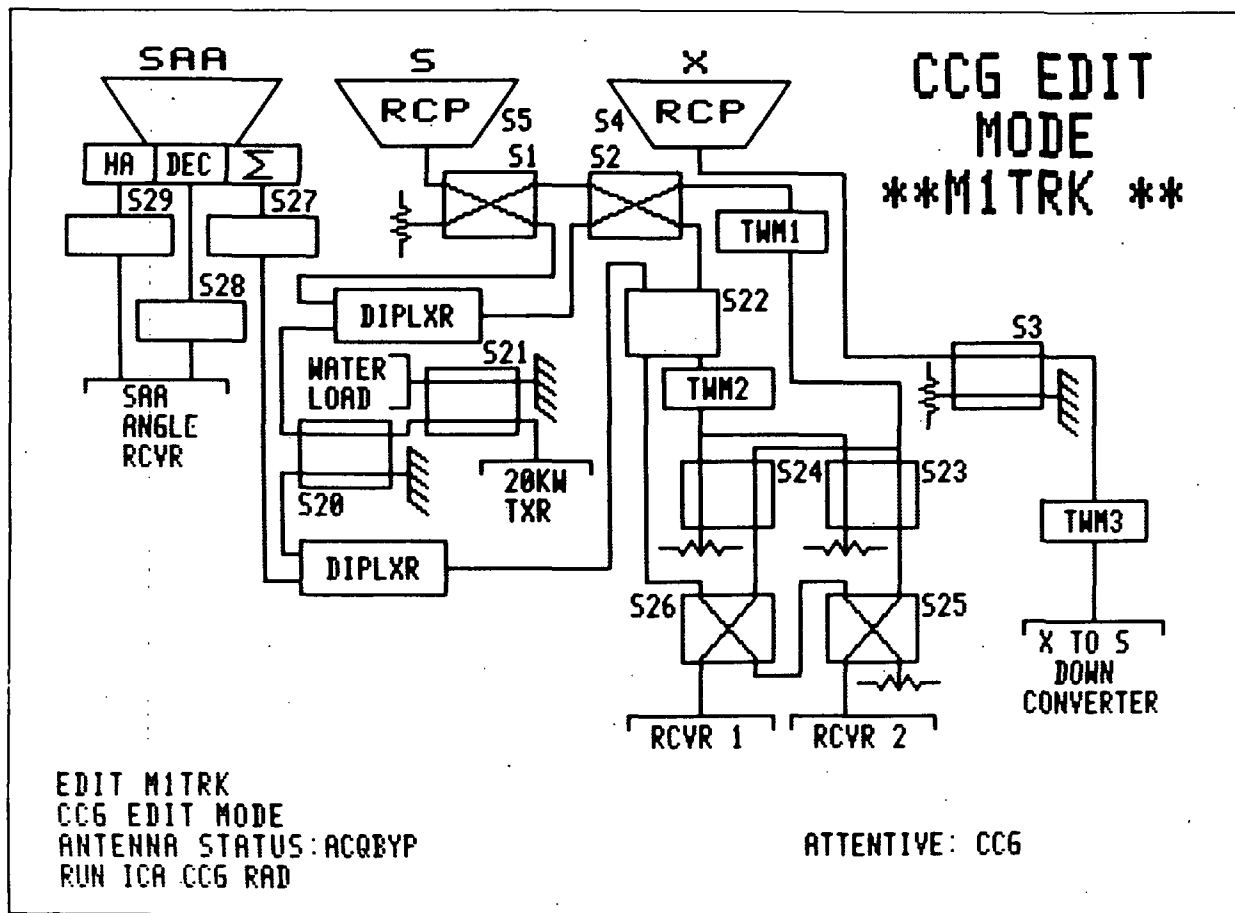


Fig. 2. Switch control standard configuration mode CRT display

# Implementation of the DSN VLBI Correlator

J. C. Peterson and J. W. Dillon  
DSN Data Systems Section

*This article focuses on the overall design and current status of the VLBI Correlator designed to accommodate DSN requirements. The two-station correlator design uses real-time digital computation with microprocessors to perform cross correlation detection of sampled signals in the 0.125 to 2 MHz range.*

## I. Introduction

The DSN is in the process of implementing a very long baseline interferometry (VLBI) network which will be directed toward tracking of spacecraft (Galileo), and determination of additional data such as polar motion, UT1, and station locations. In VLBI measurements, the radio signals produced by a distant source are recorded simultaneously at two widely spaced antennas. These recorded signals are then cross-correlated by the VLBI correlator to determine correlated amplitude as well as phase and delay. The goal of this article is to describe the overall design and status of the VLBI correlator designed to cross-correlate data from a two-station, one-bandwidth synthesis channel (BWS) for the DSN. The design work began in August 1978 and the transfer of hardware to operations is scheduled for December 1980.

## II. VLBI Correlation Processor Characteristics

The VLBI correlation processor can best be understood by reference to Fig. 1, which shows a simplified block diagram of the VLBI system. Acquisition and processing of VLBI data requires at least two stations and a central facility for

correlation and estimation processors. Sample data from the two tracking stations are brought together at the correlation processor by the wideband data line (WBL) in near real-time.

The acquisition of the VLBI data consists of two widely separate antennas pointed at the same signal. This signal is filtered, translated in frequency, sampled to one-bit, recorded at both stations and if line usage allows, sent over the wideband data line. VLBI determines the relative difference in the time of arrival of the signal at the two locations. The correlation processor performs cross-correlation detection of the sampled signals to determine this difference.

From this delay measurement, the position of the radio source and other parameters, including instantaneous rotational angle of the earth, polar motion, relative position of the two stations, and the time offset and rate of change of the clock at the two stations, can be determined. To accomplish the delay measurement the correlation processor must first compute the observing geometry and predict the phase and delay models for the correlator.

The integrated cross-product sums between the two sampled data streams are the output from the correlator as shown

in Fig. 1. The signal processing operation is completed by estimating cross-correlation magnitude, delay, delay rate, phase and phase rate from the cross-product sums.

The correlation facilities are divided by Blocks 1 and 2 (Ref. 1). The Block 1 facility serves only DSN Operations functions and, consequently, the focuses of this article are characterized by Fig. 1. The Block 2 facility will employ the same design and equipment, correlator hardware, control computer and software as Block 1. The significant difference is in the method of providing data to the correlator, ultimately expansion in the number of stations which can be simultaneously correlated, and the number of BWS channels that can be correlated in parallel.

The Block 1 correlator design will remain a two-station BWS channel correlator but is impacted by the Block 2 design requirement of being able to expand the correlator Block 1 design to multiple baseline and to process this larger volume of data at real-time rates. The increase in hardware for expansion in stations (baseline) goes by  $N^2$ , while the increase in hardware for expansion in channel goes by  $N$ . This expansion impacts the type of integrated circuits and correlator scheme used to implement the Block 1 design. These additional features and functions required of Block 2 over Block 1 capability will make the Block 1 design more acute, but it is still necessary for the correlation process to remain similar.

### III. Design Approach

The recent advances in large-scale integrated-circuits (LSI) technology have brought substantial improvements to the performance of digital machines. This technology widened the application spectrum because these new LSI devices were cheaper, smaller, required less power, and permitted a much more flexible design. In particular, microprocessor control of digital instruments brought significant advances in critical applications. Microprocessors provide the only practical means to achieve the special functions and high throughput rates required of the VLBI correlator. This eliminates a number of small scale integrated-circuits (SSI) and medium scale integrated-circuit (MSI) packages and interconnections which reduce power requirements, and increase system reliability.

Choosing the appropriate correlator scheme offers additional savings in eliminating integrated circuit count. The choices are the geocentric versus the Haystack design approach. The correlation processing must be done at a common point. The Haystack approach is to move the data point of one station to coincide with the other station. The geocentric approach is to move all station processing points to the center of the earth. The Haystack correlator contains only one basic module per baseline for each BWS channel contain-

ing a decoder, phase calibration, variable delay, digital mixer, and correlator, as shown in Fig. 2. A Block 2  $N$ -station 28 BWS channel correlator will require  $28N(N-1)/2$  copies of this module for simultaneous, all baseline cross-correlation. The geocentric, however, is basically composed of two modules, as shown in Fig. 3. The first module consists of decoding, phase calibration, variable delay and digital mixer. This module increases by  $28N$  for an  $N$ -station 28 BWS channel correlator. The second module consists of cross-correlation function only and increases by  $28N(N-1)/2$ .

The ultimate Block 2 VLBI correlator may provide 6-station 28 BWS channels simultaneously processing. Using this configuration, the Haystack correlator scheme with its SSI and MSI hardware, will require 136.5K integrated circuits. The geocentric correlator scheme, which is the DSN design approach with its wide usages of LSI hardware, is estimated at 48.7K integrated circuits — an estimated savings of 87.8K integrated circuits.

### IV. LSI Architectural Overview

Single-chip microprocessors have been popular for the past few years and have been used in an increasing number of new applications. Because of their extremely small size and low cost, these programmable devices have brought about a revolution in digital systems. The major drawback of the MOS-based devices is their relatively slow speed, which restricts them to application that does not require high execution rates.

Compared to single-chip MOS microprocessors, bit-sliced microprocessors manufactured with bipolar technology provide the digital system with more flexibility and increase effective speeds. This increase in speed and system flexibility is achieved in the architectural philosophy of their CPU's. For MOS microprocessors the data processing function and control functions are both hardwired on the same chip, while for bipolar devices these two functions are realized on separate chips. The single-chip processors have predefined and unchangeable word length, architecture, and instruction sets. The opposite holds for microprogrammable bit-sliced microprocessors. They can be configured to provide a wide variety of digital system architectures with various word lengths and instruction set capabilities. One can optimize the system's architecture and processing capabilities for the unique requirements of his application. The final system becomes more flexible, since on-site implements, enhancements, or alterations in the system's architecture and capabilities can be achieved by changing the microinstructions in the PROM control memory.

## V. Utilization of Bit-Sliced Microprocessor

The fundamental VLBI cross-correlation structures are implemented with three bit-sliced machines, as shown in Fig. 4. Two of these machines are identical in both hardware and function. These phase processor machines are used to control the final alignment of the data streams and the phase reference frequency (LO) used for digital heterodyning. The alignment is accomplished in the fine delay buffer between the computer resident course delay buffer and the correlator mixers. All adjustments for observing geometry between stations are made in these buffers. Therefore, the buffer must be large enough to shift the delay by an Earth-radius or about 22 msec. At the Block 1 data rate of 500K bits, the data shift needed is  $1.1 \times 10^4$  bits. The two delay corrected data streams are then digitally mixed with a quadrature "sine wave" from a microprocessor-produced phase reference frequency. This reference frequency mixing is necessary for doppler compensation of the two data streams. The output produced signal from the mixers is a 3-level (-1, 0, +1) complex signal now ready for cross-correlation detection.

The second data path in the phase processor bypasses the fine delay buffer, as can be seen by Fig. 4, and is digitally mixed at a second mixer. This data path and mixer are necessary to coherently detect the tones of the phase calibration signal. These tones were injected into the receiver input at each station. The calibrator signal extraction controlled by the phase processor microprocessor is necessary for accurate BWS channel characterizing.

The phase processor is running at twice the data processing speed so that at each bit time, of the data stream, a new reference frequency update can be made for both mixers. Coherent detection is then completed in the hardware by accumulating the mixed calibration results in  $2^{24}$  binary up-counters. Transfers to the controlling computer can be requested at rates up to 8 sec, beyond which the counters could overflow.

The cross-correlation detection is implemented in a digital 16 lag complex correlator with results pre-accumulated in the binary up-counters, as shown in Fig. 4. The pre-accumulated data is transferred to the correlator processor memory under microprocessor control every 5K data bits. A complex 16 point fast Fourier transform (FFT) algorithm is then used to transform the data into a frequency spectrum. A phase shift is introduced by complex multiplication of the FFT output with a displacement angle. This transforms back to the time domain as a time shift or more appropriately, a fractional bit-shift. The displacement angle is known as the twiddle factor, where a  $11\text{-}1/4^\circ$  twiddle factor relates to a half bit shift. A twiddle factor of one degree gives tenths of a bit control in the

correlator. The twiddle FFT output values are then transferred to correlator processor memory for additional accumulation. The accumulation can continue for up to 8 seconds before transfers to the controlling computer take place.

The phase microprocessor computes the phase and phase-rate data values for each of the phase reference frequencies. It uses the phase, phase rate, and phase acceleration data provided by the controlling computer. It also computes the delay, as a function of time, for the fine buffer from the delay and delay rate data provided by the computer. A new phase-rate and delay rate is computed by the phase microprocessor every 5K data bits which is sequenced with the FFT/fractional bit correction.

The following sections present internal details of the VLBI correlator design.

### A. Data Format and Alignment

The VLBI correlator data is a Mark III format that the controlling computer has aligned by data time tags and stored on disk for direct memory access (DMA) transfer to the correlator. Figure 5 shows the DMA data cycle format where each DMA cycle consists of 5 frames at 20K bits a frame. This enables both data streams (one from each station) to be a length of 6-1/4K bytes and transmitted simultaneously to the correlator. The data processing rate is fixed at 1 mega bit/sec or twice the real-time sampling rate. After each DMA operation there is an idle period when no data is being transferred. This is necessary for memory to be reinitialized and specified where the next block transfer is to begin. During this period all I/O cycles from the controlling computer to the correlator are recognized. It may provide new phase and delay models for the controlling microprocessor, or may request a correlation sum dump.

The data streams are applied to identical fine delay buffers as shown in Fig. 4. This arrangement serves to align the two data streams to an accuracy of one bit. The delay buffering of each data stream is done by eight dynamic random access memories (RAM) that have a 16K  $\times$  1 bit organization. The 0.128 million bit delay can delay the data streams (1 megabit per sec) for a maximum of 128 msec. The memory writes and reads at the DMA interface rate of one MHz. The amount of delay is set by its controlling microprocessor which computes a new delay as a function of time from delay and delay rate data provided by the computer. A new delay rate is computed every 5K data bits by the microprocessor.

### B. Digital Heterodyning

The outputs of the delay buffers are applied to multipliers that digitally "heterodyne" the center of the frequency band

of interest down to near zero frequency rate. Frequencies outside the band of interest can then be removed by cross correlation.

Traditional analog heterodyning techniques for shifting a band of frequencies into a fixed bandpass filter have image-frequency problems. In band-selectable analysis, the samples of the input waveform are multiplied digitally by samples of a complex waveform,  $\cos 2\pi fct - j \sin 2\pi fct$ , instead of using a real multiplication by  $\cos 2\pi fct$ . The effect of this complex multiplication is to slide the whole frequency spectrum to the left along the frequency axis so the selected center frequency ( $fc$ ) is at zero rate. Frequencies that otherwise would become close-in frequencies thus maintain their relative positions with respect to the desired frequency band and are readily removed by cross-correlation.

The result of the multiplication (digital mixing) is two data streams for each original delay buffered data stream. One represents the real components of the frequency-shifted spectrum and the other represents the imaginary components. The two dual data streams are cross-correlated in digital hardware to obtain the desired parameter association or interdependence and then stored in RAM where they are held for subsequent processing.

The samples of the waveform,  $\cos 2\pi fct - j \sin 2\pi fct$ , used as the local oscillator (LO) signal, are produced by a digital generator that uses sine and cosine values from a table stored in read-only memory (ROM). A block diagram of the generator is shown in Fig. 6. A binary representation of the selected center frequency is stored in a latch. This number determines the incremental phase angle between samples of the output sine and cosine wave. For a given phase, both  $\cos \theta$  and  $-\sin \theta$  are computed for a 3-level waveform, as shown in Fig. 7. This LO signal with period T does have harmonic frequencies which, when mixed with input data, will produce unwanted mixing products and reduce the signal-noise (S/N) ratio by 7.4%.

The block diagram shown in Fig. 4 also shows a second set of digital mixers. This set is used to extract the calibration signal from the data. The calibration signal is injected into the receiver input at each station, therefore there are no observing geometry differences and the path bypasses the delay buffer. Figure 7 shows the composite waveforms of the sine and cosine LO which, as shown, is a two bit approximation to a sine wave. One of these two bits, the sign of the LO, is multiplied with the calibration data stream and digitally integrated in two  $2^{12}$  binary up-counters. The second bit controls whether the calibration bits are to be counted or not.

A few words about the  $2^{12}$  bit up-counters. The 12 stages of binary counters are achieved by using VLA-2 custom integrated circuits (I/C). The custom I/C was developed for the very large array (VLA) project of the National Radio Astronomy Observatory (NRAO). The I/C eliminates the number of SSI and MSI packages in the digital integration circuit by a factor of 10.

The VLA-2 is a 12-stage integrator with 12 bits of secondary storage. The 12 stage counter can integrate the results of up to 4095 correlation products (or any number if cascaded) while the secondary storage shift register is providing access to the 12 bits of previous integration. The VLA-2 is of low power Schottky technology and is in an 8-pin dual-in-line package allowing two integrator functions per 16 pin socket to be achieved.

### C. Alignment and Heterodyning Control

The data stream alignment and heterodyning control comes from a micro-programmable bit-sliced microprocessor. The microprocessor instruction set capabilities are configured in programmable-read only memories (P-ROM). The microprocessor consists of 16 registers 32 bits each, a 32 bit arithmetic-logic unit (ALU), and decode logic. Four of the registers are called  $\phi$ ,  $\phi c$ ,  $\dot{\phi}$ , and  $\dot{\phi} c$ .

The  $\phi$  and  $\phi c$  registers hold the value of the present phase and are updated each clock (bit time) by the amount in the  $\dot{\phi}$  and  $\dot{\phi} c$  registers, respectively. The 3 most significant bits of the  $\phi$  and  $\phi c$  registers are used as the addresses to the digital generator ROM. The  $\phi$  register addresses the ROM which produces the LO data for cross-correlation, and the  $\phi c$  register addresses the ROM which produces the LO data used in extraction of the calibration signal.

Each bit time the phase registers  $\phi$  and  $\dot{\phi}$  are added together which, when integrated over time, produces a phase error accumulation. This phase error accumulation, or roundoff error, is reduced to near zero every 5K data bits by the microprocessor performing a simple algorithm. The algorithm is shown in Fig. 8 and is identical for both correlator and calibrator signal extraction.

The procedure requires three different phase correction events and several holding registers within the microprocessor. The first phase correction event provides quadratic phase tracking by register  $\phi$  being updated by register  $\dot{\phi}$  via the 32 bit ALU adder. The next event reduces the  $\phi$  register roundoff error to near zero and corrects for the time required to complete this algorithm. The last event is used to establish quadratic phase tracking for the roundoff operator of event two.

Along with the phase correction algorithm and its three events is an additional fourth event that computes the data stream alignment in the buffer delay. The delay register  $t$  is updated by delay rate register  $i$  and this updated  $t$  register is then jammed into the buffer read address counter.

The microprocessors used in data stream alignment and heterodyning control is of a type that it has to use its decision-making abilities on a fast stream of incoming data. For Block 2 this requires an intelligent front end that can process an LO for both correlation and calibration every 250 nsec or a 32 by 32 bit addition in 125 nsec. The new version of the Advanced Micro Devices 2901A, using a blend of low-power Schottky and ECL, from National Semiconductor, offers this type of speed. Using its Schottky coupled logic (SCL) process, National's IDM2901A-1 is 50% faster than standard low-power Schottky four-bit slice designs. Advanced Micro Devices is also offering an equivalent part (2901C) in June 1979.

#### D. Cross-Correlator

The correlator design includes sixteen 4-megabit correlator lags each of which computes complex cross-product sums. The correlator design also includes digital integration of these cross-product sums. This digital integration is only for intervals of 5K data bits of cross-correlation. The integrated data is then sent to RAM for further processing.

The lags of the correlator are implemented by using a 16 bit shift register, see Fig. 9. One of the 3-level complex data streams, from the heterodyning process, is sent to this shift register with each of its 16 delayed outputs multiplied by the other complex data stream. The complex data streams consist of a real and imaginary 2-bit signal approximations or a total of 4 data lines for each stream. The cross-multiplication is accomplished by the 4 data lines from each station being used as addresses to a 256 X 8 P-ROM. Sixteen P-ROMs are required, one for each of the sixteen lags being cross multiplied.

The 3-level by 3-level complex multiplication is shown below:

$$\begin{array}{l} \text{Stream 1} \quad \text{Stream 2} \\ (x + iy) \quad (u + iv) = (xu - yv) + i(xv + yu) \end{array}$$

Because of the 3-level approximation of the signal, the sign ( $S$ ) of the signal will be  $\pm 1$ . The magnitude ( $M$ ) of the signal will equal 1 or 0. Therefore, the functions  $x$ ,  $y$ ,  $u$ , and  $v$  can be replaced by the sign and magnitude of the signal.

Where:

$$x = SxMx \quad y = SxMy \quad V = SvMv \quad u = SuMu$$

Therefore the complex multiplication becomes:

$$\begin{aligned} & (SxSu MxMu - SySv MyMv) \\ & + (SxSv MxMv + SySu MyMu) \end{aligned}$$

As can be seen from the above equation the real and imaginary cross-products may have quantitative values of -2, -1, 0, 1, or 2. Because the cross-product integration is implemented in up-counters and not up/down counters, the multiplying P-ROM also does a +2 addition to each cross-product value. The new qualitative offset values become 0, +1, +2, +3, +4, from which counts are accumulated for each complex lag in VLA-2 custom integrated circuit. Four VLA-2 IC's, two real and two imaginary, are used for each lag of the cross-correlator with 24 binary counter stages per complex lag. At the end of the cross-product integration period, the data is transferred to the correlation microprocessor where it is normalized. This zeroes the offset that occurred by using upcounters. The zeroed sums are then stored in RAM for subsequent processing.

#### E. Processing the Cross-Correlated Data

The cross-product sums stored in RAM are first processed by a fast Fourier transform (FFT) algorithm. The result of the FFT processing is a series of 32 values representing the real and imaginary part of the input waveforms cross-correlated at 16 points. The second process operates on the 32 values by multiplying a predetermined phase or twiddle factor to the values. This changes the phase relationships of the frequency components that were originally derived from the real and imaginary data. The process gives the equivalent of a fractional bit shift in the time domain over a full one bit range. These 32 twiddled values are then accumulated in RAM for later transfer to the controlling computer. The microprocessor used to derive the FFT and twiddle process is also the National IDM2901A-1 organized with a 16 bit word length.

Computing the FFT for a time record consisting of  $N$  amplitude samples  $X(n)$ , where  $n=0, 1, 2, \dots, N-1$ , the fast Fourier transform calculates the frequency spectrum  $X(k)$ , where  $K = 0, 1, 2, \dots, N-1$ , at  $N$  frequencies:

$$Z(K) = \sum_{N=0}^{K-1} X(n) e^{-j2\pi nK/N}$$

To achieve the necessary processing speed, the FFT firmware in the VLBI correlator implements this calculation with integer arithmetic. The firmware is designed to achieve the highest possible processing speed without unreasonable requirement on the program memory space and to minimize noise introduced by truncation and rounding without introducing arithmetic overflow problems.

The complex FFT algorithm is applied to all 32 lag values which derive both the positive and negative frequency components of the original cross correlation record. The positive and negative frequency component results are accumulated for later post processing. Both frequency components are needed because of the non symmetric spectrum due to cross-correlating of variable state space signals.

Processing speed efficiencies are achieved in the FFT firmware by implementing the 16 point FFT as a radix 2 decimation-in-time algorithm. This is commonly referred to as the butterfly. With this organization most of the multiplications internal to the transform are by factors of  $\pm 1$  and  $\pm j$ . These do not actually take up processing time so do not slow overall processor speed. Also, because of the places in the butterfly algorithm where multiplications occur, truncation and rounding introduce less noise.

In its final form, the FFT program package will consist of about 300 program instructions, the bulk of which are devoted to the butterfly subroutine. Much smaller portions are devoted to the control routines and an even smaller part is devoted to miscellaneous subroutines.

FFT processing, twiddle multiplying, and the accumulation process take about 2.5 msec to transform a cross-correlated time record into an accumulated frequency correlated spectrum. With the microprocessor executing the FFT multiplications, frequency spans of up to 2 MHz are a real-time operation. That is to say, there is no gap between the end of one correlation record and the beginning of the next. This is because the correlator can acquire a new correlation record while simultaneously processing the previous record stored in memory.

The correlation microprocessor also computes the twiddle for fractional bit correlation from the twiddle and twiddle rate data provided by the controlling computer. The computed twiddle is used to access a sin/cos ROM lookup table which produces the bit fraction increment. Using this FFT and

twiddle digital processing algorithm, fractional bit drift of 5% or less is possible.

## VI. Summary and Status

This article looked at the specialized structures of the digital signal processors within the VLBI correlator. This correlator is designed to accommodate Block 1 DSN requirements, but it is designed with enough flexibility to allow an efficient move to also serve the radio astronomy community as well as future DSN needs.

The correlator is a geocentric design which requires a delay buffer and mixer for each station data stream. Each buffer and mixer is controlled by a 32 bit microprocessor. The microprocessor aligns the data and produces LO signals used for correlation and calibration heterodyning. The cross correlator is a 16 lag complex correlator which computes 32 cross-product sums. These 32 sums are processed by an FFT and twiddle factor algorithm under a 16 bit microprocessor control. This algorithm gives the equivalent of a fractional bit shift in the time domain. The 32 values, representing the corrected real and imaginary part of the cross-correlated input waveforms, are accumulated in RAM for later transfer to the controlling computer.

At the present time, the delay buffer, mixers and controlling microprocessor hardware have been designed, and are under construction. The cross-correlator and controlling microprocessor hardware designs are about complete. The micro-code firmware assembly has started with firmware/hardware checkout set to start at the end of hardware construction or about March 1979. The VLBI correlator has been configured on 5 DSN standard subchassis and packaged in a 48-inch-high rack.

The power of digital signal processing now becoming available through use of large-scale integrated circuits is giving instruments like the VLBI correlator unprecedented flexibility and computational power at relatively low cost. This article reviewed only the correlator signal processing techniques and did not cover other important tasks the correlator hardware is capable of performing. One of these tasks is self-diagnosis, where the microprocessor checks itself using diagnostics firmware. In this way, the microprocessor system is required to detect a failure so that it can shut down all or part of the system, provide warnings or alarms, and possibly switch in back-up systems. This and other important tasks are being designed into the VLBI correlator which will give it the widest possible range of service.

## References

1. Muhall, B.D.L., "The DSN VLBI System, Mark 1-79," *The DSN Progress Report 42-46*, August 15, 1978, pp. 5-15.
2. Lushbaugh, W. and Laylang J., "Preliminary Design Work on a DSN VLBI Correlator," *The DSN Progress Report 42-43*, February 15, 1978, pp. 90-97.

## Acknowledgements

The authors wish to acknowledge the assistance of a number of CIT and JPL personnel, and Dave Rogstad, Brooks Thomas and particularly Marty Ewing, who originally conceived the VLBI correlator architectural design.

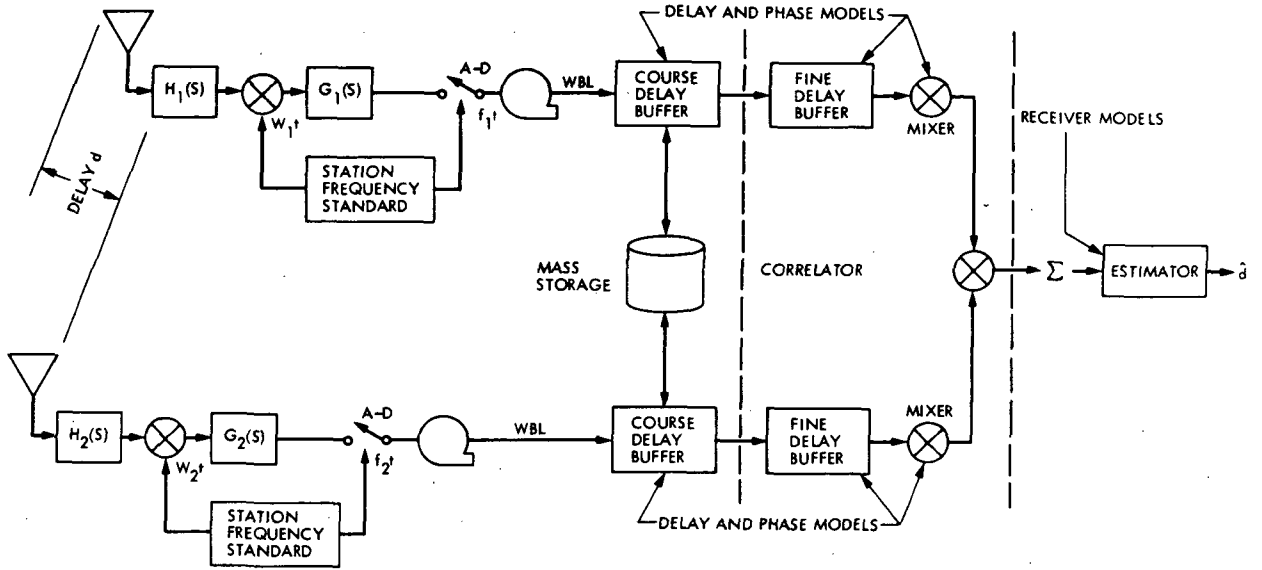


Fig. 1. VLBI data acquisition and processing (simplified)

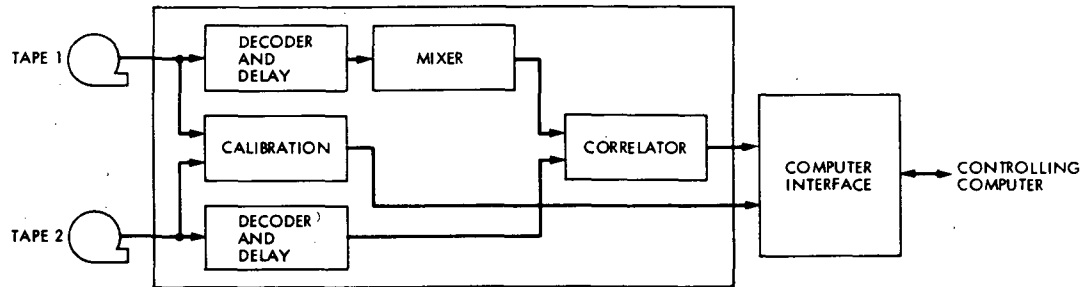


Fig. 2. Haystack correlator scheme (1 baseline, 1 frequency channel)

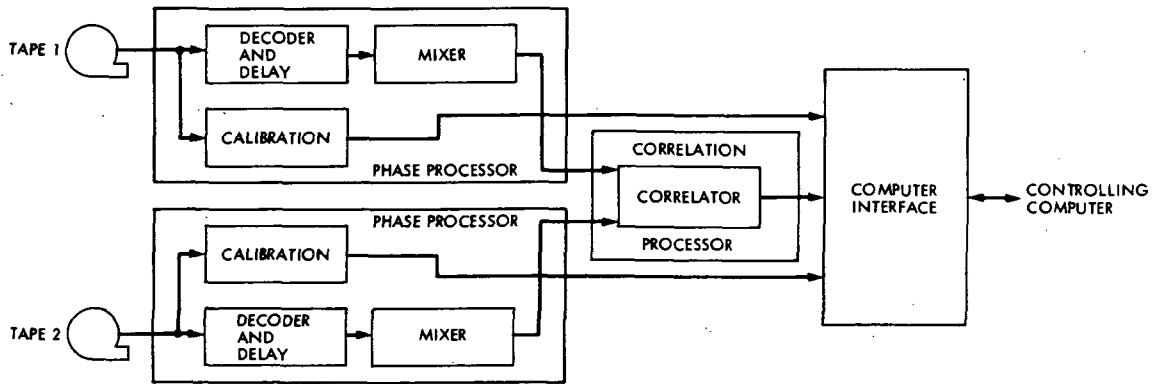


Fig. 3. Geocentric correlator scheme (1 baseline, 1 frequency channel)

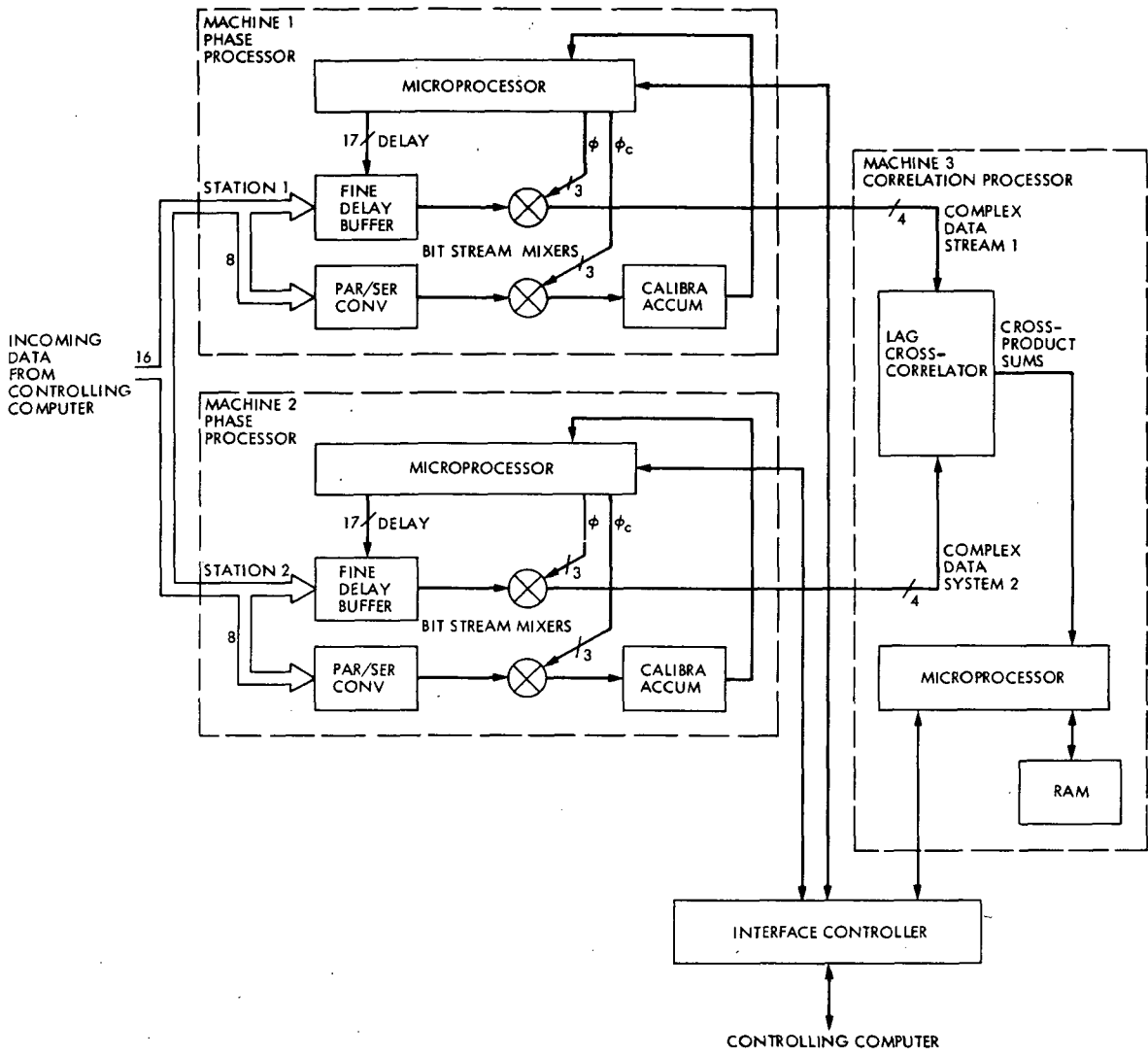


Fig. 4. Three machine VLBI correlator block program

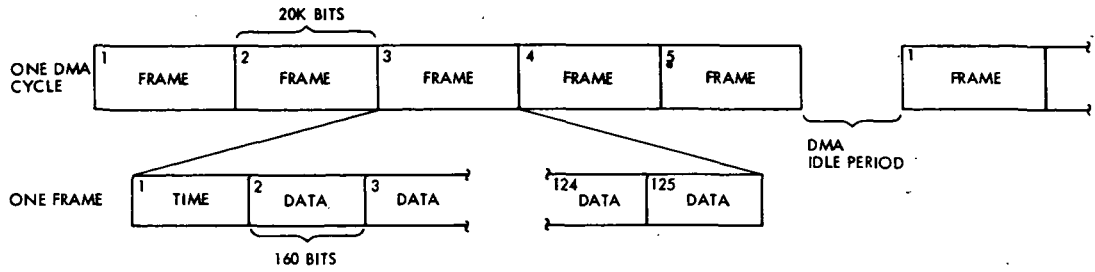


Fig. 5. DMA data cycle format

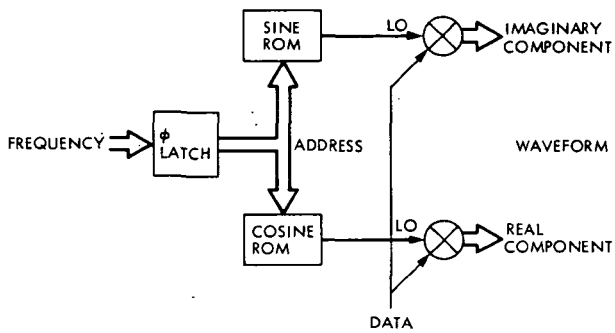


Fig. 6. Digital oscillator and mixers

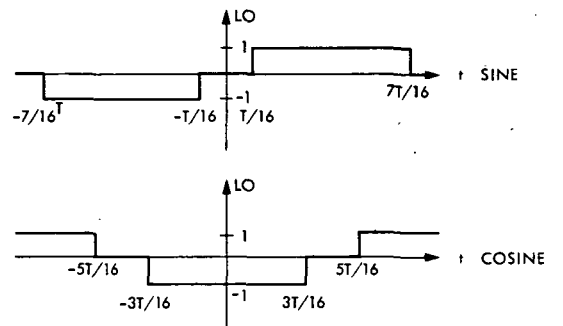


Fig. 7. Sine and cosine approximations

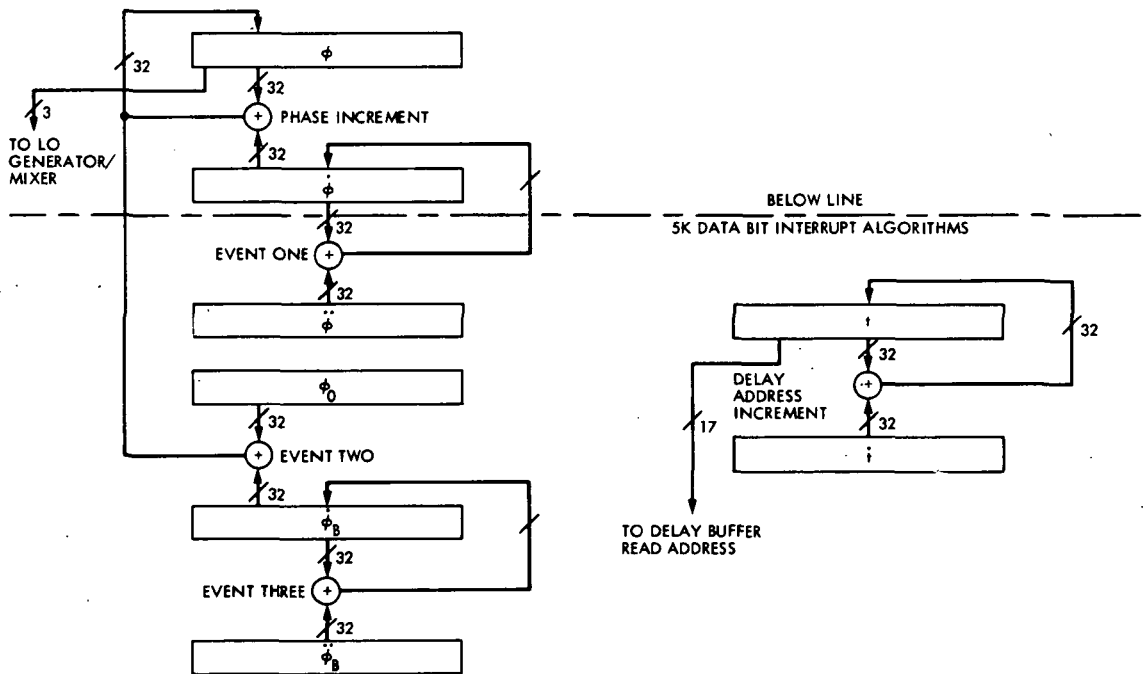


Fig. 8. Phase-delay correction algorithms

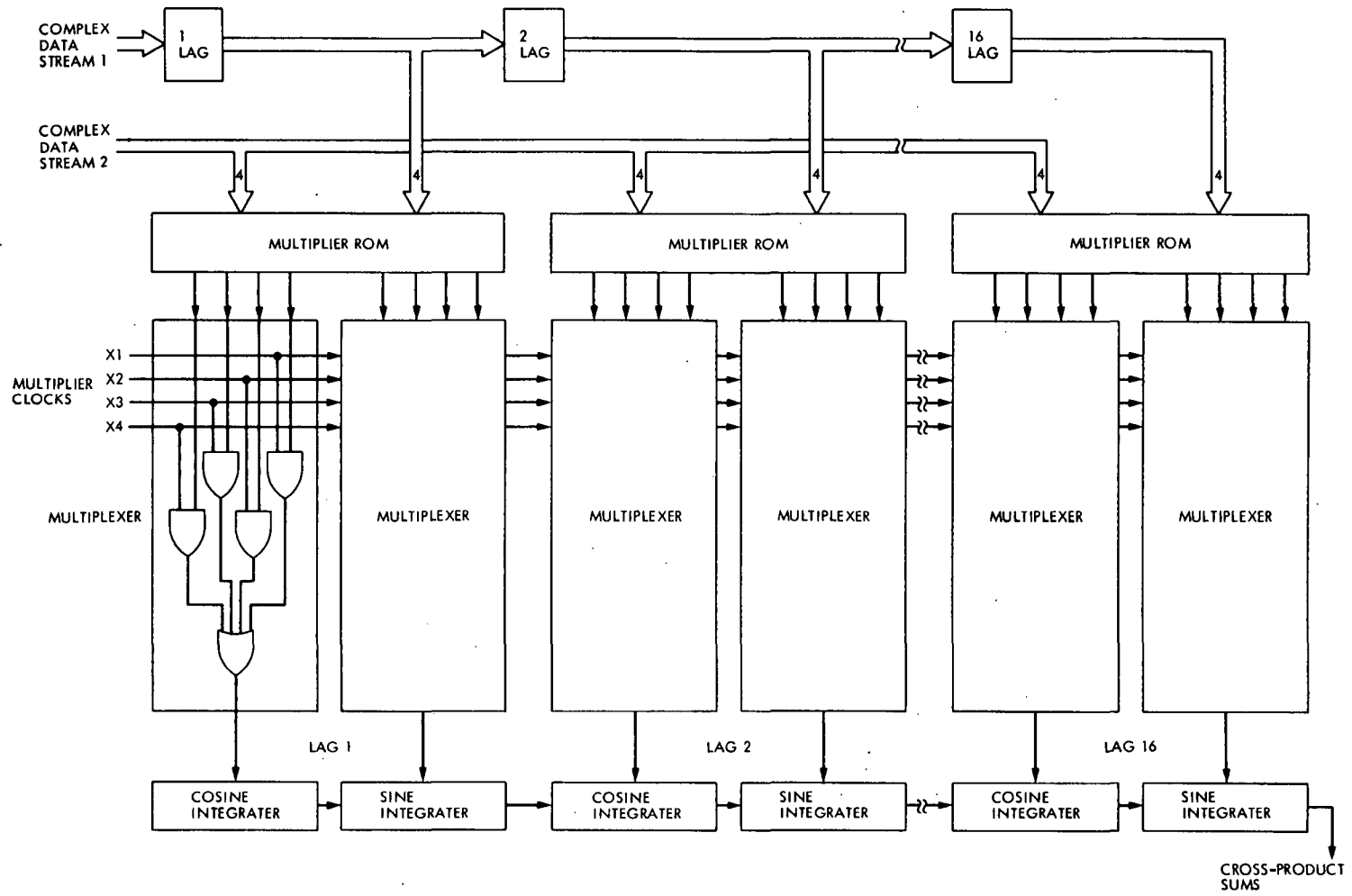


Fig. 9. VLBI cross-correlator

D31

N79-22171

# The Symbol Synchronizer Assembly

M. J. Galitzen

DSN Data Systems Section

*The Symbol Synchronizer Assembly improvement effort is directed at three goals: to increase the maintainability, operability and reliability within the analog-to-digital conversion portion of the SSA's phase lock loop and telemetry data extraction channels. In achieving these goals we propose to replace obsolete, nonmaintainable and unreliable electronic and mechanical devices with readily available electronic equipment of modular solid state design.*

## I. Introduction

The primary function of the Symbol Synchronizer Assembly (SSA) is to phase lock a local data clock with a demodulated telemetry data stream. This function is accomplished by means of a hybrid analog/digital phase-locked-loop. The SSA's phase-locked local data clock enables the SSA to perform telemetry data bit detection for encoded telemetry and symbol estimates for coded telemetry. This information is then transferred to computers or external decoders for further processing. The SSA's were implemented in the Deep Space Stations starting in 1970. While still performing the basic functions, recent failure analysis has shown that the SSA's are experiencing a higher than desired failure rate. Analysis of the failure reports showed three assemblies within the SSA's which, because of age and commercial nonavailability, are becoming increasingly difficult to maintain and calibrate at the Deep Space Network maintenance depot. These same three equipment areas can become a major DSN station reliability problem if corrective action is not taken. The specific SSA hardware areas in question are listed below:

- (1) The coaxial switch assembly.
- (2) The loop integrator board and assembly.

- (3) The analog-to-digital - digital-to-analog (A/D-D/A) converter assembly.

These three assemblies make up the input signal selection matrix, the analog telemetry signal processing channels and the analog-to-digital transition A/D-D/A equipment. It is within these three assemblies that the transition from the analog (raw telemetry data) to the digital (digitized telemetry) is accomplished.

## II. Existing Telemetry Subsystem

Figure 1 shows a fundamental block diagram of the telemetry data path from a spacecraft to the telemetry subsystem. An overview of this system will place the telemetry system in perspective with respect to the spacecraft data reception path and also show the importance of the areas that we propose to upgrade. The spacecraft transmits modulated radio frequency signals to the DSN antennas. This signal is processed and down-converted in frequency within the receiver subsystem. The Subcarrier Demodulator Assembly (SDA) extracts the raw telemetry data at its base rates of 5.6 to 250,000 symbols per second.

The SDA output level is a nominal  $\pm 141$  millivolts peak signal in noise. The telemetry input channels which process these signals are located within the SSA. The SSA is required to process and extract telemetry from an SDA signal with a signal-to-noise ratio as low as  $-5$  dB. Figure 2 shows the front end of the telemetry subsystem and emphasizes the three assemblies within the SSA that were covered in the introduction. Problems within these assemblies will be explained next.

The coaxial switches within the present SSA Interface Assembly receive four different inputs. These coaxial switches then provide isolation and data paths to the SSA logic. There are four coaxial switches associated with this function. The four inputs are typically comprised of three SDA inputs and a test input, although any input port can receive and process telemetry data. Control of the  $4 \times 1$  selection matrix is controlled by the Telemetry Subsystem Assembly (TPA) computer through the SSA interface logic.

Problems associated with these coaxial switches center in their mechanical contacts. Typical failure mode is an intermittent contact closure. Location and removal of the intermittent coaxial switches from the SSA rack is difficult. Physically, the coaxial switches are located in the bottom rear portion of an SSA equipment rack. Removal requires station floor board removal for access to the rack bottom. Also numerous cables must be disconnected before the coaxial switches can be removed from inside their mounting assembly. Besides these difficulties, the cost of these coaxial switches is now approximately 4 times the original cost. Replacement cost of a single coaxial switch is now approaching \$1000 from an initial \$250 cost. The order lead time for these units is now several months.

The Loop Integrator Assembly (LIA) and its circuit board will be the next SSA problem area covered. It is shown in Fig. 2 that the LIA receives its inputs from the coaxial switches. The LIA is located in the upper front portion of the SSA equipment rack. The long cable path from the coaxial switches to the Integrators induces noise into the telemetry.

The Loop Integrator provides precision amplification, signal integration and telemetry bit transition detection within the noise bandwidth of the telemetry channel. The SSA detects and phase locks the station data clock to the spacecraft data clock. In this manner the spacecraft data can be detected, formatted and processed. A weakness in this system is that all data and phase processing is accomplished on a large printed circuit board. Failure in one channel of this board requires removal of all analog circuitry within the SSA. Therefore, when this board is replaced, all analog adjustments must be redone to ensure proper operation. These are critical adjust-

ments that consume time. They must be made after the board has reached thermal stability, which can take hours.

Repair of the Loop Integrator board is also difficult as these boards have three layers. This means that there are three circuit etches, one on each side of the board and one centered (pancaked between the two outer layers). Because this is a multichannel board, the component density is quite high and the etch is complex. Repair of board circuitry involved in the center etch is very difficult. In some cases the board has to be cut, new components soldered in, and new epoxy applied to secure the repair. During this process, boards have been destroyed or after repair have had trouble meeting minimum Q.A. standards. There is a tendency to expend additional cost and efforts to requalify these marginal boards.

The A/D-D/A Converter Assembly is the last SSA area in which corrective measures are recommended. Figure 2 shows that the A/D-D/A Converter Assembly is driven by the LIA, which is in turn driven by the SDA through the coaxial switches.

The A/D-D/A Assembly consists of two identical 12-bit analog-to-digital converters (A/D's), one 5-bit A/D, and one 12-bit digital-to-analog (D/A) converter. The two 12-bit A/D's digitize the telemetry input from the integrate and dump circuits of the LIA. The science and engineering telemetry is then extracted from this 12-bit conversion. In addition, these 12 A/D bits provide the basis for determining the SSA loop lock within the TPA computers. The 5-bit converter is used in the SSA phase-lock-loop to digitize the telemetry signal and drive the phase-lock-loop's logic to minimize the loop's lock error at a telemetry data transition. The 12-bit D/A converter receives and converts the accumulated error of the 5-bit A/D phase channels. The 12-bit D/A then provides an analog voltage which is used to drive the SSA frequency synthesizer.

It is through this process that the phase-lock-loop is closed and the output frequency of the synthesizer is kept in phase with the spacecraft telemetry signal data transitions. The synthesized frequency is then used as a data rate to synchronize the SSA to the spacecraft.

The maintenance and repair to the approximately 10-year-old A/D-D/A converter assembly is a problem, as the manufacturer has been out of business for approximately four years. The assembly consists of 31 circuit boards containing discrete components, none of which are supported by a manufacturer. In addition to the complexity and card count, this converter is difficult to calibrate. Without factory support the DSN maintenance depot must maintain the capability to

repair and calibrate the unit, which is becoming more difficult with time.

### III. SSA Prototype Upgrade Assembly

This section will present information about a prototype SSA upgrade assembly which has been assembled and tested within three different SSA's. Figure 3 is a block diagram of the prototype assembly, which functionally performs the same telemetry process that is accomplished in the present SSA (Fig. 1). In Fig. 3, the functions are divided into seven functional blocks from the three functional blocks in Fig. 1. Seven circuit cards are used to implement the design in Fig. 3. These cards mount in a 5-1/4-inch front panel chassis along with  $\pm 15$ -volt and +5-volt power supplies. The chassis back panel contains a fan, AC power plug and fuse, 4 multipin connectors, and 6 coaxial connectors. The multipin connectors provide timing, control, and status signals used within the prototype assembly. These connectors will connect to the existing SSA harness without modification to the SSA.

The input telemetry or test inputs are switched through four 16-pin analog switches, which provide isolation, loading, and the status functions now performed by the SSA mechanical coaxial switches. These analog switches are controlled by the TPA computer through the SSA computer status and monitor board within the prototype assembly. The selected telemetry data is then reamplified in the gain select amplifiers, which are on the same card as the four analog switches. The output of this card then becomes the input to the two identical 12-bit A and B data channel cards and the 5-bit phase channel card. The two data channels contain an integrator, sample and hold amplifier circuit, and a 12-bit A/D converter. The outputs of these converters are switched through the multiplex card and sent as the digitized telemetry to the SSA and TPA.

The 5-bit phase card contains an integrator, sample-and-hold amplifier, zero crossing detector circuit, and 8-bit A/D converter. Only 5 of the 8 bits are used in the prototype assembly. These 5 bits are processed within the SSA's phase error logic. The zero crossing detector detects the telemetry data's edge transition. This transition is used in the SSA's phase and data processing logic.

The 12 bit D/A and pulse shaping card receives digital phase and clock signals from the SSA. The 12 bits of phase information are converted to an analog voltage which is proportional to the phase error between the telemetry signal and the DSN station clock. This error voltage is amplified in the gain selector logic card and then fed back as the phase-lock-loop error voltage to the SSA's frequency synthesizer. The synthesizer

output is used to clock the SSA logic and close the phase-lock-loop. The D/A card also contains pulse shaping and timing interface circuits required to interface the SSA to the prototype logic. The status and monitor card is the seventh card needed to implement Fig. 3's design. This card provides a control interface point for signal status and prototype monitoring required by the SSA and TPA.

Many of the reasons for going to this modular seven card design have been covered. This design combines the three functional blocks listed in Part II into one chassis. The switching, data processing, and A/D-D/A conversion process is then divided into functional blocks. The seven functions are then implemented on separate circuit cards of simple construction, which reduces the number of discrete components used. The present SSA A/D converter requires 31 circuit cards. This same function is accomplished on only part of each of the two data channel cards and the phase channel card. The reduced complexity of the A/D-D/A converter assembly will greatly shorten the calibration time. The modern modular replacement A/D converters can be calibrated in approximately one hour. A technician is typically required to adjust two potentiometers, which set the A/D's zero reference and gain. The D/A requires two external adjustments of equal simplicity. The A/D and D/A modules are presently being manufactured and are under GSA contract. The problem with the SSA multichannel three-layer analog board has been corrected in the seven-board prototype as the new cards are of two layer construction.

Table 1 lists the electronic components required for the prototype assembly vs the equivalent operational SSA assembly. The prototype assembly has approximately one-ninth the number of parts required in the SSA. The prototype assembly has no mechanical parts such as the 13 relays and 4 coaxial relays used in the SSA.

### IV. SSA Prototype Upgrade Testing

The telemetry system within the JPL Compatibility Test Areas-21 (CTA-21) has been used to test and evaluate the prototype assembly. The telemetry system at CTA-21 contains three SSA's. In some of the testing, an operational SSA was driven by a simulated telemetry data input from an SDA. The output of the SDA is set to give a specific SSA signal-to-noise ratio and symbol error rate. The operational SSA's output is then compared to the theoretical probability of performance. For some of the data points the prototype assembly was then connected to the SDA and SSA. The constant SDA output was then processed as an input to the prototype assembly. Comparison of SSA vs prototype assembly data is shown in

Table 2. Comparison data was taken at 250, 230.4, 100.0, 50.0, 28.0, 13.5, 12.5, and 1K symbols per second. Many additional data points for the prototype assembly were taken and are shown on Table 2. This data demonstrates that there is a good operational comparison between the prototype assembly and an operational SSA.

Further evaluation of the prototype assembly is being performed at CTA-21. The prototype assembly is now connected to one of the operational SSA's. This temporary configuration will exist for approximately a one-month evaluation period. During this time we will evaluate the prototype semi-operational performance.

**Table 1. Equivalent SSA vs prototype parts count**

	Upgraded assembly	Present SSA assembly
<b>Part description</b>		
1. Components, resistors, capacitors, transistors, integrated circuits, and diodes	395	3768
2. Relays	None	13
3. Coaxial relays	None	4
4. Power supplies	$\frac{2}{\pm 15, +5 \text{ Vdc}}$	$\frac{6}{+15, -15, +25, -25, +5, +8 \text{ Vdc}}$
5. Adjustment potentiometer	19	53
6. Operational amplifiers	10	6
<b>Total: all components</b>	<b>427</b>	<b>3850</b>

**Table 2. SSA vs upgrade assembly symbol error rate signal-to-noise data**

Symbol data rate	Data coding	Prototype		SSA	
		SNR(dB)	SER(%)	SNR(dB)	SER(%)
8 Hz	Uncoded	7.04	0.07		
100 Hz	Uncoded	3.49	1.56		
1.00 kHz	Uncoded	-0.37	8.84	-0.33	8.29
10.00 kHz	Uncoded	-2.93	16.02		
12.5 kHz	Coded	0.95	5.69	0.62	6.0
13.5 kHz	Uncoded	-4.05	18.92	-3.79	18.52
18.0 kHz	Uncoded	0.29	7.22		
22.0 kHz	Uncoded	0.27	7.14		
28.0 kHz	Uncoded	-1.54	11.81	-1.44	11.69
44.0 kHz	Coded	-1.20	11.31		
50.0 kHz	Coded	0.66	6.41	0.91	6.44
56.0 kHz	Coded	0.84	5.99		
70.0 kHz	Coded	-4.45	20.15		
80.0 kHz	Coded	0.76	6.0		
100.0 kHz	Coded	0.62	6.28	0.77	6.06
130.0 kHz	Coded	0.97	5.66		
160.0 kHz	Coded	0.36	7.03		
200.0 kHz	Coded	0.76	6.06		
230.4 kHz	Coded	-0.13	8.02	-0.71	8.22
250.0 kHz	Coded	0.42	7.04	0.48	6.84
250.0 kHz	Coded	-5.89	23.36	-3.94	20.56 <sup>a</sup>

<sup>a</sup>The operational SSA would not lock up at the -5.89 dB of the upgrade assembly. It was necessary to reduce the signal input SNR by 1.5 dB before the operational unit locked.

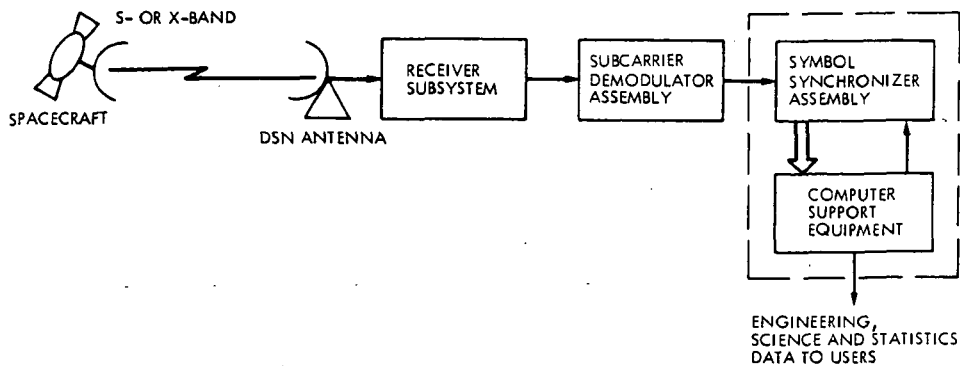


Fig. 1. Typical telemetry path at a DSN station

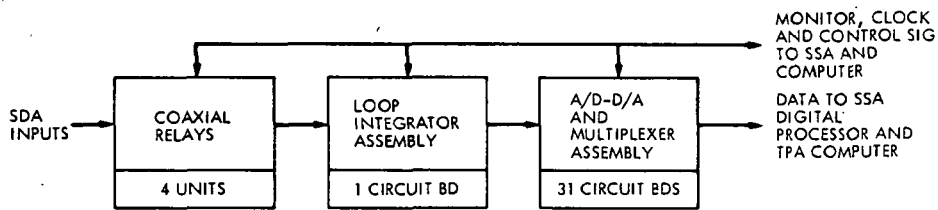


Fig. 2. Present SSA analog-to-digital conversion functional diagram

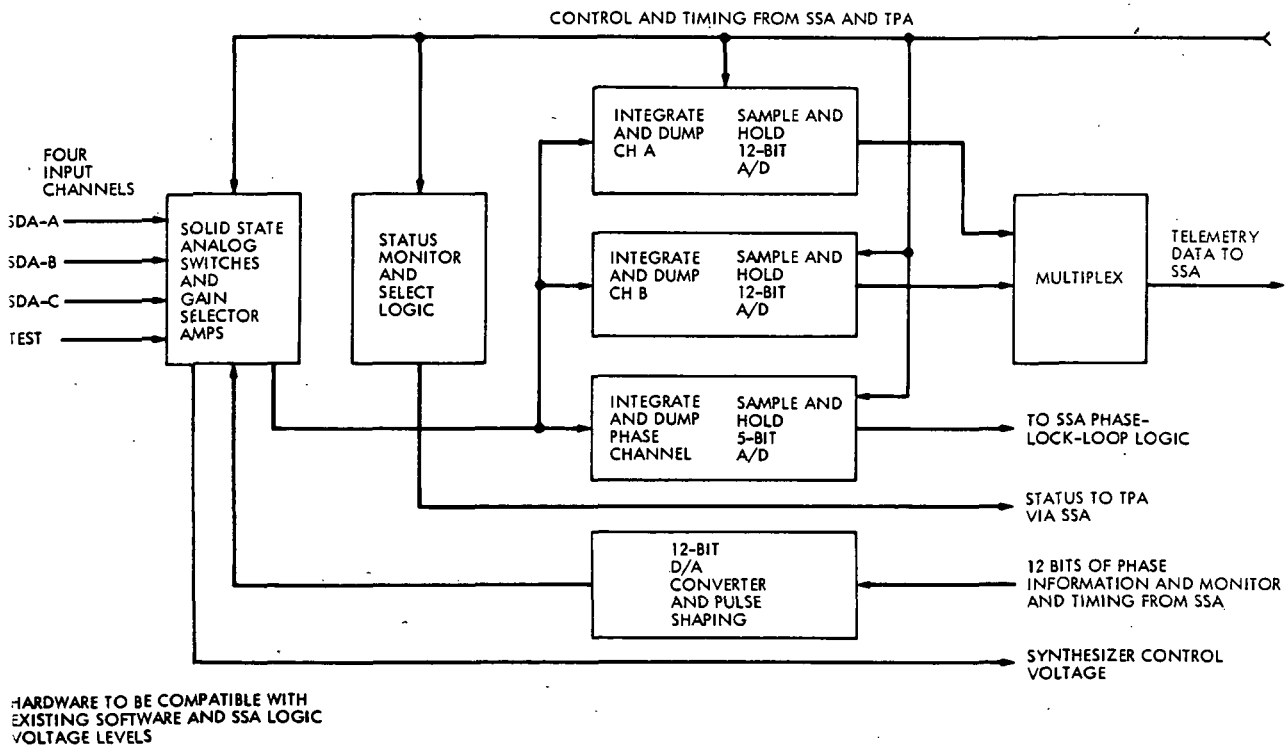


Fig. 3. SSA upgrade block diagram

NTIS does not permit return of items for credit or refund. A replacement will be provided if an error is made in filling your order, if the item was received in damaged condition, or if the item is defective.

*Reproduced by NTIS  
National Technical Information Service  
U.S. Department of Commerce  
Springfield, VA 22161*

**This report was printed specifically for your order from our collection of more than 2 million technical reports.**

For economy and efficiency, NTIS does not maintain stock of its vast collection of technical reports. Rather, most documents are printed for each order. Your copy is the best possible reproduction available from our master archive. If you have any questions concerning this document or any order you placed with NTIS, please call our Customer Services Department at (703)487-4660.

Always think of NTIS when you want:

- Access to the technical, scientific, and engineering results generated by the ongoing multibillion dollar R&D program of the U.S. Government.
- R&D results from Japan, West Germany, Great Britain, and some 20 other countries, most of it reported in English.

NTIS also operates two centers that can provide you with valuable information:

- The Federal Computer Products Center - offers software and datafiles produced by Federal agencies.
- The Center for the Utilization of Federal Technology - gives you access to the best of Federal technologies and laboratory resources.

For more information about NTIS, send for our FREE *NTIS Products and Services Catalog* which describes how you can access this U.S. and foreign Government technology. Call (703)487-4650 or send this sheet to NTIS, U.S. Department of Commerce, Springfield, VA 22161. Ask for catalog, PR-827.

Name \_\_\_\_\_

Address \_\_\_\_\_  
\_\_\_\_\_  
\_\_\_\_\_

Telephone \_\_\_\_\_

*- Your Source to U.S. and Foreign Government  
Research and Technology.*



U.S. DEPARTMENT OF COMMERCE  
Technology Administration  
National Technical Information Service  
Springfield, VA 22161 (703) 487-4650

---

---